UNIVERSITY OF SOUTHAMPTON

FACULTY OF ENGINEERING AND ENVIRONMENT

Computational Engineering and Design Group

Investigation on Meshfree Particle Methods for Fluid Structure Interaction Problems

by

Ali Javed

Supervisor: Dr. Kamal Djidjeli

Co-Supervisor: Prof. Jing Tang Xing

Thesis for the degree of Doctor of Philosophy

September 2015

Dedicated to my parents who sacrificed their present for my future

UNIVERSITY OF SOUTHAMPTON

ABSTRACT

FACULTY OF ENGINEERING AND ENVIRONMENT
Computational Engineering and Design Group

Doctor of Philosophy

INVESTIGATION ON MESHFREE PARTICLE METHODS FOR FLUID STRUCTURE INTERACTION PROBLEMS

by Ali Javed

The research aims to investigate the application of meshfree particle methods for computational modelling of the Fluid Structure Interaction problems with particular emphasis on flow around cylindrical objects and aerofoils. For this purpose, a solution scheme has been developed for solving incompressible, viscous Navier-Stokes (N-S) equations over meshfree particles. Spatial derivatives appearing in N-S equations are dealt with using radial basis functions in finite difference mode (RBF-FD). A comparative study has also been conducted between implicit and explicit in time solution schemes for N-S equations over meshfree nodes. Subsequently, a coupled meshfree and mesh-based solution scheme is proposed, over hybrid fluid grid, for incompressible, viscous flow around stationary as well as moving objects. The aim of this coupled solver is to provide efficiency and flexibility by combining the advantages of both meshfree and mesh-based methods. The coupled solution scheme suggests generating a body conformal meshfree nodal cloud around the solid body in the near field. A static Cartesian grid surrounds the meshfree cloud in the far field. The Meshfree nodes offer flexibility in dealing with solid motion by moving along the solid boundary without necessitating re-meshing. The Cartesian grid, on the other hand, provides improved performance by allowing faster computation owing to the use of efficient mesh based method. Flow equations, in Arbitrary Lagrangian-Eulerian (ALE) formulation, are solved using RBF-FD based scheme over moving meshfree nodes. Conventional finite differencing is used over static Cartesian grid for flow equations in Eulerian formulation. The coupled solution scheme, on hybrid grid, is employed for closely coupled Fluid Structure Interaction problems. The equations for solid motion are solved using classical Runge-Kutta method. Close coupling between fluid and structural solvers is realized by a sub-iterative prediction-correction algorithm. In order to reduce computational overhead due to sub-iterations, only near field flow (in meshfree zone) is solved during inner iterations. Solution over full fluid domain is sought during outer (time step) iterations only, when the convergence at fluid-solid interface has already been reached. The solution scheme is also applied for high Reynolds number problems. For this purpose, a stabilization term is included in the flow equations to suppress the spurious oscillations. The stabilization term is derived using

momentum balance equation over control volume and applying higher order Taylor series expansion of momentum flux and fluid forces. In order to avoid ill-conditioning and accuracy problems related to RBF matrices in domains having varying nodal density, use of shape adaptive RBFs are proposed. In that, the shape parameter of the radial basis function is varied according to local nodal density. Moreover, adaptive sizing of influence domain has also been introduced to maintain suitable number of neighbouring particles. These adaptive techniques are found to be useful as they allow much finer nodal distribution at regions of interest enabling accurate capturing of flow gradients and leading to better results. The use of hybrid grid offers flexibility in dealing with moving boundaries. Moreover, in addition to allowing faster computing over Cartesian grid, it also enables using the reduced fluid domain during inner FSI iterations and therefore helps reduce the number of computations in the fluid domain during fluid-solid coupling. The solution scheme was tested for problems relating to flows around static as well as moving cylinders and aerofoils. Flow induced vibrations have been studied with one and two degrees of freedom. The results are found to be in good agreement with previous numerical work and experimental results.

Contents

List of Figures

List of Tables

Declaration of Authorship

I, Ali Javed , declare that the thesis entitled *Investigation on Meshfree Particle Methods for Fluid Structure Interaction Problems* and the work presented in the thesis are both my own, and have been generated by me as the result of my own original research. I confirm that:

- this work was done wholly or mainly while in candidature for a research degree at this University;
- where any part of this thesis has previously been submitted for a degree or any other qualification at this University or any other institution, this has been clearly stated;
- where I have consulted the published work of others, this is always clearly attributed;
- where I have quoted from the work of others, the source is always given. With the exception of such quotations, this thesis is entirely my own work;
- I have acknowledged all main sources of help;
- where the thesis is based on work done by myself jointly with others, I have made clear exactly what was done by others and what I have contributed myself;
- parts of this work have been published as: (Javed et al., 2013a),(Javed et al., 2013b), (Javed et al., 2014a) and (Javed et al., 2014b)

Signed:.....

Date:.....

Acknowledgements

I thankfully acknowledge the continued and highly involved help and advices rendered by my supervisor Dr. Kamal Djidjeli in understanding the topic and shaping the aim and objectives of research. In addition to this, the valuable guidance provided by my Co-supervisor Prof. J. T Xing also helped me steer my research directions towards the right path. Thanks for various research students at the university with whom I had some good discussion which helped refine my research scope and move forward towards the intended direction.

Nomenclature

ASP	Adaptive Shape Parameter
ALE	Arbitrary Lagrangian Eulerian
CFSI	Closely coupled Fluid Structure Interaction
CFSI-FFD	Cosely coupled Fluid Structure Interaction with Full Fluid Domain
CFSI-RFD	Cosely coupled Fluid Structure Interaction with Reduced Fluid Domain
CV	Control Volume
DEM	Diffused Element Method
DQ	Direct Quadrature
EFGM	Element Free Galerkin Method
FD	Finite Difference
FE	Finite Element
FSI	Fluid Structure Interaction
IQ	Inverse Quadratic
IMQ	Inverse Multi Quadratic
LFSI	Loosely coupled Fluid Structure Interaction
MLS	Moving Least Squares
MLPGM	Meshless Local Petrov-Galerkin Method
MPS	Moving Particle Semi-implicit
MQ	Multi quadratic
N-S Equations	Navier-Stokes Equations
RBF	Radial Basis Functions
RBF-FD	Radial Basis Functions in Finite Difference mode
RBF-DQ	Radial Basis Functions-Differential Quadrature
SPH	Smoothed Particle Hydrodynamics
TVD	Time Varying Diminishing

Chapter 1

Introduction

1.1 Motivation for research

Interaction between fluid flow and structural deflection plays vital role in a number important applications such as aircraft industry (wings deformation), design of bladed machines (turbines, compressors and pumps etc.), renewable energy (e.g flapping foil energy harvesters), stability analysis of bridge structures and biomechanics (e.g. modelling of elastic artillery for stent design, blood flow simulations in vessels and vocal fold vibrations etc.). A good understanding of complex phenomena relating to fluid structure interaction (FSI) would provide valuable information relating to flow induced vibrations and dynamic stability of structure. Fluid structure interaction is therefore, the main focus of research in aero-elasticity and hydro-elasticity (Farhat et al. (1998); Dowell and Hall (2001); Feistauer et al. (2011)).

Analysis of flow around moving aerofoils or blunt bodies is one of the important applications of fluid structure interaction. The oscillations induced by flow around the wing structure can lead to unpredicted aerodynamic response, dynamic stall or even fatigue damage. Lately, the use of moving aerofoils has also been applied for flapping foil flow energy harvesting (Xiao and Zhu (2014)). These bio-inspired techniques utilize active and / or passive mechanical systems to extract renewable energy from flow induced motion of foils. It is therefore important to simulate flow induced vibrations, for various conditions, to evaluate the flow behaviour, identify the stability envelope and to understand various factors affecting the system response.

Analytical methods, used for solution of FSI problems, are restricted to some special cases only with simplified assumptions (Holmes and Marsden (1978)). The real life problems are however, often more complex and diversified. For example, consideration of viscous effects, transient response of fluid domain, non-linear structural deformation and simultaneous evolution of fluid and vibrating structural models are the aspects

of fluid-structure interaction which cannot be addressed using analytical approaches. Many researchers therefore resort to numerical techniques for solution and analysis of flow induced vibrations e.g. Duarte et al. (2004); Farhat et al. (2006); Badia and Codina (2007); Badia et al. (2008); Feistauer et al. (2011).

FSI problems are encountered when deforming or moving solid structures interact with the surrounding fluid. This movement changes boundary conditions for the fluid around the structure affecting the fluid motion. In addition to the changing boundary conditions, the phenomenon is often coupled with large deformation. A numerical solution scheme thus requires adaptive refinement, re-meshing and ability to accurately capture large deformations. These are the areas where grid based methods start to show limitations in terms of accuracy and flexibility of use. Traditional mesh based methods like the finite element (FE), finite volume (FV), finite difference (FD) are widely accepted as mainstream computational solution tools. However, despite their great success in numerical modelling and wide acceptability, grid based methods suffer from inherent limitations when applied to problems relating to moving boundaries (like FSI or Aero-elasticity). Such limitations impede their utilization in various applications and scenarios.

In this respect, the usability of commercially available packages like NASTRAN and ANSYS is limited. For example, in case of wing flutter analysis, NASTRAN can be used to determine critical flow velocities but post-flutter behaviour cannot be evaluated. Moreover, other non-linear phenomena associated with large amplitude of vibration cannot be captured (Sváček et al. (2007); Sváček (2008)). Therefore, in the realm of recent advancements in computational power, where numerical modelling has been made more efficient, there is a strong need to investigate the challenging problem of interacting fluid and structure using contemporary computational approaches.

Meshfree particle methods were developed as a result of efforts to find the solutions to the difficulties faced by mesh based methods (like those experienced in large deformation, complex geometries and free surface flow problems). The idea behind developing the meshfree method is that a domain represented only by a set of node or particles (without constraints of grid) would provide greater flexibility in dealing with the problems which are difficult to be addressed by mesh-based methods. Using meshfree methods, the connectivity constraints among the nodes are somehow eliminated which allows the nodes to move and morph more flexibly. Meshfree particle methods are therefore considered to be better suited for the problems involving moving boundaries, large deformations and adaptive refinement. As these are the attributes which are required for any numerical scheme dealing with FSI problems, use of meshfree particle methods is increasingly becoming popular for such applications. In fact, Fluid Structure Interaction is amongst the many areas where use of meshfree methods has proven be a better choice than grid based methods (Rabczuk et al. (2010); Chew et al. (2006); Yeo et al. (2010); Li et al. (2011)). However, despite their stated advantages, meshfree methods developed so far, happen to be computationally more expensive compared with their mesh based

counterparts (Chew et al. (2006)). Higher computational cost is stated to be a big hindrance in their widespread applicability (Ding et al. (2004)).

For highly convective flows, stability is a major consideration for numerical solution (Fornberg and Lehto (2011); Gu and Liu (2002); Shen (2010); Chan et al. (2014); Shu et al. (2005a); Oñate (1998). This area has extensively been studied for mesh-based methods and various stabilization techniques (like use of upwinding, inclusion of artificial viscosity and flux limiter etc.) are well developed for FE, FV and FD methods. However, stability of convection dominated flows solved over meshfree domain still needs to be studied further.

FSI problems are often modelled using partitioned approaches which employ separate solvers for flow and structural subsystems. The results of these solvers are coupled at fluid-solid interface. Partitioned procedures offer flexibility in choosing different solvers for fluid and structures but these cause coupling errors and instabilities at interface boundaries. These errors can be reduced by using closely coupled algorithms. However, computational cost is significantly increased with the use of closely coupled algorithms due to several sub-iteration in a single time step (Farhat et al. (1995)).

In view of foregone, there is a strong need to work out a solution scheme for fluid-structure interaction problem which can provide improved computational performance by still ensuring required flexibility to deal with moving boundary. Moreover, there is a need to investigate other areas like stabilized flow at high Reynolds number and well conditioning of the problem while applying meshfree methods on flow problems.

1.2 Conventional mesh based methods and their limitations

Since the advent of numerical simulations in early 1950s, FEM, FVM and FDM have emerged as distinct methods which have widely been employed for a large number of engineering applications. These are robust and well developed methods used commercially worldwide. However, these so called *grid based* methods, rely on computational nodes which are connected by a topological map called *mesh*. Presence of grid or mesh enforces a pre-defined connectivity constraint over the nodes thus causing some inherent limitations to these methods. These limitations are discussed below.

1.2.1 Grid generation around complex geometries

Generation of an efficient mesh, which could ensure accurate results, is generally a tedious and time consuming task. Cartesian grids are generally considered to be much more efficient to generate but their applications are limited to simpler geometry. In fact,

grid generation is generally the most time consuming process during numerical solution process (G. R. Liu (2003)) and is therefore expensive as it consumes operators time.

Composite grids and domain decomposition techniques have often been used for traditional mesh-based methods to overcome the difficulty posed by complex geometries (Perng and Street (1991); Hinatsu and Ferziger (1991); Chow and Addison (2002)). Hinatsu and Ferziger (1991) proposed a multigrid method for geometrically complex flow problems. Perng and Street (1991) used a domain decomposition technique for flow in regions with complex geometries. The Momentum equation was solved separately in each sub domain and pressure field was computed simultaneously in the entire domain. However these methods rely on interpolation approximations at the grid interchanges and suffer from inaccuracies especially when high gradients exist at these junctures. Some researchers (Pember et al. (1995), Falcovitz et al. (1997), Calhoun (2002),Günther et al. (2011),Schneiders et al. (2013),Örley et al. (2015)) have also proposed the use of Cartesian grids on irregular shapes using boundary-fitted methods. However, these methods necessitate special treatments close to the boundary and suffer from time step restrictions due to small cut cell to accurately embed irregular boundaries in the Cartesian grid. Another approach is to use non-body conformal methods (Glowinski et al. (1994)), Gilmanov et al. (2003),Gilmanov and Sotiropoulos (2005),Ge and Sotiropoulos (2007),Wang et al. (2014),Wang et al. (2015)) in which a background structured mesh is defined behind the solid boundary. The interface between fluid and solid is traced using *marker nodes*. These schemes however suffer from inaccuracies coming from accurate tracing of the boundary which is limited by the grid resolution.

1.2.2 Dealing with moving boundaries

Traditional mesh based methods (like FD, FV and FE) make use of computational grids which have some sort of pre-defined connectivity amongst the grid nodes. This constraint strongly inhibits the capability of mesh based methods to effectively deal with moving boundaries. Therefore, use of traditional mesh based methods for FSI problems brings in the cumbersome tasks of extensive re-meshing, and data interpolations. Adaptive meshing is in fact, a challenging task for problems relating to Fluid Structure interaction, explosion, fragmentation, impact and penetration (Li Shaofan (2007)).

1.2.3 Other issues

In addition to the aspects discussed above, grid based methods are also difficult to be employed for problems involving free surface flows where domain of the fluid is not predefined. Moreover, for high velocity impact (HVI) problems which involve phenomena like large deformation, moving particle interfaces and free surface flow, it becomes very difficult to handle the solution using grid based methods (G. R. Liu (2003)). Also in

computational failure mechanics, grid based methods cannot accurately predict crack growth behaviour in solids (Zhuang et al. (2014)).

1.3 Meshfree methods as an Alternative to Grid Based Methods

Since the 1970s, efforts have been underway to seek better alternatives to overcome the limitations of grid based systems for various problems. In this regard, early efforts were devoted to modifying the existing grid based methods to render them less susceptible to the afore mentioned shortcomings. Development of auto-meshers, use of automated adaptive meshing techniques and development of the Arbitrary Lagrangian Eulerian (ALE) method are the prominent examples of such efforts. However, these modifications were unable to completely eliminate the limitations inherent in the use of mesh-based methods. In fact, connectivity of nodes in mesh based methods was seen as the biggest contributor to these limitations.

Meshfree methods refer to the class of computational techniques in which, at least, the structure of the mesh is eliminated and the solution is approximated over a set of arbitrarily distributed data points (or nodes). In the absence of pre-specified grid connectivity constraint, computational nodes can be moved, added or removed more flexibly, from computational domain, during the simulation. Owing to these features, meshfree methods are considered to be better suited for problems involving large deformation, moving boundaries and complex geometries (Chew et al. (2006)). Meshfree methods therefore, offer a good alternative for the limitations experienced during grid based analyses. Some the advantages are listed below (Li Shaofan (2007)):

1. Meshfree methods can easily handle the problems with large deformations Ding et al. (2004). Unlike the grid based methods, nodes are not connected to each other. Therefore, any displacement of nodes (followed by deformation of domain) is not restricted by inter-node connectivity constrained (as in FEA).

2. Significant design effort is saved due to the fact that the meshing is not required. It makes the analysis process much simpler and faster.

3. Unlike mesh based methods, it is very easy to add or remove data points during the analysis. This makes the adaptive refinement very flexible, simple and accurate during analysis. The computational accuracy and efficiency can be controlled by adding the particles to the areas where more refinement is required. Such flexibility is not provided by mesh based methods.

4. Boundary fitted nodal meshfree nodal cloud can follow the movement of deformable boundary without element shape distortion restrictions. Therefore, accurate geometric representation is possible using meshfree methods. Moreover, the data can be transferred to CAD database more efficiently as the requirement for mesh generation is eliminated.

5. Meshfree methods have been found to be extremely useful in accurately determining the behaviour of free surface flows (Monaghan (1994)).

6. For structural applications, one of the prominent applications of meshfree methods is accurate determination of damage, crack growth and disintegration behaviour of the continuum (Zhuang et al. (2014)). The methods are implicitly adaptive to topological changes in the structure. Hence, they are proving useful in computational failure mechanics.

7. Meshfree methods have the ability to effectively incorporate the enrichment provided by features of fine scale solutions into coarse scale solutions. This means that there is no restriction on adaptive refinement in different regions of computational domain as coarse and refined distributions of nodes can easily work together.

Owing to these features, application of meshfree methods has extensively been investigated for fluid flow problems. For example, Shu et al. (2005b) used Local RBF based differential quadrature method for incompressible flow around single and a pair of staggered cylinders. Later Shan et al. (2008) extended the method for curved 3-D problems with simple geometries. Shadloo et al. (2012) presented a solution scheme for flow around aerofoil and square obstacle using compressible and incompressible SPH methods. They proposed an artificial particle displacement method to overcome inhomogeneous particle distribution when Lagrangian schemes are used for for such problems. Shen (2010) presented collocation based meshfree method for boundary layer problems. Chan et al. (2014) proposed a method for solving convection dominated flows using upwind radial basis functions. Wu et al. (2010) proposed a method for solving incompressible flow problems, in primitive variables, using meshless local Petrov-Galerkin Method (MLPG). Later, Najafi et al. (2012) extended MLPG method for high Reynolds number flow problems using characteristic-based split (CBS) scheme.

1.3.1 Higher computational cost - Limiting factor of meshfree methods

Despite above stated advantages, meshfree methods developed so far, are, in general, computationally more expensive than conventional mesh based methods. This is mainly because, meshfree methods require more number of data points to achieve desired level of accuracy than conventional mesh based methods (Wright and Fornberg (2006)). This leads to overall lesser computational efficiency compared with traditional mesh based

methods (Chew et al. (2006)). For example in RBF based methods, calculation of RBF weights corresponding to the neighbouring particles of a data point requires expensive square root and matrix inversion processes. Moreover, calculation of derivative approximation at a given order of accuracy usually requires much more number of neighbouring particles (or nodes) for meshfree methods on an irregular grid than for finite difference methods on Cartesian grid. As a result, the bandwidth of matrices representing the governing algebraic equations greatly expands in case of meshfree methods (Ding et al. (2004)). Therefore, the iteration process is slowed down due to relatively dense matrix equations and the computational efficiency is reduced.

Efforts are under way to overcome this limitation using different novel techniques. For example, Hamed Meraji et al. (2012) presented a point pressure-velocity iteration method to work out an efficient solution scheme for N-S equations in primitive variables using local RBFs. Bollig et al. (2012) presented a parallelization strategy for radial basis function in a finite difference method using multiple GPUs. They used message passing interface (MPI) for inter-processor communication and synchronization to have faster computing using the meshfree method. Some researchers have proposed the use of coupled mehsfree/mesh-based methods to overcome the computational efficiency issue. Fries and Matthies (2006a) and Fries and Matthies (2006b) coupled mesfhree Galerkin method with conventional FEA over a composite grid using Chimera technique (Steger and Benek (1987)). Chew et al. (2006) and Ding et al. (2004) coupled generalized finite difference with conventional finite difference scheme using a meshfree nodal grid was superimposed by a background Cartesian mesh grid. It is considered that composite grid schemes can be highly useful in overcoming the performance related issues of meshfree methods.

Today, meshless methods are one of the hottest areas of research which have promising applications for different problems pertaining to Computational Fluid Dynamics (CFD) and Computational Structure Mechanics (CSM). Particularly, for fluid structure interaction problems, where large deformations and interface problems limit the accuracy of conventional numerical methods, meshfree methods can prove to be extremely accurate and efficient. However, their higher computational cost is one of the biggest limitations which impedes their wide applicability (Ding et al. (2004)). Therefore, mesh based methods are outclassed by their meshfree counterparts in terms of flexibility and handling of moving boundaries and complex geometries. However, mesh based methods are well developed and offer better computational performance compared with existing meshfree methods. None of the methods can therefore, be termed as 'superior' to the other especially for modelling the flow problems.

1.4 Partitioned methods for FSI and their limitations

Partitioned procedures are more commonly used for FSI problems in general and non-linear aero-elastic problems in particular (Park (1980); Farhat et al. (1995, 1998); De Rosis et al. (2013); Dowell and Hall (2001); Ii et al. (2011); Piperno et al. (1995); Kamakoti and Shyy (2004)). These methods employ different time integration schemes for fluid and structure subsystems. Partitioned procedures use three field formulation, constituting fluid and structure subsystems and the moving grid. They provide flexibility in choosing different solvers for fluid and structure subsystems. However, coupling errors, at fluid-structure interface of these solvers, is often advocated as a limitation to this approach. Such inaccuracies are more pronounced in loosely coupled systems where solutions from fluid and structural subsystems are not necessarily converged at the interface boundary before marching to the next time step (De Rosis et al. (2013)). This deficiency of partitioned problems is overcome by the use of strongly coupled systems. In this approach, several *inner* or sub-iterations are run of fluid and structure solvers, within a single time step, to reach convergence at the interface before moving on to the next time iteration. These *inner* iteration cause significantly high computational overheads which affect the overall efficiency of the solution scheme. In fact, closely coupled systems attempt to improve accuracy and stability in exchange of increased computational cost caused by a higher number of computations in each time step (Farhat et al. (2006)).

1.5 Stabilization of convection-diffusion problems

Viscous flow equations are primarily the convection-diffusion equations. It is well known that dealing with the convection terms often becomes a challenging task, in view of numerical simulations, especially for high Reynolds number problems. Increased convection causes spurious oscillations in the solution which leads to inaccuracies and instabilities. In this regard, significant work has been conducted to overcome the instabilities caused by convection when approaching the flow problems using FEM, FVM and FDM. Presently, well developed stabilization techniques exist for mesh based methods. For meshfree methods, Gu and Liu (2002) have proposed several techniques to deal with instabilities of numerical solutions. These techniques include nodal refinement, support domain enlargement and use of upwind domains. Fornberg and Lehto (2011) introduced a filter mechanism to overcome stabilization issues related to purely convective PDEs when solved using RBF-FD method. Shen (2010) and Chan et al. (2014) introduced upwind schemes for using RBF differential quadrature methods. However these schemes require constant reshaping of local support domains in accordance with flow velocities to ensure larger number of neighbouring particles in the upwind direction. Shu et al. (2005a) presented an upwind RBF Differential Quadrature (DQ) method for compressible flows. An effective stabilization scheme was presented by Oñate et al. in their work

(Oñate (1998); Oñate et al. (1996)). They worked out stabilized momentum equations by introducing higher order approximations in the derivation of governing equations. Nevertheless, flow stabilization techniques still require significant research as far as their application to meshfree methods is concerned.

1.6 Scope of Research

The current research effort focuses on benefiting from the strengths of meshfree particle methods for simulating flow around moving solid objects. The aim is to suggest a solution scheme which provides flexibility in dealing with moving boundaries as well as offering better computational performance compared with current techniques using meshfree methods. For this purpose, problems relating to 2-D incompressible, viscous, laminar flows are considered. Airfoils and cylindrically shaped solid objects are modelled as flexibly supported rigid bodies allowing translational and rotational movements. Such models sufficiently demonstrate flutter behaviour, flapping foils used in energy harvesters, offshore cylindrical structures and underwater flexibly mounted pipelines.

The ambit of research was confined to collocation based meshfree methods since the beginning. In this regard, after a comparative study of various candidate methods, local radial basis functions in finite difference mode (RBF-FD) is chosen for spatial discretization of flow equation in meshfree domain. Application of RBF-FD method is investigated for solution of flow equations, in vorticity-stream function as well as pressure-velocity formulations. Ill-conditioning effects, experienced by RBF matrices, are addressed by using adaptive shape parameters over non-uniform nodal distribution.

It is well known that meshfree methods are computationally expensive compared with their mesh based counterparts. In order to overcome this limitation, the research has been focused on developing a coupled meshfree and mesh-based solution scheme on hybrid fluid grid which could benefit from flexibility of meshfree methods as well as from computational efficiency of mesh based methods. The solution scheme couples RBF-FD on meshfree nodes with conventional finite difference on Cartesian mesh in the fluid domain.

A partitioned method is used with loose / closed coupling models at fluid-solid interface. Efforts are made to reduce the computational cost associated with closed coupling algorithms. For this purpose, a scheme is worked out to reduce computational effort involved in fluid solution during inner FSI iterations.

The research efforts are also directed to developing stabilized solution schemes over hybrid meshfree-Cartesian grid for high Reynolds number problems. At such conditions, increased convection in the flow causes spurious fluctuations which needs to be suppressed to maintain stability and accuracy. The aim is to develop an efficient, accurate

and stable FSI solution scheme which could provide insightful information about flow behaviour around moving boundaries with an emphasis on flow induced vibration.

Chapter 2

Fundamentals of incompressible, viscous flow and its interaction with rigid solids

In this chapter, fundamental aspects relating to viscous flow modelling and fluid-solid interaction have been discussed. These aspects include Eulerian and Lagrangian descriptions of continuum, mathematical formulation of incompressible and viscous flows and their time discretization methods, coupling of fluid and structures, treatment of highly convex boundaries and dealing with moving boundaries in flow. The detail is given in the subsequent sections.

2.1 Eulerian, Lagrangian and ALE descriptions

Numerical simulations of fluid dynamics and solid mechanics problems often require coping with large deformation of the continuum. The problems relating to Fluid-Structure Interaction particularly entail clear delineation of fluid and structure interfaces during continuum distortion. Therefore, the choice of an appropriate kinematic description of the continuum is highly important for defining relationship between the deforming continuum and the finite grid of the computational domain. Such description of the continuum enables the numerical scheme to provide an accurate resolution of material interfaces and mobile boundaries as well as dealing with large deformations. Models in continuum mechanics may be formulated using two classical descriptions of motion:

1. Lagrangian description
2. Eulerian description

The Lagrangian approach allows each node of the computational mesh to follow the associated material particle as shown in Figure 2.1(a). This approach facilitates the treatment of materials with history dependent constitutive relations as well as allowing easy tracking of free surfaces and interfaces between different materials (Sarrate et al. (2001)). However, Lagrangian description cannot accurately deal with large distortions without incorporating frequent re-meshing. On the contrary, the Eulerian approach does not allow movement of nodal points at all. Therefore, continuum distortion is calculated from a stationary view point and grid retains its original shape as shown in Figure 2.1(b). However, it cannot incorporate moving boundaries for boundary fitted grids.

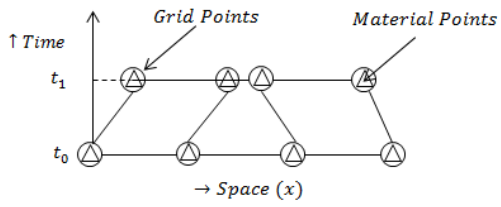

(a) Lagrangian description

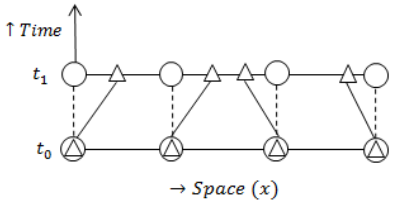

(b) Eulerian description

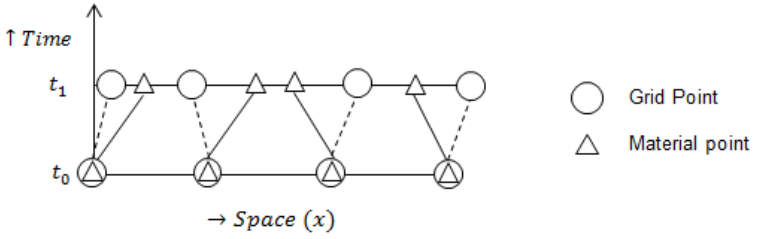

(c) ALE description

Figure 2.1: Lagrangian, Eulerian and ALE descriptions

Arbitrary Lagrangian Eulerian (ALE) description combines the features of both classical descriptions and minimizes their limitations (Hirt et al. (1974)). In ALE description, the grid points are not completely fixed. However, they are neither bound to exactly follow the material particles. Therefore, the material particles are tracked from a moving reference frame. Figure 2.1 depicts these three descriptions of motion.

2.1.1 ALE Formulation

Consider a material domain $\Omega_X \epsilon \mathbb{R}^d$, where d is the dimension of space. Image of Ω_X at time t is represented by the spatial domain Ω_x. The motion of material domain can be mapped as $\phi : \Omega_x \times (0, T) \rightarrow \mathbb{R}^d$. The reference (or ALE) domain is represented as

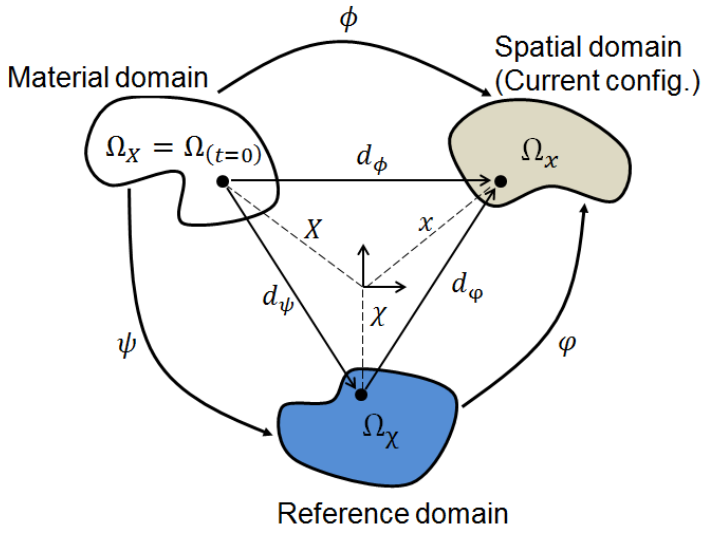

Figure 2.2: Motion of ALE reference domain independent to material motion

Ω_X and its motion is defined by the mapping $\varphi : \Omega_\mathcal{X} \times (0, T) \rightarrow \mathbb{R}^d$. Another mapping $\psi : \Omega_X \times (0, T) \rightarrow \mathbb{R}^d$ can also be introduced such that $\psi = \varphi^{-1} \circ \phi$ exists for sufficiently smooth, bijective functions ϕ and φ. An overview of different domains along with the mapping is shown in Figure 2.2.

Let us assume three coordinates x, X and $\mathcal{X}$ such that

$$x \, \epsilon \, \Omega_x, \qquad X \, \epsilon \, \Omega_X, \qquad \mathcal{X} \, \epsilon \, \Omega_\mathcal{X}$$

So, we can show that:

$$\begin{aligned} x = \phi(X, t), \qquad & x = \varphi(\mathcal{X}, t), \qquad & \mathcal{X} = \psi(X, t) \\ d_\phi = x - X, \qquad & d_\varphi = x - \mathcal{X}, \qquad & d_\psi = \mathcal{X} - X \end{aligned}$$

Now, realizing that $dX/dt = 0$, we can deduce the following time derivatives:

$$\dot{d}_\phi = \left.\frac{\partial d_\phi}{\partial t}\right|_X = \left.\frac{\partial x}{\partial t}\right|_X = \dot{\phi}, \qquad \dot{d}_\psi = \left.\frac{\partial d_\psi}{\partial t}\right|_X = \left.\frac{\partial \mathcal{X}}{\partial t}\right|_X = \dot{\psi}$$

In practice $\dot{d}_\phi$ may be taken as real advection velocity with respect to spatial domain and $\dot{d}_\psi$ as relative velocity of mesh with respect to real advection velocity. d_φ is the

mesh (nodal) velocity of ALE mesh. Any function defined in one of the three domains implies the definition of two other functions defined in other domains. That is to say,

$$\underbrace{f(\mathcal{X},t)}_{\text{Referential ALE}} = \underbrace{g(x,t)}_{\text{Spatial Eulerian}} = \underbrace{h(X,t)}_{\text{Material Lagrangian}} \tag{2.1}$$

Time derivative of each function can be expressed using chain rule as:

$$\frac{\partial f}{\partial \mathcal{X}}\dot{d}_\psi + \frac{\partial f}{\partial t} = \frac{\partial g}{\partial x}\dot{d}_\phi + \frac{\partial g}{\partial t} = \frac{\partial h}{\partial t} \tag{2.2}$$

Variable x can be expressed as $x = \varphi(\psi(X,t),t)$. Therefore, the time derivative of $x = \varphi(\psi(X,t),t)$ leads to:

$$\frac{dx}{dt} = \dot{d}_\phi = \frac{\partial \varphi}{\partial \psi}\dot{d}_\psi + \dot{d}_\varphi \tag{2.3}$$

$$\dot{d}_\psi = \frac{\partial \mathcal{X}}{\partial x}(\dot{d}_\phi - \dot{d}_\varphi) \tag{2.4}$$

Substituting the value of $\dot{d}_\psi$ into Eq. (2.2):

$$\underbrace{\frac{\partial f}{\partial \mathcal{X}}(\dot{d}_\phi - \dot{d}_\varphi)}_{\text{Referential ALE}} = \underbrace{\frac{\partial g}{\partial x}\dot{d}_\phi + \frac{\partial g}{\partial t}}_{\text{Spatial Eulerian}} = \underbrace{\frac{\partial h}{\partial t}}_{\text{Material Lagrangian}} \tag{2.5}$$

Therefore, any time derivative in Eulerian or Lagrangian formulation may directly be transferred to ALE (reference) formulation using Eq. (2.5).

2.2 Flow equations in pressure-velocity formulation

The time dependant, incompressible and viscous Navier-Stokes equations in non-dimensional primitive (pressure-velocity) variable form are expressed as:

$$\textit{Continuity equation}: \quad \nabla.\vec{\mathbf{u}}(\mathbf{x},t) = 0 \tag{2.6}$$

$$\textit{Momentum equation}: \quad \frac{\partial \vec{\mathbf{u}}(\mathbf{x},t)}{\partial t} = -\nabla P - (\vec{\mathbf{u}}(\mathbf{x},t).\nabla)\vec{\mathbf{u}}(\mathbf{x},t) + \frac{1}{Re}\nabla^2\mathbf{u}(\vec{\mathbf{x}},\mathbf{t}) \tag{2.7}$$

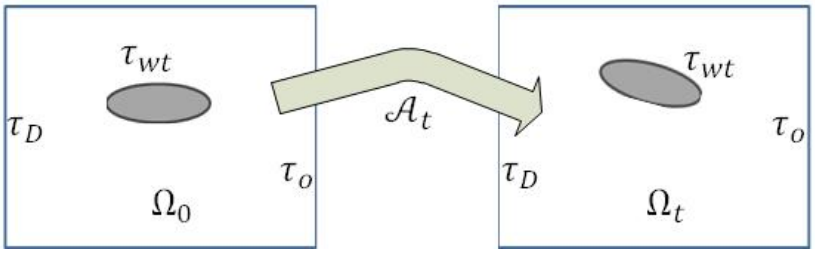

Figure 2.3: ALE mapping of reference configuration Ω_0 over current configuration Ω_t

with boundary condition:

$$\vec{\mathbf{u}}(\mathbf{x},t)|_{\partial\Omega} = \vec{\mathbf{u}}(\mathbf{x},t)|_{\Gamma} \tag{2.8}$$

where Ω is the domain bounded by Γ, $\mathbf{x}$ is the spatial coordinate vector, t is the time, $\vec{\mathbf{u}}(\mathbf{x},t)$ is the velocity vector and P is the pressure. ∇ is the spatial differential operator. Re is the Reynolds number ($Re = UL/\nu$, where U is the free stream velocity, L is the characteristic length and ν is the kinematic flow viscosity)

In case of non-stationary computational domain, the flow equations can be expressed in Arbitrary Lagrangian Eulerian (ALE) description to account for the nodal movement. In this case, the computational domain at initial time t_0 is taken as a reference configuration Ω_0 as shown in Figure 2.3. At any arbitrary time t, the reference configuration Ω_0 can be mapped over the current configuration Ω_t using mapping $\mathcal{A}_t$ as (Hirt et al. (1974)):

$$\mathcal{A}_t : \Omega_0 \rightarrow \Omega_t \tag{2.9}$$

$$\mathbf{X} \rightarrow x(\mathbf{X},t) = \mathcal{A}_t(\mathbf{X}) \tag{2.10}$$

ALE velocity is calculated as $\vec{\mathbf{v}} = \partial\mathcal{A}_t/\partial t$. Flow momentum Eq. (2.6) is written, in ALE formulation, as follows (Takashi and Hughes (1992)):

$$\partial_t\vec{\mathbf{u}}(\mathbf{x},t) = -\nabla P - (\vec{\mathbf{u}}(\mathbf{x},t) - \vec{\mathbf{v}})).(\nabla\vec{\mathbf{u}}(\mathbf{x},t)) + (1/\mathbf{Re})\nabla^2\vec{\mathbf{u}}(\mathbf{x},t) \tag{2.11}$$

The continuity equation remains unchanged in ALE form. ALE velocity is set equal to the velocity of the computational domain at each point. For static domain, ALE velocity $\vec{\mathbf{v}}$ becomes zero and the momentum Eq. (2.11) transforms to its corresponding Eulerain form Takashi and Hughes (1992).

2.3 Time discretization methods for Navier Stokes equations

One of the major difficulties faced during numerical solution of transient Navier-Stokes equations in primitive variable form is that the continuity equation does not contain a time derivative. In order to address this problem, the constraint of mass conservation is achieved by coupling the pressure term with continuity equation. For this purpose, an intermediate velocity term $\vec{\mathbf{u}}^*$ is introduced, between two consecutive time steps, to decouple pressure term from momentum equation. Momentum equation is advanced to determine the intermediate velocity $\vec{\mathbf{u}}^*$. Then an elliptic equation is solved that enforces the divergence free constraint on velocity field at the next time step. The method is called fractional step method. Following is the general procedure for this method (Guermond et al. (2006)):

1. Solve for intermediate velocity field $\vec{\mathbf{u}}^*$:

$$\frac{\vec{\mathbf{u}}^* - \vec{\mathbf{u}}^n}{\partial t} = -\nabla q - [(\vec{\mathbf{u}}.\nabla)\vec{\mathbf{u}}]^{n+1} + \frac{1}{2Re}\nabla^2(\vec{\mathbf{u}}^n + \vec{\mathbf{u}}^*) \tag{2.12}$$

$$and\ B(\vec{\mathbf{u}}^*) = 0 \tag{2.13}$$

   where q is a function of pressure P and $B(\vec{\mathbf{u}}^*)$ is the boundary condition for intermediate velocity. n is the current time step.

2. Project divergence free constraint:

$$\vec{\mathbf{u}}^* = \vec{\mathbf{u}}^{n+1} + \Delta t \nabla \phi^{n+1} \tag{2.14}$$

$$\nabla.\vec{\mathbf{u}}^{n+1} = 0 \tag{2.15}$$

$$\vec{\mathbf{u}}|_{\partial\Omega} = \vec{\mathbf{u}}_\Gamma \tag{2.16}$$

   where ϕ is an auxiliary variable which has some correlation with pressure defined by a function $L(\phi)$

3. Finally, update the pressure field:

$$P^{n+1/2} = q + L(\phi^{n+1}) \tag{2.17}$$

In general, the intermediate velocity field $\vec{\mathbf{u}}^*$ does not satisfy divergence free constraint after being evaluated from the momentum equation. However, continuity conditions are fulfilled at the end of time step.

Various researchers have presented different variants of these methods (Kim and Moin (1985); Van Kan (1986); Bell et al. (1989, 1991)). The difference lies in the selection of

pressure approximation in momentum equation (q), the boundary conditions for intermediate velocity $B(\vec{\mathbf{u}}^*)$ and the function $L(\phi^{n+1})$. A brief description of some of these methods is given here.

2.3.1 Method of Kim and Moin

Kim and Moin (1985) first introduced the relationship between auxiliary variable and pressure. They used the following expression for this purpose:

$$\nabla P^{n+1/2} = \phi^{n+1} - \frac{\nu \Delta t}{2} \nabla^2(\phi^{n+1}) \tag{2.18}$$

It can be observed that variable q is missing in Eq. (2.18). The reason for this is that the pressure does not appear, at all, in the momentum equation for $\vec{\mathbf{u}}^*$ (i.e. $q = 0$ in Eq. (2.12)). By using this procedure, Kim and Moin (1985) avoided the contribution of errors from the pressure terms in the momentum equation. However, intermediate velocity $\vec{\mathbf{u}}^*$ does not remain equal to $\vec{\mathbf{u}}^{n+1}$ within $O(\Delta t^2)$. Therefore, $\vec{\mathbf{u}}^*$ is related to $\vec{\mathbf{u}}^{n+1}$ using the relation $\vec{\mathbf{u}}^* = \vec{\mathbf{u}}^{n+1} + \Delta t \nabla \phi^n$ at the boundary. A later investigation by Brown et al. (2001) showed that this was, in fact, a necessary condition to obtain second order accuracy for solution in this approach.

2.3.2 Method of Bell, Colella and Glaz

This is a well-known projection method which has been presented by Bell et al. (1989) and Bell et al. (1991) and has been implemented to various complex physical problems (Brown et al. (2001)). It is an incremental pressure update method which includes pressure update in intermediate momentum equation for $\vec{\mathbf{u}}^*$. This method uses the pressure value calculated in previous iteration in momentum equation as $q = P^{n-1/2}$. The boundary condition for intermediate velocity is applied as $(\vec{\mathbf{u}}^* - \vec{\mathbf{u}}^{n+1})|_{\partial\Omega} = 0$. The boundary condition on intermediate velocity leads to the boundary condition on ϕ^{n+1} while solving the elliptic equation as $\hat{n}.\nabla\phi^{n+1}|_{\partial\Omega} = 0$. The method offers second order accuracy ($O(\Delta t^2)$) for velocity field and first order accuracy ($O(\Delta t)$) for pressure field. Pressure is related to ϕ as:

$$\nabla P^{n+1/2} = \phi^{n+1} - \nabla(\phi^{n+1}) \tag{2.19}$$

However, unlike the method of Kim and Moin (1985), the term $\nabla^2\phi$ does not appear in the expression for time centred pressure $P^{n+1/2}$ here. This results in inaccuracies in pressure calculations around the boundary and generation of a numerical boundary layer (Temam (1991)).

2.3.3 Other fractional step methods

There are various other variants of fractional step methods. For example, Perot (1995) proposed a method in which truncation error associated with calculation of pressure gradient ∇P was reduced by adding a correction term. So, the pressure update expression became:

$$(1 + \frac{\nu \Delta t}{2}) P^{n+1/2} = \phi^{n+1} \tag{2.20}$$

At the boundaries, $\hat{n}.\nabla P = 0$ is used for elliptic pressure equation which results in first order accuracy for the method. This is a non-incremental pressure update method and therefore $q = 0$.

Botella (1997) introduced a third order integration equation for intermediate velocity evaluation in the momentum equation. They used the following expression for q:

$$q = P^{n-1/2} + \phi^n \tag{2.21}$$

The intermediate velocity was related to velocity at the next time step as:

$$\vec{\mathbf{u}}^{n+1} = \vec{\mathbf{u}}^* - \Delta t(\phi^{n+1} - \phi^n) \tag{2.22}$$

with boundary condition:

$$\hat{n}.\nabla \phi = 0 \tag{2.23}$$

The pressure was updated using the following equation:

$$P^{n+1/2} = P^{n-1/2} + \phi^{n+1} \tag{2.24}$$

Botella (1997) demonstrated higher convergence rates for both velocity and pressure in L^2-norm. However, Brown et al. (2001) remarked that the method was inaccurate at the boundaries as $\hat{n}.\nabla P$ must stay constant due to the pressure update formula.

There are numerous other modifications and variations proposed by different researchers. However, the discussion here is restricted to the famous methods only.

2.4 Flow equations in vorticity-stream function formulation

Non-dimensionalized flow equations in 2-D coordinate plane $\mathbf{x} = (x, y)$ can be expressed in vorticity-stream function formulation as:

$$\frac{\partial \omega}{\partial t} + u\frac{\partial \omega}{\partial x} + v\frac{\partial \omega}{\partial y} = \frac{1}{Re}\left(\frac{\partial^2 \omega}{\partial x^2} + \frac{\partial^2 \omega}{\partial y^2}\right) \tag{2.25}$$

$$\frac{\partial^2 \psi}{\partial x^2} + \frac{\partial^2 \psi}{\partial y^2} = -\omega \tag{2.26}$$

where ω is the vorticity, ψ is the stream function and u, v are the components of flow velocity along x and y directions respectively ($\vec{\mathbf{u}}(\mathbf{x}, t) = (u, v)$). Vorticity ($\omega$) is expressed as:

$$\omega = \frac{\partial u}{\partial y} - \frac{\partial v}{\partial x} \tag{2.27}$$

The components of velocity vector $\vec{\mathbf{u}}(\mathbf{x}, t) = (u, v)$ can be obtained from derivatives of stream function (ψ) as:

$$u = \frac{\partial \psi}{\partial y}, \qquad v = -\frac{\partial \psi}{\partial x} \tag{2.28}$$

The vorticity-stream function formulation of Navier Stokes equations offers simpler representation of flow equations. However, there are certain limitations which inhibit the use of this formulation for various types of problems. The limitations are:

1. The formulation cannot be extended to 3-D (Except for axi-symmetric cases).
2. Vorticity boundary conditions are relatively complicated and are difficult to use on complex boundaries.
3. Physical parameters (velocity and pressure) are not directly calculated.
4. Problem cannot be extended to compressible flow.

The pressure-velocity formulation, on the other hand, offers generalized set of equations for flow problems. Nevertheless, vorticity stream-function still provides an efficient way of solving incompressible flow problems in 2-D.

2.4.1 Solid equations

The problems considered for current study include flow around spring mounted airfoil and cylindrical objects which are able to vibrate due to fluid forces. Cylindrical objects can perform translational oscillation in horizontal and vertical directions as shown in Figure 2.4(a). The equations of motion for cylindrical vibration are given by:

$$m\ddot{x} + d_x\dot{x} + k_x x = D(t) \tag{2.29}$$

$$m\ddot{y} + d_y\dot{y} + k_y y = L(t) \tag{2.30}$$

where m is the mass of cylinder (in kg), d_x, d_y are damping constants (N.s/m) and k_x, k_y are spring stiffness values (N/m) along x and y directions respectively. $L(t)$ and $D(t)$ are time dependant lift and drag values.

The airfoil is able to vibrate vertically as well as rotate about its elastic axis as depicted in Figure 2.4(b). The motion of airfoil, along translational axis y and rotational direction α, is therefore described by a set of coupled non-linear differential equations as follows (Dubcová et al. (2009)):

$$m\ddot{y} + S_\alpha\ddot{\alpha}\cos\alpha - S_\alpha\dot{\alpha}^2\sin\alpha + d_y\dot{y} + k_y y = L(t) \tag{2.31}$$

$$S_\alpha\ddot{y}\cos\alpha + I_\alpha\ddot{\alpha} + k_\alpha\alpha + d_\alpha\dot{\alpha} = M(t) \tag{2.32}$$

Here S_α and I_α represent first moment (kg.m) and second moment (kg.m^2) of inertia of airfoil about the elastic axis respectively. The terms k_α and d_α are the rotational stiffness (N.m) and rotational damping constants (N.m.s). $M(t)$ is the time dependant pitching moment about the elastic axis. For small vibrational amplitudes, the non-linear terms appearing in Eqs. (2.31) and (2.32) can be ignored resulting in the following system of linear equations:

$$m\ddot{y} + S_\alpha\ddot{\alpha} + d_y\dot{y} + k_y y = L(t) \tag{2.33}$$

$$S_\alpha\ddot{y} + I_\alpha\ddot{\alpha} + k_\alpha\alpha + d_\alpha\dot{\alpha} = M(t) \tag{2.34}$$

External forces and moment appearing in Eqs. (2.29) - (2.34) can be evaluated by integrating fluid stresses (τ_{ij}) and their corresponding moments about elastic axis over the entire solid surface Ω_t. For a unit thickness of solid, the fluid forces and moments acting on solid objects can be expressed as (Sváček et al. (2007)):

$$Drag = D = \int_{\Gamma_{W_t}} \left(\sum_{j=1}^{2} \tau_{1j} n_j \right) \partial\Omega_t \tag{2.35}$$

$$Lift = L = \int_{\Gamma_{W_t}} \left(\sum_{j=1}^{2} \tau_{2j} n_j \right) \partial\Omega_t \tag{2.36}$$

$$M = \int_{\Gamma_{W_t}} \left(\sum_{i,j=1}^{2} \tau_{ij} n_j r_i \right) \partial\Omega_t \tag{2.37}$$

Here, n_i is the component along x_i, of unit vector $\hat{n}$ towards outward normal to the surface $\partial\Omega_t$ on Γ_{W_t}. r_i is the moment arm of force defined as $r_i = -(X_i - X_{EO_i})$, where X_i is the coordinate of point on surface and X_{EO_i} is the coordinate of elastic axis. Differential equations for motion of solid are solved using explicit Runge Kutta-4 method to get displacements at next time step.

2.5 Computational modelling of Fluid-Structure Interaction problems

Implementation of coupled fluid-structure interaction problems in computational environment can be realized using two different approaches. The monolithic approach refers to the fully coupled method which attempts to find simultaneous solution of the problem. In monolithic schemes, fluid and structural equations are reformulated, combined and then solved simultaneously using single time integration method (Kamakoti and Shyy (2004)). The method sounds appealing as it provides a single set of equations for mathematical analysis and does not pose inaccuracies at fluid-structure interface. However, difference in mathematical properties of fluid and solid subsystems, issues related to software modularities and loss of generalization of solution scheme strictly limit their widespread application (Farhat et al. (1995)).

The other way to solve FSI problems is through partitioned approach. Partitioned method treats fluid and solid as different entities during solution process and attempts to seek a coupling methodology to model the interaction of the two solutions. This has traditionally been achieved by coupling the high level computational fluid dynamics (CFD) and Computational Structural Dynamics (CSD) approaches. Usually, CFD approach employs Eulerian or spatially fixed coordinate system whereas Lagrangian or material fixed coordinate system is used by CSD approach. Therefore, coupling of the two modules using suitable interfacing techniques is necessitated (Kamakoti and Shyy (2004)) to ensure accuracy and stability.

2.6 Categories of FSI models

FSI problems can be classified into three major categories based on fluid-structure coupling. These are

1. Fully coupled models
2. Closely coupled models
3. Loosely coupled models

A short description of each model is outlined below.

2.6.1 Fully coupled models

In this approach, the governing equations for fluid and structure domains are reformulated and a single set of equations is worked out. The new set of equations is applicable to both solid and fluid phases. The equations are then solved simultaneously to get the solution. The approach is also called monolithic approach. Guruswamy and Byun (1995) coupled an Euler flow equation with plate structure in finite element formulation. Later similar approach was extended to couple Navier Stokes equations with shell FE structure (Guruswamy and Byun (1995)). Garcia and Guruswamy (1999) performed aeroelastic analysis of transonic wing by coupling Navier Stokes equations and nonlinear beam FE model. Fully coupled approach provides a unified solution to system of equations for both solid and fluid domains. They have minimum coupling errors. However, this comes with several limitations. The fluid and structure equations are written in Eulerian and Lagrangian formulations respectively. This makes the order of magnitude of the matrices stiffer for structure system as compared to fluid. Therefore, a monolithic approach to solve the system does not remain possible for complex systems. The application of such methods is therefore limited to simple and 2D problems only (Kamakoti and Shyy (2004)).

2.6.2 Loosely coupled models

Loosely coupled approach refers to the models in which fluid and solid domains are solved separately using separate set of equations in separate solvers. Both domains have different computational grids which may not coincide at fluid-solid boundaries. Exchange of information takes place at the boundary nodes using some interfacing technique. Loosely coupled models allow the flexibility of choosing solvers from a range of available fluid and structural solution packages. Therefore, the requirement of generating an

exclusive solver for a particular set of problems is alleviated. This allows the use of well-established and tested solver packages which enhance the confidence level in results. For example, Siegel Jr et al. (1998) developed a multidisciplinary computing environment which allows various modules to communicate over a distributed network of computers in a user-defined simulation environment. The model was used to study steady and transient flow behaviour over AGARD 445 and delta wing structures. Loosely coupled models provide only external interaction between fluid and solid modules. Therefore, exchange of information takes place only after partial or full convergence is achieved in a particular time step (Smith et al. (1996)). This leads to loss of accuracy at the grid interface. Loosely coupled models are therefore used for problems with moderate nonlinearity and small perturbations (Kamakoti and Shyy (2004)).

2.6.3 Closely coupled models

Closely coupled models take a step forward from loosely coupled models by introducing the interface between fluid and structural solver modules during the process of convergence. In this approach, fluid and structure equations are solved separately but the two solvers are tightly coupled at interface or boundary through interface module. Interface ensures that both the modules reach mutually converged results after every time step. At the interface, surface loads are mapped from CFD grid to structural grid and displacement field is mapped from structural grid to CFD grid (Kamakoti and Shyy (2004)). Liu et al. (2002) presented a fully implicit model to couple an unsteady CFD solver and CSD solver based time integration model dynamic equations. Parallel, multiblock moving mesh algorithm with finite volume was used to solve Navier Stokes equations. The coupled system was used to study stability of aeroelastic system in time domain. Farhat et al. (1995) presented a three field formulation for mixed implicit / explicit time integration of coupled aeroelastic problem. Arbitrary Lagrangian Eulerian (ALE) approach was used for solution of equation on moving grids. The solution of the coupled governing equations was obtained with explicit fluid and implicit structure solver.

Closely coupled approach offers a way for generating more complex non-linear problems. Selection of fluid, structure and interface model depends upon the type of problem, accuracy requirements and computational resources available. However, this algorithm runs several iterations of fluid and structural solver, within a single time step, in an attempt to attain mutual convergence at fluid-solid boundary. These *inner iteration* cause significantly high computational overheads which affects the overall efficiency of the solution scheme. This in fact, is the major limitation of closely coupled models (Farhat et al. (2006)).

2.7 Time coupling algorithms for FSI problems

As described earlier, loosely coupled and closely coupled models require an interface module to exchange information during solution process. Stability of solution and loose / tight behaviour of coupling strongly depends upon the coupling algorithm. Coupling is carried out to map pressure forces, calculated by solving fluid equations, over structural grid and to map structural deformation to move fluid grid after every time step. Loosely coupled models usually perform only one (or few in some cases) iteration (of data transfer) in each time step. On the contrary, closely coupled models iteratively perform the data transfer, in each time step, until convergence is reached. Carlos et al. (2001) presented an analysis of various coupled systems. The simple staggering approach for loosely coupled presented by Carlos et al. (2001) is reproduced in Figure 2.5.

Marching process of the two field solution is carried out in the following manner:

1. Structural displacement W^{n+1} is predicted at time t^{n+1}, and mapped over the fluid grid.
2. Fluid grid is displaced according to predicted structure displacement and fluid equations are solved to get pressure values P^{n+1} at time t^{n+1}.
3. Pressure field obtained by fluid solver is mapped over structural grid to get applied loads at t^{n+1}.
4. Structural solver uses these applied forces to get the corrected structural deflection W^{n+1} at t^{n+1}.

This type of staggered marching corresponds to a loosely coupled system because structure and fluid variables do not achieve mutual convergence prior to moving to the next time step. De Rosis et al. (2013) presented three different partitioned coupling strategies and worked out the accuracy and convergence properties of resulting algorithms along with their computational efficiency. They suggested two explicit and one implicit schemes. Staggering diagrams of explicit scheme are shown in Figure 2.6(a). The staggering of implicit scheme is the same as the explicit scheme shown in Figure 2.6(b). However, for implicit scheme, the iterations are repeated until fluid and structure parameters are converged to specific values. This practice is computationally expansive but leads to a closely coupled solution which is more robust, stable and accurate (De Rosis et al. (2013)).

2.8 Treatment of discontinuities

Presence of strong non-convex boundaries in the domain requires special attention while dealing with meshless methods. If a sharp concave corner exists in the domain, then the

influence domain of any node near the concave boundary may extend to the opposite side of the corner. The situation is illustrated in Figure 2.7(a) where a sharp concave boundary cuts the support domain of node x_I. In this case, node x_J falls in the influence domain of node x_I. If special treatment is not applied, the shape function of node x_I may be non-zero at node x_J and field variables at node x_J will influence the approximant variables at node x_I. However, in reality, field parameters at node x_I should not be affected by those at node x_J due to presence of discontinuity between these nodes. Therefore, use of globally continuous shape function would cause undesirable results. For example, for flow around aerofoil, the situation is particularly important for nodes close to the trailing edge of the aerofoil. The flow variables at one side of the aerofoil can unrealistically influence the flow patterns at the nodes on the other sides which would lead to errors in the solution. Therefore, special treatment is required to suppress these numerically generated effects.

In order to overcome this problem, some researchers have suggested incorporating discontinuous approximations as enrichment to the basis function (Krongauz and Belytschko (1998); Belytschko et al. (2001); Belytschko (2002)). For example Belytschko et al. (2001) have proposed a technique for modelling arbitrary discontinuities in function and derivative approximations. Other set of approaches suggests modifying the shape function approximation to preclude (or suppress) the weight of those nodes which actually have no (or reduced) effects due to the presence of a concave boundary. Following is the description of three such methods which are found interesting in this respect.

2.8.1 Visibility Method

Visibility method (Belytschko et al. (1994)) is based on line-of-sight criterion. The method suggests that, in the vicinity of a non-convex boundary, only those nodes should fall in the influence domain of node x_I, which can be linked with node x_J through a straight line without intersecting the boundary. This can be understood by considering the discontinuity as opaque and a ray of light originating from node x_I. The influence domain of node x_I will be truncated to exclude that portion where the ray of light cannot reach due to opaque obstruction (the discontinuity) as shown in Figure 2.7(b).

Application of visibility method is limited by the resulting artificial discontinuity in the influence domain due to the truncation introduced by the opaqueness of concave boundary. The truncated domain can still have same order of accuracy, however accuracy of the results is compromised especially for larger dilatation parameters (Belytschko (2002)).

2.8.2 Diffraction Method

Diffraction method proposes an improvement in visibility method by introducing diffraction of rays of light around the tip of the discontinuous boundary (Belytschko (2002)). In this manner, the artificial discontinuity in the influence domain is somewhat circumvented and smoothed truncation of domain is possible as shown in Figure 2.7(c). For this purpose, the shape function $\phi|(|\mathsf{x}-\mathsf{x}_I|)|$ at point x with respect to point x_I is modified to make $\phi|(|\mathsf{x}-\mathsf{x}_I|)| = \phi|(|d_I|)|$. The parameter d_I is called wrap-around distance which defined by distances $s_0 = |(|\mathsf{x}-\mathsf{x}_I|)|$, $s_1 = |(|\mathsf{x}_c-\mathsf{x}_I|)|$ and $s_2 = |(|\mathsf{x}_c-\mathsf{x}|)|$ where x_c is the node at tip of the discontinuous boundary as shown in Figure 2.7(c). Parameter d_I is calculated as (Organ et al. (1996)):

$$d_I = \left(\frac{s_1+s_2}{s_0}\right)^{\gamma} s_0 \tag{2.38}$$

The exponent γ is used to limit the domain behind the concave boundary. The reasonable choices for its numerical values are $\gamma = 1$ or 2 (Organ et al. (1996)). This method can easily be implemented for 2-D problems.

2.8.3 Transparency method

Transparency method is also introduced to smooth the influence domain around the tip of discontinuous boundary. The method was presented as an alternative to diffraction method as it is easily applicable to 3-D problems (Organ et al. (1996)). Underlying concept behind this method is that the boundary of concave object is made transparent near the tip and degree of transparency depends upon the distance from the tip. This method wraps the boundary of influence domain around the concave solid boundary where the wrap-around parameter d_I is calculated as:

$$d_I = s_0 + d_{mI}\left(\frac{s_c}{\bar{s_c}}\right)^{\gamma} \qquad \gamma \geq 2 \tag{2.39}$$

where s_0 is the same as for diffraction method, d_{mI} is the radius of influence domain of node x_I, s_c is the distance from tip to the intersection point and $(\bar{s_c})$ is the distance from tip to the point where the boundary is completely opaque. An illustration of transparent method is presented in Figure 2.7(d).

2.9 Treatment with moving boundaries

Selection of appropriate approach for grid generation around moving objects is imperative for problems relating to Fluid Structure Interaction. Various methods have

been devised to accommodate moving boundaries in a meshed domain. Grid generation methods for simulating moving boundaries can be classified as Boundary fitted and Non-boundary fitted methods. This classification is characterized by the manner in which the grid interacts with the moving boundary. An overview of these methods is presented in the following.

2.9.1 Boundary fitted grid methods

Grids generated using these methods are also called Body conformal grids. The nodes (or grid points) of this type of grids exactly coincide with the boundary (or interface). Therefore, the boundary is clearly demarcated by the location of grid points. The boundary conditions can directly be applied to the grid points and motion of the boundary is explicitly tracked by the movement of grid points. Elements near the solid boundary move and morph with the moving interface. Boundary fitted grid methods can further be classified into those which employ finite difference schemes and those which are suitable for finite volume and finite element schemes.

Boundary fitted grids which are suitable for finite difference schemes are commonly known as composite grids (Chesshire and Henshaw (1990); Tang et al. (2003)). In this approach, a main mesh is generated within the entire domain. However, sub-meshes are generated around the embedded bodies which interact with the main mesh close to their outer boundary. The schematic of such composite grids is shown in Figure 2.8. Sub meshes are generated using orthogonal or algebraic grid generation algorithms. Each sub mesh uses a separate local coordinate frame. These methods use finite difference approach which offers simple mathematical modelling and efficient computing. However, information exchange over the grid interfaces is carried out using computationally expansive interpolation techniques. Moreover, morphing of sub meshes is limited due to the use of generalized coordinates.

Unstructured Boundary fitted grids are suitable for finite element and finite volume schemes. These schemes are usually applied in an Arbitrary Lagrangian Eulerian (ALE) formulation (Hu et al. (2001); Sarrate et al. (2001)). The grid points coinciding with the moving boundaries exactly follow the movement of the interface. Movement of nodes away from the moving boundaries is progressively decayed using some mathematical algorithm. ALE offers an elegant approach to incorporate motion in the grid points. The movement of the interface is accurately tracked and boundary conditions are directly imposed. Grid resolution can be controlled to achieve to accurately capture the flow behaviour. However, excessive smearing of grid may necessitate re-meshing during the computational process. Computational overheads caused by constant re-meshing and inaccuracies introduced during data transfer to new grid points are the major disadvantages of these methods.

2.9.2 Non-boundary fitted grid methods

These methods are also known as 'Non-body-conformal methods'. These methods employ a background mesh which may be structured or non-structured. The solid body is embedded in the background mesh and the background grid does not conform to the solid boundary. These methods are further classified as Cartesian and Immersed boundary methods. Cartesian method can be called as a simplified version of non-body fitted Methods which was proposed by Clarke et al. (1986) and De Zeeuw and Powell (1991). This method used a standard Cartesian grid to solve inviscid flows around complex embedded solid boundaries. Distinguishing features Cartesian grid method are (Ye et al. (1999)):

1. Grid generation process is greatly simplified.
2. Grid distortion is not experienced near the boundaries of complex shapes.
3. Governing equations can be retained in simple Cartesian coordinate form.
4. Requirement of re-meshing is alleviated for problems pertaining to moving boundaries.

However, complications are experienced during imposition of boundary conditions at the immersed boundaries. Moreover, the immersed boundary may cut the background cells in an arbitrary manner which could adversely affect the accuracy and conservation properties of numerical solver (Mittal and Kumar (2001)). Especially for viscous flow simulations, the resolution of boundary layer along the immersed boundary may be compromised resulting in lower fidelity of the solution. Therefore, use of Cartesian grid methods is restricted to Euler flows. Udaykumar et al. (1996) and Ye et al. (1999) has however proposed extension of this method to viscous unsteady flows.

Immersed boundary methods (Peskin (1977); Glowinski et al. (1994)) employ force term as a source term in the governing equations (mass conservation equations, no-slip conditions etc) to cater for the effect of boundary. The boundary topology is identified through interpolation from background cells. This class of methods is useful for viscous flows. However, one of the limitations of these methods is that the boundary is smeared over the scale of a few cell-width due to representation of point-force on finite mesh (Ye et al. (1999)). Inaccuracies generated by this smearing effect are typically large if solid boundary is closely coupled with flow field evolutions (Udaykumar et al. (1996)). Another limitation associated with non-body conformal methods is that the grid has limited control over flow resolution. This is due to the fact that they solely rely on background grid for flow calculations. However, these method are able to better manage the phase jumps and deforming interfaces and therefore are well suited for FSI problems encountered in biological applications (Chew et al. (2006)).

2.10 Conclusion

Coupled fluid-structure interaction problems can be modelled using various algorithms, each having its own strengths and limitations. For problems relating to flow induced vibrations, a partitioned approach seems more appealing due to its underlying flexibility and generality. Also for these problems, closely coupled models offer higher accuracy but consume more computational resources in bargain. Choice of any particular FSI algorithm is therefore based on required accuracy, system behaviour and available computational resources.

For treatment of moving boundaries, both body conformal and non-body conformal methods have their own pros and cons. However, with the use of meshfree methods, requirement for a structured grid is somehow relaxed and dealing with moving boundaries becomes simpler. Therefore, use of body conformal grid appears to a better option. Various methods were considered to modify influence domain near sharp concave boundary. Line of sight method is found to provide the simplest way of dealing with the sharp discontinuity in the domain.

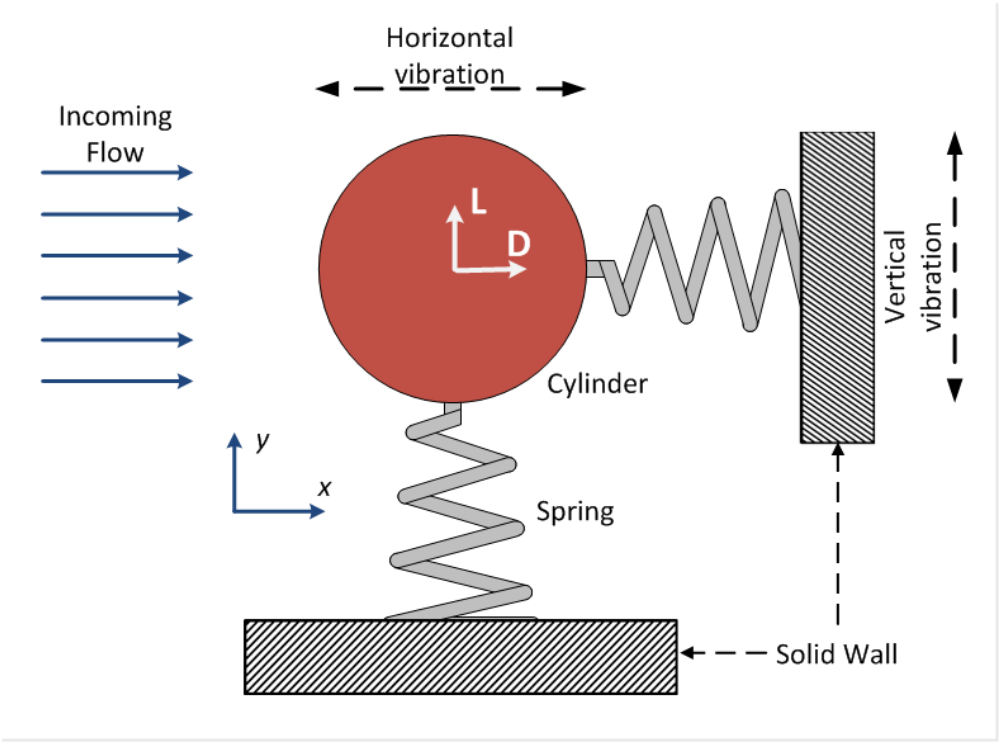

(a) Spring mounted cylinder with two degrees of freedom

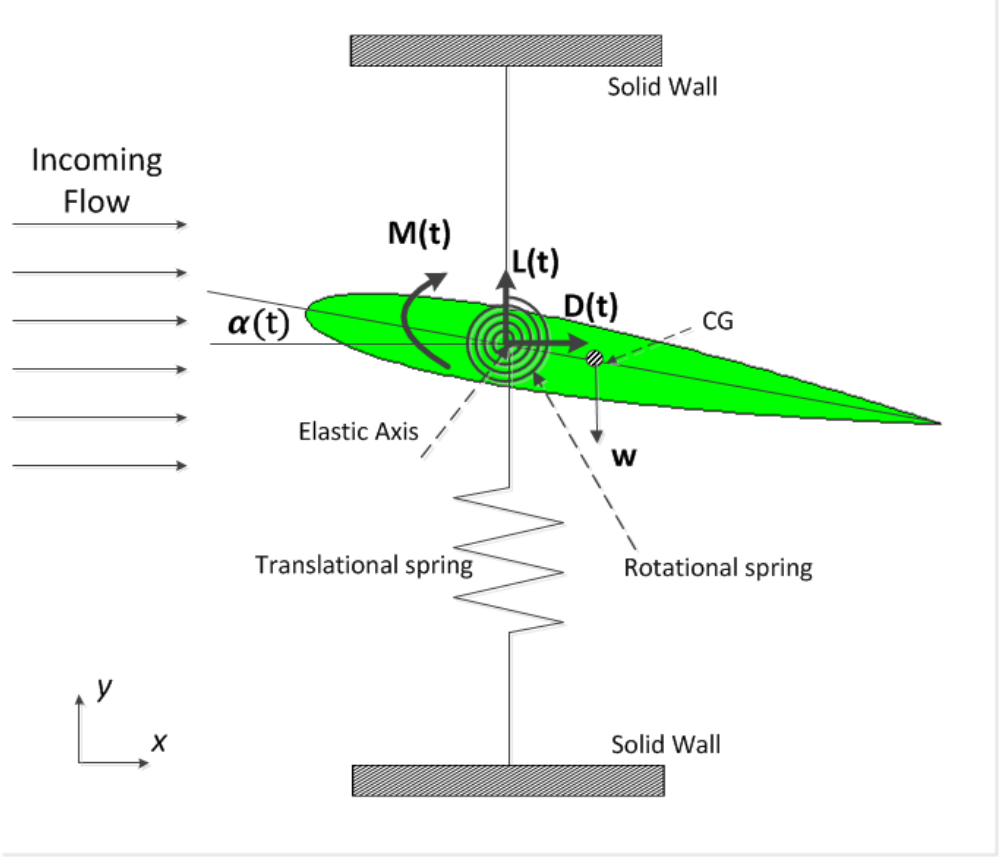

(b) Airfoil with two degrees of freedom

Figure 2.4: Schematic of elastically mounted solid objects in fluid

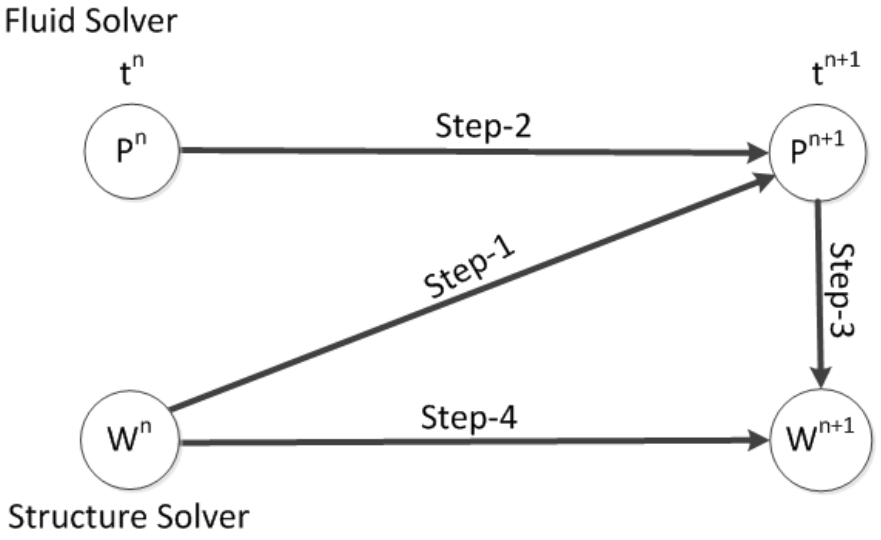

Figure 2.5: Marching of two field staggered solutions (conceived from Carlos et al. (2001))

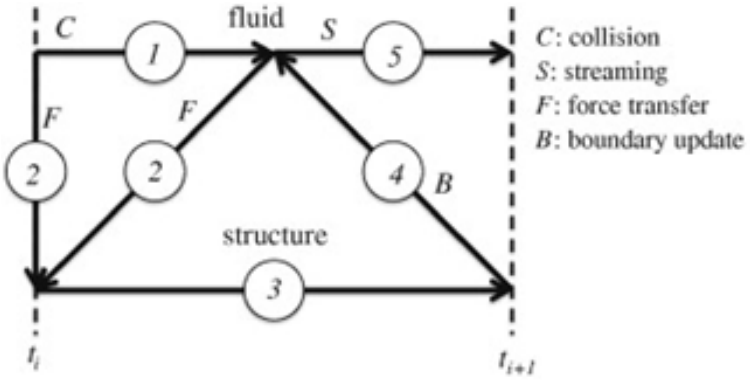

(a) 1^{st} Explicit scheme

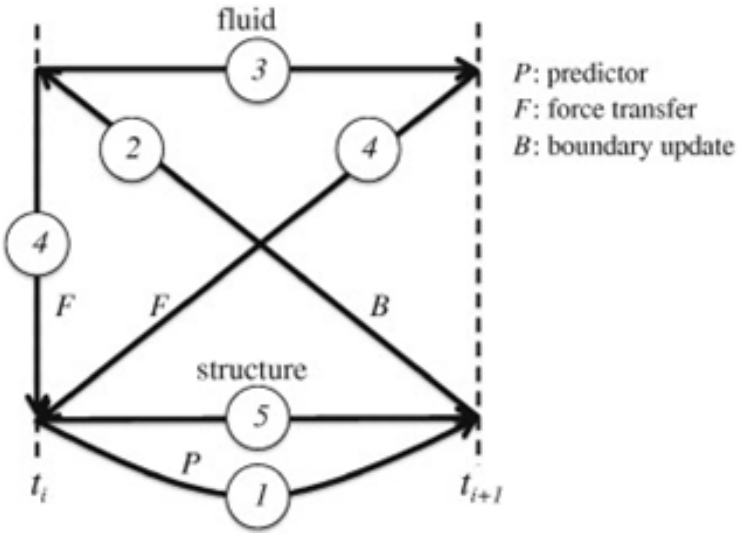

(b) 2^{nd} Explicit scheme

Figure 2.6: Partitioned system coupling Algorithms presented by De Rosis et al. (2013)

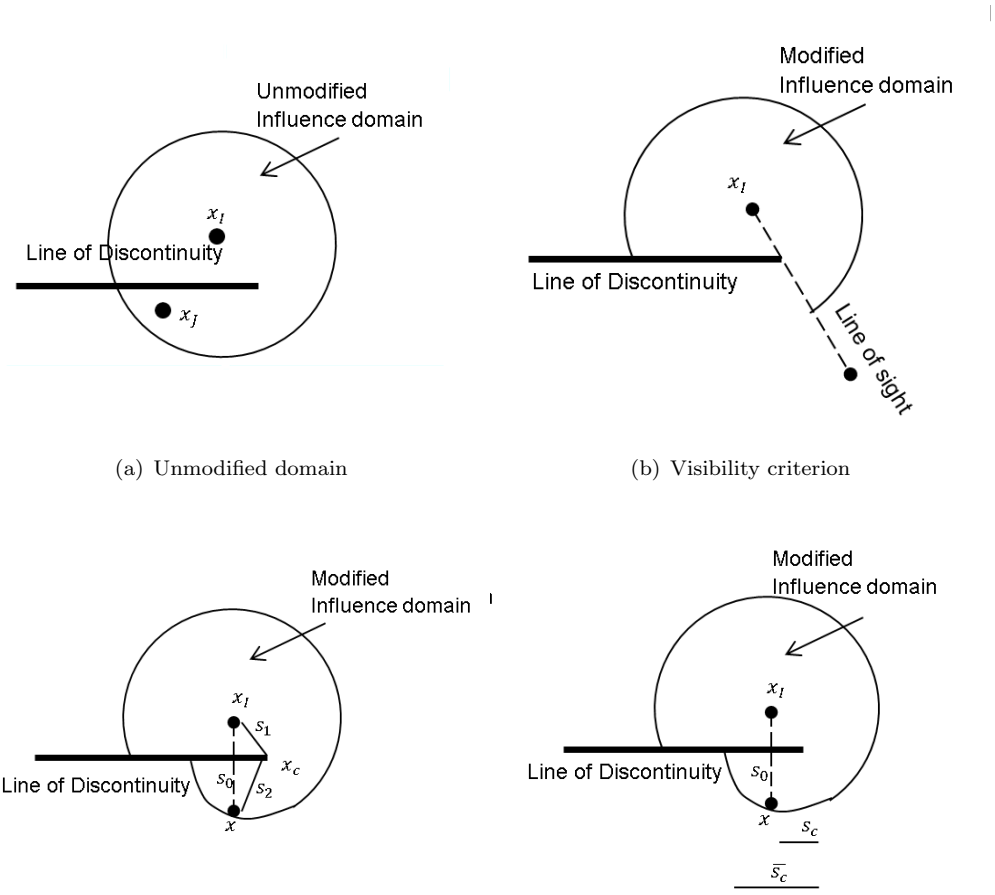

(a) Unmodified domain

(b) Visibility criterion

(c) Diffraction method

(d) Transperancy method

Figure 2.7: Criteria for modifying influence domain near line of discontinuity

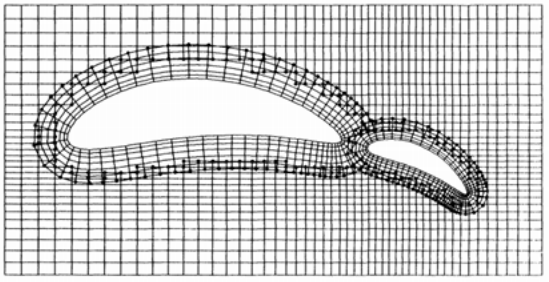

Figure 2.8: A typical composite mesh around 2D wing and flap (Henshaw and Chesshire (1987))

Chapter 3

Fundamentals of meshfree methods and their comparison

3.1 Evolution of meshfree particle methods

3.1.1 Early developments

Development of meshfree methods can be traced back to the advent of collocation methods in 1930s. Slater (1934) used a collocation method for problems relating to electronic energy bands in metals. Frazer and Skan (1937) studied the approximation of functions and solutions of differential equations using collocation methods. Lanczos (1938) studied trigonometric interpolation of various functions. However, the evolution of contemporary meshless methods started in 1970s when they were studied as an alternative to FDM and FEM. Chorin (1973) suggested a vortex method while performing numerical studies on mildly viscous flows. Later, Piperno et al. (1995) extended the concept by applying it to boundary layer flow. Pavlin and Perrone (1979) used energy concepts to show the ability to use arbitrary and irregular meshes within the framework of FDM. In the same context, Liszka and Orkisz (1980) demonstrated the use of FDM on irregular meshes. Snell et al. (1981) studied the application of general finite difference methods (GFDM) on boundary value problems having complex geometries.

3.1.2 Research since 1990

From the early 90s, there has been an increased interest by the researchers in meshfree methods. The reason for this was the increased dependency on simulations to solve engineering design problems and limitations of mesh based methods started to be felt more prominently. That was the time when two separate classes of meshfree methods namely Meshfree Weak-form and Strong-form methods started to emerge. Nayroles et al. (1992)

introduced a method of smooth approximation of function by generalizing the widely used finite element method. The method was termed as the Diffuse Element Method (DEM) and it was aimed to remove the limitations of FEM pertaining to regularity of approximated function and requirement of mesh generation. Belytschko et al. (1994) introduced Element Free Galerkin (EFGM) Method which was based on moving least square (MLS) approximation of the weak form of differential equations. Later, motivated by the theory of wavelets, Wing Kam et al. (1995) proposed reproducing kernel particle method (RKPM). The method possessed the desirable attributes of previously developed meshfree methods like SPH (Smoothed Particle Hydrodynamics), DEM and EFGM and was claimed to be more accurate than SPH and computationally more efficient than DEM and EFGM. Later, Liu et al. (1997) presented moving least square reproducing kernal methd (MLSRK) by formulating moving least square interpolation scheme in the framework of reproducing kernal method. Recently, generalization of MLSRK has been proposed as moving least square radial reproducing polynomial (MLSRRP) by Salehi and Dehghan (2013) which is shown to provide better accuracy compared with the previous method. Moreover, complex variable reproducing kernel particle method (CVRKPM) has been presented by Chen and Cheng (2010) to overcome the high computational cost associated with conventional RKPM. A hybrid CVRKPM-FE method was also presented by Li et al. (2013) for transient heat conduction problems. The hybrid method aims to lower the computational cost as well as improve the implementation of essential boundary conditions by combining meshfree and meshed methods.

3.1.2.1 Development of Smoothed Particle Hydrodynamic

Smoothed Particle Hydrodynamic is another widely used meshless method which was originally proposed by Gingold and Monaghan (1977) for astrophysical applications and later applied to free surface flows by Monaghan (1994). G. R. Liu (2003) presented a general approach to construct an analytical smoothing function for SPH approximation. The scheme is extensively being used for fluid mechanics problems with particular applications to free surface flows. Ferrari et al. (2009) suggested a time varying diminishing (TVD) Runge Kutta scheme for time marching of the problem. Dehnen and Aly (2012) presented a generalized smoothed kernel to overcome instabilities induced by particle disorder in SPH. Moreover, various researchers have also suggested different techniques to overcome artificial surface tension effects associated with SPH (e.g. Price (2008), Read et al. (2010), Hopkins (2013), Saitoh and Makino (2013)).

3.1.2.2 Moving Particle Semi-implicit method

The MPS (Moving Particle Semi-implicit) is a Lagrangian mesh-free method which was originally proposed by Koshizuka and Oka (1996) for viscous incompressible flows. The method was found effective especially for free surface flows. However, it may suffer from

instabilities caused by non-uniform particle distribution (Tsuruta et al. (2013)). Various improvements and modifications have been proposed in the original method since its inception. For example, Khayyer and Gotoh (2009) proposed a modified MPS method by introducing new formulation of pressure gradient and allowing slight compressibility. Lee et al. (2011) suggested improvements to overcome the shortcomings related to non-optimal source term, gradient and collision models and free surface particle search. Tsuruta et al. (2013) proposed a method to introduce sufficient repulsive forces between colliding particles to avoid inter-particle penetration. More recently, Sun et al. (2014) has suggested a technique for particle position shifting and collision handling for MPS which is found to be effective in suppressing the pressure fluctuations.

3.1.2.3 Polynomial Interpolation methods

In 2002, Liu and Gu (2001b) proposed polynomial interpolation on set of arbitrarily distributed points using a method called Point Interpolation method (PIM). The polynomials having delta function property were used as approximating shape functions which means that the interpolation function will passes through each data point in the influence domain. However, the method showed some singularity problems due to ill conditioning of moment matrices. These issues relating to PIM were later removed by proposing Point Interpolation methods based on radial basis function by Wang and Liu (2002b). The method benefits from excellent interpolation stability characteristics of RBFs which makes the method very robust at randomly distributed particles (G. R. Liu (2005)). Atluri and Zhu (1998) suggested meshless local petrov Galerkin Method (MLPGM) which employed local symmetric weak form (LSWF) to solve the differential equations using least square method. The method does not require a mesh either for variable interpolation or for integration of energy. Other methods developed in this regard are Boundary node method (Mukherjee and Mukherjee (1997)), Boundary point interpolation method (Gu and Liu (2002)), radial point interpolation method (RPIM) (Liu and Gu (2001a)) and meshfree weak-strong form method (Liu and Gu (2003)). Recently, Shivanian (2014) has applied radial point interpolation method for 3-D non-linear wave equations. They proposed a variation in current method and introduced spectral meshless radial point interpolation method (SMRPI) which is shown to possess better convergence rate compared with the conventional method. Zhuang et al. (2014) has proposed a mixed sub-region radial point interpolation method (MS-RPIM) for analysing crack tip fields. The suggested approach coupled Williams expansion with classical RPIM to accurately perform fracture analysis near crack tip.

3.1.2.4 RBF based techniques

During the same period, the so called Radial Basis Function (RBF) interpolation based meshfree methods were also emerging as another class of meshless methods. RBFs are

primarily the tools for multivariate data and function interpolating in higher dimensional problems (Driscoll and Fornberg (2002). They however find an important application in meshless methods where global solution of a PDE can be evaluated by translating the space spanned RBFs to a set of RBF centres.

In 1971, Hardy (1971) first used RBFs to generate topographic surfaces through sparse set of data points. However, in 1990, Kansa (1990) proposed application of RBFs for solving PDEs. The method was later found highly useful for solution of flow problem with irregular (or scattered) computational nodes arrangement (Sanyasiraju and Chandhini (2008); Wang and Liu (2002a); Shu et al. (2003, 2005b)). Franke and Schaback (1998) proposed Hermite type interpolation using RBFs. This method guarantees the solution of linear equations. Larsson and Fornberg (2005) investigated the behaviour of increasingly flat RBFs. Other significant contributions in this area were made by Chen and Brebbia (1998),Hon et al. (2015), Mai-Duy and Tran-Cong (2001), Driscoll and Fornberg (2002), Wang and Liu (2002a) and Chen and Tanaka (2002).

One approach of employing RBFs is the direct approximation of function for PDEs like in the work of Driscoll and Fornberg (2002); Hon et al. (2015); Franke and Schaback (1998)) and Chen and Tanaka (2002). Another approach is to approximate the derivatives appearing in PDEs rather than the function approximation. This approach simplifies the procedure especially for non-linear problems. RBF direct quadrature (DQ) method by Shu et al. (2003) and RBF finite difference method by Tolstykh and Shirobokov (2003) are the examples where derivative approximation is achieved using RBFs.

RBF based meshfree methods are collocation methods which are truly meshfree and spectrally accurate. However, they suffers from the problem of ill-conditioned set of equations. Various researchers have suggested use of local RBFs to cope with ill-conditioning effect (Shu et al. (2003), Tolstykh and Shirobokov (2003), Wright and Fornberg (2006)). These local RBF methods compromise on spectral accuracy and come up with a sparse, well-conditioned linear system which is also more flexible in handling non-linearity. Among these, RBF-FD has been independently proposed by Tolstykh and Shirobokov (2003) and Wright and Fornberg (2006) for different types of applications. The technique provides a better conditioned spectrally accurate and sparse linear system with more flexibility to handle non-linearities. The idea is to generalize the use of finite difference on a grid containing arbitrary / random nodes instead of a regular grid. Subsequent contribution in RBF-FD were made by Fornberg and Lehto (2011), Chinchapatnam et al. (2007), Chinchapatnam et al. (2009) and Bayona et al. (2010). Wang and Liu (2002a) discussed the effect of shape parameter of RBF-FD and RBF-HFD type formulation. Chinchapatnam et al. (2007) demonstrated solution of Navier Stokes Equations using RBF-FD technique. Bayona et al. (2010) discussed the convergence properties of RBF-FD formulas. Javed et al. (2013a) and Javed et al. (2014b) proposed adaptive shape parameters for local RBFs to overcome the inaccuracies in domains having large variation of nodal density. The scheme was used for solution of

flow equations in primitive variable form. In order to overcome high computational cost associated with the meshfree scheme, hybrid grid methods were proposed which coupled RBF based schemes with and conventional finite differencing. The methods were applied to flow problems around stationary as well as moving solid objects by Javed et al. (2013b) and Javed et al. (2014a).A comparison of global and local RBFs was presented, by Waters and Pepper (2015), for solving incompressible flow with heat transfer. Local RBFs were also applied for the solution of coupled heat transfer and free surface flow problems by Hon et al. (2015).

3.2 Classification of meshfree methods

There are different ways to classify the meshfree methods. However the following three are the most common manner of classifying these:

1. Classification according to formulation procedure
2. Classification according to function approximation
3. Classification according to domain representation

3.2.1 Classification according to formulation procedure

Formulation procedure appears to be the most effective way of categorizing the meshfree methods. These methods can be classified into two different categories based on the formulation procedures.

3.2.1.1 Meshfree weak form methods

These methods make use of the governing differential equations and corresponding derivative boundary conditions in their respective weak form. The integral equations in their weak forms are then worked to get a system of algebraic equations over the background cells in the domain. Due to the requirement of background mesh, these methods may not be termed as *truly* meshfree. However, weak form methods show excellent numerical stability. Moreover, Neumann boundary conditions are naturally satisfied by weak form (G. R. Liu (2003)). Meshfree weak form methods started getting interest of researchers since early 90s when Nayroles et al. (1992) devised Diffused Element Method (DEM) by employing Moving Least Square (MLS) method, proposed by Lancaster and Salkauskas (1981), to Galerkin weak form. Subsequently, the popularity of these techniques increased even more when Belytschko et al. (1994) proposed Element Free Galerkin method (which was actually based on DEM) and made significant contributions by employing it to many mechanics problems. Atluri and Zhu (1998) presented

meshfree local Petrov-Gaerkin (MLPG) method which employed shape functions in local weak form of differential equations using moving least square (MLS). The method was later extended for solving flow equations in primitive variable form by Wu et al. (2010).

3.2.1.2 Meshfree collocation methods

Meshfree collocation methods are based on strong form of governing equations and boundary conditions. The system of equations is obtained by discretizing the differential equations over the finite number of nodes using collocation techniques. Collocation methods refer to truly meshfree in nature, as these do not require any background mesh for integral evaluation. These methods offer relatively simpler computational modelling and are generally faster than weak form methods (Liu and Gu (2003)). However, special treatment may be required for implementation of Neumann Boundary conditions while using strong form methods. Meshfree Strong form methods have a long history. The general finite difference method (GFDM) was developed in 1970s (Girault (1974), Pavlin and Perrone (1979), Snell et al. (1981)). A common collocation method is the Smoothed Particle Hydrodynamics (SPH) in which state of the system is represented by finite number of particles arbitrarily distributed inside the domain. SPH has been successfully implemented for free surface flows (Monaghan (1994)) incompressible flows (Liu et al. (2003)), gravity currents, elastic flow problems, heat transfer (Cleary and Monaghan (1999)) and high velocity impact problems (Libersky et al. (1997)). In order to simulate discontinuities at the front of shock waves, discontinuous SPH has been suggested by Lam et al (G. R. Liu (2003)).

Another important class of such methods uses radial basis functions for collocation methods. Radial basis functions (RBFs) are multivariate interpolation functions. In early 90s, Kansa (1990) proposed their use for the solution of differential equations over scattered data points. Further, improvements in these methods have been made by suggesting local RBF methods (Shu et al. (2003); Fornberg and Lehto (2011); Chinchapatnam et al. (2006, 2007); Javed et al. (2013a, 2014b); Hon et al. (2015); Waters and Pepper (2015)) which improve the accuracy by making the coefficient matrices better conditioned.

3.2.2 Classification according to function approximation

Function approximation is very important during solution of problem. Therefore, meshless methods are often categorized according to the approximation function used at the nodes. Some of the common categories in this regard are as follows:

1. Methods based on moving least square approximations like in diffuse element method (DEM) (Nayroles et al. (1992)), Element Free Galerkin (EFG) method

(Belytschko et al. (1994)) and meshless local Petrov Galerkin (MLPG) (Atluri and Zhu (1998)).

2. Methods based on integral representation of function like in smooth particle hydrodynamics (SPH) (Gingold and Monaghan (1977); Price (2008); Read et al. (2010); Hopkins (2013); Saitoh and Makino (2013)) and reproducing kernel particle method (RKPM) (Wing Kam et al. (1995); Chen and Cheng (2010); Salehi and Dehghan (2013); Li et al. (2013)).

3. Methods based on point interpolation method like the one used by Liu and Gu (2001b), Wang and Liu (2002b), and methods employing Radial Basis Function (RBFs) (Franke and Schaback (1998); Liu et al. (2002); Mai-Duy and Tran-Cong (2001); Liu and Gu (2001a); Shu et al. (2003); Tolstykh and Shirobokov (2003); Shivanian (2014); Zhuang et al. (2014)

3.2.3 Classification according to domain representation

Another way of classification of meshfree method is the domain representation. The meshless methods can be categorized in domain type and boundary type methods. In domain type representation, the domain as well as the boundary is represented by the field nodes. However, for boundary type methods, the boundary integral equations are setup by the field nodes at the boundary only. No nodes are present inside the domain. Boundary node method proposed by Mukherjee and Mukherjee (1997) Galerkin boundary node method by Li and Zhu (2009) are the example of boundary type meshfree methods. More recently these methods have been applied for magnet-hydrodynamics (MHD) (Tatari and Ghasemi (2014)) and for 3-D problems (Li (2011)).

3.3 A comparative study of different meshfree methods

Navier Stokes equations are non-linear partial differential equations and any numerical technique used for their solution should be able to provide accurate approximation of the underlying derivatives at grid points. Meshfree methods are no exception to this. Therefore, prior to moving towards the actual solution of Navier Stokes equations using meshfree methods, a study has been conducted to compare the accuracy of some candidate methods. As mentioned earlier, the scope of current research has been restricted to collocation based methods. These methods are truly mehsfree as they do not require any background mesh for function approximation or numerical integration. Moreover, they offer relatively straightforward solution algorithm. Following three meshfree methods are therefore chosen for their comparison of accuracy:

1. Smoothed Particle Hydrodynamics (SPH) method

2. Moving Particle Semi Implicit (MPS) method
3. Radial Basis Functions in Finite Difference Mode (RBF-FD)

For the purpose of analysis, 1^{st} and 2^{nd} derivatives and Laplacian (∇^2) of a pre-defined function were approximated using above mentioned meshfree methods. Accuracy of derivative approximation was worked out by comparing the results from respective method with *true* values obtained by evaluating the analytical expressions. The formulation of gradients, using each method, is however important before performing the actual comparison. Therefore, the formulation of expressions for gradients and Laplacian, using each meshfree method considered in this study, is outlined in the following subsections.

3.3.1 Smoothed Particle Hydrodynamics (SPH)

Let us consider a domain represented by finite number of particles. The approximation of any field variable ϕ at a particle i in the domain can be expressed, using SPH, in terms of the neighbouring particles j as follows (G. R. Liu (2003)):

$$\phi_i = \sum_{j \neq i} \frac{m_j}{\rho_j} \phi_j \omega_{ij} \tag{3.1}$$

Where, m_j and ρ_j are the mass and density values of neighbouring particle, ω_{ij} is the kernel for particle i with respect to particle j and ϕ_j is the evaluation of ϕ at particle j. Similarly, the gradient and Laplacian of ϕ_i can be approximated as:

$$\nabla \phi_i = \sum_{j \neq i} \frac{m_j}{\rho_j} \phi_j . \nabla_i \omega_{ij} \tag{3.2}$$

$$\nabla \left(\frac{1}{\rho} \nabla \phi \right)_i = \sum_{j \neq i} m_j \frac{8}{(\rho_i + \rho_j)^2} . \frac{(\phi_i - \phi_j) X_{ij} \nabla_i \omega_{ij}}{r_{ij}^2 + \delta^2} \tag{3.3}$$

Here, δ used as a parameter to avoid singularity. Usually $\delta = 0.01 r_e$ is set (where r_e is the radius of influence domain). For these calculations, a B-Spline Kernel Function is used for SPH and MPS formulation. It is a cubic spline function suggested by Monaghan and Lattanzio (1985) and is expressed as:

$$\omega = \frac{15}{7\pi h^2} \begin{cases} 2/3 - R^2 + 1/2R^3 & 0 \leq R \leq 1 \\ 1/6(2-R)^3 & 1 \leq R < 2 \\ 0 & R \geq 2 \end{cases} \tag{3.4}$$

where, $R = r_{ij}/h$, h is the smoothing particle length and

$$r_{ij} = \sqrt{(x_i - x_j)^2 + (y_i - y_j)^2} \tag{3.5}$$

h is set as 2.1 times the nodal displacement in this case. Derivative of kernel function are expressed as:

$$\nabla\omega_{ij} = \frac{X_i - X_j}{r_{ij}} \frac{\partial\omega_{ij}}{\partial r_{ij}} \tag{3.6}$$

here, X_k is the coordinate value of x or y of point k in a particular direction. Therefore,

$$\frac{\partial\omega}{\partial x} = \left(\frac{x_i - x_j}{r_{ij}}\right) \frac{15}{7\pi h^2} \begin{cases} -\frac{2r_{ij}}{h^2} + \frac{3}{2}\left(\frac{r_{ij}^2}{h^3}\right) & 0 \le R \le 1 \\ -\frac{1}{2}\left(2 - \frac{r_{ij}}{h}\right)^2 . \frac{1}{h} & 0 \le R < 2 \\ 0 & R \ge 2 \end{cases} \tag{3.7}$$

$$\frac{\partial\omega}{\partial y} = \left(\frac{y_i - y_j}{r_{ij}}\right) \frac{15}{7\pi h^2} \begin{cases} -\frac{2r_{ij}}{h^2} + \frac{3}{2}\left(\frac{r_{ij}^2}{h^3}\right) & 0 \le R \le 1 \\ -\frac{1}{2}\left(2 - \frac{r_{ij}}{h}\right)^2 . \frac{1}{h} & 0 \le R < 2 \\ 0 & R \ge 2 \end{cases} \tag{3.8}$$

3.3.2 Moving Particle Semi Implicit (MPS)

Gradient of parameter ϕ (defined by Eq (3.1)) at point i is expressed using MPS method as (Koh et al. (2012)):

$$\nabla\phi_i = \frac{D}{n_0} \sum_{j \neq i} \frac{(\phi_j - \phi_i)(\vec{r}_j - \vec{r}_i)}{|\vec{r}_j - \vec{r}_i|^2} \omega_{ij} \tag{3.9}$$

Similarly, Laplacian of ϕ_i is expressed as:

$$\left(\nabla^2\phi\right)_i = \frac{2D}{n_0\lambda} \sum_{j \neq i} (\phi_j - \phi_i)\omega_{ij} \tag{3.10}$$

where D is the dimension number (2 in case of two dimensional domain). n_0 and λ are expressed as:

Table 3.1: Commonly used radial basis functions $\varphi(r)$, where r is the radial distance from point of interest. σ is the shape parameter

Type of radial basis function	Expression of $\varphi(r)$
Multi-quadratic (MQ)	$\varphi(r) = \sqrt{r^2 + \sigma^2}$
Inverse Multi-quadratic (IMQ)	$\varphi(r) = 1/\sqrt{r^2 + \sigma^2}$
Inverse Quadratic (IQ)	$\varphi(r) = 1/(r^2 + \sigma^2)$
Gaussian (GA)	$\varphi(r) = \exp(-(\sigma r)^2)$

$$n_0 = \sum_{j \neq i} \omega_{ij} \tag{3.11}$$

$$\lambda = \frac{\sum\limits_{j \neq i} (r_{ij})^2 \omega_{ij}}{\sum\limits_{j \neq i} \omega_{ij}} \tag{3.12}$$

3.3.3 Formulation of Radial Basis Function

For N scattered data points ($x_i \, \epsilon \, \mathbf{R}^{d+1}$, $1 \leq i \leq N$), the approximation $\bar{\psi}(x)$ to a real valued function $\psi(x)$ using Radial Basis Function (RBF) is written as:

$$\bar{\psi}(x) = \sum_{i=1}^{N} \lambda_i \varphi(\|x - x_i\|), \qquad x \epsilon \mathbf{R}^d \tag{3.13}$$

where $\varphi(\|x - x_i\|)$ is a radial basis function, $\|.\|$ is a standard Euclidean norm and λ_i is the expansion coefficient. d is the number of dimensions. Some of the common radial basis functions have been defined in table 3.1. The unknown parameter $\lambda_i = 1, 2, \ldots N$ can be obtained by setting $\bar{\psi}(x_i) = \psi_i, i = 1, 2, \ldots N$. This leads to the system of linear equations:

$$A\underline{\lambda} = U \tag{3.14}$$

where, $\underline{\lambda} = \{\lambda_1, \lambda_2, ...\lambda_N\}^T, U = \{u_1, u_2, ...u_N\}^T$ and $A_{i,j} = \varphi(\|x_j - x_i\|)$

3.3.4 RBF in Finite Difference mode (RBF-FD)

As mentioned before, local RBFs have been proposed to overcome the shortcomings of global RBFs. One of the local RBF techniques suggests using RBF in Finite Difference Mode (the so called RBF-FD method). RBF-FD is the generalization of classical finite difference method over scattered data points. The scheme has particularly been found highly effective in solving lid driven cavity flow problems (Chinchapatnam et al. (2009)).

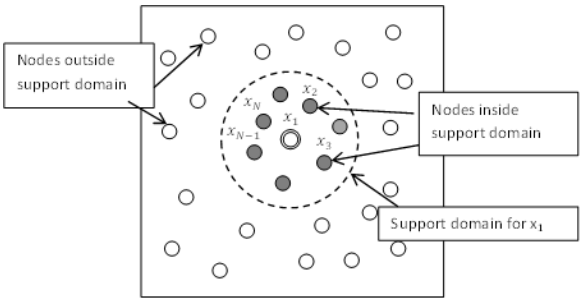

Figure 3.1: Support domain of a reference node

RBF-FD method directly approximates the spatial derivative of field variables to be used in differential equations.

The essence of RBF-FD is that derivative of any dependant variable, at a spatial location i, can be expressed as a weighted linear sum of same variable values at surrounding data points in the support domain (Chinchapatnam et al. (2007)). For this purpose, the interior and boundary of domain is represented by a set of scattered data points. A supporting stencil is identified for each data point by choosing N neighbouring particles. RBF-FD weights are then calculated for any differential operator $\mathcal{L}$, at each data point, by setting up local RBF interpolation.

Using classical finite difference approach, the derivative of any parameter ψ at any node, say x_1, can be expressed as

$$\mathcal{L}\psi(x_1) = \sum_{j=1}^{N} \mathbf{W}_{1,j}^{(\mathcal{L})} \psi(x_j) \tag{3.15}$$

where N is the number of nodes in the support domain of node x_1, $\psi(x_j)$ is the value of parameter ψ at node x_j and $\mathbf{W}_{1,j}^{(\mathcal{L})}$ is the weight of corresponding differential operator $\mathcal{L}$ at node x_j for node x_1 as shown in figure 3.1.

Recall that the standard RBF interpolation for a set of distinct points $x_j \epsilon \mathbf{R}^d$, $j = 1, 2, ...N$ is given by (Wright and Fornberg (2006)):

$$\psi(x) \approx s(x) = \sum_{j=1}^{N} \lambda_j \varphi(\|x - x_j\|) + \beta \tag{3.16}$$

where λ_j and β are the expansion coefficients. Eq. (3.16) can be written in Lagrange form as:

$$\bar{s}(x) = \sum_{j=1}^{N} \mathcal{X}\left(\|x - x_j\|\right) \psi\left(x_j\right) \tag{3.17}$$

where $\mathcal{X}(\|x - x_j\|)$ satisfies the cardinal conditions as

$$\mathcal{X}(\|x_k - x_j\|) = \begin{cases} 1, & \text{if } k = j \\ 0, & \text{if } k \neq j \end{cases} \qquad k = 1, 2, ...N \tag{3.18}$$

Applying the differential operator $\mathcal{L}$ on Eq. (3.17) at node x_1 we have:

$$\mathcal{L}\psi(x_1) \approx \mathcal{L}\bar{s}(x_1) = \sum_{j=1}^{N} \mathcal{L}\mathcal{X}(\|x_1 - x_j\|)\psi(x_j) \tag{3.19}$$

Using Eqs. (3.15) and (3.19), RBF-FD weights $\mathbf{W}_{1,j}^{(\mathcal{L})}$ are given by

$$\mathbf{W}_{1,j}^{(\mathcal{L})} = \mathcal{L}\mathcal{X}(\|x_1 - x_j\|) \tag{3.20}$$

The weights can be computed by solving the following linear system (Chinchapatnam et al. (2009)):

$$\begin{bmatrix} \Phi & e \\ e^T & 0 \end{bmatrix} \begin{bmatrix} W \\ \mu \end{bmatrix} = \begin{bmatrix} \mathcal{L}\Phi_1 \\ 0 \end{bmatrix} \tag{3.21}$$

where $\Phi_{i,j} = \varphi(\|x_j - x_i\|), i, j = 1, 2, \ldots, N$, $e_i = 1, 2, \ldots, N$, $\mathcal{L}\Phi_1$ represents the column vector $\mathcal{L}\Phi_1 = [\mathcal{L}\varphi\|x - x_1\|\mathcal{L}\varphi\|x - x_2\| \ldots \mathcal{L}\varphi\|x - x_N\|]^T$ evaluated at node x_1 and μ is a scalar parameter which enforces the condition:

$$\sum_{j=1}^{N} \mathbf{W}_{1,j}^{(\mathcal{L})} = 0 \tag{3.22}$$

Eq. (3.21) can be written in matrix form as:

$$[A]\{\mathrm{W}\} = \{\mathcal{L}\Phi\} \tag{3.23}$$

Evaluation of Eq. (3.23) at each node x_1 gives weights $\mathbf{W}_{1,j}^{(\mathcal{L})}$ of all the nodes in the support domain for particular differential operator $\mathcal{L}$. Corresponding weights and location of nodes in support domains are then used to approximate the complete differential equation at node x_1. However, solution of Eq. (3.23) requires that coefficient matrix $[A]$ be non-singular. Moreover, the matrix $[A]$ needs to be well-conditioned so as to avoid inaccuracies resulting from loss of precision from arithmetic methods. The possibility of having a non-singular and well-conditioned coefficient matrix $[A]$ depends upon the type of radial basis function and corresponding value of shape parameter used for the problem (Rippa (1999)).

The derivative of parameter ϕ can be expressed in RBF-FD as under (Chinchapatnam et al. (2007)):

$$\nabla\phi_i = \sum_{j=i}^{n} \mathbf{W}_{ij}^{(x)} \phi_j + \sum_{j=i}^{n} \mathbf{W}_{ij}^{(y)} \phi_j \tag{3.24}$$

where n is the number of neighbouring particles in influence domain and $\mathbf{W}_{ij}^{y}$ and $\mathbf{W}_{ij}^{x}$ are RBF weights for node i with respect to neighbouring node j for partial derivatives $\partial/\partial x$ and $\partial/\partial y$ respectively. Laplacian of a parameter ϕ can similarly be expressed as :

$$\left(\nabla^2\phi\right)_i = \sum_{j=i}^{n} \mathbf{W}_{ij}^{\nabla^2} \phi_j \tag{3.25}$$

In two dimensional space, Eq (3.25) can be expressed as:

$$\left(\nabla^2\phi\right)_i = \sum_{j=i}^{n} \mathbf{W}_{ij}^{(xx)} \phi_j + \sum_{j=i}^{n} \mathbf{W}_{ij}^{(yy)} \phi_j \tag{3.26}$$

Where $\mathbf{W}_{ij}^{xx}$ and $\mathbf{W}_{ij}^{yy}$ are RBF-FD weights for node i with respect to node j for derivatives $\partial^2/\partial x^2$ and $\partial^2/\partial y^2$ respectively. A Multi-Quadratic (MQ) basis function is used for evaluating RBF-FD weights.

3.3.5 Calculation of gradients and Laplacians

In order to compare the accuracy of derivatives obtained from three different methods, the gradients and Laplacians of a known function are calculated over 2-D rectangular domain. Following function is used for this purpose:

$$\phi(x, y) = \sin(xy) \tag{3.27}$$

Derivatives and Laplacian of $\phi(x, y)$ is expressed as:

$$\frac{\partial\phi}{\partial x} = y\cos(xy) \tag{3.28}$$

$$\frac{\partial\phi}{\partial y} = x\cos(xy) \tag{3.29}$$

$$\frac{\partial^2\phi}{\partial x^2} = -y^2\sin(xy) \tag{3.30}$$

$$\frac{\partial^2\phi}{\partial y^2} = -x^2\sin(xy) \tag{3.31}$$

$$\nabla^2(\phi(x, y)) = -(x^2 + y^2)\sin(xy) \tag{3.32}$$

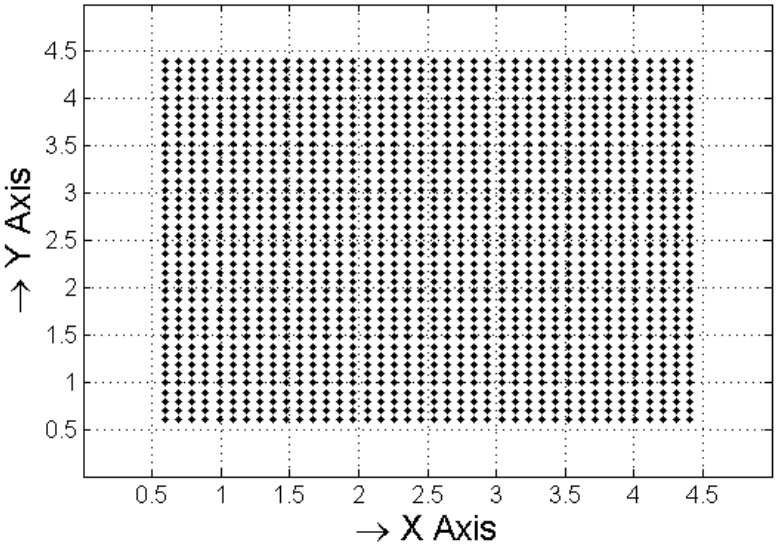

(a) Uniform grid

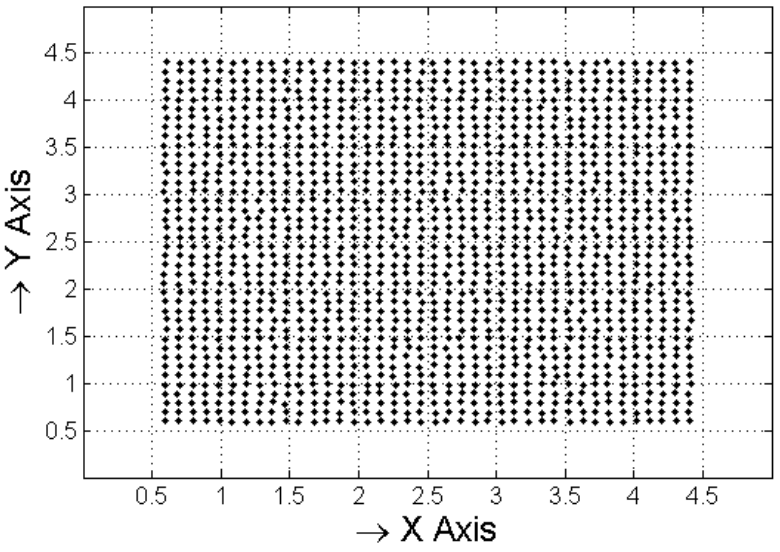

(b) Randomized grid

Figure 3.2: Nodal distribution in 2-D computational domain

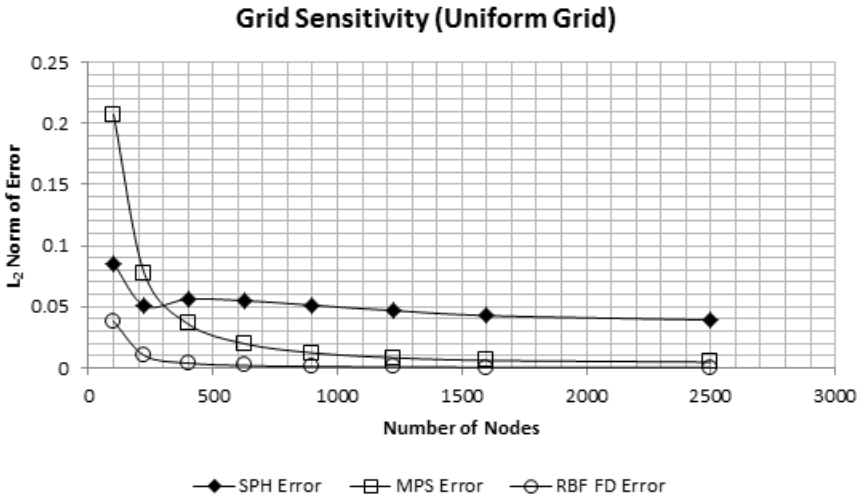

(a) For uniform grid

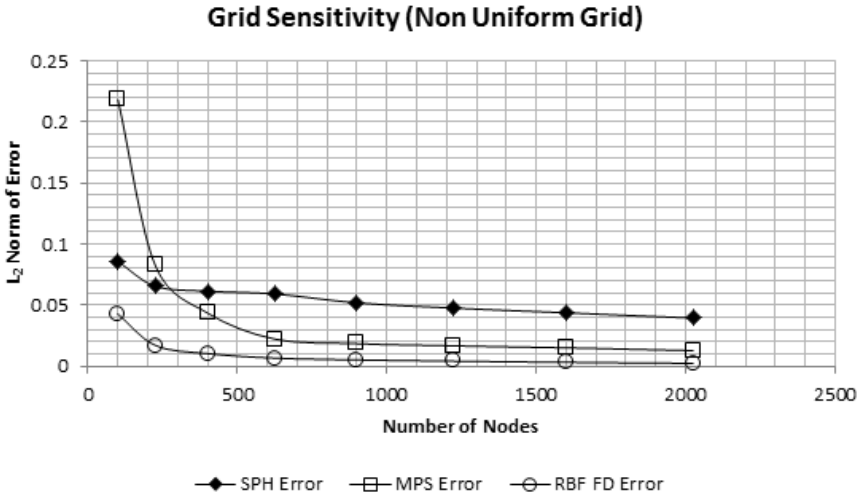

(b) For randomized grid

Figure 3.3: Norm-2 of error with changing number of nodes

Derivatives of Eq. (3.27) are calculated using SPH, MPS and RBF-FD methods over a domain $[0.5,\ 4.5] \times [0.5,\ 4.5]$. Computational domain is represented by finite number of particles (nodes) distributed over the domain. The test is carried out on both uniform and random particle distribution over the domain. Uniform grid is shown in Figure 3.2(a). Randomness is introduced by adding a noise of the order of $0.1L_0$ in the coordinate locations of nodes (L_0 is the grid spacing). Resultant non-uniform nodal distribution is shown in Figure 3.2(b). Influence domain for each particle was chosen to be 2.1 times the grid spacing.

Grid sensitivity study was conducted to find out the behaviour of results from each approach by reducing the grid spacing. For this purpose, the resultant values of Laplacian, from each method (SPH, MPS and RBF-FD), are compared with corresponding analytical value at every node. Norm-2 of the error has thus been obtained at each tested

grid size. The plots of norm-2 of error against total number of computational nodes are shown in Figure 3.3(a) and 3.3(b) for uniform and random grids respectively. It can be observed that the derivative approximations using RBF are more accurate than those from MPS and SPH. Although the solutions are more accurate for uniform grid, the convergence behaviour is similar on both (random and uniform) particle distribution and grid independence is achieved at a grid spacing $L_0 = 0.1$ (corresponding to 1600 nodes). Therefore, further comparative study is performed at the same grid size.

Plots of Laplacians obtained from all the three methods (SPH, MPS and RBF-FD) along with analytically obtained plots, for uniform grid of size $L_0 = 0.1$, are shown in Figure 3.4. Similar plots on random grid are shown in Figure 3.5. On uniform grid all the three methods (SPH, MPS and RBF-FD) produce reasonably smooth surfaces for Laplacian of function defined in Eq. (3.28). However, norm-2 of error obtained from RBF-FD is the smallest amongst the all at this grid size as shown in Figure 3.3(a). For randomized particle distribution, significant loss of smoothness is experienced for both SPH and MPS methods as shown in Laplacian surfaces in Figures 3.5(b) and 3.5(c). Similar behaviour (loss of smoothness of Laplacian surfaces on irregular particle distribution) of MPS and SPH method was observed by Koh et al. (2012) during a comparative study of different methods. This loss of smoothness is translated into increased error as depicted in Figure 3.3(b). However, resultant Laplacian surface obtained from RBF-FD method is still smooth even on randomized particle distribution. The error values do not increase with randomization (see corresponding curve in Figure 3.3(b)).

Similar behaviour is observed in the values of first derivatives ($\partial\phi/\partial x$ and $\partial\phi/\partial x$) of the given function ϕ. The values of derivatives, obtained on uniform and randomized grids, are plotted and compared and shown in Figures 3.6 and 3.7, respectively. Values of $\partial\phi/\partial x$ are plotted at mid height ($y = 2.5$) and those of $\partial\phi/\partial x$ were plotted at mid span ($x = 2.5$). The resultant profiles from RBF-FD method are found to closely match the analytical curve in all the cases. Spurious fluctuations are observed in the profiles from SPH and MPS at randomized grid. The fluctuations are more pronounced for SPH curves.

3.4 Conclusion

The comparative study carried out in this chapter has shown that RBF-FD is able to provide more accurate derivative approximations especially at random particle distribution. Loss of accuracy in SPH and MPS is mainly attributed to the generation of spurious oscillations. This observation is in agreement with a previous study from Koh et al. (2012). Moreover, SPH and MPS are fully Lagrangian methods which are known for producing nodal clustering and domain fracturing for flows around bluff bodies even at low Reynolds numbers (Shadloo et al. (2011, 2012)) as the nodes tend to follow the

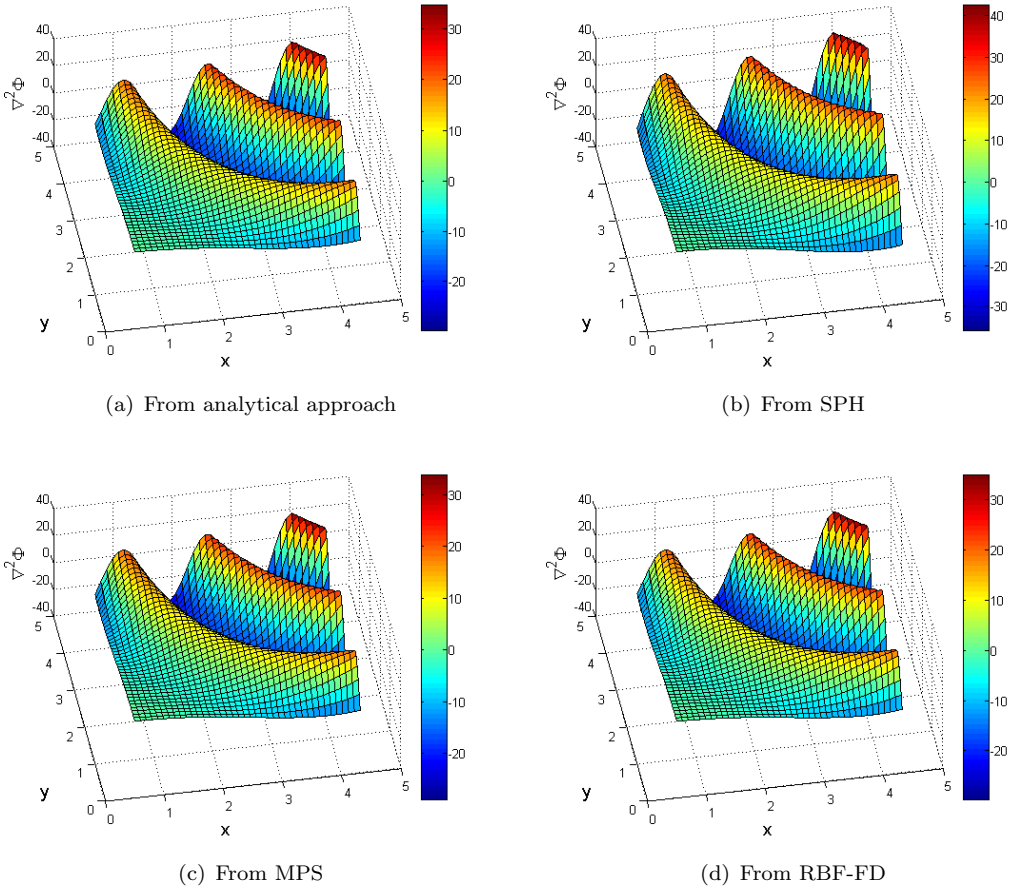

(a) From analytical approach

(b) From SPH

(c) From MPS

(d) From RBF-FD

Figure 3.4: Plots of Laplacian surfaces on uniform nodal arrangement. Smooth surfaces are obtained for SPH, MPS and RBF-FD

streamlines. Special treatment of nodes is therefore necessitated to maintain grid uniformity in such cases. Nevertheless, these Lagrangian methods are highly effective in dealing with free surface flows where boundary of the domain cannot be pre-specified. However, the problems where domain boundaries are pre-defined (like the ones used for flow around bluff bodies), can be well treated by RBF-FD method.

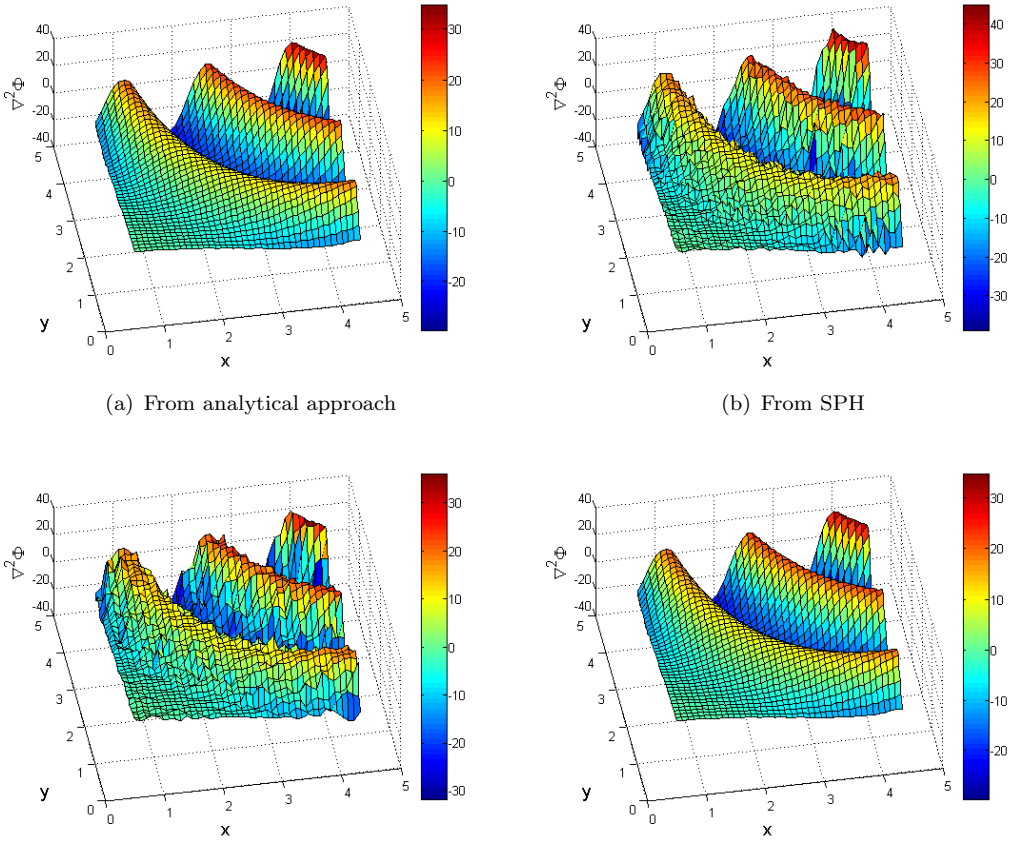

(a) From analytical approach

(b) From SPH

(c) From MPS

(d) From RBF-FD

Figure 3.5: Plots of Laplacian surfaces on randomized nodal arrangement. Surface for SPH and MPS are not smooth. Surface from RBF-FD is smooth

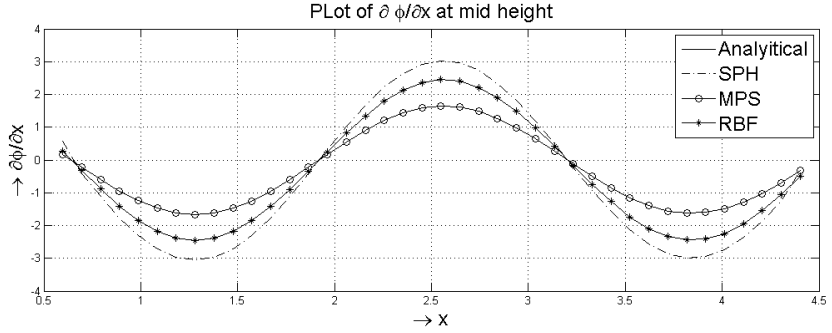

(a) $\partial\phi/\partial x$ at $y = 2.5$

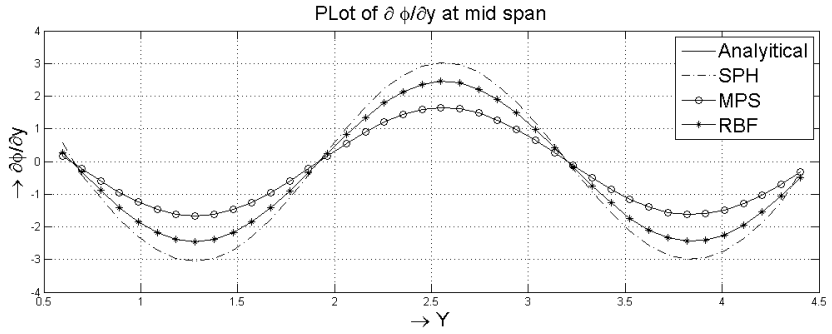

(b) $\partial\phi/\partial y$ at $x = 2.5$

Figure 3.6: Comparison of derivatives using SPH, MPS and RBF-FD on uniform nodal arrangement. Curves from RBF-FD are more accurate compared with those from SPH and MPS

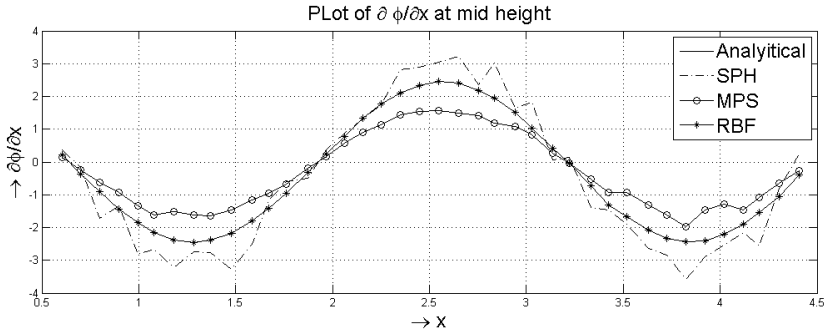

(a) $\partial\phi/\partial x$ at $y = 2.5$

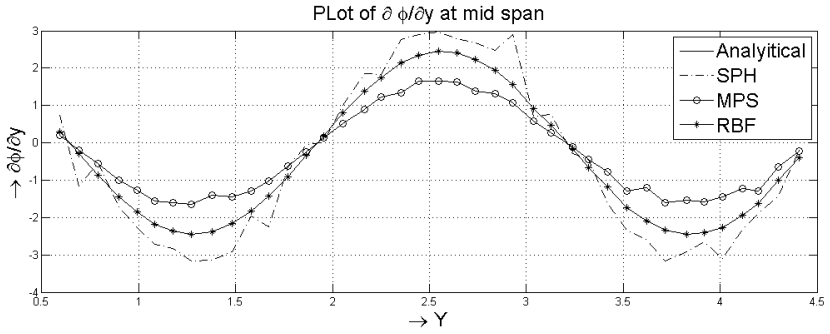

(b) $\partial\phi/\partial y$ at $x = 2.5$

Figure 3.7: Comparison of derivatives using SPH, MPS and RBF-FD on randomized nodal arrangement. Curves from RBF-FD are smoother and more accurate compared with those from SPH and MPS

Chapter 4

Shape Adaptive RBFs for flow problems

In this chapter, Radial basis functions in finite difference mode (RBF-FD) method is used for solving flow problems. Since Kansa (1990) proposed the use of RBFs for solution of partial differential equations (PDEs) over scattered data points, there has been a growing interest of researchers to use RBFs for solution of flow problems on irregular domains by collocation approach (Sanyasiraju and Chandhini (2008); Wang and Liu (2002a); Shu et al. (2003, 2005b)). On the other hand, it is well known that the coefficient matrices for RBF collocation methods become dense, large sized and ill-conditioned when the number of nodes increases. Various researchers have suggested use of local RBF methods to cope with ill-conditioning problem (Wright and Fornberg (2006); Shu et al. (2003); Tolstykh and Shirobokov (2003)).

Local RBFs compromise on spectral accuracy and produce well-conditioned and sparse linear systems which are capable of efficiently handling the non-linearities (Shu et al. (2003)). These methods are therefore considered well suited for fluid dynamics problems which involve a large number of data points in meshfree domains. RBF in Finite Difference Mode (RBF-FD) is a local RBF method which was independently proposed by Tolstykh and Shirobokov (2003) and Wright and Fornberg (2006) for different set of applications. RBF-FD allows the use of Finite Difference method on randomly distributed data points (or nodes). The method has been successfully applied to lid driven cavity flow problems by Shu et al. (2003), Chinchapatnam et al. (2007) and Chinchapatnam et al. (2009).

4.1 Adaptive Shape Parameter (ASP) for RBF

Accuracy of RBF interpolation mainly depends upon the *"flatness"* of basis function. Huang et al. (2007) suggested that accuracy of interpolation can be improved by making the basis function flatter. On the other hand, an increased flatness of basis function results in higher condition number of coefficient matrix. Large condition number of coefficient matrix of RBF weights causes inaccuracies in the solution for expansion coefficients coefficient (Kansa (1990)). Therefore, choice of basis function should be a balance between flatness and conditioning of coefficient matrices.

It has been known that the behaviour of basis functions (especially for Multi-quadratic and inverse multi-quadratic) depends heavily on th choice of shape parameter. Wang and Liu (2002a) stated that the sensitivity of results with choice of shape parameter was one of the biggest limitation of RBF. Various researchers (Huang et al. (2007); Wang and Liu (2002a); Gherlone et al. (2012); Rippa (1999)) have presented different methodologies to find the optimum values of shape parameters for RBFs. Franke and Schaback (1998) suggested optimal value of shape parameter based on total number of neighbouring particles and minimum diameter enclosing all the neighbouring particles around the data point. Rippa (1999) studied the selection of optimal shape parameter for RBFs and concluded that a scheme for determining good value of shape parameter should take the number and distribution of data points, radial basis function, condition number of coefficient matrix and precision of computation into account. For any particular interpolation problem, the radial basis function and precision of computation remains similar throughout the domain. However, if the distribution of data points is not uniform, the optimal value of shape parameter will differ for each data point in local RBFs and would depend upon the number and distribution of data points within its own influence domain.

During flow simulations, nodal distribution within the domain is varied to achieve optimal nodal density. Moreover, use of randomly distributed nodes is necessitated in many cases. In such situations, each data point will have different node distribution patterns within its influence domain. Therefore, use of a globally similar value shape parameter, for all the particles within the entire domain, will adversely affect the well conditioning of the coefficient matrix. Figure 4.1 depicts the trend of condition number of coefficient matrix with varying value of shape parameter (σ) for various RBFs. The plots are obtained on 41×41 pseudo random grid where node locations are disturbed slightly from their corresponding uniform grid positions. It can be observed that, irrespective of the basis function used, the range of shape parameter, corresponding to lower condition numbers of coefficient matrix, varies with the nodal spacing. Hence the accuracy of the solution would vary by changing the number and distribution of nodes for a constant shape parameter. For such domains, if fixed values are used, the round

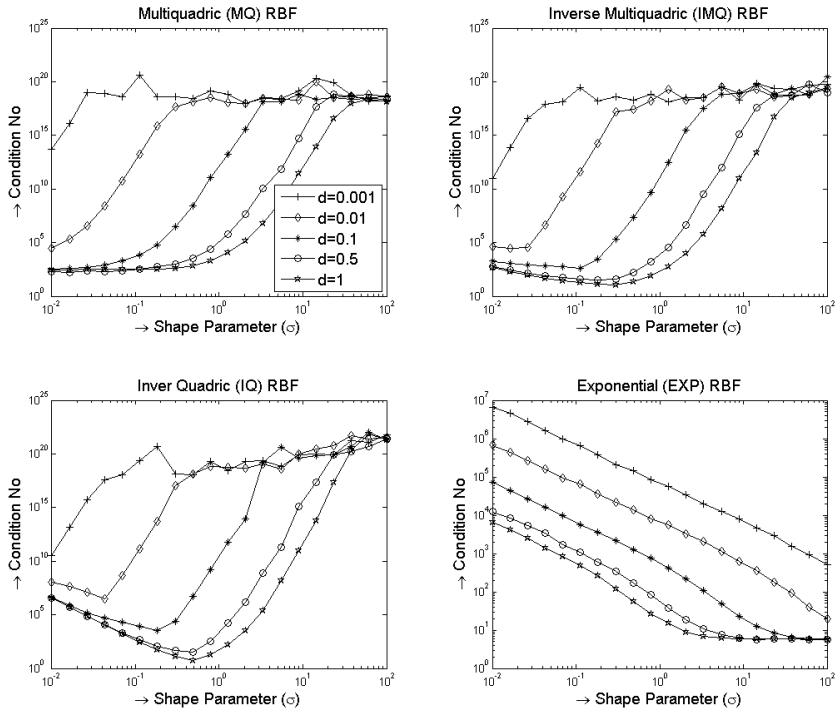

Figure 4.1: Variation of condition number of coefficient matrix with shape parameter

off errors caused by ill-conditioning sometimes dominates and the matrix solution becomes unstable hence causing breakdown of the solution process Gherlone et al. (2012). This puts severe limitations on the use of non-uniform or random particle distribution within the domain. Therefore, for the problems where same RBF function is used for the entire domain, choosing shape parameter value based on number and distribution of neighbouring data points could keep the condition number of coefficient matrix to the minimum.

The choice of the good value of shape parameter is still a hot topic in research and various authors have suggested different methods of finding an optimum shape value for different problems (Franke (1982); Rippa (1999); Wang and Liu (2002a); Huang et al. (2007); Gherlone et al. (2012)). However, for present study, a commonly used scheme, presented by Franke (1982), has been used which suggests the shape parameter as $\sigma_i = 1.25D/\sqrt{N}$ (Where N is the number of data points in the influence domain of the particle i and D is the diameter of the minimal circle enclosing all the data point). The method suggested by Franke (1982) is straightforward and has extensively been used. Other schemes for calculating optimum shape parameters can also be tested to further validate the concept.

For the adaptive shape parameter concept, the value of (σ) is calculated exclusively

for each data point and its value is decided based on the number and distribution of neighbouring particles in the influence domain. Besides ensuring accuracy and a well-conditioned coefficient matrix, use of adaptive shape parameter also allows larger variation of nodal density within the domain.

4.2 Comparison of accuracy between fixed and adaptive shape parameters

Accuracy of adaptively shaped radial basis functions in finite difference mode, has been tested by calculating 1^{st} and 2^{nd} derivatives and Laplacian of a known function over meshfree domain. For this purpose, a function has been chosen which results in varying values of first and second derivatives over different spatial regions. Following test function is used over a 2D domain with dimensions $[0.5,\ 4.5] \times [0.5\ 4.5]$:

$$f(x, y) = \sin\left[3(x - 2.5)(y - 2.5)\right] \tag{4.1}$$

The function $f(x, y)$, its first derivative $(\partial f/\partial x)$ and Laplacian $(\nabla^2 f = \partial^2 f/\partial x^2 + \partial^2 f/\partial x^2)$ have been plotted in Figures 4.2(a) to 4.2(c), respectively. Variation of $(\partial f/\partial y)$ is similar to that of $(\partial f/\partial x)$. Therefore, plots for $(\partial f/\partial y)$ are not included here. It can be observed that the gradients and Laplacian values of function are rather uniform in the middle of the domain. However, towards the edges and corners, sharp gradients are encountered. Therefore, an efficient meshing strategy should consider having higher nodal density towards corners which gradually coarsens while moving towards the middle of the domain. Hence, a 60×60 non-uniform particle distribution (as shown in Figure 4.3) has been chosen for the calculation of gradients using RBF-FD method.

Figure 4.4 shows the optimum values of σ over the entire domain using the criterion $(\sigma_i = 1.25D/\sqrt{N})$ proposed by Franke and Schaback (1998). This figure indicates that optimum values change by almost 400 percent across various regions of the domain. Therefore, use of globally similar values of σ will likely cause inaccuracies. The derivatives of given function have been calculated using globally similar values of σ as well as using ASP technique. The absolute error has been calculated for each approach by comparing the results with known values of derivatives of the function $f(x, y)$. Figures 4.5 and 4.6 show the error values of $\partial f/\partial x$ and $\nabla^2 f$ respectively, along the diagonal line (shown as thick line in figure 4.3) through the domain. Calculations have been done using Multiquadratic and Inverse Multiquadratic radial basis functions. For constant values of σ the results have been obtained using three different values ($\sigma = 0.5$,$\sigma = 1.0$ and $\sigma = 2.0$) and compared with ASP results to have better understanding of how results behave with varying the value of shape parameter.

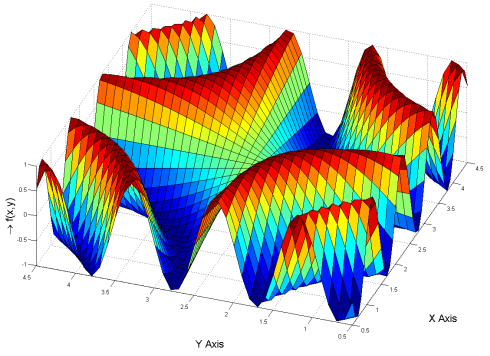

(a) Function f(x,y)

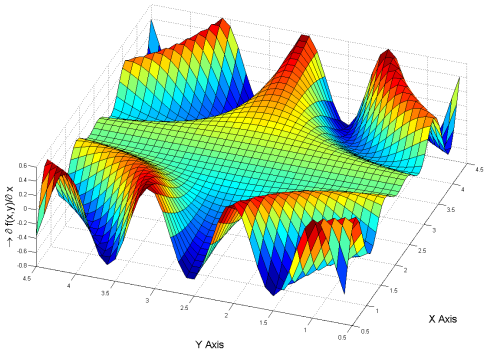

(b) First derivative $\partial f/\partial x$

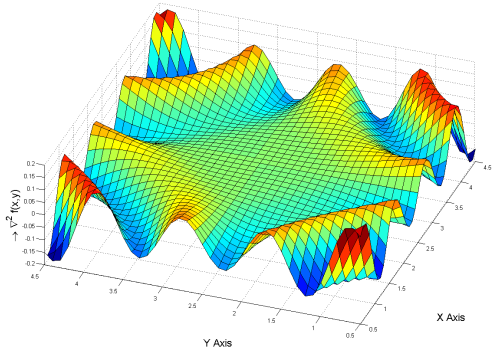

(c) Laplacian $\nabla^2 f$

Figure 4.2: Plot of Pre assumed function, first derivative and Laplacian

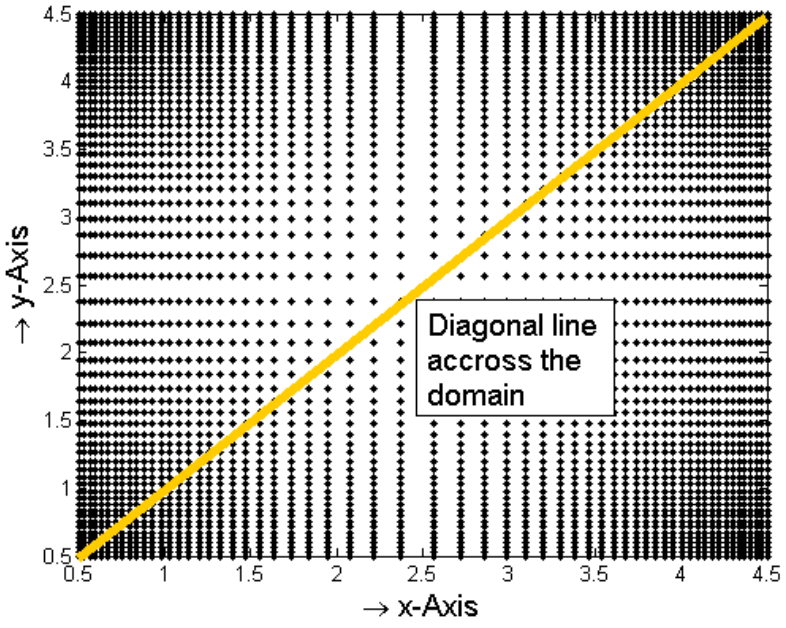

Figure 4.3: 60×60 Non-uniform Nodal Distribution within the Domain

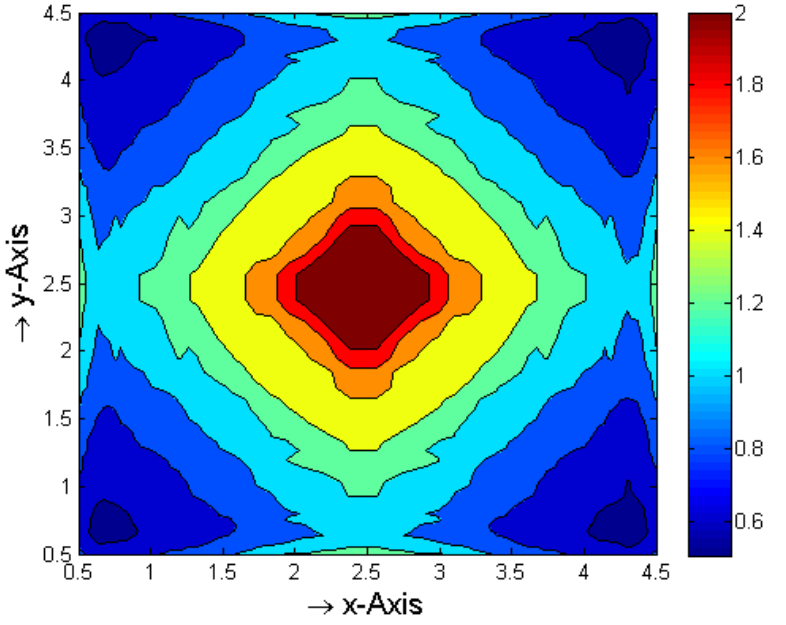

Figure 4.4: Profile of Optimum Values of Shape Parameter (σ)

Figure 4.3 shows that density of nodes varies along the diagonal from maximum (at bottom left corner) to minimum (in the middle) and then again to maximum (at top right corner). Therefore, optimum value of σ should vary accordingly. The plots in figures 4.5 and 4.6 show that, for fixed value of shape parameter (σ), the results are accurate only on partial range of the diagonal. Therefore, global accuracy is not achieved. However, adaptively varying the shape parameters (using ASP technique) results in good agreement with the analytical values throughout the range. For example, fixed value of $\sigma = 0.5$ provides good accuracy close to corners but the results tend to become erroneous in the middle of the domain. As the fixed value of σ is increased from 0.5 to 2.0, the large error region tends to shift towards the corners. This is due to the deviation from the suggested optimum value of shape parameter at various regions (Figure 4.4) that causes these errors.

In order to further explain the situation, curve of $\nabla^2 f$ has been plotted in Figure 4.7. It can be observed, in closed views, that RBF curve with fixed shape parameter tends to deviate from analytical values near the central part of the domain. However, the curve obtained by adaptively changing the shape parameter tends to closely follow the analytical value curve. Therefore, globally accurate results are achieved with adaptively changing the shape of the basis function according to the arrangement of neighbouring particles around the data points.

4.3 RBF-FD for flow equations in vorticity-stream function formulation

The applicability of shape adaptive RBFs has been studied for the solution of transient, incompressible and viscous flow equations in vorticity-stream function formulation. For this purpose, solution of Eqs. (2.25) - (2.28) has been sought using RBF based spatial derivatives. Time descritization is achieved using Crank-Nicolson scheme. Spatial derivatives appearing in Eqs. (2.25) and (2.26) can be approximated using RBF-FD as:

$$\frac{\partial \omega_i}{\partial t} + u_i \sum_{j=1}^{N} \mathbf{W}_{i,j}^{(x)} \omega_j + v_i \sum_{j=1}^{N} \mathbf{W}_{i,j}^{(y)} \omega_j = \frac{1}{Re} \left(\sum_{j=1}^{N} \mathbf{W}_{i,j}^{(xx)} \omega_j + \sum_{j=1}^{N} \mathbf{W}_{i,j}^{(yy)} \omega_j \right) \tag{4.2}$$

$$\sum_{j=1}^{N} \mathbf{W}_{i,j}^{(xx)} \psi_j + \sum_{j=1}^{N} \mathbf{W}_{i,j}^{(yy)} \psi_j = -\omega_i \tag{4.3}$$

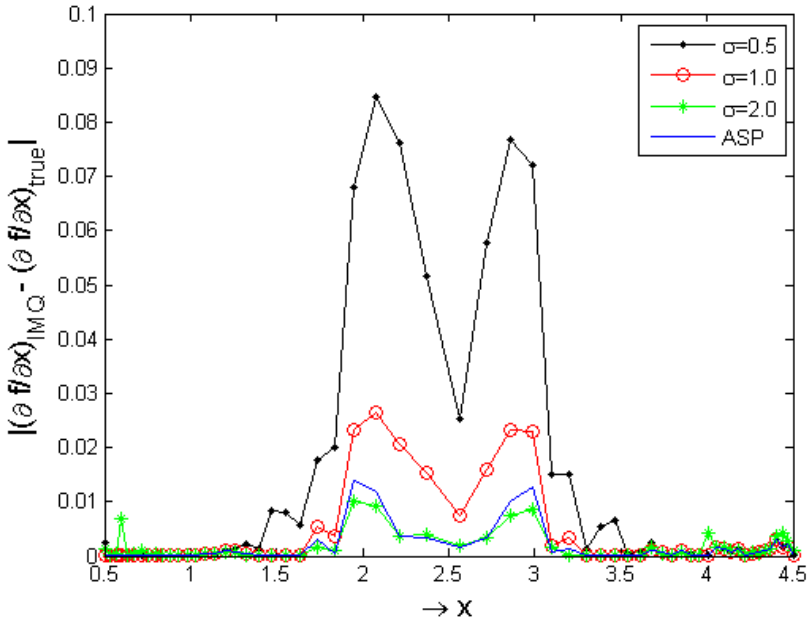

(a) IMQ RBF

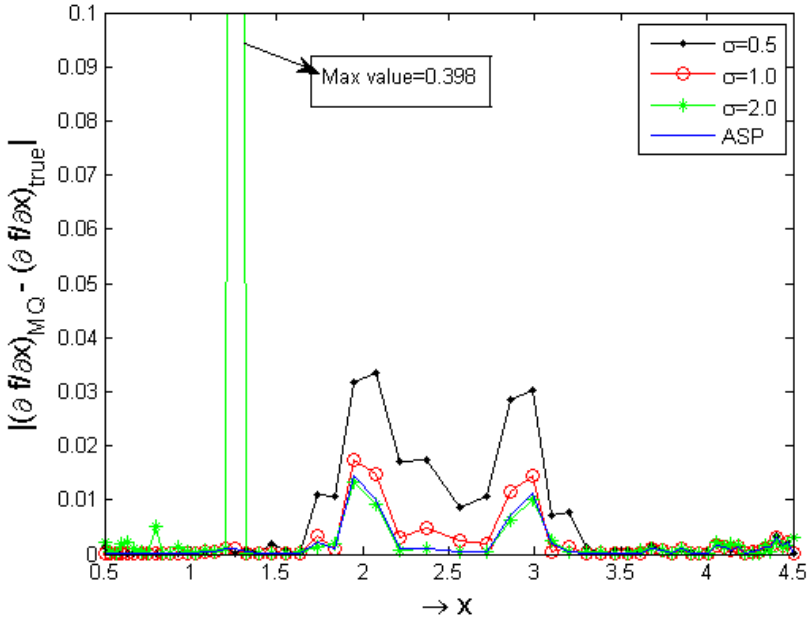

(b) MQ RBF

Figure 4.5: Error Plots of $\partial f/\partial x$ along Diagonal Line through the Domain for MQ and IMQ RBFs (Fixed and Adaptively Changing Values of shape parameter σ)

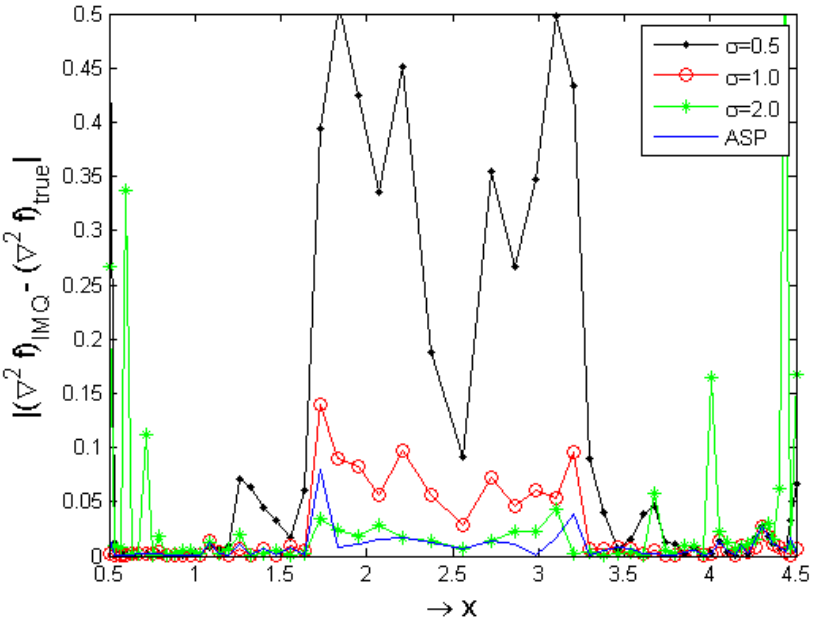

(a) IMQ RBF

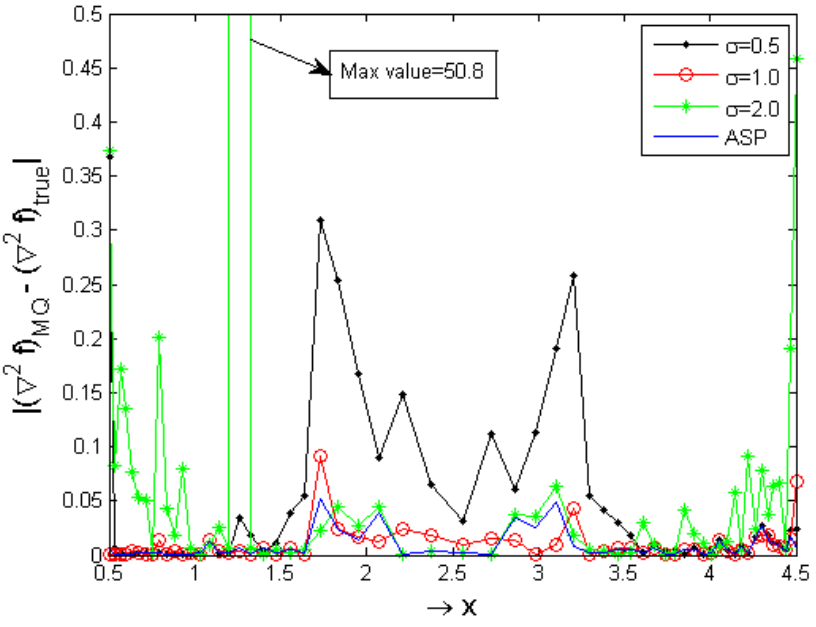

(b) MQ RBF

Figure 4.6: Error Plots of $\nabla^2 f$ along Diagonal Line through the Domain for MQ and IMQ RBFs (Fixed and Adaptively Changing Values of shape parameter σ)

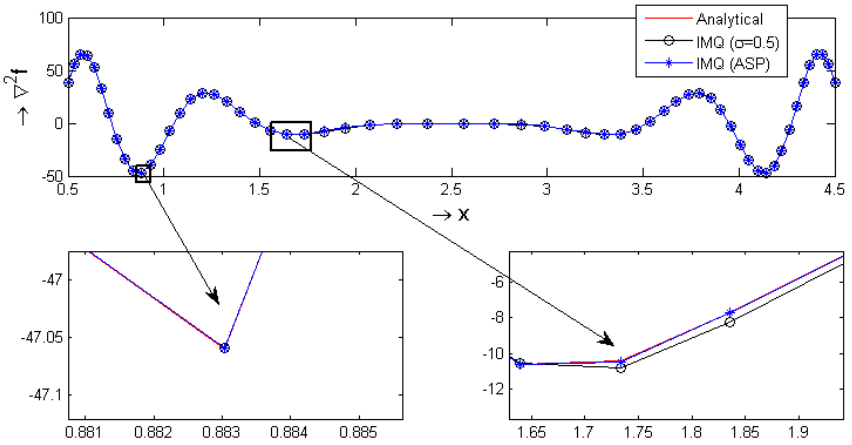

Figure 4.7: Comparison of Laplacian ($\nabla^2 f$) Curves along the diagonal

Temporal discretization of Eq. (4.2) can be obtained using Crank Nicolson scheme as follows (Hirsch (2002)):

$$\begin{aligned}\frac{\omega_i^{n+1}-\omega_i^n}{\delta t} = &\frac{1}{2Re}\left(\sum_{j=1}^{N}\mathbf{W}_{i,j}^{(xx)}\omega_j^{n+1}+\sum_{j=1}^{N}\mathbf{W}_{i,j}^{(yy)}\omega_j^{n+1}\right)\\ &-\frac{1}{2}\left(u_i\sum_{j=1}^{N}\mathbf{W}_{i,j}^{(x)}\omega_j^{n+1}+v_i\sum_{j=1}^{N}\mathbf{W}_{i,j}^{(y)}\omega_j^{n+1}\right)\\ &\frac{1}{2Re}\left(\sum_{j=1}^{N}\mathbf{W}_{i,j}^{(xx)}\omega_j^{n}+\sum_{j=1}^{N}\mathbf{W}_{i,j}^{(yy)}\omega_j^{n}\right)\\ &-\frac{1}{2}\left(\sum_{j=1}^{N}\mathbf{W}_{i,j}^{(x)}\omega_j^{n}+v_i\sum_{j=1}^{N}\mathbf{W}_{i,j}^{(y)}\omega_j^{n}\right)\end{aligned} \tag{4.4}$$

where ω_j^n and ω_j^{n+1} are the values of ω at node j at n^{th} and $(n+1)^{th}$ time step respectively. After rearrangement, Eq. (4.4) can be expressed in matrix form as:

$$\begin{bmatrix} a_{1,1}+1 & a_{1,2} & \dots & a_{1,N} \\ a_{2,1} & \ddots & \dots & \vdots \\ \vdots & \dots & \ddots & \vdots \\ a_{N,1} & a_{N,2} & \dots & a_{N,N}+1 \end{bmatrix} \begin{Bmatrix} \omega_1^{n+1} \\ \omega_2^{n+1} \\ \vdots \\ \omega_N^{n+1} \end{Bmatrix} = \begin{bmatrix} b_{1,1}+1 & b_{1,2} & \dots & b_{1,N} \\ b_{2,1} & \ddots & \dots & \vdots \\ \vdots & \dots & \ddots & \vdots \\ b_{N,1} & b_{N,2} & \dots & b_{N,N}+1 \end{bmatrix} \begin{Bmatrix} \omega_1^{n} \\ \omega_2^{n} \\ \vdots \\ \omega_N^{n} \end{Bmatrix} \tag{4.5}$$

where

$$a_{i,j} = -\frac{\delta t}{2}\left\{\frac{1}{Re}\left(\sum_{j=1}^{N}\mathbf{W}_{i,j}^{(xx)} + \sum_{j=1}^{N}\mathbf{W}_{i,j}^{(yy)}\right) - u_i\sum_{j=1}^{N}\mathbf{W}_{i,j}^{(x)} - v_i\sum_{j=1}^{N}\mathbf{W}_{i,j}^{(y)}\right\}$$

$$b_{i,j} = \frac{\delta t}{2}\left\{\frac{1}{Re}\left(\sum_{j=1}^{N}\mathbf{W}_{i,j}^{(xx)} + \sum_{j=1}^{N}\mathbf{W}_{i,j}^{(yy)}\right) - u_i\sum_{j=1}^{N}\mathbf{W}_{i,j}^{(x)} - v_i\sum_{j=1}^{N}\mathbf{W}_{i,j}^{(y)}\right\}$$

Similarly, Eq. (4.3) can be written in matrix form as:

$$\begin{bmatrix} \mathbf{W}_{1,1}^{(xx)} + \mathbf{W}_{1,1}^{(yy)} & \dots & \mathbf{W}_{1,N}^{(xx)} + \mathbf{W}_{1,N}^{(yy)} \\ \mathbf{W}_{2,1}^{(xx)} + \mathbf{W}_{2,1}^{(yy)} & \ddots & \vdots \\ \vdots & \dots & \vdots \\ \mathbf{W}_{N,1}^{(xx)} + \mathbf{W}_{N,1}^{(yy)} & \dots & \mathbf{W}_{N,N}^{(xx)} + \mathbf{W}_{N,N}^{(yy)} \end{bmatrix} \begin{Bmatrix} \psi_1 \\ \psi_2 \\ \vdots \\ \psi_N \end{Bmatrix} = -\begin{Bmatrix} \omega_1 \\ \omega_2 \\ \vdots \\ \omega_N \end{Bmatrix} \tag{4.6}$$

Velocity components at each node can be evaluated as:

$$u_i = \sum_{j=1}^{N}\mathbf{W}_{i,j}^{(y)}\psi_j, \qquad v_i = -\sum_{j=1}^{N}\mathbf{W}_{i,j}^{(x)}\psi_j \tag{4.7}$$

Starting from initial conditions, values of vorticity at next time step can be determined by solving linear system of Eqs. (4.5). During each iteration, Eq. (4.6) can be solved to find the values of stream function (ψ) at each node. The values of stream function can then be used to find velocity components using Eqs. (4.7).

4.3.1 Lid driven cavity flow

Lid driven cavity flow constitutes complex flow features like primary, secondary and tertiary eddies despite the fact that it has very simple geometry. The flow problem is therefore widely used to validate new computational techniques and novel schemes for flow simulations. Therefore, application of shape adaptive RBF-FD has been validated by simulating lid driven cavity flow in a square domain and comparing the results with

the benchmark solutions by Ghia and Shin (1982). Reynolds number ($Re = U_0 L/\nu$, where U_0 is the velocity of moving lid, L is the length of domain side and ν is the kinematic flow viscosity) is set as 400 and 1000 for the flow simulations. The fluid domain has been represented by 81×81 and 101×101 nodal grids for for $Re = 400$ and $Re = 1000$ cases respectively. The solutions have been obtained for constant as well as adaptively shaped radial basis functions. Non-uniform particle distribution has been introduced to capture higher gradients expected near solid walls and corners.

On all the four wall boundaries Γ, velocity components normal to boundary are assumed to be zero. This non-penetration flow boundary condition leads to $\vec{u}_n = \partial\psi/\partial\vec{t} = 0$ or $\psi = C_1$ at $x \in \Gamma$, where $\vec{u}_n$ is the velocity component in the outward normal direction to the boundary (Γ), n and t are normal and tangential directions to the boundary and C_1 is a constant. No slip boundary condition at the walls implies that tangential component of flow velocity along the boundary Γ remains constant and equal to the speed of the boundary itself. Therefore, $\vec{u}_t = \partial\psi/\partial\vec{n} = C_2$ at $x \in \Gamma$, where $\vec{u}_t$ is the velocity component parallel to the boundary (Γ) and C_2 is a constant. The values of stream function (ψ) near the boundary can be used to define the boundary conditions for vorticity (ω). Following higher order finite difference expressions for vorticity at the four boundaries, as suggested by Spotz and Carey (1995), are used here:

$$Left : \omega_{i,j} = -\frac{3}{h}\left[v_{i,j} + \frac{\psi_{i+1,j} - \psi_{i,j}}{h} + \frac{h}{6}\omega_{i+1,j}\right] \tag{4.8}$$

$$Right : \omega_{i,j} = \frac{3}{h}\left[v_{i,j} + \frac{\psi_{i,j} - \psi_{i-1,j}}{h} - \frac{h}{6}\omega_{i-1,j}\right] \tag{4.9}$$

$$Top : \omega_{i,j} = -\frac{3}{h}\left[v_{i,j} + \frac{\psi_{i,j} - \psi_{i,j-1}}{h} + \frac{h}{6}\omega_{i,j-1}\right] \tag{4.10}$$

$$Bottom : \omega_{i,j} = \frac{3}{h}\left[v_{i,j} + \frac{\psi_{i,j} - \psi_{i,j+1}}{h} - \frac{h}{6}\omega_{i,j+1}\right] \tag{4.11}$$

For lid driven cavity flow, all the boundaries are stationary except the top boundary which moves with a velocity U_0 in horizontal direction. Implementation of boundary conditions using Eqs. (4.8) - (4.11) necessitates the presence of locally orthogonal grid near the boundary. For uniform particle distribution, condition of locally orthogonal grid is naturally satisfied. However, for random particle distribution, inner particles may not remain orthogonal to the boundary. Therefore, special care has to be taken to ensure locally orthogonal grid near the boundary. In order to capture high flow gradients near the corners of the domain, refined grid is required. Therefore, non-uniform grid spacing with finer grid near the walls will improve the accuracy. In case of constant value of shape parameter (σ), the ratio of nodal spacing between corner-to-centre nodes is limited due to ill-conditioning effect of coefficient matrix for RBF weights in Eqs. (3.23) as discussed in Section 4.2. However, with introduction of adaptively shaped radial basis functions, the ratio of nodal spacing between corner-to-centre nodes

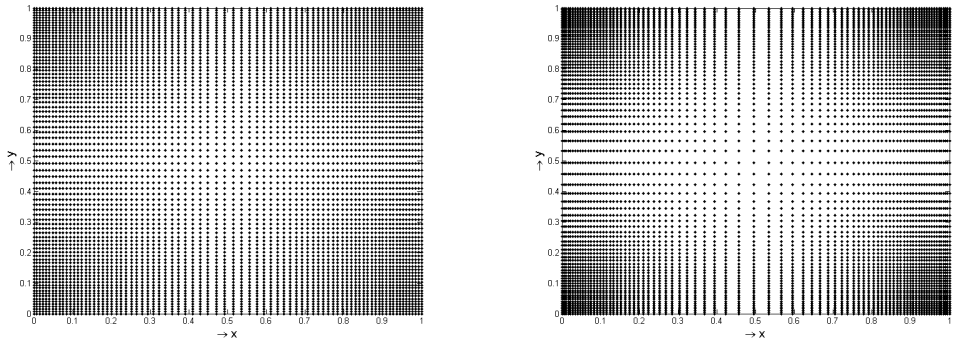

(a) For fixed shape parameter σ

(b) For adaptive shape parameter σ

Figure 4.8: Arrangement of nodes for lid driven cavity flow problem

can be increased without producing ill-conditioning effect. The grid can therefore be made much more refined, close to the walls, than same sized grid used for fixed shape parameter approach. The results are therefore more accurate for same number of nodes within the domain. Figures 4.8(a) and 4.8(b) show the nodal distributions for fixed and adaptive shape parameter cases for $Re = 400$. Due to the ill-conditioning effect with the use of fixed shape parameters, the ratio of nodal spacing between corner-to-centre nodes was limited to 4.0 only. Further refinement near the walls and corners resulted in inaccurate RBF-FD weights leading to erroneous solutions with the use of conventional RBF-FD approach. However, ratio of nodal spacing between corner-to-centre nodes could be increased to 8.0 with the use of adaptively shaped basis functions. Therefore much refined nodal distribution was obtained close to the corners as shown in figure 4.8(b). Finer grids were able to capture the gradients of field variables more accurately. Moreover, with the use of shape adaptive RBFs, optimized shape of basis function was maintained throughout the domain thus reducing the error. As a result, an improved accuracy was achieved. Figures 4.9(a) and 4.9(b) show profile of horizontal velocity component (v_x) at mid span and vertical velocity component (v_y) at mid plane respectively, for $Re = 400$ case. The results have been obtained using adaptively shaped RBF-FD. Similar velocity profiles have been calculated for $Re = 1000$ are shown in Figures 4.10(a) and 4.10(b), respectively. Contour plots of stream function (ψ) and vorticity (ω), obtained at $Re = 400$ using current method, have been compared with results from previous studies in Figure 4.11. Similar comparison, at $Re = 1000$ has been shown in Figure 4.12. At both Reynolds numbers, a primary vortex appears in the middle of the rectangular domain along with two opposite secondary vortices near bottom corners. The shape and strength values of these vortices agree well with previous solutions.

A comparison of results obtained from fixed and adaptively shaped RBF-FD has been presented, in Table 4.1. The error values are evaluated using standard results from

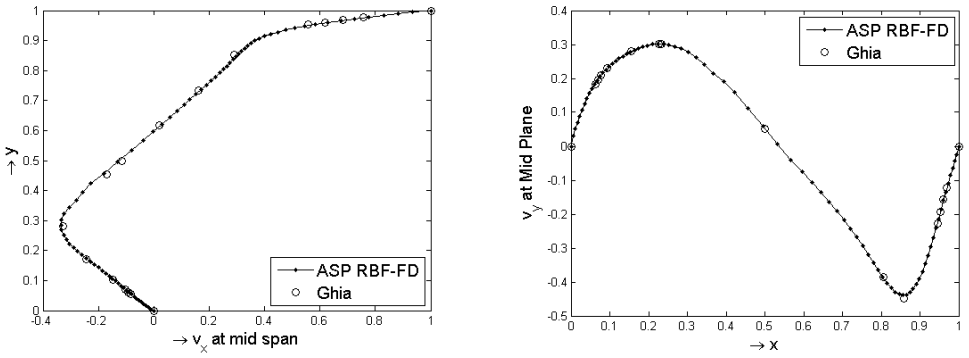

(a) v_x at mid span (b) v_y at mid plane

Figure 4.9: Velocity profiles for lid driven cavity flow at $Re = 400$ solved with adaptively shaped RBF-FD method

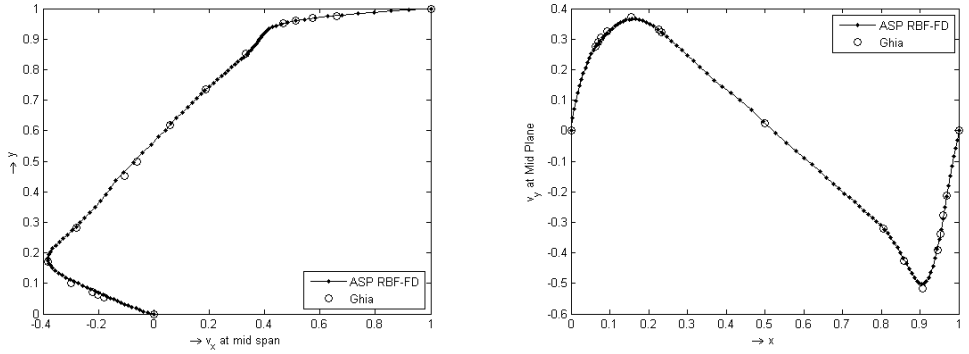

(a) v_x at mid span (b) v_y at mid plane

Figure 4.10: Velocity profiles for lid driven cavity flow at $Re = 1000$ solved with adaptively shaped RBF-FD method

Ghia and Shin (1982). Maximum relative error and norm of relative error for fixed and adaptive shape parameter cases have been shown. A significant reduction in error is achieved with the use of adaptively shaped basis functions. This is due to the possibility of having finer grids at critical regions and accurate approximation of gradients due to optimized shape of basis functions.

4.4 Conclusion

The concept of adaptive shape parameters (ASP) is found to be useful for flow problems where solutions are sought through local RBFs and nodal density is required to be varied significantly within the domain to capture high flow gradients. Adaptively shaped basis functions provide greater flexibility to change the nodal density thus enabling

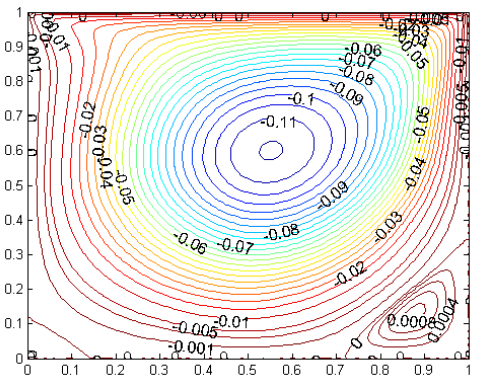

(a) Stream function (ψ) plot from present work

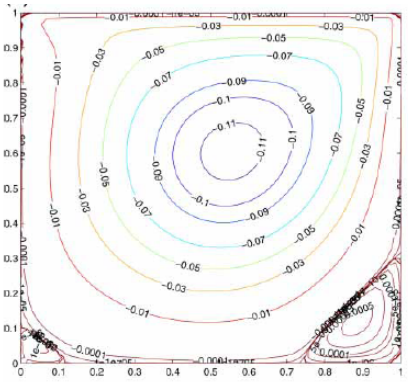

(b) Stream function (ψ) plot from Chinchapatnam et al. (2007)

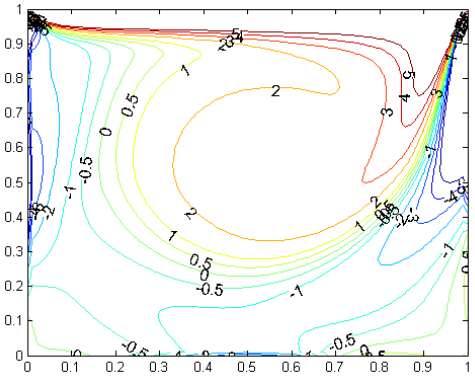

(c) Vorticity (ω) plot from present work

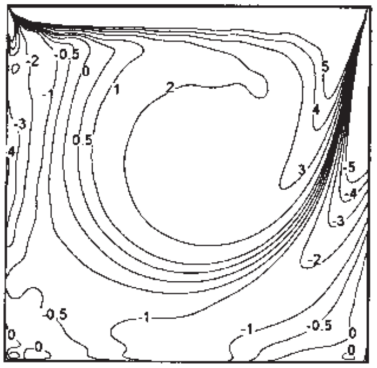

(d) Vorticity (ω) plot from Shu et al. (2004)

Figure 4.11: Stream function (ψ) and vorticity (ω) contour plots for lid driven cavity flow at $Re = 400$

Table 4.1: Maximum error and norm of error for Re 400 and Re 1000 with fixed and adaptively shaped basis functions

Case	Fixed RBF-FD	Adaptive RBF-FD
Results for v_x at mid span		
Max relative error (Re 400)	0.0372	0.0150
Norm of relative error (Re 400)	0.0787	0.0203
Max relative error (Re 1000)	0.0459	0.0250
Norm of relative error (Re 1000)	0.2071	0.1104
Results for v_y at mid plane		
Max relative error (Re 400)	0.0404	0.0089
Norm of relative error (Re 400)	0.1121	0.0556
Max relative error (Re 1000)	0.0439	0.0156
Norm of relative error (Re 1000)	0.1190	0.0549

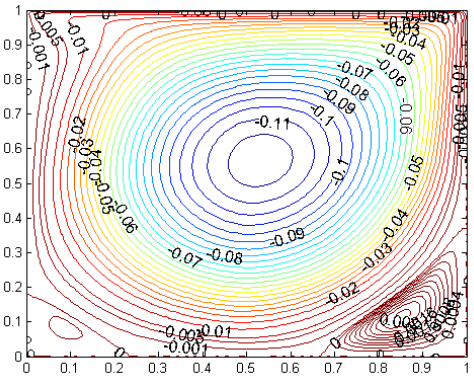

(a) Stream function (ψ) plot from present work

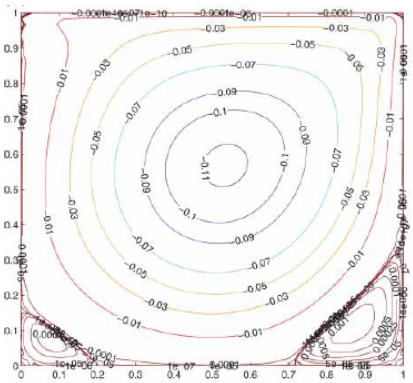

(b) Stream function (ψ) plot from Chinchapatnam et al. (2007)

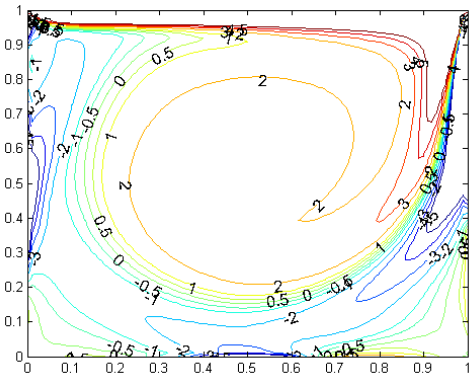

(c) Vorticity (ω) plot from present work

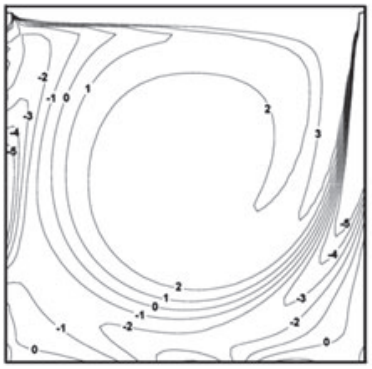

(d) Vorticity (ω) plot from Hamed Meraji et al. (2012)

Figure 4.12: Stream function (ψ) and vorticity (ω) contour plots for lid driven cavity flow at $Re = 1000$

an improved accuracy. Moreover, the basis functions can retain their optimum shape throughout the domain and produce accurate approximations of differential operators. On the contrary, the conventional approach of using fixed shaped basis functions results in ill-conditioning effect when large variation of nodal density is introduced within the domain. Therefore, grid refinement is required to be introduced over the entire domain so as to avoid large variation in nodal spacing at different locations. This practice increases the total number of data points (or nodes) thus making the solutions computationally expensive. Therefore, use of ASP with local RBFs helps improve the computational efficiency and accuracy in these cases. Adaptive shape parameter technique for flow equations in vorticity-stream function formulation has also been presented in Javed et al. (2013a).

Chapter 5

RBF-FD for incompressible, viscous N-S equation in primitive variables

A scheme for solving incompressible and viscous Navier Stokes equation in vorticity streamfunction formulation using RBF-FD based meshfree method was presented in Chapter 4. Due to its "localized" characteristic, RBF-FD was found to provide accurate derivative approximations with large number of computational nodes. However, there are certain limitations associated with vorticity-stream function formulation as discussed in Section 2.4. These may inhibit its applications for more advanced problems.

It is therefore considered logical to investigate the application of RBF-FD for N-S equations in their primitive variable form. A method of solution of Navier-Stokes equations in their primitive variable form is therefore presented using RBF-FD based spatial discretization technique. Pressure-Velocity decoupling, in N-S equations, has been achieved by fractional step method proposed by Chorin (1973). Time discretization of resultant momentum equation after decoupling the pressure term has been achieved using following two methods:

1. **Explicit approach:** The explicit approach employs a first order Euler method for temporal discretization of momentum equations.
2. **Implicit approach:** For implicit approach, a second order Crank-Nicolson scheme has been used for viscous term whereas the convective term is discretized using a second order Adams-Bashforth scheme.

The solution schemes are tested for uniform, non-uniform and random particle distributions and have been validated by the benchmark solutions of lid driven cavity flow

problems provided by Ghia and Shin (1982). Accuracy of Implicit and explicit schemes has been compared. Subsequently, further tests are conducted to investigate the application of implicit RBF-FD scheme for steady and unsteady laminar flow around circular cylinder at different Reynolds numbers.

5.1 RBF-FD for Incompressible N-S Equations

RBF-FD scheme is used for spatial descritization of non-dimensionalized, time dependant, incompressible and viscous Navier-Stokes equations in pressure-velocity form. The set of governing equations are shown in Eqs. (2.6) and (2.7). The chosen solution scheme, for the equations, uses the algorithm suggested by Chorin (1973). The algorithm is based on the non-incremental pressure correction which provides a simple method of time discretization using fractional step approach. Using this approach, the momentum Eq. (2.7) can be written as:

$$\frac{\vec{\mathbf{u}}^{*} - \vec{\mathbf{u}}^{n}}{\Delta t} = -\left(\vec{\mathbf{u}}.\nabla\right)\vec{\mathbf{u}} + \left(1/Re\right)\nabla^{2}\vec{\mathbf{u}} \tag{5.1}$$

the pressure term in momentum equation can then be linked with velocity as:

$$\frac{\vec{\mathbf{u}}^{n+1} - \vec{\mathbf{u}}^{*}}{\Delta t} = -\nabla P^{n+1} \tag{5.2}$$

where $\vec{\mathbf{u}}^{n}$ and $\vec{\mathbf{u}}^{n+1}$ are the velocity values at n^{th} and $(n+1)^{th}$ time step respectively and P^{n+1} is the pressure value at $(n+1)^{th}$ time step. Intermediate velocity field at boundary Γ is evaluated using the following equation:

$$\vec{\mathbf{u}}^{*}|_{\Gamma} = \vec{\mathbf{u}}|_{\Gamma} + \Delta t \nabla P^{n+1} \tag{5.3}$$

Now, from continuity Eq. (2.6):

$$\nabla.\vec{\mathbf{u}}^{n+1} = 0 \tag{5.4}$$

Substituting the value of $\vec{\mathbf{u}}^{n+1}$ from Eq. (5.2) into (5.4) leads to,

$$\nabla^{2} P^{n+1} = (1/\Delta t)\nabla.\vec{\mathbf{u}}^{*} \tag{5.5}$$

subject to following boundary condition:

$$\mathbf{n}.\nabla P^{n+1}|_{\Gamma} = \frac{1}{\Delta t}[\mathbf{n}.(\vec{\mathbf{u}}^{*} - \vec{\mathbf{u}}^{n+1})_{\Gamma}] \tag{5.6}$$

where $\mathbf{n}$ is the unit vector towards outward normal direction to boundary Γ. Eq. (5.4) is called pressure Poisson equation. By incorporating pressure term into continuity equation, the continuity is satisfied in the process of solution of transient flow problem.

5.1.1 Space splitting

RBF-FD scheme is used to approximate spatial derivatives appearing in Eqs. (5.1), (5.2) and (5.5). Detailed explanation of formulation for RBF-FD scheme has been given in Chapter 4. RBF-FD approximation of spatial derivatives appearing in Eqs. (5.5) and (5.2), in 2-D Cartesian component form, with velocity vector $\vec{\mathbf{u}} = (u, v)$, can be written as:

$$\sum_{j=1}^{N} \left(\mathbf{W}_{i,j}^{(xx)} + \mathbf{W}_{i,j}^{(yy)} \right) P_j^{n+1} = \frac{1}{\Delta t} \left(\sum_{j=1}^{N} \mathbf{W}_{i,j}^{(x)} u_j^* + \sum_{j=1}^{N} \mathbf{W}_{i,j}^{(y)} v_j^* \right) \tag{5.7}$$

$$\frac{u_i^{n+1} - u_i^*}{\Delta t} = -\sum_{j=1}^{N} \mathbf{W}_{i,j}^{(x)} P_j^{n+1} \tag{5.8}$$

$$\frac{v_i^{n+1} - v_i^*}{\Delta t} = -\sum_{j=1}^{N} \mathbf{W}_{i,j}^{(y)} P_j^{n+1} \tag{5.9}$$

where, u_i and v_i are the Cartesian of velocity components at node i, N is the total number of interior and boundary nodes which lie in the supporting region/stencil for the node i and $\mathbf{W}_{i,j}^{(x)}$, $\mathbf{W}_{i,j}^{(y)}$, $\mathbf{W}_{i,j}^{(xx)}$ and $\mathbf{W}_{i,j}^{(yy)}$ are the RBF-FD weights corresponding to the differential operator $\partial/\partial x$, $\partial/\partial y$, $\partial^2/\partial x^2$ and $\partial^2/\partial y^2$ respectively. These weights are obtained by solving the system of Eq. (3.21) for corresponding differential operators applied to the basis functions.

5.1.2 Time splitting

Explicit and implicit discretization schemes are used to approximate time derivatives appearing in Eq. (5.1). Description of each approach has been detailed below:

5.1.2.1 Explicit approach

Explicit Euler discretization of time derivative appearing in Eq. (5.1) can be written as

$$\frac{\vec{\mathbf{u}}^* - \vec{\mathbf{u}}^n}{\partial t} = -\left(\vec{\mathbf{u}}^n . \nabla\right) \vec{\mathbf{u}}^n + (1/Re)\, \nabla^2 \vec{\mathbf{u}}^n \tag{5.10}$$

At the end of each time step, continuity condition is satisfied by Poisson Eq. (5.5) with non-zero source term. However, intermediate velocity field may not satisfy continuity (Xia and Leung (2003); Perot (1995)). RBF-FD approximation of spatial derivatives of Eq. (5.10), in 2D Cartesian form, can be written as:

$$\begin{aligned}\frac{u_i^* - u_j^n}{\Delta t} &= -u_i^n \sum_{j=1}^{N} \mathbf{W}_{i,j}^{(x)} u_j^n - v_i^n \sum_{j=1}^{N} \mathbf{W}_{i,j}^{(y)} u_j^n \\ &\quad + \frac{1}{Re} \sum_{j=1}^{N} \left(\mathbf{W}_{i,j}^{(xx)} + \mathbf{W}_{i,j}^{(yy)} \right) u_j^n \qquad (5.11) \\ \frac{v_i^* - v_j^n}{\Delta t} &= -u_i^n \sum_{j=1}^{N} \mathbf{W}_{i,j}^{(x)} v_j^n - v_i^n \sum_{j=1}^{N} \mathbf{W}_{i,j}^{(y)} v_j^n \\ &\quad + \frac{1}{Re} \sum_{j=1}^{N} \left(\mathbf{W}_{i,j}^{(xx)} + \mathbf{W}_{i,j}^{(yy)} \right) v_j^n \qquad (5.12)\end{aligned}$$

Intermediate velocity components can be determined from velocity field values of n^{th} time iteration using Eqs. (5.11) and (5.12). The pressure field values for next time step (P^{n+1}) are then calculated by solving Poisson Eq. (5.7) using intermediate velocity values. Velocity field for next iteration ($\vec{\mathbf{u}}^{n+1} = (u^{n+1}, v^{n+1})$) can then be evaluated using Eqs. (5.8) and (5.9).

Although explicit methods are known to be computationally efficient and are low on memory consumption; their stability is subjected to strict stability requirements known as the CFL condition. This condition is defined as:

$$\frac{|\vec{\mathbf{u}}|\Delta t}{\Delta x} \leq C \qquad (5.13)$$

where Δt is time step, Δx is minimum space step, $\vec{\mathbf{u}}$ is magnitude of flow velocity and C is a dimensionless number (known as Courant number). For an explicit time marching scheme, $C = 1$ is typically used Hirsch (2002). For implicit time marching schemes, relatively larger values of C can however be used. Therefore, the limitations put on the nodal spacing and time step value, by CFL conditions, are relatively relaxed for the implicit schemes compared with the explicit time marching schemes. Moreover, the Euler explicit scheme is only first order accurate in time. Therefore, accuracy of the solution is compromised, especially at regions of high gradients, unless very small time step is used which will slow down the time step marching process.

5.1.2.2 Implicit approach

The following approach has been used to achieve time implicit marching scheme for velocity momentum Eq. (5.1):

1. Second order explicit Adams-Bashforth scheme is used for the convective term appearing in Eq. (5.1). The descritized form of convective equation is written as:

$$\left(\vec{\mathbf{u}}^{n}.\nabla\right)\vec{\mathbf{u}}^{n} = \frac{1}{2}\left[3\left(\vec{\mathbf{u}}^{n}.\nabla\right)\vec{\mathbf{u}}^{n} - \left(\vec{\mathbf{u}}^{n-1}.\nabla\right)\vec{\mathbf{u}}^{n-1}\right] \tag{5.14}$$

2. Second order implicit Crank-Nicolson scheme is used for viscous term appearing in Eq. (5.1) as shown below:

$$\frac{1}{Re}\nabla^{2}\vec{\mathbf{u}}^{n} = \frac{1}{2Re}\left[\nabla^{2}\left(\vec{\mathbf{u}}^{n} + \vec{\mathbf{u}}^{*}\right)\right] \tag{5.15}$$

Due to explicit treatment of convective term, the scheme may not be termed as *"fully-implicit"* in true sense. The fractional step methods in which convective term is treated with explicit time stepping are called *"semi-implicit"* methods (Ryoichi Amano (2011)). Fully-implicit methods refer to the techniques in which both convective and viscous terms are treated with implicit time stepping. However, the scheme used in this work (Adams-Bahsforth for convective and Crank-Nicolson for viscous terms) will be called 'implicit method' for simplicity.

The time splitting schemes for convective as well as viscous terms are second order accurate. This helps reduce time discretization error of the overall equation. However, as viscous term is treated with implicit method, the overall treatment of time splitting becomes implicit. Although Adams-Bahsforth scheme is explicit in time and is somehow affected by CFL stability conditions; the restrictions are more relaxed than for Euler Explicit scheme (Deriaz (2010)). Moreover, numerical viscous stability restrictions are eliminated due to implicit treatment of viscous term (Kim and Moin (1985)). Therefore, larger time steps values can be chosen to enable faster marching in time. Intermediate velocity momentum Eq. (5.1) can now be expressed as:

$$\begin{aligned}\frac{\vec{\mathbf{u}}^{*} - \vec{\mathbf{u}}^{n}}{\Delta t} = &-\frac{1}{2}\left[3\left(\vec{\mathbf{u}}^{n}.\nabla\right)\vec{\mathbf{u}}^{n} - \left(\vec{\mathbf{u}}^{n-1}.\nabla\right)\vec{\mathbf{u}}^{n-1}\right] \\ &+\frac{1}{2Re}\left[\nabla^{2}\left(\vec{\mathbf{u}}^{n} + \vec{\mathbf{u}}^{*}\right)\right]\end{aligned} \tag{5.16}$$

Eq. (5.16) can be rearranged to bring all intermediate velocity terms on one side of the equation. Resulting form is written as:

$$\begin{aligned}\vec{\mathbf{u}}^{*} - \frac{\Delta t}{2Re}\nabla^{2}\vec{\mathbf{u}}^{*} = \vec{\mathbf{u}}^{n} &- \frac{\Delta t}{2}\left[3\left(\vec{\mathbf{u}}^{n}.\nabla\right)\vec{\mathbf{u}}^{n} - \left(\vec{\mathbf{u}}^{n-1}.\nabla\right)\vec{\mathbf{u}}^{n-1}\right] \\ &+\frac{\Delta t}{2Re}\nabla^{2}\vec{\mathbf{u}}^{n}\end{aligned} \tag{5.17}$$

Spatial derivatives appearing in Eq. (5.17) are evaluated using RBF-FD approximation. Spatial descritization of convective and viscous terms appearing in Eq. (5.17) for u component of velocity $\vec{\mathbf{u}} = (u, v)$, are shown bellow:

$$(\vec{\mathbf{u}}^n.\nabla)\, u^n = u_i^n \sum_{j=1}^{N} \left(\mathbf{W}_{i,j}^{(x)} + \mathbf{W}_{i,j}^{(y)} \right) u_j^n \tag{5.18}$$

$$\nabla^2 u^n = \sum_{j=1}^{N} \left(\mathbf{W}_{i,j}^{(xx)} + \mathbf{W}_{i,j}^{(yy)} \right) u_j^n \tag{5.19}$$

Similar expressions can be written for v component of velocity $\vec{\mathbf{u}} = (u, v)$. RBF-FD approximation of complete Eq. (5.17), in 2-D Cartesian domain, can therefore, be expressed as

$$\begin{aligned} u_i^* - \frac{\Delta t}{2Re} \sum_{j=1}^{N} \left(\mathbf{W}_{i,j}^{(xx)} + \mathbf{W}_{i,j}^{(yy)} \right) u_j^* = u_i^n + \\ \Delta t \Bigg[-\frac{1}{2} \Bigg\{ 3 \Big(u_i^n \sum_{j=1}^{N} \mathbf{W}_{i,j}^{(x)} u_j^n + v_i^n \sum_{j=1}^{N} \mathbf{W}_{i,j}^{(y)} u_j^n \Big) \\ - \Big(u_i^{n-1} \sum_{j=1}^{N} \mathbf{W}_{i,j}^{(x)} u_j^{n-1} + v_i^{n-1} \sum_{j=1}^{N} \mathbf{W}_{i,j}^{(y)} u_j^{n-1} \Big) \Bigg\} \\ + \frac{1}{2Re} \sum_{j=1}^{N} \left(\mathbf{W}_{i,j}^{(xx)} + \mathbf{W}_{i,j}^{(yy)} \right) u_j^n \Bigg] \end{aligned} \tag{5.20}$$

$$\begin{aligned} v_i^* - \frac{\Delta t}{2Re} \sum_{j=1}^{N} \left(\mathbf{W}_{i,j}^{(xx)} + \mathbf{W}_{i,j}^{(yy)} \right) v_j^* = v_i^n + \\ \Delta t \Bigg[-\frac{1}{2} \Bigg\{ 3 \Big(u_i^n \sum_{j=1}^{N} \mathbf{W}_{i,j}^{(x)} v_j^n + v_i^n \sum_{j=1}^{N} \mathbf{W}_{i,j}^{(y)} v_j^n \Big) \\ - \Big(u_i^{n-1} \sum_{j=1}^{N} \mathbf{W}_{i,j}^{(x)} v_j^{n-1} + v_i^{n-1} \sum_{j=1}^{N} \mathbf{W}_{i,j}^{(y)} v_j^{n-1} \Big) \Bigg\} \\ + \frac{1}{2Re} \sum_{j=1}^{N} \left(\mathbf{W}_{i,j}^{(xx)} + \mathbf{W}_{i,j}^{(yy)} \right) v_j^n \Bigg] \end{aligned} \tag{5.21}$$

Eqs. (5.20) and (5.20) can be written in more concise form as:

$$[A]\{u^*\} = [B]\{u^n\} + [C]\{u^{n-1}\} \tag{5.22}$$

$$[A]\{v^*\} = [B]\{v^n\} + [C]\{v^{n-1}\} \tag{5.23}$$

where

$$A_{i,j} = \begin{cases} 1 - \Delta t/2\,((\mathbf{visc})_{i,j}) & (i = j) \\ -\Delta t/2\,((\mathbf{visc})_{i,j}) & (i \neq j) \end{cases}$$

$$B_{i,j} = \begin{cases} 1 + \Delta t/2\left(-3(\mathbf{conv})^n_{i,j} + (\mathbf{visc})_{i,j}\right) & (i = j) \\ \Delta t/2\left(-3(\mathbf{conv})^n_{i,j} + (\mathbf{visc})_{i,j}\right) & (i \neq j) \end{cases}$$

$$C_{i,j} = \Delta t/2\left((\mathbf{conv})^{n-1}_{i,j}\right)$$

$$(\mathbf{conv})^n_{i,j} = u^n_i \mathbf{W}^{(x)}_{i,j} + v^n_i \mathbf{W}^{(y)}_{i,j}$$

$$(\mathbf{conv})^{n-1}_{i,j} = u^{n-1}_i \mathbf{W}^{(x)}_{i,j} + v^{n-1}_i \mathbf{W}^{(y)}_{i,j}$$

$$(\mathbf{visc})_{i,j} = 1/Re\left(\mathbf{W}^{(xx)}_{i,j} + \mathbf{W}^{(yy)}_{i,j}\right)$$

Intermediate velocity components are therefore, calculated by solving matrix Eqs. (5.22) and (5.23). Subsequently, Eqs. (5.7) to (5.9) are used to calculate pressure and velocity values for next time step. The process requires simultaneous solution of matrix equations which is computationally expensive. However due to *local* feature of RBF-FD, sparse coefficient matrices are generated which make the solution process fast and are low on memory. The larger time steps allowed by the implicit treatment make the convergence process faster. Therefore, overall computational efficiency improves for Implicit RBF-FD.

5.2 Solution algorithm

After representing the domain with finite number of particles (or nodes) and applying initial conditions, the following numerical procedure is used:

1. At any time step n, components of intermediate velocity vector $\vec{\mathbf{u}}^* = (u^*, v^*)$ are calculated at each node.

   (a) For Euler explicit approach, Eqs. (5.11) and (5.12) are used.

   (b) For implicit approach, system of equations formed by evaluating Eqs. (5.22) and (5.23) at each node is solved to obtain ($\vec{\mathbf{u}}^*$).

   The boundary conditions for intermediate velocity are calculated using Eq. 5.3.

2. Eq. (5.7) is solved using known values of intermediate velocities ($\vec{\mathbf{u}}^*$) at the time step to find the values of pressure at each node. The Pressure values on the boundaries are obtained using Eq. (5.6).

3. Finally, Eqs. (5.8) and (5.9) are used to update the velocity components for next time step.

4. Convergence is monitored by calculating the norm of difference in velocity vectors between two consecutive time steps. The process (Step 1 - 3) is repeated until desired convergence is achieved.

As RBF-FD generates a sparse matrix, Generalized Minimum Residual (GMRES) method with incomplete LU decomposition for preconditioning, as presented by Saad and Schultz (1986), is used for solution of matrix Eqs. (5.7), (5.22) and (5.23). The sparse matrix equation greatly reduces the computational load and memory requirement of the program.

5.2.1 Computer Program

The solution algorithms discussed in Section 5.2 are used to write computer programs for flow solvers using C-program. The flow chart of the program for implicit RBF-FD scheme is shown in Figure 5.1. The program first performs the preliminary calculations which are carried out to prepare for the iterative steps. The process starts by finding the total number of computational nodes needed to produce the grid with required size. Subsequently, the dynamic memory is allocated to the different pointer variables. The grid points are then generated and initial values of field variables are assigned. The non-dimensionalization of variables is then carried out before calculating the RBF weights at each data point. These RBF weights are used to formulate the coefficient matrices for pressure and velocity equations. Formulation of coefficient matrices is not needed for explicit time marching.

After the preliminary calculations, iterative calculations are carried out. During these, the values of pressure and velocity fields are calculated at each time step by solving the respective matrix equations. For explicit time marching, solution of matrix equations is not needed for velocity field. The detail of the process has been mentioned in Section 5.2. The flow charts for preliminary and iterative calculations are shown in Figures 5.1(a) and 5.1(b) respectively.

5.3 Order of convergence tests

Convergence tests have been conducted for Implicit RBF-FD method to establish spatial and temporal order of convergence. For this purpose, decaying vortex problem has been selected. The problem has a known analytical solution and is often used to verify the accuracy of new methods (Kim and Moin (1985); Kim and Choi (2000); Chew et al.

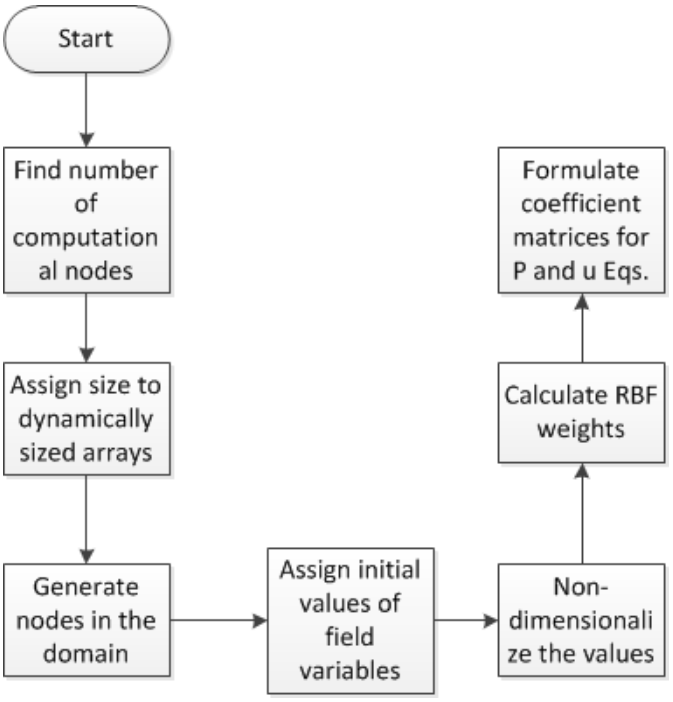

(a) Preliminary Calculations

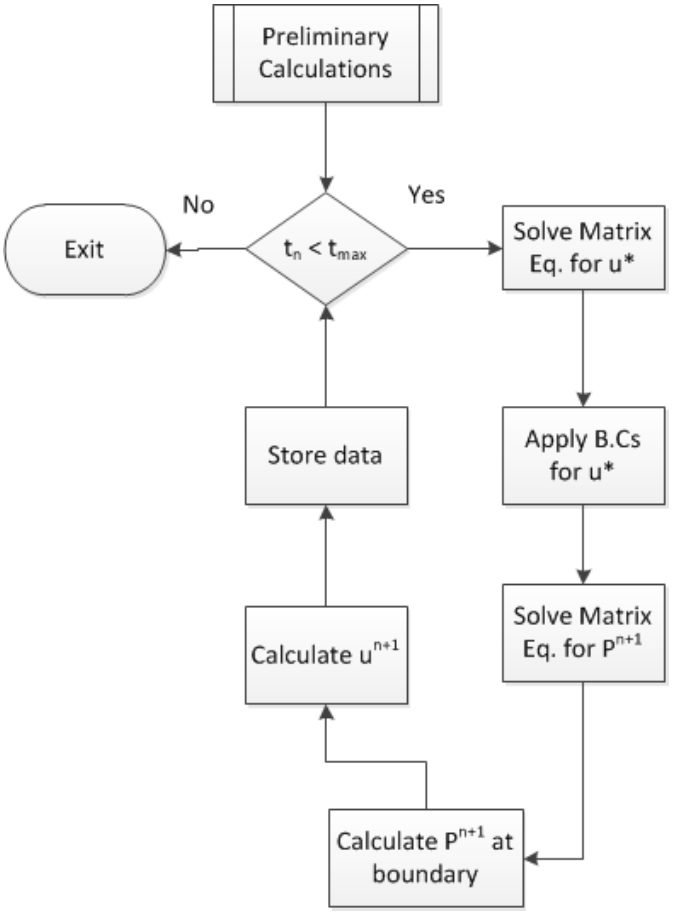

(b) Iterative Steps

Figure 5.1: Flow chart of computer program for flow solver based on implicit RBF-FD solution scheme

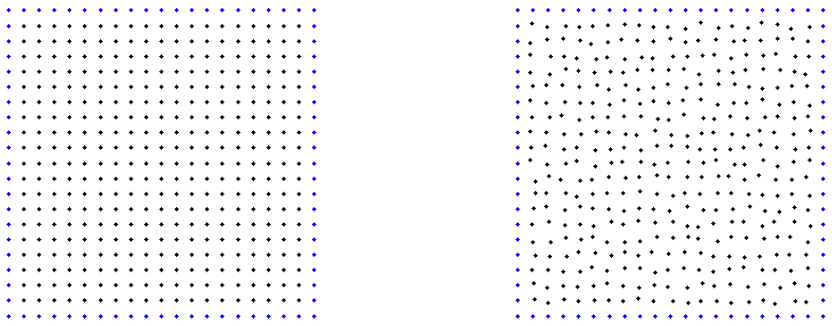

(a) Uniform nodal arrangement (b) Random nodal arrangement

Figure 5.2: Uniform and random nodal arrangement over square domain $[-0.5, 0.5] \times [-0.5, 0.5]$ with grid spacing $h = 0.05$

(2006)). Followings are the theoretical expressions for time varying pressure and velocity fields $(u(x, y, t), v(x, y, t), p(x, y, t))$:

$$u(x, y, t) = -\cos(\pi x)\sin(\pi y)\exp[-(2\pi^2 t)/Re] \tag{5.24}$$

$$v(x, y, t) = \sin(\pi x)\cos(\pi y)\exp[(-2\pi^2 t)/Re] \tag{5.25}$$

$$p(x, y, t) = -0.25\,[\cos(2\pi x) + \cos(2\pi y)]\exp[(-4\pi^2 t)/Re] \tag{5.26}$$

The flow Reynolds number is defined as $Re = \rho U L/\mu$, where ρ is the fluid density, U is maximum initial flow velocity, L is the length of vortex and μ is the dynamic viscosity. Numerical solution of the problem has been obtained over a square domain which spans $[-0.5, 0.5] \times [-0.5, 0.5]$. The domain is represented by uniform as well as pseudo random nodal arrangement. Uniform and random grid with grid spacing $h = 0.05$ are shown in Figure 5.2. Randomness has been introduced by perturbing the nodes from their original positions over uniform grid. This Random perturbation is however restricted to 20% of the grid spacing to avoid excessive clustering of nodes. The initial conditions have been defined by using analytical solutions of velocity and pressure (Eqs. (5.24) - (5.26)) on respective nodal coordinates at $t = 0$. Dirichlet boundary conditions have also been defined at all the four boundaries using theoretical expressions for velocity and pressure at time instant t.

In order to evaluate spatial order of convergence, numerical solutions are obtained at $t = 0.4$ sec for different values of nodal spacing. Flow Reynolds number has been set as 10 and time step value has been chosen to be 10^{-4} sec. Error has been calculated, for each case, by evaluating norm-2 of the difference between values of velocity and pressure evaluated using flow solver and their analytical values obtained from Eq. (5.24) - (5.26). Logarithmic values of Norm-2 of error $(\log_{10}(\|\varepsilon\|_2))$ have been plotted against logarithmic values of grid spacing $(\log_{10}(h))$ for uniform grid in Figure 5.3(a) and for random grid in Figure 5.3(b). Linear fitting curves are then drawn, for each type of

Table 5.1: Spatial Order of convergence for Implicit RBF-FD

Grid Size (h)	$\|\varepsilon\|_2$ for u-velocity		$\|\varepsilon\|_2$ for Pressure	
	Uniform Grid	Random Grid	Uniform Grid	Random Grid
0.05	4.44E-4	2.82E-4	3.56E-4	3.40E-4
0.04	2.93E-4	1.74E-4	2.19E-4	2.41E-4
0.025	9.09E-5	5.90E-5	5.80E-5	6.60E-5
0.02	4.56E-5	3.48E-5	2.72E-5	3.76E-5
0.01	3.53E-6	3.51E-6	3.53E-6	4.57E-6
Order of convergence	3.16	2.096	2.85	2.38

error, using least square data fitting. Orders of convergence have been calculated as slopes of these error curves on logarithmic scale. Numerical values of error for pressure and velocity have also been shown in Table 5.1. Results for v-component of velocity have not been shown because these are similar to those of u-component of velocity. Spatial order of convergence for velocity field is found to be 3.16 on a uniform grid. However, this order of convergence reduces to 2.096 on a random grid. The orders of convergence for pressure are 2.85 and 2.38 on uniform and random grids respectively.

The order of convergence in time has been calculated by running similar test cases at different time step values but keeping same grid size (h). The tests are conducted on a 51×51 uniform grid which corresponds to grid spacing $h = 0.02$. Time step values are varied from 5×10^{-2} to 10^{-3}. Resulting values of $\log_{10}(\|\varepsilon\|_2)$ are plotted against logarithmic values of time step ($\log_{10}(\Delta t)$) in Figure 5.4 along with the linear fitting curve. The slope for velocity curve is 1.3 and that for pressure curve is 1.27. The order of convergence in time for both velocity and pressure is lower than spatial order of convergence. These results are consistent with the observation of Brown et al. (2001) and Guermond et al. (2006). Brown et al. (2001) suggests that order of convergence in time can be improved further by incorporating strict divergence constraints on intermediate velocity field. Guermond et al. (2006) has suggested an improvement in temporal order of convergence by introducing incremental pressure correction in fractional step schemes, such as proposed by Goda (1979). The scope of current research is however restricted to same formulation which has been presented above. Further improvements can be made by using more accurate solution schemes.

5.4 Lid driven cavity flow problem

Explicit and implicit solution schemes have been used to solve Lid Driven Cavity Flow problem at various Reynolds Numbers ($Re = UL/\nu$, where U is the velocity of moving lid, L is the length of side and ν is the kinematic viscosity of flow). The results are compared with benchmark solutions by Ghia and Shin (1982). Applicability of schemes

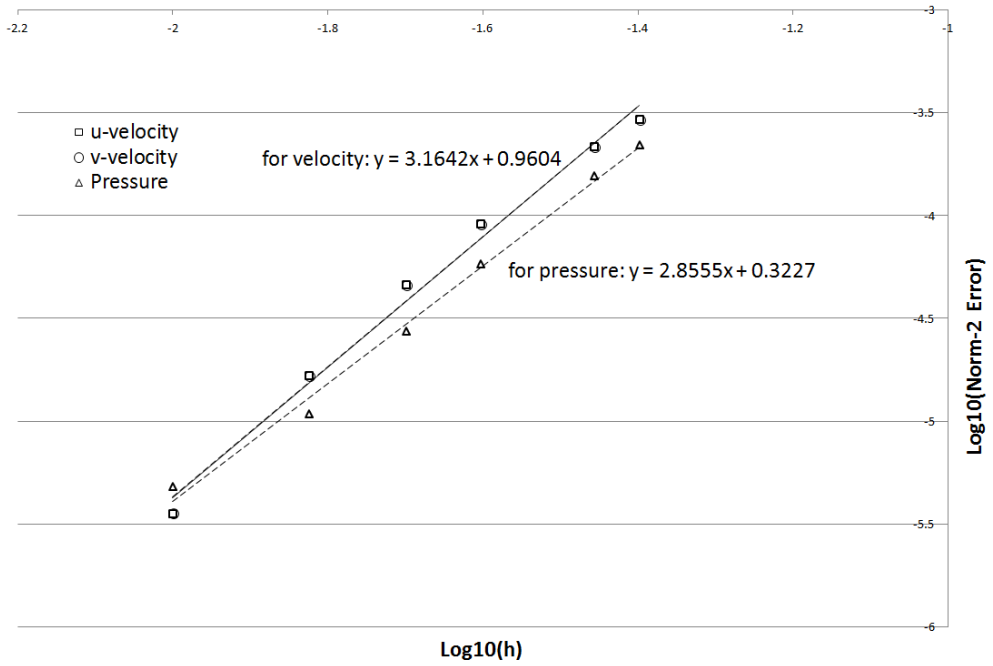

(a) On uniform grid

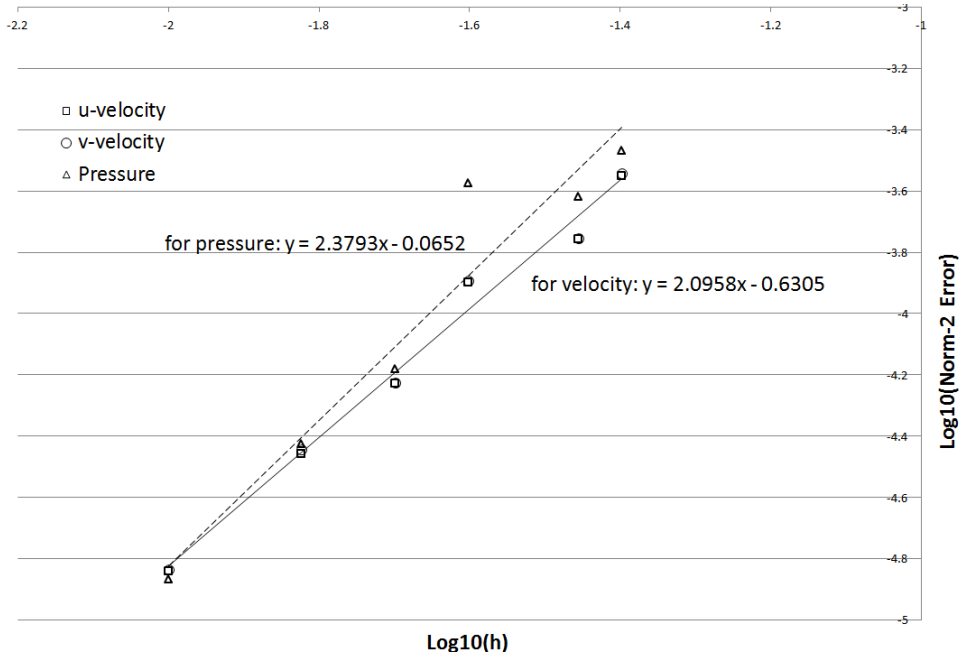

(b) On random grid

Figure 5.3: Variation of Norm-2 error for velocity and pressure with changing grid size (h) on logarithmic scale. Reynolds number is $Re = 10$ and Time step value is $\Delta t = 10^{-4}$

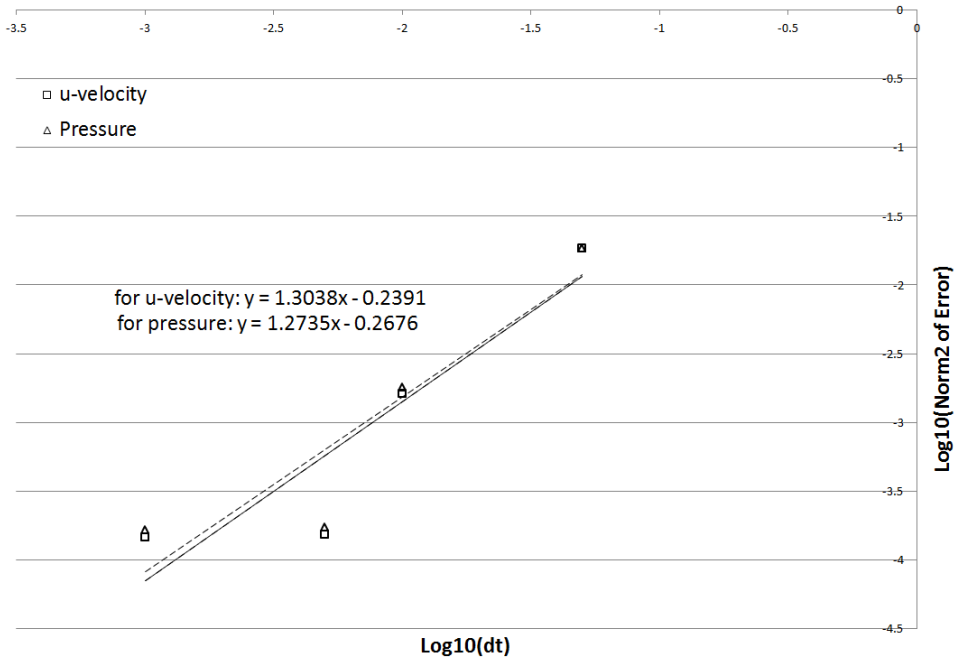

Figure 5.4: Variation of Norm-2 error for velocity and pressure with changing time step (Δt) on logarithmic scale. Solutions are sought on a uniform grid with grid spacing $h = 0.01$ and $Re = 10$.

has been verified on uniform, non-uniform and random nodal distribution. For uniform grid (or nodal distribution), the nodal spacing has been kept constant throughout the domain as shown in Figure 5.5(a). For non-uniform grid, nodal spacing has been varied in a controlled manner, as shown in Figure 5.5(b), in order to keep a higher the nodal density at regions where large gradients of field variables are expected. This has been done to optimize the computational effort so as to achieve greater accuracy with less number of nodes. Random grid corresponds to the domain where nodes have been distributed randomly as shown in Figure 5.5(c). The random distribution of nodes has been achieved by incorporating *Sobol* sequence in coordinate location of the nodes. Low discrepancy *Sobol* sequence randomizes the nodal spacing while still maintaining an overall uniformity in distribution of nodes.

During solution of N-S equations in primitive formulation, the velocity boundary conditions are directly obtained from physical constraints. On all the four walls, velocity component normal to boundary is zero. This ensures that there is no penetration of flow across the boundary. Moreover, no-slip boundary conditions dictate that tangential component of velocity of flow along the boundary Γ remains constant and equal to the speed of the boundary itself. So, $(\vec{u}_{\mathbf{n}}) = 0$ and $(\vec{u}_{\mathbf{t}}) = C_2$ at boundary Γ where, $(\vec{u}_{\mathbf{n}})$ and $(\vec{u}_{\mathbf{t}})$ are the velocity components in outward normal and tangent direction of boundary respectively and C_2 is a constant. For pressure, Neumann boundary conditions are introduced as per Eq. (5.6). Implementation of Neumann boundary condition for pressure has been achieved through locally orthogonal grid near the boundary. For uniform and non-uniform particle distribution, condition of locally orthogonal grid is

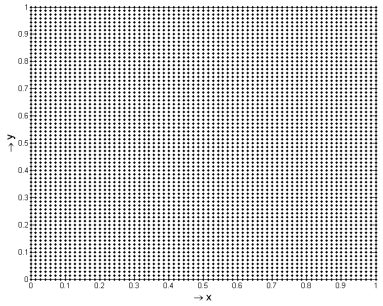

(a) Uniform distribution

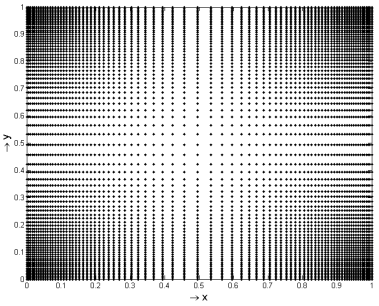

(b) Non-uniform distribution

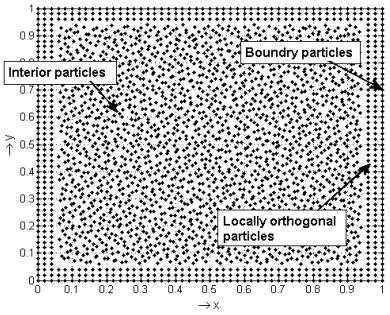

(c) Random Distribution (for interior nodes)

Figure 5.5: Various configurations of particle distribution

naturally satisfied. However, for random particle distribution, inner particles may not remain orthogonal to the boundary. Therefore, special care has to be taken to ensure locally orthogonal grid near the boundary. Implementation of locally orthogonal grid for random nodal distribution has been shown in Figure 5.5(c).

5.4.0.1 Comparison of Implicit and Explicit RBF-FD schemes

The results for Lid Driven cavity flow have been obtained at $Re = 100,\ 400$ and 1000, respectively. For Explicit RBF-FD approach, the time step has been kept at 5×10^{-4} whereas for implicit approach, a time step of 10^{-3} has been chosen. Grid configuration has been kept similar for all the cases to ensure a valid comparison. Therefore, non-uniform grid, with nodal spacing ratio of 2.5 between corner-to-centre nodes, has been used for all the cases. Constant values of shape parameters have been used here.

At higher Reynolds numbers, finer nodal grids are required to accurately capture flow gradients. Therefore, at every Reynolds number, the solutions are sought at different grid sizes and results are compared with standard solutions from Ghia and Shin (1982). The aim is to work out the optimum grid size at each Reynolds number, both for explicit and implicit approach, which provides good solutions. Resultant velocity plots, at all three Reynolds numbers, obtained from explicit RBF-FD solution are shown in Figures

Table 5.2: Required grid sizes for each test case (Lid driven cavity flow)

Reynolds number (Re)	Required grid size	
	Explicit RBF-FD	Implicit RBF-FD
100	91×91	71×71
400	121×121	71×71
1000	151×151	101×101

5.6(a) - 5.6(c). Similar plots for implicit RBF-FD approach are shown in Figures 5.7(a) - 5.7(c). The optimum grid sizes, which give accurate solution in each case, are tabulated in Table 5.2.

It can be observed that for implicit solutions, required accuracy can be achieved with relatively coarser grid compared to the explicit solution. This is due to higher order of accuracy achieved during time splitting of governing equations which suffer from less discretization error. Moreover, implicit treatment also eliminates the numerical viscous stability restrictions. These restrictions are particularly sever at low Reynolds numbers and near the boundaries, as mentioned by Kim and Choi (2000). Therefore, implicit schemes work well even for larger time step values. Significant improvement in CPU time was observed during numerical tests while using implicit scheme. For example, the computation times, to reach steady state solutions using explicit and implicit approach at Re 100, were compared on a 91×91 grid. For implicit scheme, the steady state solutions were reached for CPU time of 7114 sec on Intel ® 3.1 GHz Processor. On the other hand, computation time for similar case was recorded as 36306 sec on same machine using explicit scheme. Therefore, the computation time was reduced by a factor of 5 using implicit scheme. Possibility of using larger time step and higher accuracy at relatively coarser grids makes the implicit RBF-FD computationally more efficient and stable technique for solution of Navier-Stokes equations in primitive variable form.

5.4.0.2 Effect of nodal distribution

In order to study the effect of changing nodal distribution within the domain, a comparison of results from uniform and non-uniform grids has been presented. The test cases have been run at Reynolds Numbers 100 and 400 on 71×71 grids using implicit approach. The results obtained on both uniform and non-uniform grids have been plotted together in Figure 5.8. It can be observed that non-uniform grid was able to capture the velocity gradients more accurately due to higher nodal density at critical areas. Therefore, selectively distributing the particles in the domain to achieve the nodal density according to expected flow characteristics and gradient of field variables; helps achieve accurate results even for less number of nodes.

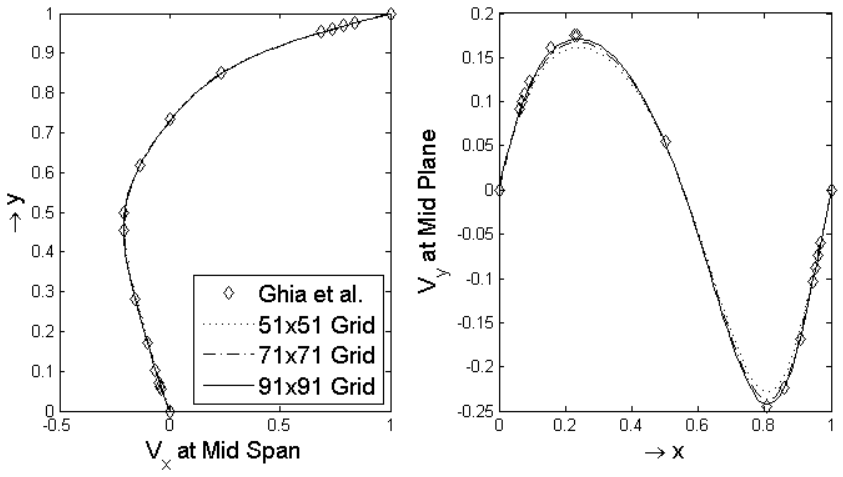

(a) Re 100

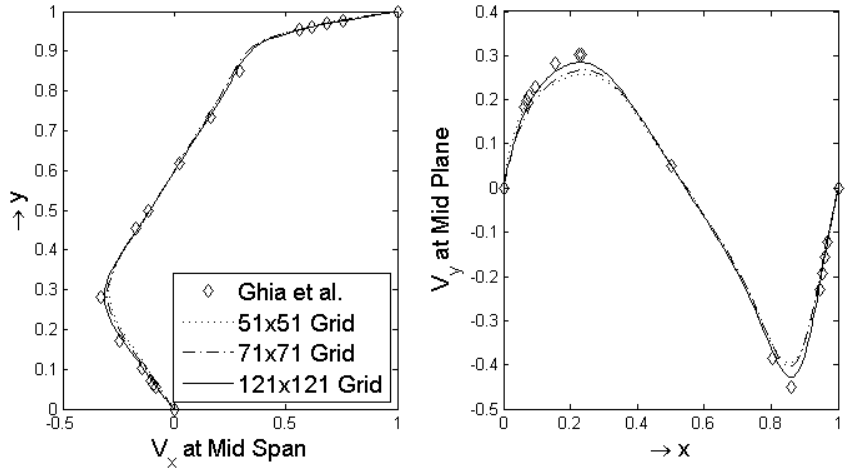

(b) Re 400

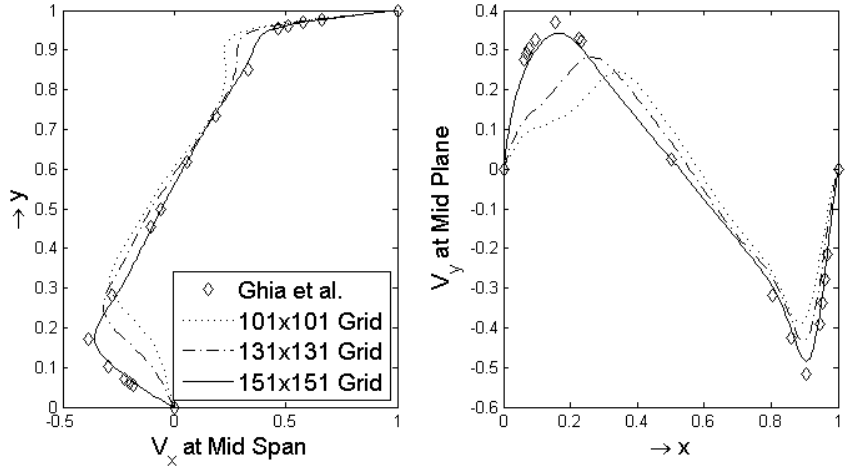

(c) Re 1000

Figure 5.6: Velocity profiles for lid driven cavity flow (results for explicit approach). V_x plots are obtained at mid span ($x = L/2$) and V_y plots are obtained at mid height ($y = H/2$).

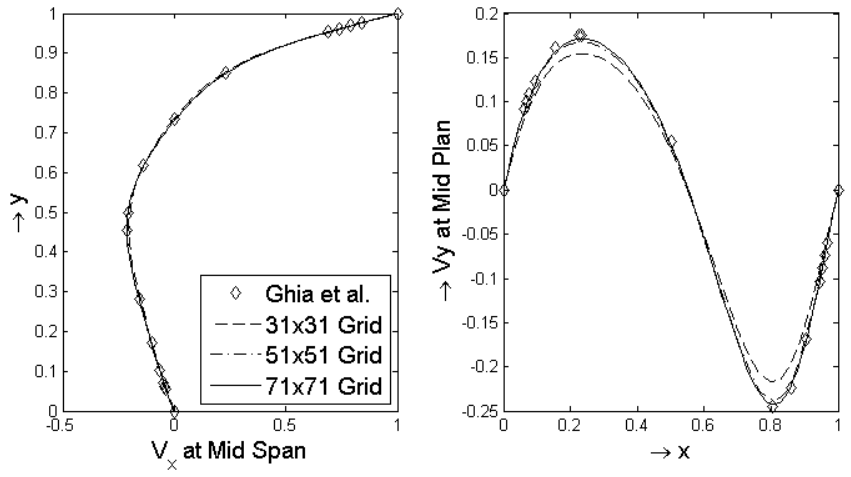

(a) Re 100

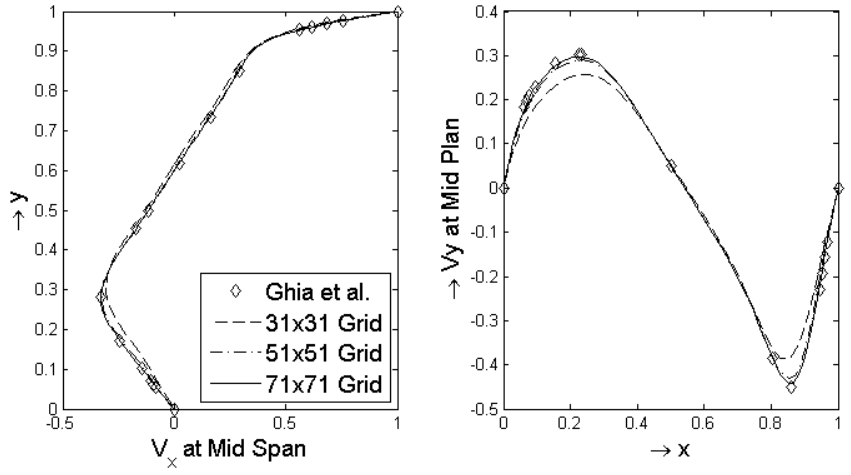

(b) Re 400

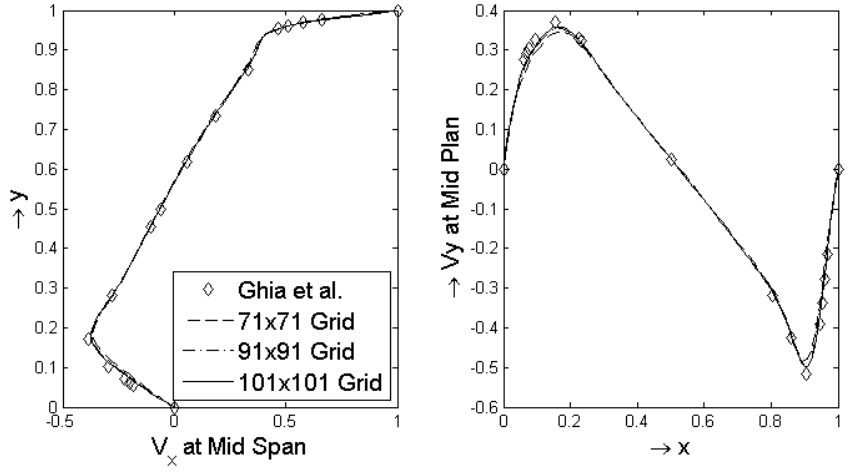

(c) Re 1000

Figure 5.7: Velocity profiles for lid driven cavity flow (results for implicit approach). V_x plots are obtained at mid span ($x = L/2$) and V_y plots are obtained at mid height ($y = H/2$).

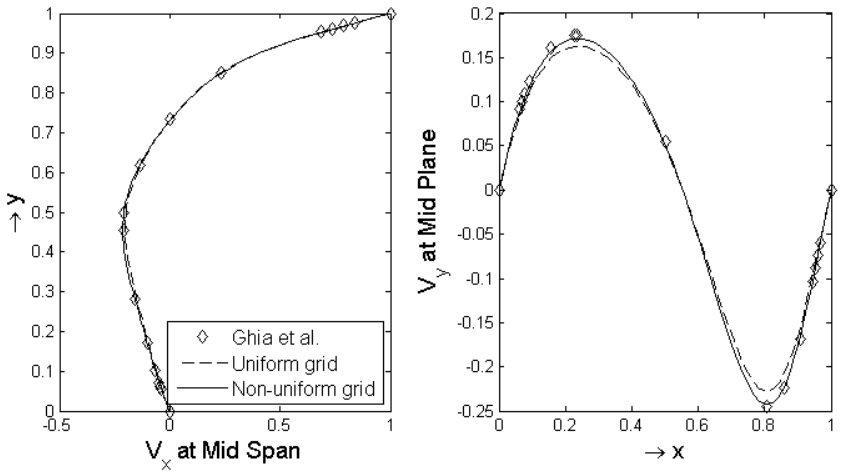

(a) $Re = 100$

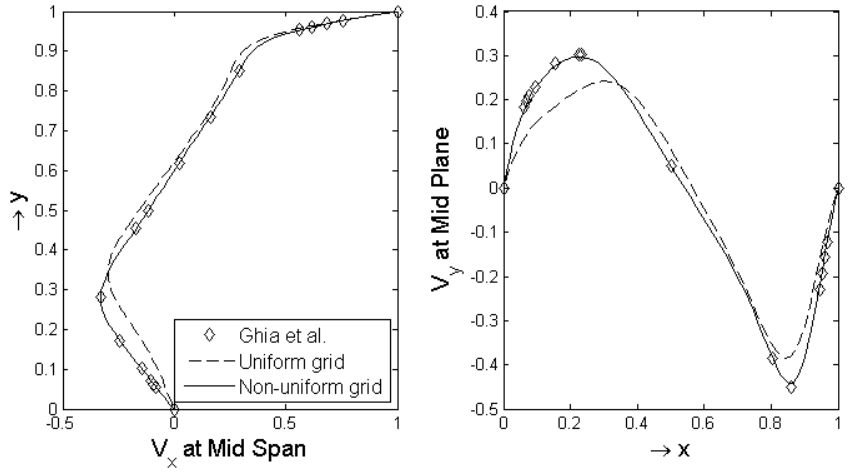

(b) $Re = 400$

Figure 5.8: Comparison of velocity profiles on uniform and non-uniform 71×71 grids. V_x plots are obtained at mid span ($x = L/2$) and V_y plots are obtained at mid height ($y = H/2$).

Meshless particle methods often employ random particle distribution. Therefore, implicit scheme has been used to solve the flow case over random particle distribution at Re 100. Grid size of 51×51 was chosen. Resultant velocity profiles in Figure 5.9, show good agreement with benchmark solution which validates the application of suggested scheme on random grid.

5.4.0.3 Comparison of constant and adaptive shape parameters

It can be observed from Figure 5.5(b) that the nodal spacing, and thus the distribution of nodes, varies considerably within the domain. Therefore, the condition number of coefficient matrix can go higher for certain data points thus affecting the accuracy

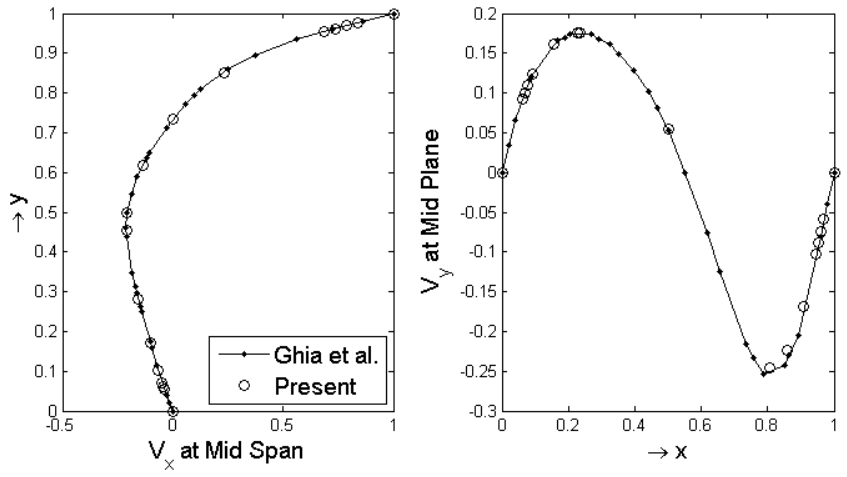

Figure 5.9: Velocity profiles on a random 51×51 grid at $Re = 100$. V_x plots are obtained at mid span ($x = L/2$) and V_y plots are obtained at mid height ($y = H/2$).

of solution. In order to avoid the possible ill-conditioning of coefficient matrix shape adaptive RBF-FD can be used.

The results of lid driven cavity flow problem at Re 400 and 1000 with fixed and adaptive shape parameter using implicit RBF-FD technique have been compared. Non-uniform grid size of 51×51 is used at $Re = 400$ whereas 101×101 sized grid is used for $Re = 1000$. For non-uniform grid, if a constant value of shape parameter (σ) is used, the ratio of nodal spacing between corner-to-centre nodes is limited to 2.5. Any value higher than 2.5 will cause ill-conditioning and solution will break down without reaching convergence. However, when adaptive shape parameter technique is used, the ratio of nodal spacing between corner-to-centre nodes can be increased up to 4.0 without introducing ill-conditioning. The grid can therefore be made much more refined close to the walls than for fixed shape parameter approach. The results are therefore, more accurate for same number of nodes within the domain. The velocity plots at $Re = 400$ and $Re = 1000$ are shown in Figures 5.10 and 5.11, respectively (for fixed and adaptive RBF shape parameters). Significant improvement in results is observed with the use of adaptive shape parameters.

As the implicit RBF-FD scheme is found to be more accurate and stable compared with its explicit counterpart scheme, subsequent works for this research employ implicit RBF-FD scheme. Moreover, shape adaptive RBF-FD are used to circumvent the ill-conditioning effects while using variable nodal density.

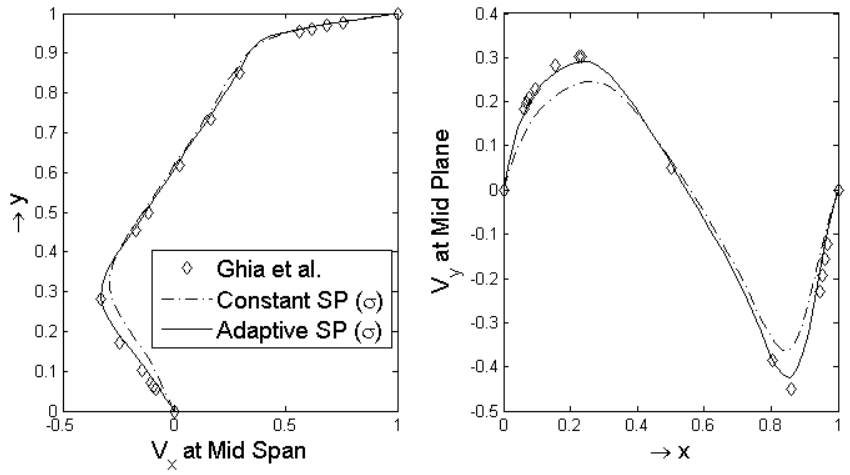

Figure 5.10: Results for fixed and adaptive RBF shape parameter (σ)at $Re = 400$ on a 51×51 grid. V_x plots are obtained at mid span ($x = L/2$) and V_y plots are obtained at mid height ($y = H/2$).

5.5 Flow past static circular cylinder

In this work, implicit RBF-FD scheme with adaptive shape parameter has been used to simulate laminar flow over a circular cylinder. The flow problem has extensively been studied by previous researchers (Tuann and Olson (1978), Takami and Keller (1969), Fornberg (1980), Dennis and Chang (1970), Liu et al. (1998), Belov et al. (1995), Braza et al. (1986)) and is often used as benchmark problem to examine the performance of new numerical techniques. Flow Reynolds number has been defined as $Re = (U_\infty D)/\nu$ for this problem, where U_∞ is the free stream velocity, D is the diameter of cylinder and ν is the kinematic flow viscosity. Flow around cylinder demonstrates a periodically unsteady pattern when its Reynolds number is larger than the critical value ($Re > 49$) (Shu et al. (2003)). For low Reynolds numbers ($Re < 50$), steady flow field is obtained around cylinder. However at moderate range of Reynolds numbers ($50 < Re < 190$), the flow remains laminar but a vortex shedding phenomenon (also known as Karman Vortex Street) is observed. In the present work, flow around circular cylinder has been solved at $Re = 10,\ 20,\ 40,\ 100$ and 200 to simulate both steady and unsteady flow patterns. Configuration of domain geometry is shown in Figure 5.12. Total length of the rectangular domain is kept 30 times the diameter of the cylinder. Inlet is placed 5 times the diameter away from the centre of cylinder. Top and bottom boundaries are located at a transversal distance of 6 times the cylindrical diameter. Free Stream velocity U_∞ has been specified at inlet boundary to correspond to Reynolds number of flow. Boundary conditions at top and bottom boundaries are the same as inflow boundary. No slip boundary conditions are specified at cylinder surface ($u = v = 0$, where u and v are Cartesian components of velocity) and zero velocity gradient condition ($\partial u/\partial x = \partial v/\partial x = 0$) has been applied at outflow boundary. Pressure at outflow boundary has been obtained by the use of Eq. (5.6).

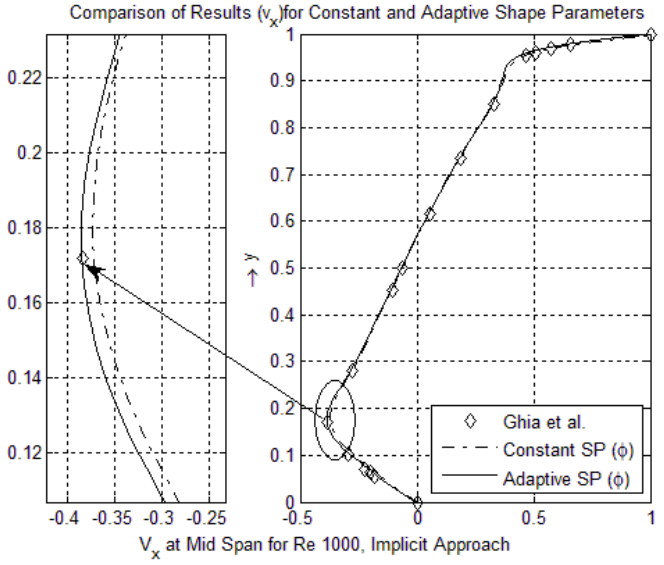

(a) vx

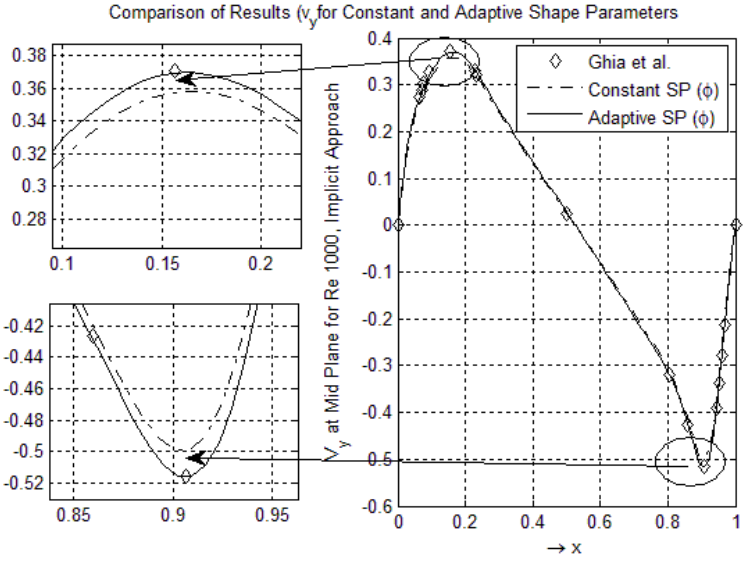

(b) vy

Figure 5.11: Velocity profiles for fixed and adaptive RBF shape parameter (σ) at $Re = 1000$ on a 101×101 grid. . V_x plots are obtained at mid span ($x = L/2$) and V_y plots are obtained at mid height ($y = H/2$).

The nodal distributions have been shown in Figure 5.13 for steady and unsteady flow cases. For unsteady flow cases, a finer grid is used near the cylinder to accurately capture time varying flow. A total of 16061 and 17758 nodes have been used to represent the domain for steady and unsteady flow cases, respectively. A total of 60 nodes are placed on the cylindrical surface for steady flow cases. Number of boundary nodes on solid boundary is increased to 80 for unsteady cases. The nodal arrangement is somewhat like a polar mesh close to the cylinder. However in the far field (about 1.5 times the diameter from the centre of cylinder), the nodal arrangement switches to resemble regular Cartesian stencil. The particles are closely spaced in the region where wake is expected. However in the far field and outside the expected wake region, density of particle has progressively been reduced. In order to implement Neumann pressure boundary condition at solid boundary, first two layers of nodes around the solid are arranged orthogonally with the boundary nodes as shown in Figure 5.14. The condition of orthogonal grid at the outlet boundary is naturally satisfied due to Cartesian grid. Non-dimensional time step value has been chosen to be 5×10^{-3}.

Lift and drag forces at the solid boundary are evaluated by summing up vertical and horizontal components of pressure and viscous forces at all the boundary nodes as shown in Figure 5.15. Lift (F_L) and drag (F_D) forces can therefore be expressed as:

$$Lift\ Force\ = F_L\ =\ \rho U_\infty^2 \left(\sum_{i=1}^{N_s} \left(-P_i \sin\theta_i r + \frac{1}{Re}\omega_i \cos\theta_i \right) d\theta \right) \tag{5.27}$$

$$Drag\ Force\ = F_D\ =\ \rho U_\infty^2 \left(\sum_{i=1}^{N_s} \left(-P_i \cos\theta_i r - \frac{1}{Re}\omega_i \sin\theta_i \right) d\theta \right) \tag{5.28}$$

Where ρ is the flow density, P_i and ω_i are the pressure and vorticity values at boundary node i, N_s is the number of nodes at solid boundary, r is the radius of circle, θ_i is the angular position of the node i from horizontal (as shown in Figure 5.15) and $d\theta$ is the angular displacement between two consecutive boundary nodes. The lift and drag coefficients (C_D and C_L) around the solid boundary are then evaluated using following expressions:

$$Lift\ coefficient\ =\ C_L\ =\ \frac{F_L}{\rho U_\infty^2} \tag{5.29}$$

$$Drag\ coefficient\ =\ C_D\ =\ \frac{F_D}{\rho U_\infty^2} \tag{5.30}$$

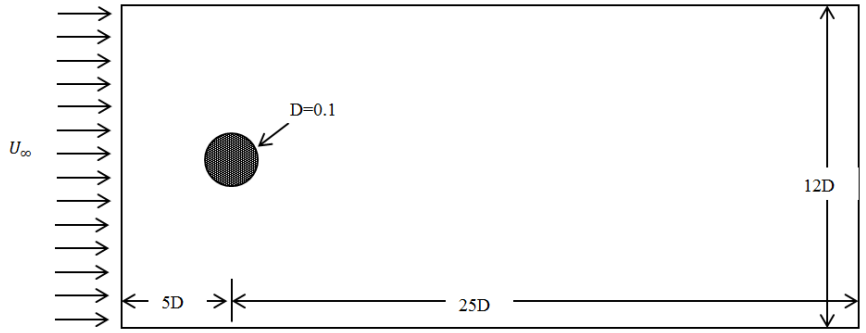

Figure 5.12: Geometric configuration for flow around Circular Cylinder

Table 5.3: Comparison of length of recirculating region (L_{sep}) and drag coefficient (C_D) for Re 10, 20 and 40

Source	Re=10		Re=20		Re=40	
	L_{sep}	C_D	L_{sep}	C_D	L_{sep}	C_D
Dennis and Chang (1970)	0.252	2.85	0.94	2.05	2.35	1.52
Takami and Keller (1969)	0.249	2.80	0.935	2.01	2.32	1.54
Tuann and Olson (1978)	0.25	3.18	0.90	2.25	2.10	1.68
Fornberg (1980)	-	-	0.91	2.00	2.24	1.50
Present Study	0.25	2.86	0.90	2.06	2.40	1.60

5.5.0.4 Steady laminar flow around static cylinder

Vortex plots for steady flow cases ($Re = 10,\ 20$ and 40) have been illustrated in Figure 5.16(a) - 5.16(c). In all the three cases, a pair of perfectly aligned vortices forms behind the cylinder which is consistent with the results from Tuann and Olson (1978), Takami and Keller (1969), Fornberg (1980), Dennis and Chang (1970), Braza et al. (1986) and Firoozjaee and Afshar (2011). The length of the vortex behind the cylinder increases with increasing the flow Reynolds number. This increases the length of recirculating region (L_{sep}) also which is the distance from rearmost point of the cylinder to the end of the wake. The quantitative values of length of recirculating region (L_{sep}) and drag coefficient (C_D) have been compared with the results obtained during previous studies by Tuann and Olson (1978), Takami and Keller (1969), Fornberg (1980), Dennis and Chang (1970) and Braza et al. (1986) in Table 5.3. The drag values tend to reduce with increasing Reynolds numbers. This is due to reduced viscous effects at high Re flows. The flow parameters obtained are in good agreement with the results of previous researchers for the three Reynolds numbers.

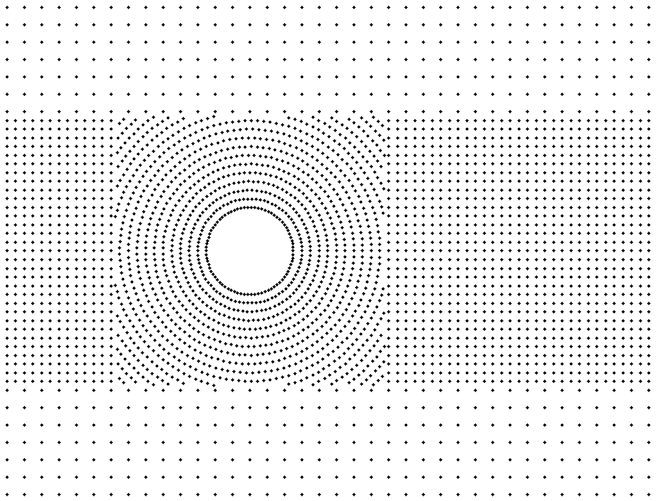

(a) For steady flow ($Re < 50$) cases

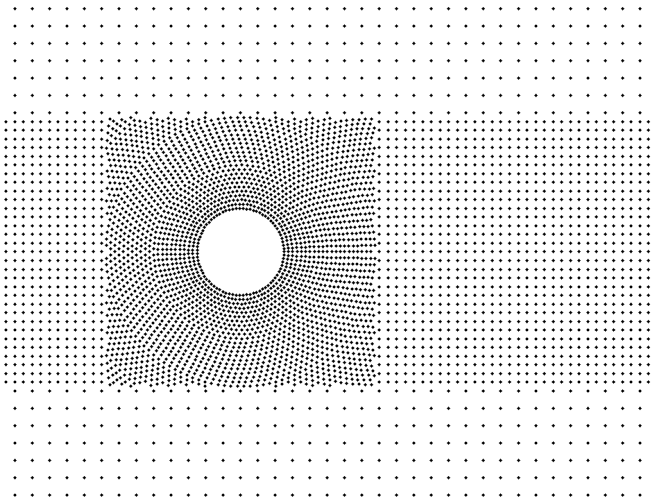

(b) For unsteady flow ($Re > 50$) cases

Figure 5.13: Nodal distribution for flow around circular cylinder

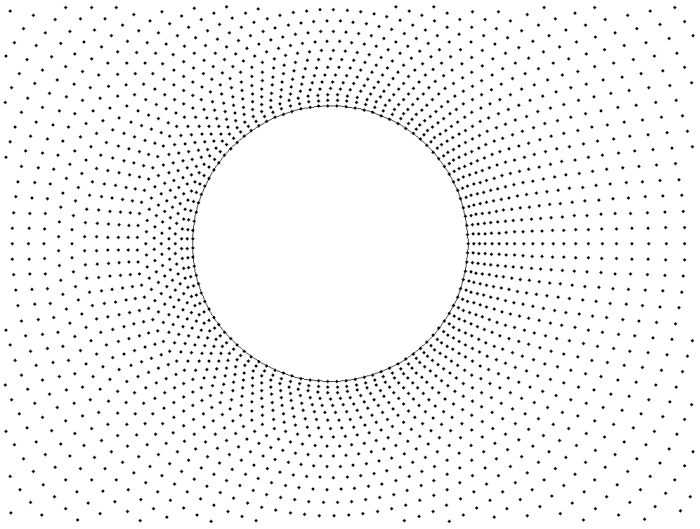

Figure 5.14: Orthogonal nodal arrangement around solid boundary

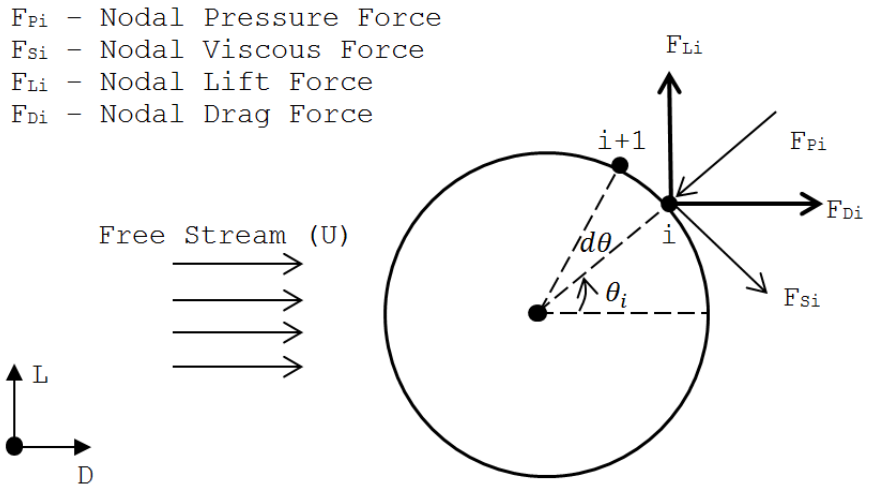

Figure 5.15: Calculation of lift and drag forces on solid boundary

5.5.0.5 Unsteady laminar flow around static cylinder

Unsteady behaviour of flow behind the cylinder is studied at $Re = 100$ and 200. The resulting instantaneous vortex plots, at $Re = 100$, during complete oscillation cycle of flow have been shown in Figure 5.17. Similar vortex plots were obtained by Placzek et al. (2009) during study of incompressible flow around cylinders. The plots obtained by Placzek et al. (2009) are shown in Figure 5.18. Vortex plots obtained during current study at $Re = 200$ are shown in Figure 5.19. These plots are similar to those obtained by Liu et al. (1998) as shown in Figure 5.20.

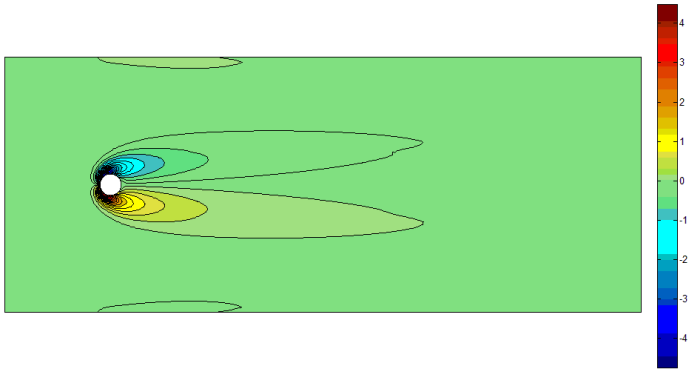

(a) Re=10

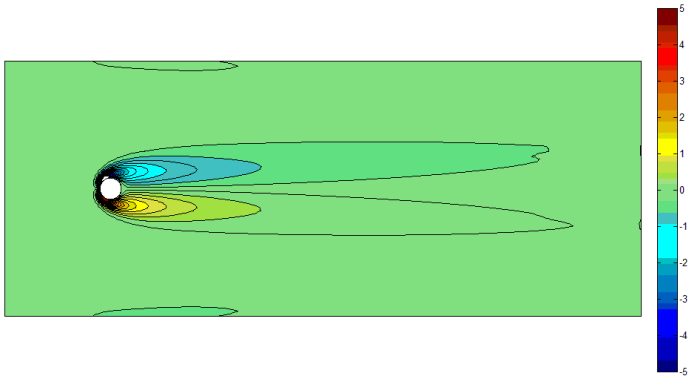

(b) Re=20

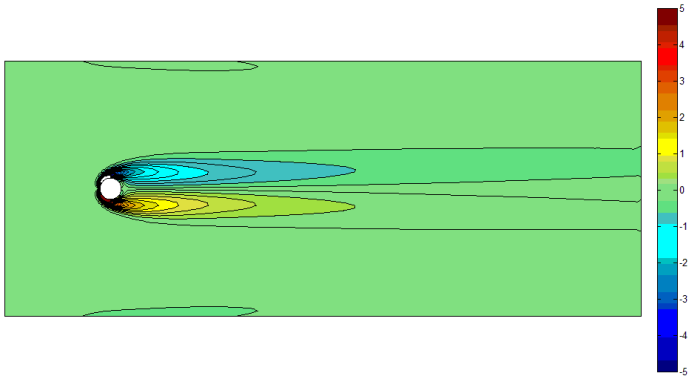

(c) Re=40

Figure 5.16: Vorticity plots for steady flow at different Reynolds numbers

Table 5.4: Comparison of Strouhal Number (St), mean drag coefficient ($\bar{C}_D$) and maximum lift coefficient ($C_{L_{max}}$) for Re 100 and 200

Source	St	$\bar{C}_D$	$C_{L_{max}}$
Re=100			
Braza et al. (1986)	0.160	1.364 ± 0.015	± 0.25
Liu et al. (1998)	0.164	1.350 ± 0.012	± 0.34
Belov et al. (1995)	-	-	-
Present Study	0.1646	1.344 ± 0.011	± 0.32
Re=200			
Braza et al. (1986)	0.200	1.40 ± 0.05	± 0.75
Liu et al. (1998)	0.192	1.31 ± 0.005	± 0.69
Belov et al. (1995)	0.193	1.19 ± 0.042	± 0.64
Present Study	0.200	1.3945 ± 0.07	± 0.77

Oscillating flow pattern also affects the lift and drag coefficients (C_L and C_D) with changing time. Frequency of oscillation of lift profile can be represented in terms of Strouhal number ($St = fD/U$, where f is vortex shedding frequency) which is equal to the vortex shedding frequency in case of non-dimensionalized length and time parameters (as non-dimensionalized values of D and U are equal to 1.0). Peak values of lift coefficients ($C_{L_{max}}$), mean values of drag coefficients ($\bar{C}_D$) and Strouhal number (St) values are tabulated in Table 5.4. The solutions are compared with the results from previous studies by Liu et al. (1998), Belov et al. (1995) and Braza et al. (1986) and are found to be in good agreement with these. The vortex shedding frequency increases with increase in Reynolds number. Moreover, oscillation profile of flow is followed by similar pattern of variation in lift and drag coefficients. These observations are also in agreement with the results of previous researchers.

5.6 Conclusion

The RBF-FD implicit scheme shows better accuracy and stability, and is able to accurately capture higher gradients of field variables even with coarser grids; unlike the RBF-FD explicit scheme where loss of accuracy was especially prominent at places with larger gradients. Excellent numerical results are obtained on non-uniform node distribution using the implicit RBF-FD method. Findings of this study have been published in Javed et al. (2014b).

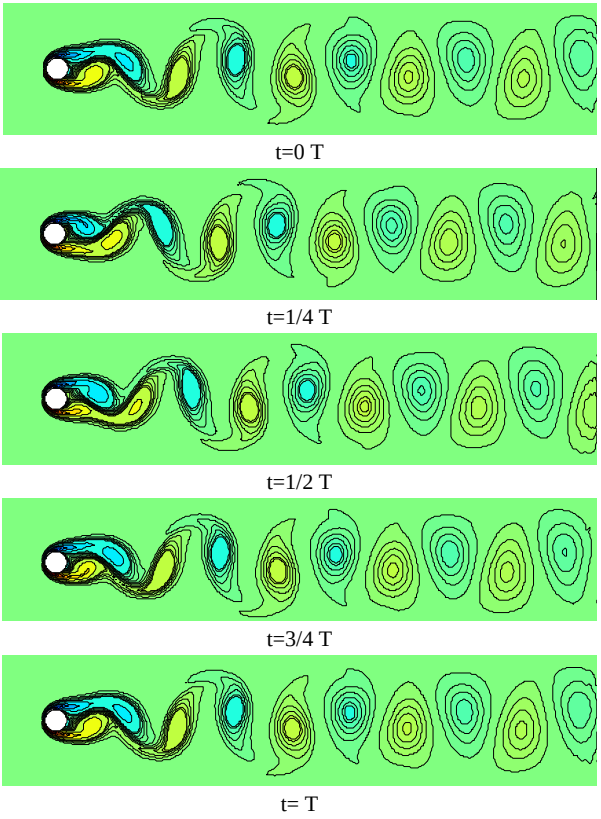

Figure 5.17: Instantaneous vortex plots around static cylinder during single oscillatory period ($Re = 100$)

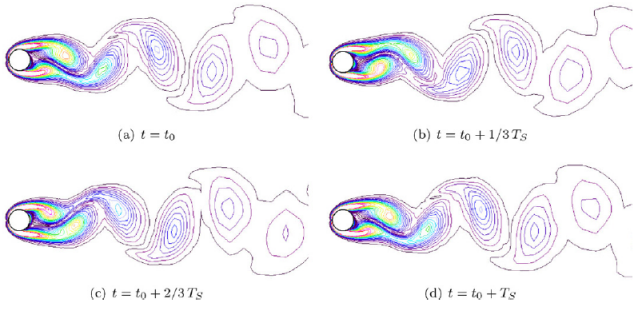

Figure 5.18: Instantaneous vortex plots around static cylinder at $Re = 100$ obtained by Placzek et al. (2009)

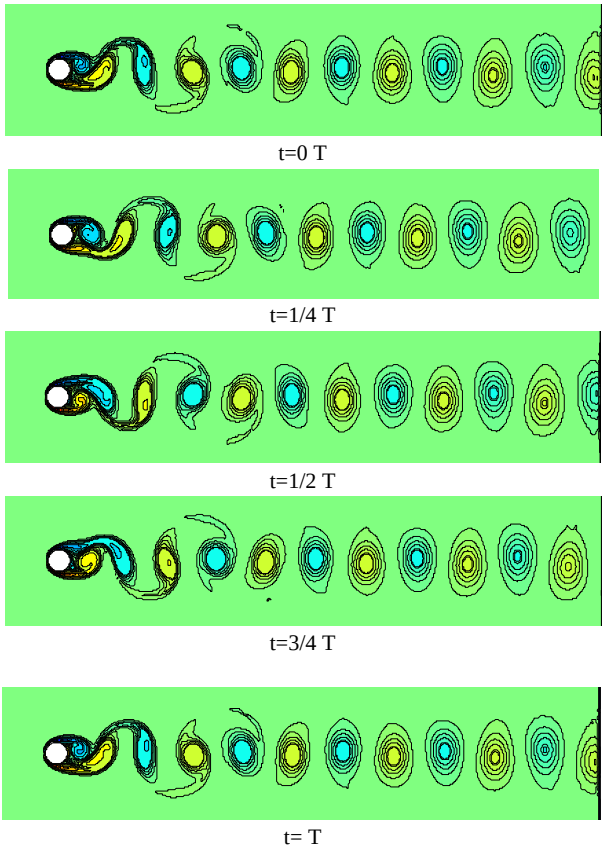

Figure 5.19: Instantaneous vortex plots around static cylinder during single oscillatory period ($Re = 200$)

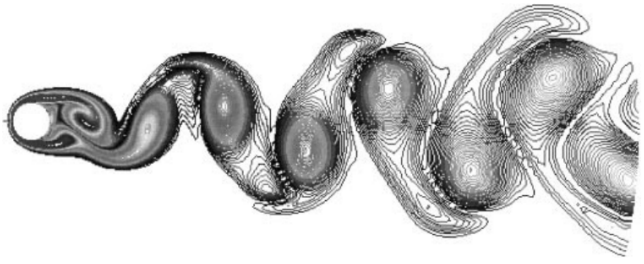

Figure 5.20: Instantaneous vortex plots around static cylinder at $Re = 100$ obtained by Liu et al. (1998)

Chapter 6

A coupled meshfree-mesh based solution scheme on hybrid fluid grids

6.1 Background

Traditional mesh-based methods (Finite Element, Finite Volume, and Finite Difference) have widely been employed for solving flow problems since the advent of Computational Fluid Dynamics (CFD). These methods have therefore evolved as well-developed and robust flow simulation techniques and are commercially employed worldwide. On the other hand meshfree methods have evolved, over past two decades, as a class of promising computational techniques which can overcome various limitations experienced by traditional mesh based methods. Meshfree methods have the potential to alleviate the mesh generation complexities arising in traditional methods. They can therefore, significantly reduce the time, effort and cost associated with grid generation. Moreover, they can easily handle flow problems around moving boundaries and deforming structures. However, their higher computational cost is a major limitation for their widespread applicability for such problems.

Recently, coupled solution schemes have been proposed by Chew et al. (2006) and Ding et al. (2004), over hybrid meshfree and mesh-based grids, to minimize the computational overheads caused by the use of meshfree methods. These techniques introduce composite meshes comprising of meshfree and meshed zones in different parts of fluid domains. Ding et al. (2004) proposed a hybrid grid consisting of body conformal meshfree cloud embedded over a background Cartesian grid for static problems. In that, a coupled solution scheme employing moving least square finite difference (MLSFD) on meshfree cloud and central differencing on Cartesian grid was used. Chew et al. (2006) extended

similar approach to moving objects. They used generalized finite difference (GFD) approximation in weighted least square (WLS) form over meshfree zone.

6.2 Hybrid Meshfree-Cartesian grid scheme

In view of the foregone, a solution scheme has been proposed which combines the inherent strengths of both meshfree and mesh-based methods. The scheme couples RBF-FD based meshfree solver and conventional finite difference based solver for viscous, incompressible flow around arbitrarily shaped moving objects. The solution is sought over a hybrid meshfree-Cartesian grid in fluid domain. For this purpose, the fluid domain is divided into two zones. A boundary fitted meshfree nodal cloud is generated around the solid object. On the outer side, the meshfree cloud is surrounded and partially overlapped by a static Cartesian grid. The aim is to optimize the performance and flexibility of the solver by limiting the use of computationally expensive meshfree method only to the regions where it can actually outclass mesh-based method in dealing with moving boundaries or complex geometries. Schematic of the hybrid grid around cylindrically shaped objects and airfoils are shown in Figures 6.1(a) and 6.1(b) respectively.

The proposed technique couples RBF-FD method on meshfree zone around the solid body and conventional Finite difference method applied to the Cartesian grid zone in rest of the domain. Meshfree nodes efficiently adapt to the irregular shaped boundaries and effectively deal with movement of solid by moving during simulation. Computationally expensive RBF-FD method is therefore limited to only small meshfree zone of the computational domain where it is required to deal with irregularly shaped moving solid boundaries. The remaining computational domain is dealt with conventional finite difference method on a static Cartesian grid which enjoys computational efficiency over its meshfree counterpart. Values of field variables at collocation points on meshfree boundary serve as boundary conditions for Cartesian grid zone. Therefore, an overall efficient solution scheme is achieved which can effectively handle arbitrarily shaped moving solid boundaries.

6.3 Treatment of computational domain in hybrid grid

Configuration of meshfree and Cartesian zones are shown in Figure 6.1 for flow around moving objects. As mentioned before, the fluid domain is represented by a hybrid grid comprising of meshfree nodal cloud and Cartesian mesh. The near field flow region, around the solid, is represented by a body conformal meshfree nodal cloud. These meshfree nodes follow the movement of solid boundary during the simulation. In the far field, static Cartesian grid is used which surrounds the meshfree nodal cloud. Moreover,

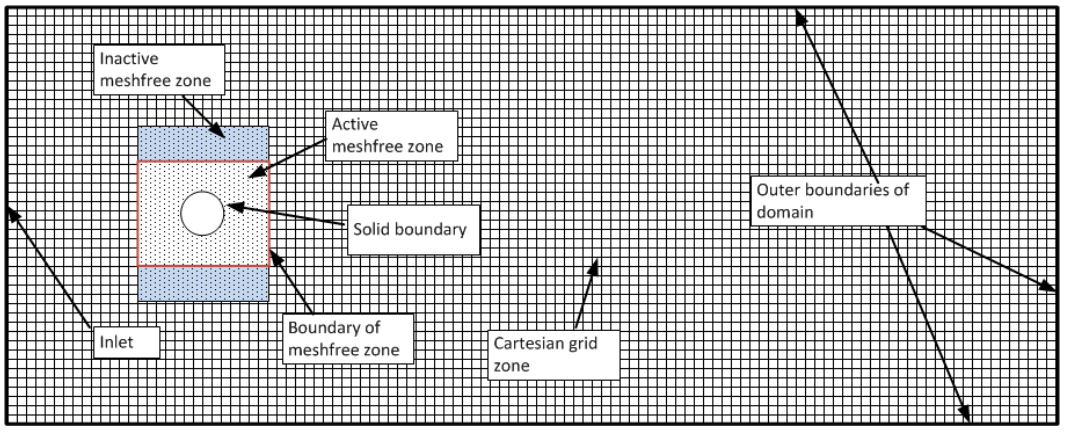

(a) For cylindrically shapped objects

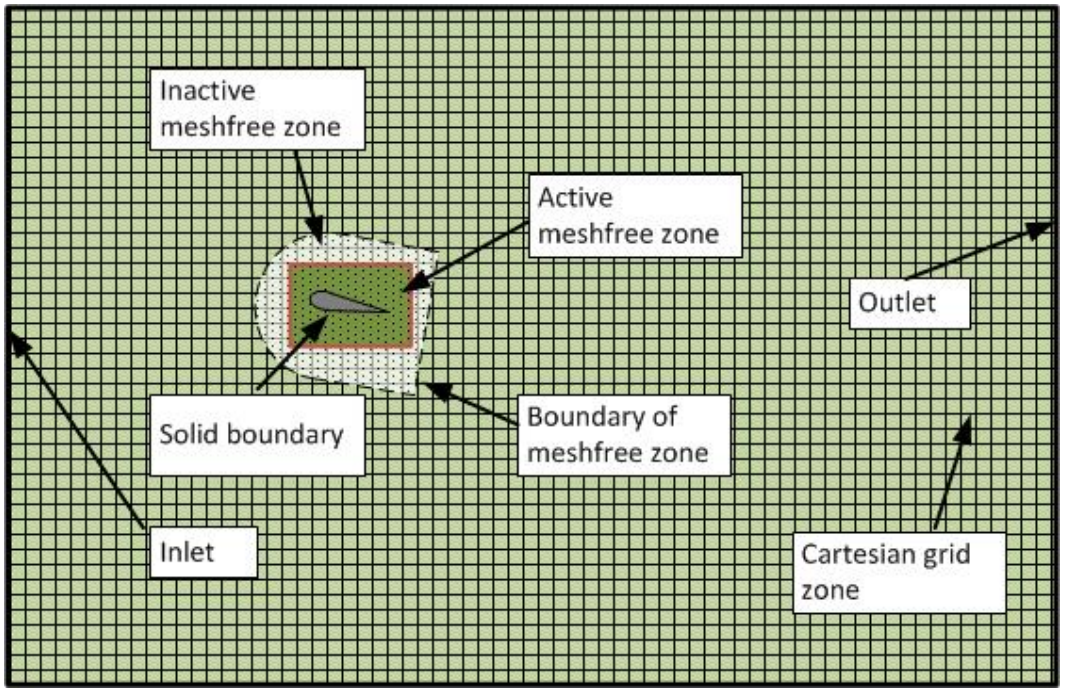

(b) For airfoil

Figure 6.1: Hybrid grid configuration in fluid domain

some parts of meshfree cloud are overlapped by surrounding Cartesian mesh. The fluid grid can therefore be divided into following three zones:

1. Cartesian zone: This comprises of Cartesian mesh. Conventional finite difference scheme is here used for spatial discretization of flow equations

2. Active meshfree zone: This zone consists of meshfree nodes which are not overlapped by Cartesian mesh. RBF-FD scheme is used here for evaluation of spatial derivative.

3. Shadowed (or inactive) meshfree zone: This zone represents the meshfree nodes which are overlapped by Cartesian mesh. This zone is treated as *inactive* and solution is not computed on nodes falling in this zone.

Different zones of typical hybrid grid generated around cylinder and airfoil are shown in Figures 6.2(a) and 6.2(b) respectively. The computational nodes falling in meshfree and Cartesian zones are treated differently. Therefore, in order to apply respective spatial treatment in meshfree and Cartesian zones, the computational nodes are classified in five different categories according to the regions they fall in. This classification of nodes is depicted in Figure 6.3. Detail of nodes falling in each category is given below:

- **Category-I nodes**: These are the nodes which lie on Cartesian stencil and are sufficiently away from meshfree zone. These nodes are stationary and spatial derivatives at these nodes are calculated using five points central difference scheme.
- **Category-II nodes**: These nodes also lie on Cartesian stencil and are treated with central difference scheme. However, they are located close to the meshfree zone and can directly influence the results on neighbouring meshfree nodes. Category-II nodes can therefore fall in the influence domain of nearby meshfree nodes. These nodes are also included in the neighbourhood particle search for meshfree nodes.
- **Category-III nodes**: These nodes fall exactly at the boundary of meshfree-Cartesian zones. Category-III nodes are stationary and aligned with Cartesian stencil. However, these are part of active meshfree zone and are treated with RBF-FD method. Although these are meshfree nodes but they also act as boundary nodes for Cartesian grid. During solution over Cartesian zone, the values of field variables at category-III nodes are taken as boundary condition.
- **Category-IV nodes**: These nodes fall in *active* meshfree zone. These nodes are part of moving grid which are treated with RBF-FD method and ALE formulation of N-S equations.
- **Category-V nodes**: These are the nodes which fall in *inactive* meshfree zone. These are part of meshfree grid but are *overshadowed* by superimposing Cartesian grid. The nodes are therefore treated as *inactive* and do not participate in current time step computations.

A summary of different categories of nodes and their computational treatment is outlined in Table 6.1. During the simulation, the two way exchange of data between Cartesian and meshfree zones takes place in the following manner:

- Information from meshfree to Cartesian grid is transferred through Category-III nodes. These nodes are treated with RBF-FD method. However, they are static

and fall exactly on Cartesian stencil. Therefore, these nodes can act as boundary nodes for Cartesian grid. During simulation process, the most updated values of field parameters at Category-III nodes are taken as Dirichlet boundary conditions for surrounding Cartesian nodes.

- Transfer of data from Cartesian to meshfree zone takes place through Category-II nodes. These nodes fall in the influence domain of neighbouring meshfree nodes. Therefore, the flow parameters at Category-II nodes affect the derivative approximations at respective meshfree nodes through corresponding RBF weights. As a result, flow parameters values at meshfree nodes are influenced by the results at Category-II nodes.

During the simulation, the movement of solid is accommodated in fluid grid by allowing the meshfree (Category-IV and V) nodes to move along the solid boundary. Relative positions of these moving nodes are however kept unchanged during the cloud motion. Figure 6.4 shows the movement of meshfree grid surrounded by static Cartesian grid between time instance t_0 to t_1. A case for vertically vibrating cylinder is shown in Figure 6.4(a). Similarly, movement grid around pitching airfoil is shown in Figure 6.4(b). As the grid position changes, some inactive (category-V) nodes may come out of the *shadowed* region and appear in the active meshfree zone (see group-A nodes, for example, in Figures 6.4(a) and 6.4(b)). These nodes will be activated and put in Category-IV for subsequent calculations. These *fresh* nodes are assigned the values of field variable by averaging the data from surrounding nodes. Movement of meshfree grid will also pushes some other nodes behind the Cartesian grid (for example group-B nodes shown in Figures 6.4(a) and 6.4(b)). These nodes are put in Category-V and do not participate in further calculations unless they reappear in the active meshfree zone.

Using this treatment of moving meshfree grid, the number and location of nodes in Cartesian zone do not change during the simulation. This has a computational advantage as the matrix Eqs. (5.7), (5.22) and (5.23), for solving the flow in Cartesian zone, remain unchanged and are required to be formulated only once (at the start of iteration process). Moreover, as the relative positions of meshfree nodes are not varied, the arrangement of neighbourhood particles of meshfree nodes do not change unless these neighbouring particles include some stationary nodes (Category-II or III nodes). Therefore, RBF weights of only those meshfree nodes are re-calculated during simulation which have category-II or category-III nodes in their influence domain. Coefficient Matrices for solving Eqs. (5.7), (5.22) and (5.23) in meshfree zone are however needed to be updated regularly as the number and location of active meshfree nodes changes.

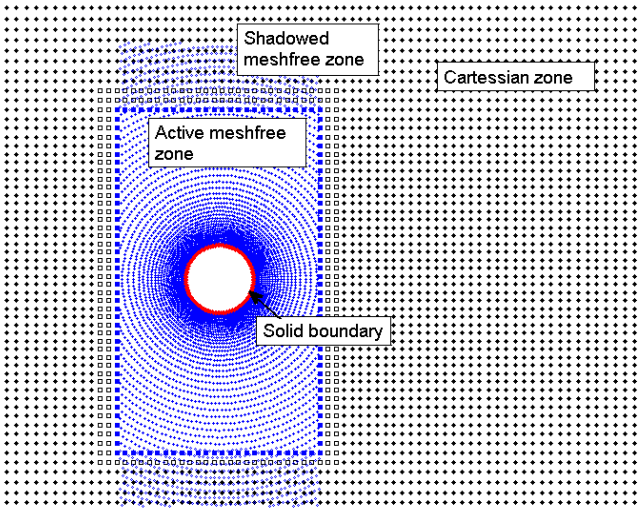

(a) For cylindrically shapped objects

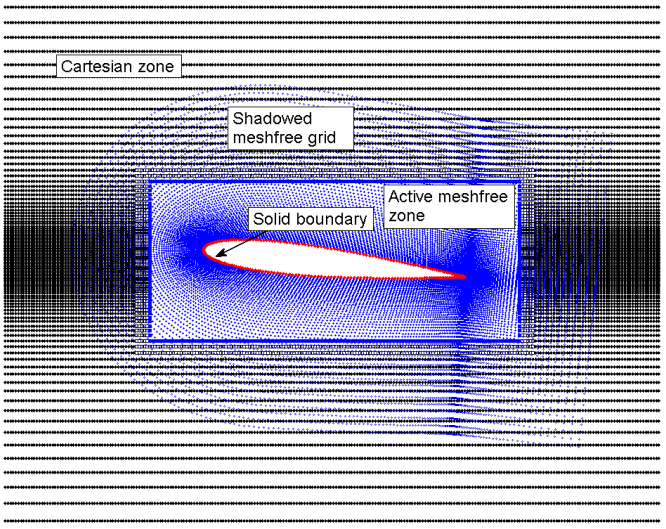

(b) For airfoil

Figure 6.2: Hybrid grid generated around cylinder and airfoil. Meshfree nodal cloud is surrounded and partially overlapped by Cartesian grid

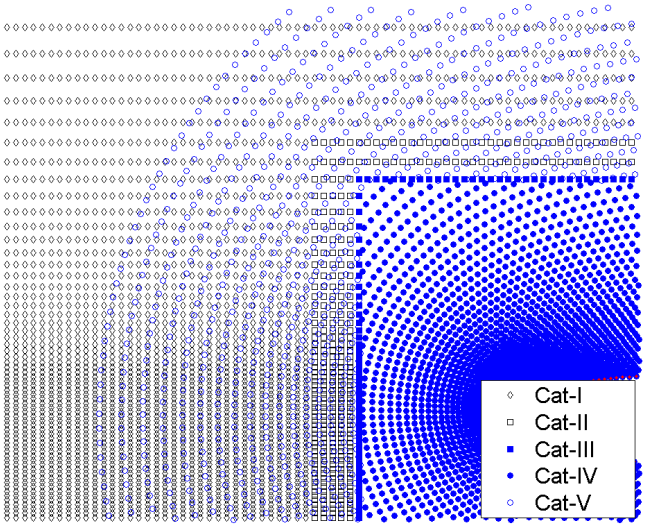

Figure 6.3: Classification of computational nodes in hybrid fluid grid

Table 6.1: Categorization of computational nodes in hybrid grid

Category	Zone	Method	Stationary / Moving	Remarks
Cat-I	Cartesian	FD	Stationary	
Cat-II	Cartesian	FD	Stationary	Fall in the influence domain of neighbouring mesfhree particles
Cat-III	Meshfree	RBF-FD	Stationary	Act as boundary particles for Cartesian grid
Cat-IV	Meshfree	RBF-FD	Moving	Active meshfree nodes
Cat-V	Meshfree	RBF-FD	Moving	Inactive meshfree nodes

6.4 Solution of 1-D Convection-Diffusion equation

Before moving on to the solution of incompressible Navier Stokes equation over two dimensional fluid domain, the applicability of hybrid grid is verified on one dimensional domain. For this purpose, following convection diffusion equation has been solved over 1-D nodal arrangement:

$$\frac{\partial u}{\partial t} = -u\frac{\partial u}{\partial x} + \frac{1}{Re}\frac{\partial^2 u}{\partial x^2} \tag{6.1}$$

The equation is in non-dimensionalized form. $u(x,t)$ is the normalized velocity, x is non-dimensionalized spatial coordinate and Re is the Reynolds number defined as $Re = UL/\nu$ (where U is the maximum velocity at t_0, L is half the length of velocity step at t_0 and ν is the kinematic flow viscosity). The equation is solved over domain $0 \leq x \leq 10$.

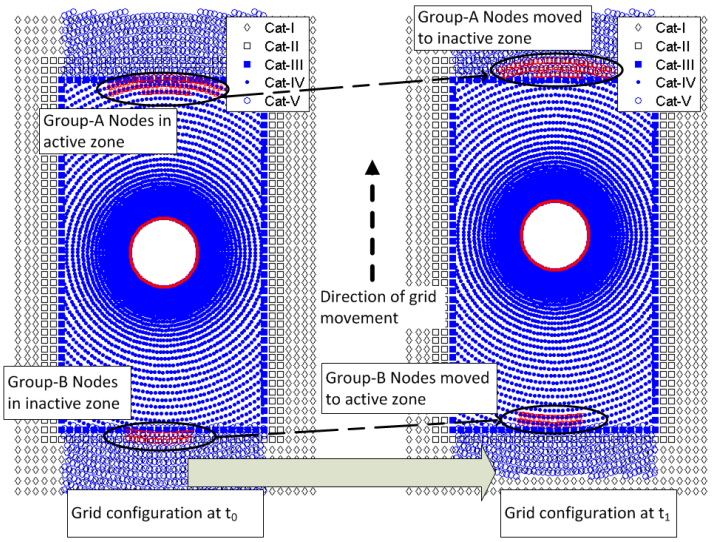

(a) For cylindrically shapped objects

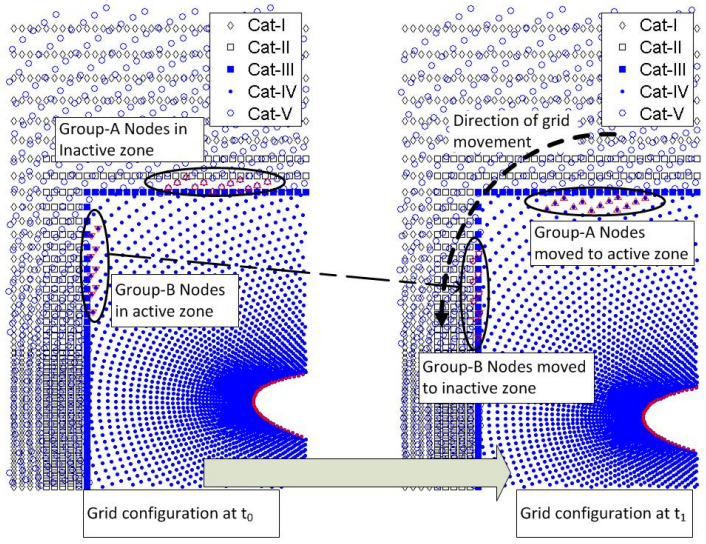

(b) For airfoil

Figure 6.4: Activation and deactivation of meshfree nodes during movement of meshfree grid

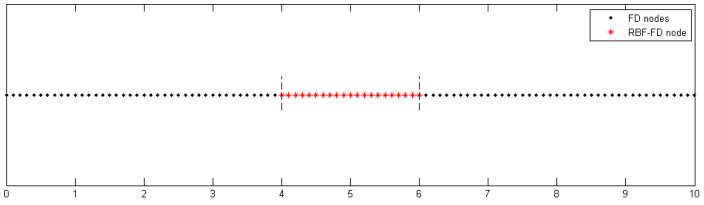

Figure 6.5: One dimensional hybrid nodal array used for solution of convection diffusion equation.

Initial velocity field $u(0,x)$ is defined by two step functions with opposite signs. So, the initial conditions are:

$$\begin{aligned} u(x,0) &= 1 && for\ 2 \leq x \leq 3 \\ u(x,0) &= -1 && for\ 7 \leq x \leq 8 \\ u(x,0) &= 0 && elsewhere \end{aligned}$$

At both ends of domain, Neumann boundary conditions are applied with $\partial u/\partial x = 0$. Time marching for transient variable $u(x,t)$ is carried out using Euler explicit method. So, at every time step t^n, velocity at next time iteration u^{n+1}, at any node, are calculated as:

$$u^{n+1} = u^n + \Delta t \left[-u^n \frac{\partial u^n}{\partial x} + \frac{1}{Re} \frac{\partial^2 u^n}{\partial x^2} \right] \tag{6.2}$$

Solution are sought over 1-D array of nodes with uniform space step $dx = 0.1$ as shown in Figure 6.5. Three different test cases are run for spatial derivatives calculated using three different approaches:

- **Case-1:** Applies central difference scheme on all the computational nodes (for $0 \leq x \leq 10$)
- **Case-2:** Applies RBF-FD scheme on all the computational nodes (for $0 \leq x \leq 10$)
- **Case-3:** Applies RBF-FD scheme for spatial derivatives on nodes falling within $4.0 \leq x \leq 6.0$. Central difference scheme is used on remaining nodes ($x < 4.0$ and $x > 6.0$).

Distinction between FD and RBF-FD nodes, as depicted in Figure 6.5, is therefore required only for Case-3. For Case-1 or 2 where central differencing or RBF-FD scheme is used over the entire domain, all the nodes are treated equally according to the respective method being employed. The solutions are obtained at $Re = 10,\ 20$ and 40. Figures 6.6(a) to 6.6(c) show velocity profiles at $t = 0$ and $t = 2$ for $Re = 10,\ 20$ and 40

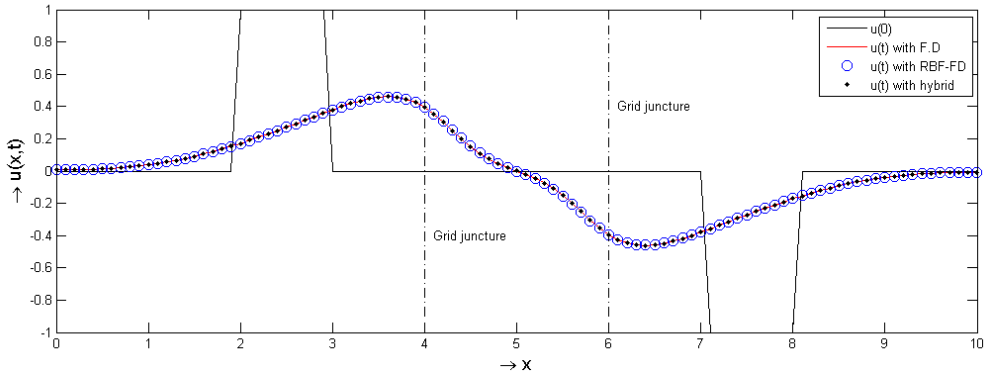

(a) $Re = 10$

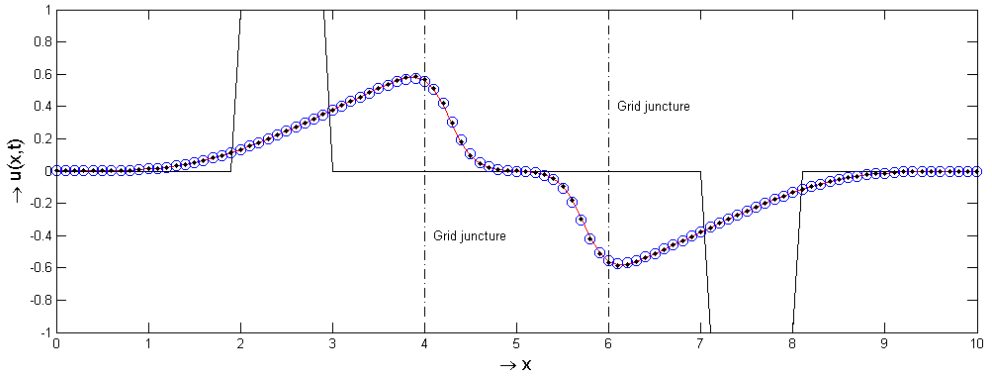

(b) $Re = 20$

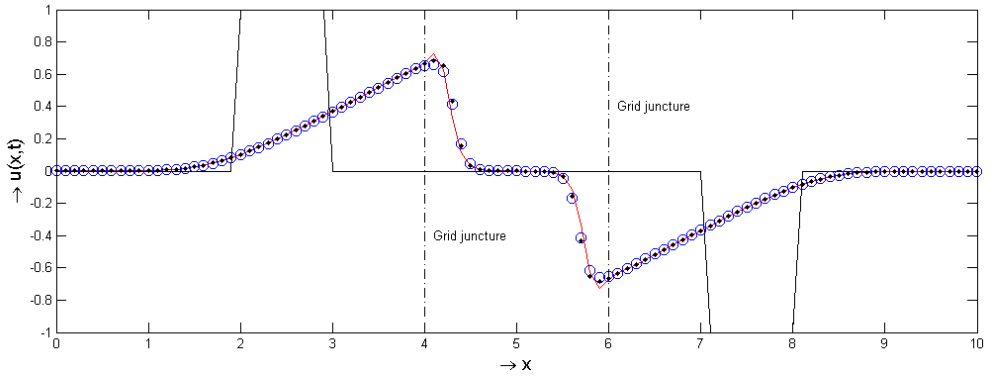

(c) $Re = 40$

Figure 6.6: Solution of 1-D convective-diffusive equation for domain $0 \leq x \leq 10$ at t=2. $u(x, 0)$ is defined by two unit step functions in opposite directions. Solutions are obtained using central differencing (-), RBF-FD (O) and hybrid approach (*).

respectively. Resultant velocity profiles at $t = 2$, obtained from all the three cases, are co-plotted for comparison. The results are found to be in good agreement with each other. Particularly for hybrid grid approach, the transition of velocity profile at grid juncture ($x = 4.0$ and $x = 6.0$) is fairly smooth which indicates effective transfer of data between the two sets of nodes. The error for RBF-FD (Case-2) and hybrid grid scheme (Case-3) are calculated by taking root mean square (rms) of the difference between respective velocity profile obtained from central differencing method (Case-1). The error values are shown in Table 6.2. RMS error for Case-3 is lower than that for Case-2 because in Case-3, computational domain is partially treated with central differencing and therefore error from full central difference scheme (Case-1) is reduced. There is a growing trend in error with increasing Reynolds number. This is due to increased spurious fluctuations in the solution caused by greater contribution of convective term.

Table 6.2: rms of error values for RBF-FD and hybrid approaches. Error values, calculated using central difference results, are standard

Reynolds number (Re)	rms of error	
	Full RBF-FD scheme (Case-2)	Hybrid grid scheme (Case-3)
10	0.0019343	0.00053235
20	0.0055908	0.0027456
40	0.017558	0.017969

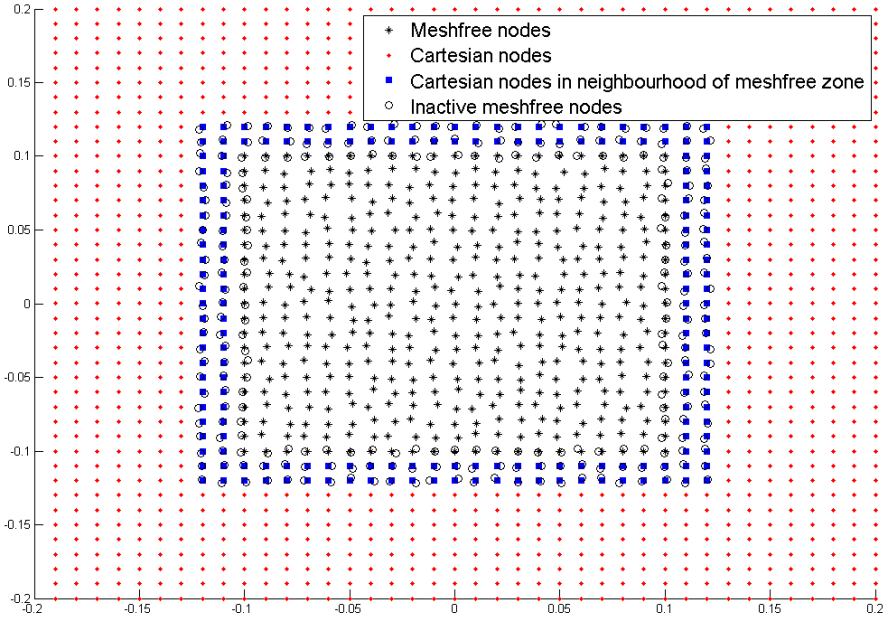

Figure 6.7: Hybrid grid in rectangular domain $[-0.5,\ 0.5] \times [-0.5,\ 0.5]$ with randomized meshfree particles. Meshfree zone spans $[-0.1,\ 0.1] \times [-0.1,\ 0.1]$. Grid size is $h = 0.01$.

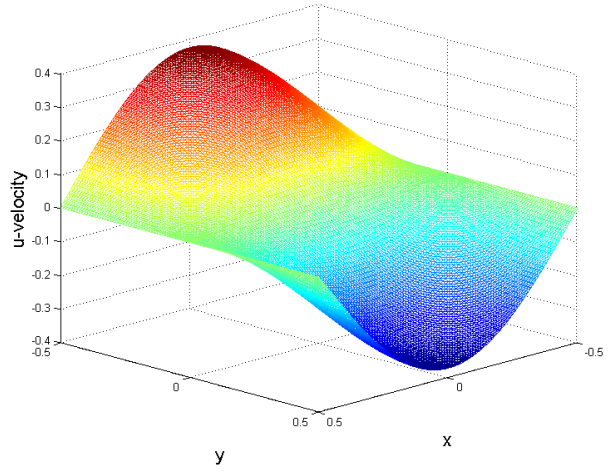

(a) u-velocity profile

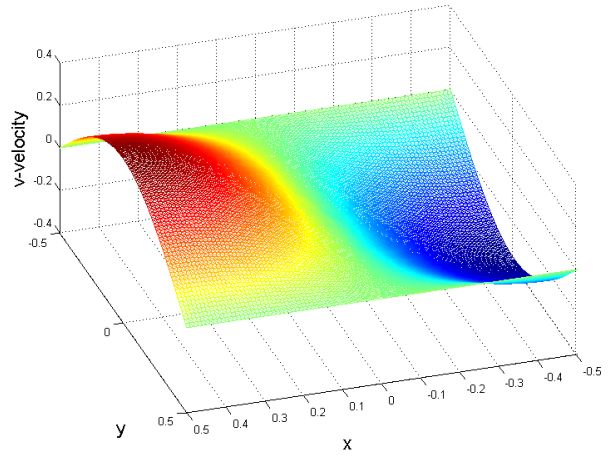

(b) v-velocity profile

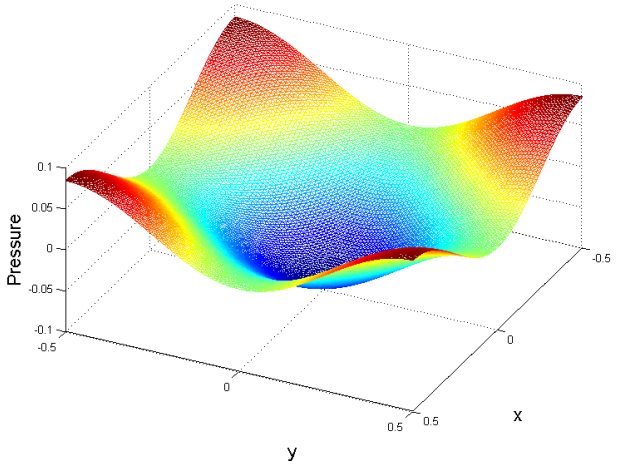

(c) Pressure profile

Figure 6.8: Solutions of velocity $\vec{\mathbf{u}} = (u, v)$ and pressure at $t = 0.5$ sec in rectangular domain $[-0.5,\ 0.5] \times [-0.5,\ 0.5]$ with hybrid fluid grid. Meshfree zone spans $[-0.1,\ 0.1] \times [-0.1,\ 0.1]$. Grid size is $h = 0.01$.

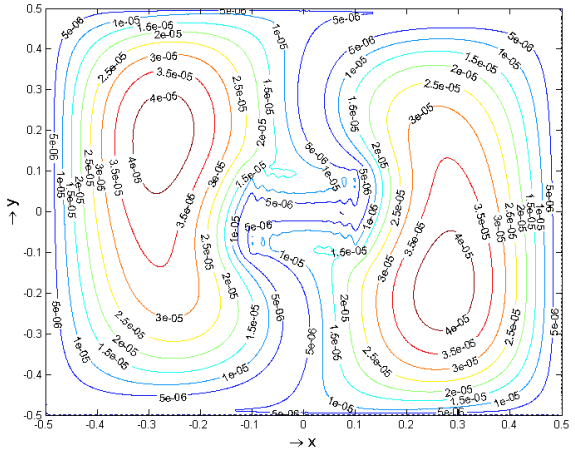

(a) Error for u-velocity

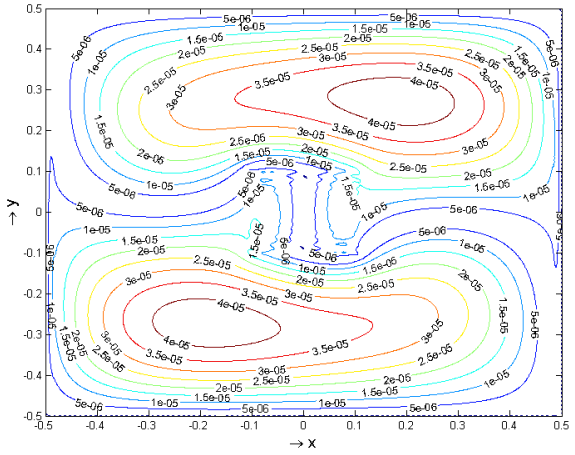

(b) Error for v-velocity

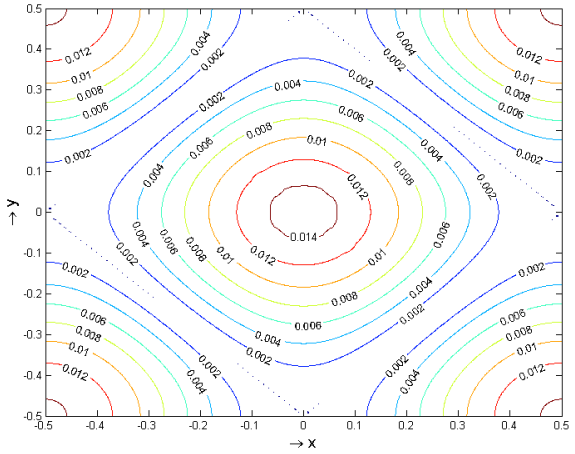

(c) Error for Pressure

Figure 6.9: Contours of error for velocity $\vec{\mathbf{u}} = (u, v)$ and pressure at $t = 0.5$ sec in rectangular domain with hybrid fluid grid. Grid size is $h = 0.01$.

6.5 Order of convergence over 2-D domain

This section deals with convergence and accuracy analysis of hybrid grid scheme. Time implicit solution scheme (as mentioned in Section 5.1.2.2) has been used for incompressible N-S equations over 2-dimensional rectangular domain. Validation has been done by solving decaying vortex case as described in Section 5.3 and comparing the calculated solutions with true solutions from Eqs. (5.24) - (5.26). However, this time, order of convergence studies are conducted over hybrid fluid grid. Computational domain is rectangular with dimensions $[-0.5,\ 0.5] \times [-0.5,\ 0.5]$. Central region, spanning $[-0.1,\ 0.1] \times [-0.1,\ 0.1]$, is set as meshfree zone and remaining region is meshed with Cartesian grid. Convergence tests are run for uniform as well as random meshfree nodal arrangement. For random nodal arrangement, randomness is introduced in meshfree nodes by disturbing their position from corresponding locations on a uniform lattice using a random function of the order of $0.4h$ (where h is space step). Figure 6.7 shows the hybrid mesh with space step $h = 0.1$ and randomized meshfree nodes. The order of convergence tests have been performed with different settings in order to study the effects of following factors on accuracy:

- Changing grid size
- Changing time step
- Dirichlet and Neumann Pressure boundary conditions
- Randomness of meshfree particles
- Speed of moving meshfree particles
- Grid update frequency for moving grid case

For this purpose, six different test cases are run. Detail of each test case is summarized in Table 6.3. Flow Reynolds number is set as 10 for all tests. For each test case, initial conditions for pressure, velocity and boundary conditions for velocity are introduced using Eqs. (5.24) - (5.26) at given time and space coordinates (t, x, y).

6.5.1 Convergence over static grid

Static test cases are run for evaluating spatial and temporal orders of convergence and determining the effects of pressure boundary conditions and randomness of grid. Test Case-1 is run for evaluating rate of convergence with changing space step (h). This has been achieved by running different solutions at a constant time step value of 10^{-5} but with varying grid sizes. Smaller value of time step has been chosen to keep temporal errors to minimum. At boundaries, Dirichlet pressure boundary conditions are introduced

which means that pressure values, at boundary nodes, are directly evaluated using Eq (5.26). The solutions are run for $t = 0.5$. Resultant solutions of velocity and pressure for grid spacing $h = 0.01$ are shown in Figure 6.8. It can be observed that the profiles of velocities and pressure vary smoothly across meshfree and Cartesian zones in hybrid grid. This indicates efficient transfer of data across zone boundaries. Accuracy of the solution is established by comparing these calculated profiles with true solutions at the same time instant t (using (Eqs (5.24) - (5.26)). Contour plots of error for velocities and pressure obtained at hybrid grid, with $h = 0.01$, are shown in Figures 6.9(a) - 6.9(c) respectively. The error values remain significantly low over the domain and behaviour of variation of error remains unchanged irrespective of meshfree and Cartesian zone. Subsequently, RMS (root mean square) and maximum error values over the entire domain are worked out. Logarithmic values of error ($\log_{10}(\varepsilon)$) for u-velocity and pressure are plotted against logarithms of space step ($\log_{10}(h)$) in Figures 6.10(a) and 6.10(b) respectively. Error profiles for v-velocity are the same as for u-velocity and are not included. The error plots show that RMS error values are always lower than corresponding maximum error values which is logical as RMS values give overall effect of the entire domain and should always be lower than the maximum values. However, the two curves (for RMS and maximum error) are not very far apart. This indicates that order of error did not vary significantly within the domain and remained generally *uniform*. Slope of velocity error curves tend to increase as the grid becomes coarser. However, this trend is not very prominent with pressure error curves.

Test Case-2 has been run to determine spatial order of convergence with Neumann boundary conditions for pressure. In this case, pressure values, at boundaries, are obtained from velocity field using Eq (5.6) instead of being directly evaluated by equation (5.26). Therefore, flow is constrained only by velocity at the boundaries. u-velocity and pressure error plots for this case are shown in Figures 6.10(c) and 6.10(d) respectively. No significant change in velocity error profile is observed with Neumann pressure boundary conditions. This is primarily because velocity values at boundary remain unaffected as these are being calculated as before. On the other hand, slight increase in pressure error is observed. However, this increase does not seem to be very significant and overall trend remains the same. Test Case-3 has been run to find spatial order of convergence over random meshfree nodal arrangement. The error plots are shown in Figures 6.10(e) and 6.10(f). Randomization of meshfree nodal grid has altered the shape of error curve but overall change in the error values, within the test range of space step values, is the same. This indicates that convergence behaviour of the solution might be affected on random grid, but overall convergence rate does not suffer much variation.

Similarly, temporal convergence is studied by keeping grid size constant at $dx = 0.005$ and changing the time step values. Test cases-4 and 5 are run for Dirichlet and Neumann pressure boundary conditions respectively on uniform grids. Simulation time is kept the same ($t = 0.5$). Plots of $\log_{10}(\varepsilon)$ versus $\log_{10}(\Delta t)$ are shown in Figures 6.11(a) and

Table 6.3: Spatial order of convergence for static tests

Test Case No	Moving / Static case	Type of test (Spatial / Time)	Distribution of mesfhree nodes	Pressure B.Cs
Case-1	static	Spatial	Uniform	Dirichlet
Case-2	static	Spatial	Uniform	Neumann
Case-3	static	Spatial	Random	Dirichlet
Case-4	static	Time	Uniform	Dirichlet
Case-5	static	Time	Uniform	Neumann
Case-6	moving	-	Uniform	Dirichlet

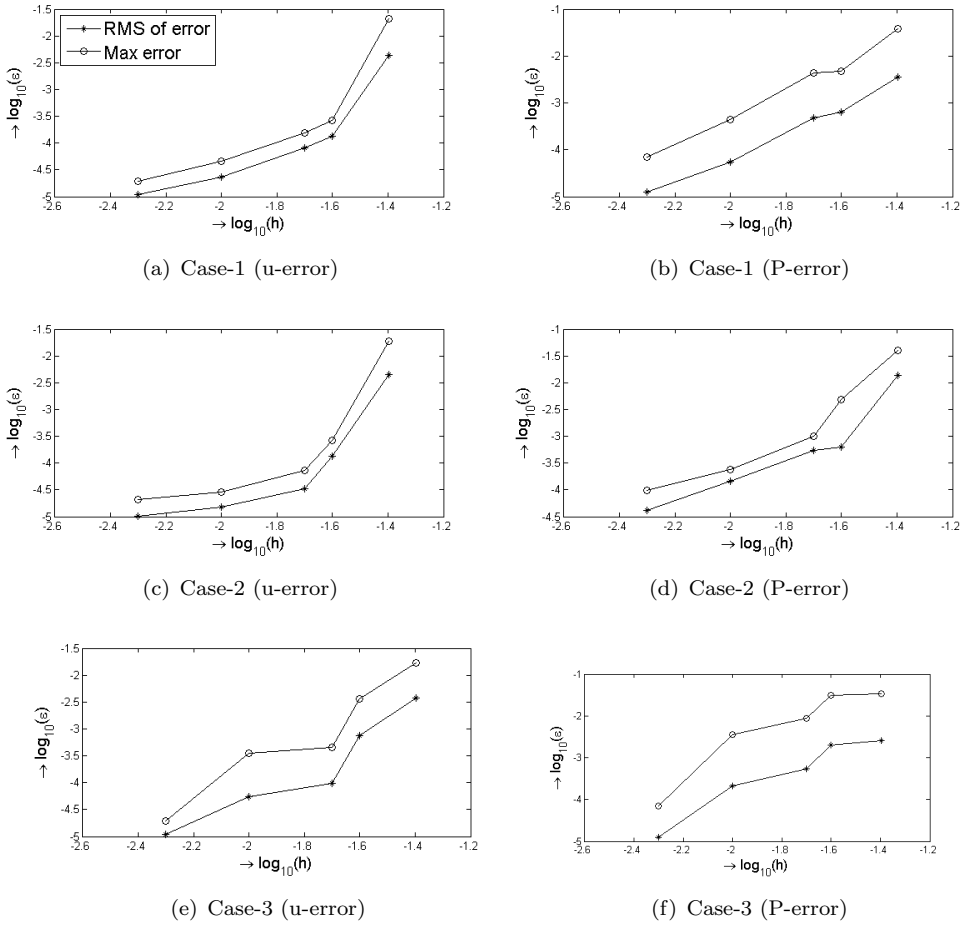

(a) Case-1 (u-error)

(b) Case-1 (P-error)

(c) Case-2 (u-error)

(d) Case-2 (P-error)

(e) Case-3 (u-error)

(f) Case-3 (P-error)

Figure 6.10: Spatial convergence tests. Error Plots at t=0.5, for changing grid sizes and constant time step ($\Delta t = 10^{-5}$) (*-RMS error, o-Max error)

6.11(b) for Dirichlet and in Figures 6.11(c) and 6.11(d) for Neumann pressure boundary conditions. On logarithmic scale, convergence rates fall uniformly with reducing time step values. At larger time steps, the error values are higher for Neumann pressure B.Cs. However, the error remains unaffected by change in type of pressure B.Cs at lower time steps.

After having error plots on logarithmic scales, spatial and temporal orders of convergence

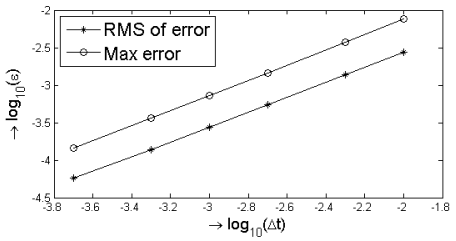

(a) Case-4 (u-error)

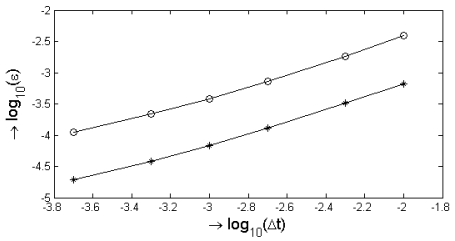

(b) Case-4 (P-error)

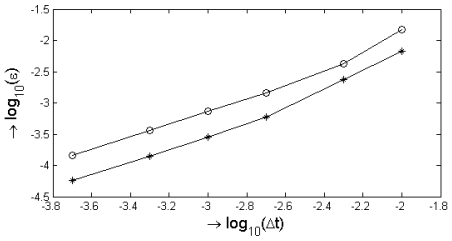

(c) Case-5 (u-error)

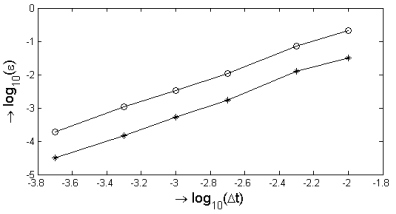

(d) Case-5 (P-error)

Figure 6.11: Temporal convergence tests. Error Plots at t=0.5, for changing time step and constant grid size ($h = 5 \times 10^{-3}$) (*-RMS error, o-Max error)

Table 6.4: Spatial order of convergence for static tests

Test case No	Description	Spatial / Time	Order of convergence	
			u-velocity	pressure
Case-1	Uniform meshfree grid, Dirichlet pressure B.Cs	Spatial	2.56	2.7
Case-2	Uniform meshfree grid, Neumann pressure B.Cs	Spatial	2.59	2.49
Case-3	Random meshfree grid, Dirichlet pressure B.Cs	Spatial	2.66	2.58
Case-4	Uniform meshfree grid, Dirichlet pressure B.Cs	Time	0.99	0.9135
Case-5	Uniform meshfree grid, Neumann pressure B.Cs	Time	1.22	1.8

have been calculated. The order of convergence is defined as the slope of linear curve obtained by least square fit on RMS error data points shown in Figures 6.10 and 6.11. Order of convergence values, calculated using this approach, are tabulated in Table 6.4. It can be observed that spatial order of convergence for both velocity and pressure remains close to 2.5. Order of convergence in time is found to be around 1.0 for both pressure and velocity field with known pressure boundary conditions. Use of Neumann boundary conditions however tends to increase the convergence rate especially for the pressure field.

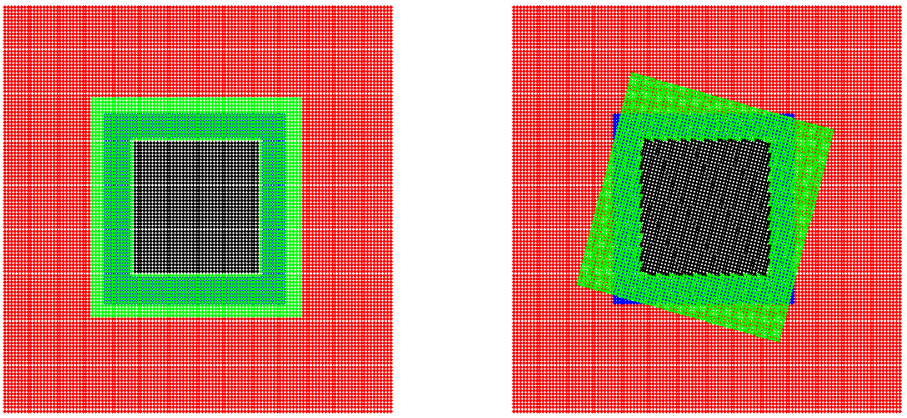

(a) Configuration at t_0 (b) Configuration at t_1

Figure 6.12: Grid configuration at initial time $t_0 = 0$ and at time $t_1 = 0.5$ for rotating meshfree zone with angular orientation ($\Theta(t)$) defined by $\Theta(t) = 0.3\pi[1 - \cos(\pi t/2)]$

6.5.2 Convergence over moving meshfree grid

Moving grid cases are run by making the mesfhree grid rotate about its centre with a variable angular velocity. Angular orientation ($\Theta(t)$) of meshfree grid at any time instant t is defined as:

$$\Theta(t) = \mathbf{A}\left[1 - \cos\left(\frac{\pi t}{2}\right)\right] \tag{6.3}$$

Value of parameter $\mathbf{A}$ is set to control angular speed and total grid rotation in a given time. Grid configuration at initial time t_0 and at later time $t_1 = 0.5$ are shown in Figures 6.12(a) and 6.12(b) respectively for $\mathbf{A} = 0.3\pi$. Moving grid tests are run for different values of $\mathbf{A}$ to get different nodal velocities. Space step is set as $h = 0.005$ and time step is kept as $\Delta t = 10^{-4}$. Simulations are run for $t = 0.5$ and error values are obtained by comparing the solutions with true values. Logarithmic ($\log_{10}$) values of RMS and maximum error are plotted against the changing grid speeds in Figure 6.13. On the plot, the point at $\mathbf{A} = 0$ corresponds to static grid case. For moving grid, the error values tend to increase with increasing grid speeds and are higher compared with static grid. However, slope of the error curve reduces at higher speeds making error to stabilize and not to increase with further increase in grid velocities.

During motion of mesfhree cloud, *grid update* calculations are required to be carried out continuously during the simulation. *Grid update* step includes following operations:

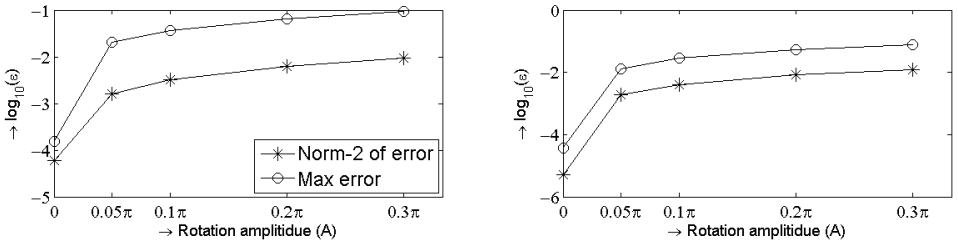

(a) u-error (b) p-error

Figure 6.13: Error Plots at different angular speeds of rotating meshfree grid at t=0.5 (*-RMS error, o-Max error)

1. Re-categorization of meshfree nodes according to their current location (in active or inactive zone).
2. Reallocation of neighbouring particles.
3. Recalculation of RBF weights for meshfree particles which have static nodes in their neighbourhood.

Grid update is particularly important for nodes laying close to meshfree-Cartesian zone interface. However, this process requires extensive computational resources (in terms of computer memory and time) and is not considered viable after every iteration. Instead *grid update* can be performed after the grid has been displaced by a certain distance (say, Δd_{update}). Grid movement can be monitored by motion of a *reference node* to find out when *grid update* is necessary. For current test cases, the node at bottom left corner of meshfree zone is considered as *reference node*. During simulation, displacement of a this node is continuously monitored and *grid update* calculations are performed when the *reference node* has been displaced by distance Δd_{update}. In order to determine the effect of *grid update distance* on accuracy of solution, moving grid case with $\mathbf{A} = 0.3\pi$ is run for two different values of Δd_{update}. First case is run for $\Delta d_{update} = 0.5h$ and second test is run for $\Delta d_{update} = 0.05h$, where h is the space step. Time profiles of RMS error for pressure values are shown in Figure 6.14. A reference case is also run in which grid was updated after every iteration. RMS error profile for reference is also co-plotted as dotted line. For $\Delta d_{update} = 0.05h$ and $\Delta d_{update} = 0.5h$, each grid update is followed by a spike in the error profile. These spikes are caused by variation in RBF weights for calculating spatial derivatives. The spikes are more pronounced for larger values of Δd_{update}. When the grid is updated less frequently during simulation (as in case of larger *grid update distance*), RBF weight values experience larger variation after update and resulting spikes are more pronounced. A reasonable value of *grid update distance* is therefore necessary as very high spike can even lead to instabilities. However, as long as *grid update distance* is kept within reasonable range, changing its value is not found to significantly affect time averaged error values.

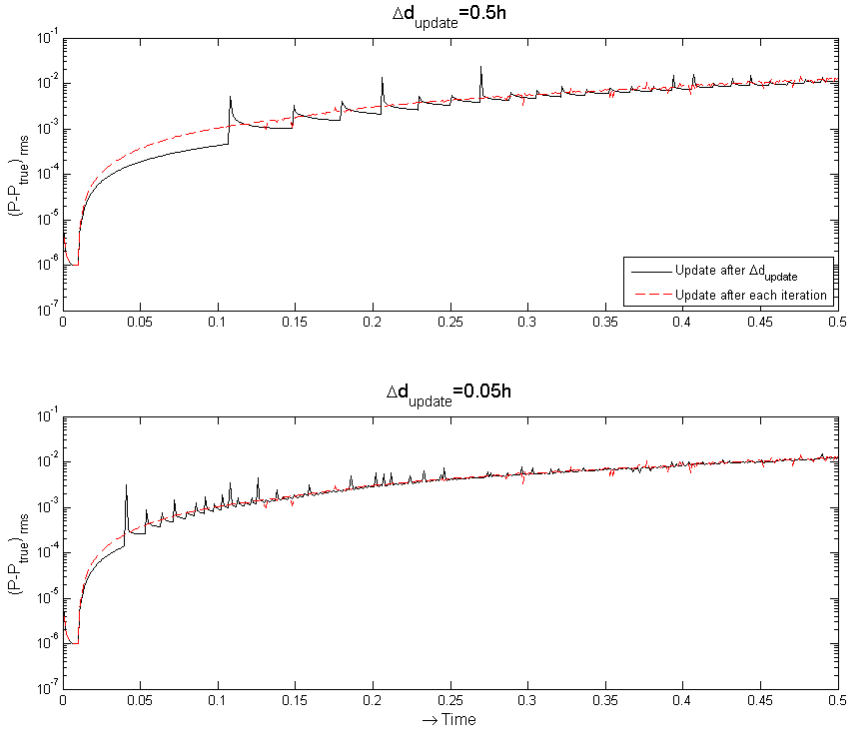

Figure 6.14: Time profiles of RMS error for pressure values at different *grid update distance* Δd_{update}

6.6 Flow around cylinders

The solution scheme has been used for flow around cylindrical objects. For this purpose, steady and unsteady flows around static cylinder and flow around vertically vibrating cylinder have been studied. Flow Reynolds number is defined as $Re = \rho U D/\mu$, Where ρ is the fluid density, U is the free stream velocity, D is the diameter of the cylinder and μ is the dynamic viscosity of the fluid. The detail of each case is described below.

6.6.1 Flow around static cylinder

Flow around static cylinder has been solved using implicit RBF-FD solution scheme over hybrid fluid grid. Steady flow cases are run at $Re = 10,\ 20$ and 40 and unsteady cases are run at $Re = 100$ and 200. The results are compared with standard solutions from previous studies (Dennis and Chang (1970); Takami and Keller (1969); Tuann and Olson (1978); Braza et al. (1986); Ding et al. (2004); Liu et al. (1998)). The purpose of running static cylinder cases is to establish the accuracy of presented solution scheme over hybrid grid before moving on to moving boundary cases. For present work, a rectangular fluid domain is chosen with dimensions $38D \times 12D$. Center of the cylinder is located at a distance of $8D$ from inlet and $6D$ from each of the side walls. This ensures

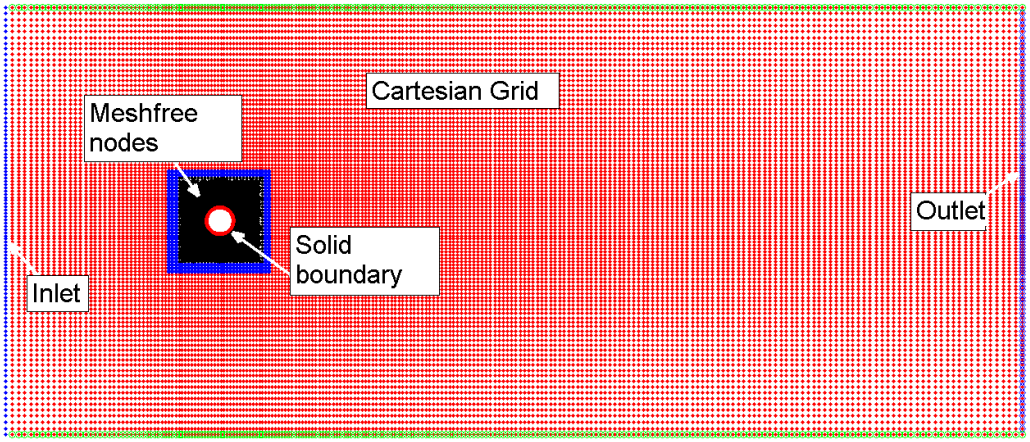

(a) Full domain

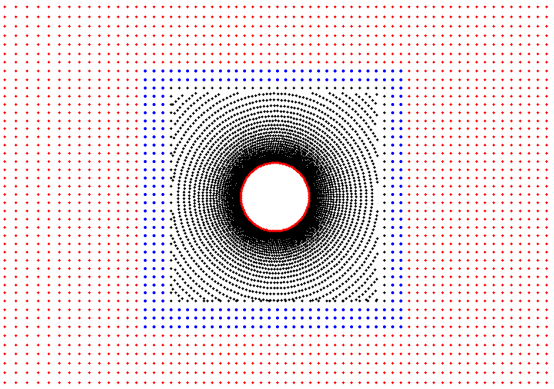

(b) Closed up view of meshfree-Cartesian juncture

Figure 6.15: Computational domain around static cylinder. Hybrid fluid grid is generated with meshfree cloud of size $3D \times 3D$ around the cylinder

that the flow remains unaffected by any non-physical disturbance at domain boundary. Meshfree cloud spans $3D \times 3D$ around the cylinder. Remaining fluid domain is meshed with a Cartesian grid. Therefore, meshfree zone constitutes only 1.974 percent of the total domain area. Figure 6.15(a) shows the meshed domain around the cylinder. In meshfree zone, nodes are arranged radially around the cylinder. A total of 140 nodes are placed at solid boundary. There are total of 4122 meshfree nodes and 21500 Cartesian nodes in the hybrid grid. A closed up view of juncture of meshfree and Cartesian zones is shown in Figure 6.15(b). As this is a static problem, meshfree cloud is not required to move during simulation. Therefore, overlapped part of meshfree zone is not needed for this problem (though presence of overlapped inactive meshfree nodes will not make any difference).

Boundary conditions are applied as mentioned in Section 5.5. In order to implement Neumann pressure boundary conditions at solid boundary, orthogonal nodal arrangement is required at least in two nodal layers immediately after the boundary. Therefore, special care has been taken to ensure that nodes are arranged orthogonally in immediate

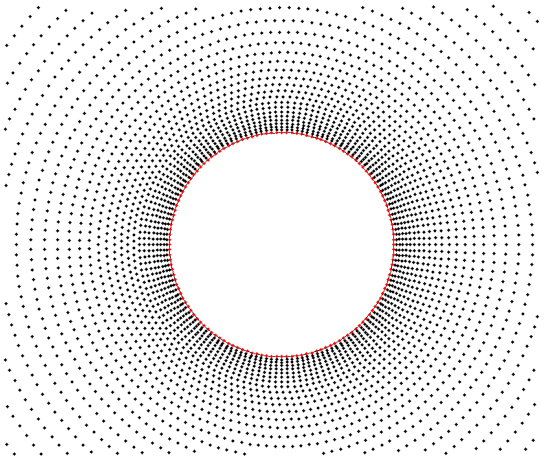

Figure 6.16: Arrangement of meshfree nodes around circular solid

Table 6.5: Solution parameters (separation angle θ_{sep}, length of recirculation region L_{sep} and drag coefficient C_D) for steady flow around static cylinder at Re =10, 20 and 40

Re	10			20			40		
Source	θ_{sep}	L_{sep}	C_D	θ_{sep}	L_{sep}	C_D	θ_{sep}	L_{sep}	C_D
Dennis and Chang (1970)	29.6	0.265	2.85	43.7	0.94	2.05	53.8	2.35	1.52
Takami and Keller (1969)	29.3	0.249	2.80	43.7	0.935	2.01	53.6	2.32	1.54
Tuann and Olson (1978)	29.7	0.25	3.18	44.1	0.9	2.25	54.8	2.10	1.68
Present case (Hybrid)	28.6	0.280	3.09	44.1	0.95	2.19	53.13	2.18	1.63
Present case (Full meshfree)	-	0.250	2.86	-	0.90	2.06	-	2.40	1.60

layers around the cylinder as shown in Figure 6.16. Time step is kept as 5×10^{-3} sec. Lift and drag forces (F_L and F_D) are calculated by integrating vertical and horizontal components of normal and shear stresses at the solid boundary using Eqs. (5.27) - (5.30).

Resultant velocity vector plots for steady flow cases are shown in Figure 6.17 for all the three Reynolds numbers. These plots are used to calculate separation angle (θ_{sep}) and length of recirculation region (L_{sep}). Figure 6.18 shows 3D plots of u-velocity over the entire domain. Vorticity profiles for steady state cases are shown in Figure 6.19. Resultant Drag coefficient C_D, separation angle (θ_{sep}) and length of recirculation region (L_{sep}) are shown in Table 6.5 along with the results from previous researches by Dennis and Chang (1970); Takami and Keller (1969) and Tuann and Olson (1978) at each Reynolds number. Results from present work show good agreement with previous solutions.

Unsteady flow cases are run at Reynolds numbers 100 and 200. Figure 6.20 shows velocity vector plots captured during simulation. 3D plots of u-velocity at same time instances are shown in Figure 6.21. However, these profiles keep changing as the flow is oscillatory in nature. Figure 6.22 shows the oscillating vortex profiles captured at

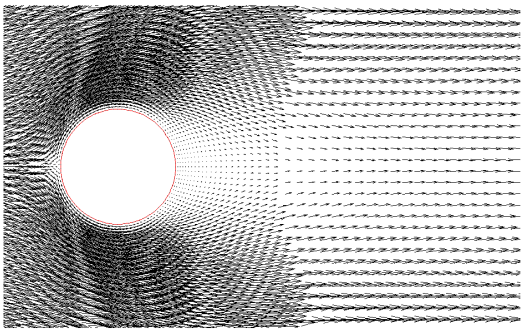

(a) $Re = 10$

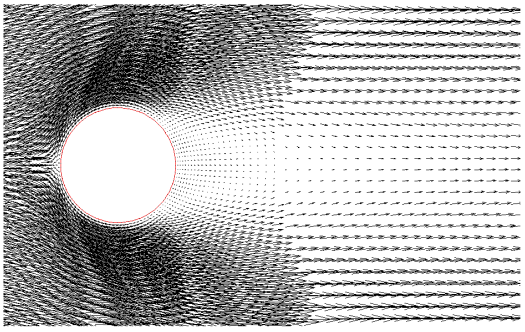

(b) $Re = 20$

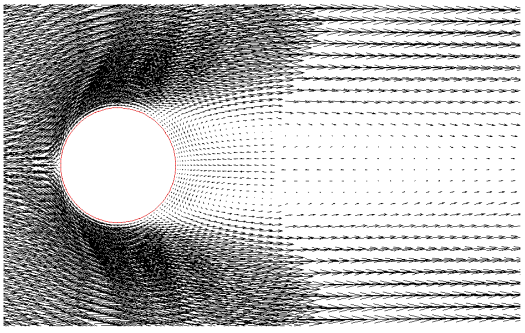

(c) $Re = 40$

Figure 6.17: Velocity vector plots around static cylinder for steady flow cases ($Re = 10,\ 20$ and 40).

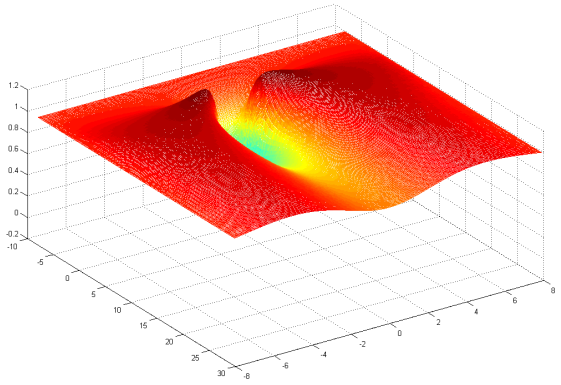

(a) $Re = 10$

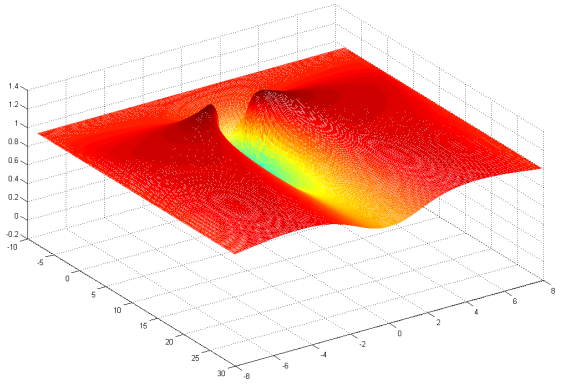

(b) $Re = 20$

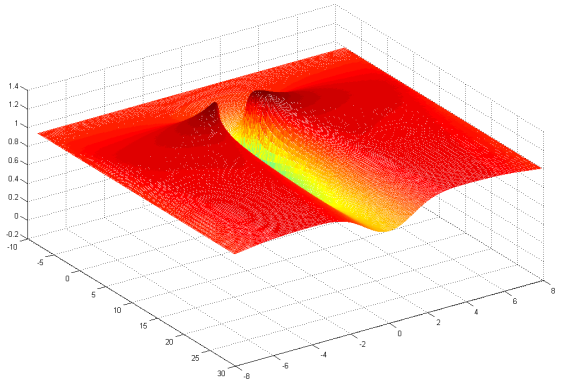

(c) $Re = 40$

Figure 6.18: 3-D profiles of u-velocity for steady flow cases ($Re = 10,\ 20$ and 40).

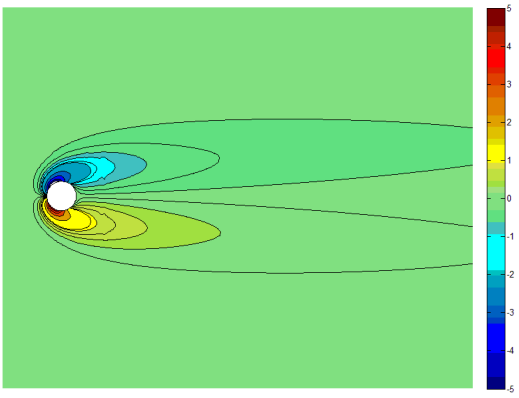

(a) $Re = 10$

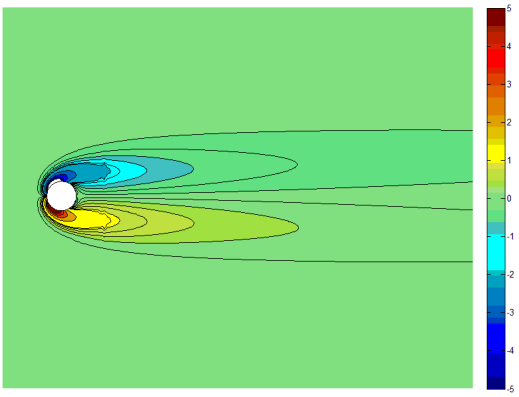

(b) $Re = 20$

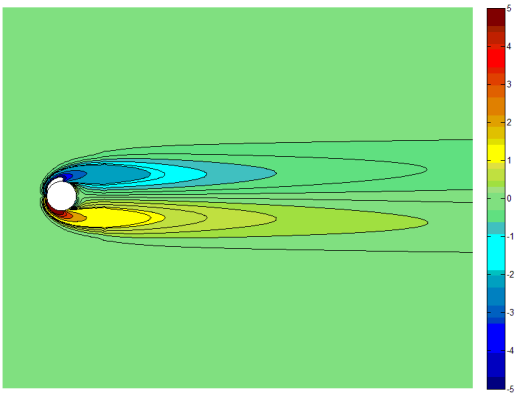

(c) $Re = 40$

Figure 6.19: Vorticity profiles for steady flow cases ($Re = 10,\ 20$ and 40).

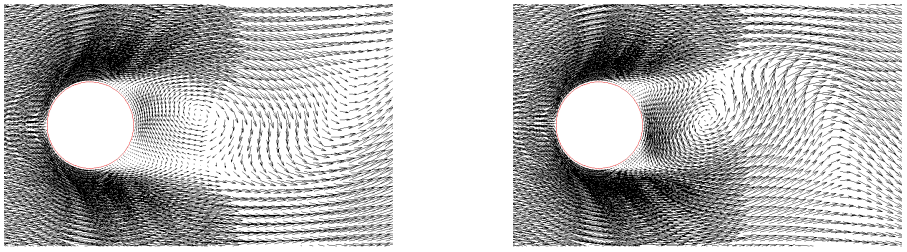

(a) $Re = 100$ (b) $Re = 200$

Figure 6.20: Velocity vector plots around static cylinder for unsteady flow cases ($Re = 100$ and 200).

various time instances during a complete vortex shedding cycle at $Re = 100$. Similar plots for $Re = 200$ are shown in Figure 6.23. The vortex profiles shown here are similar to those obtained from previous studies by Placzek et al. (2009) (at $Re = 100$) and Liu et al. (1998) (at $Re = 200$). The vortex plots from previous studies are shown in Figures 5.18 and 5.20 respectively.

The oscillatory flow results in corresponding fluctuation in lift and drag forces over time. Variation of C_L and C_D has therefore been plotted against time in Figures 6.24 and 6.25 for $Re = 100$ and 200, respectively. It can be observed that magnitude of lift and drag coefficients and frequency of oscillation tend to increase with the increase in Reynolds number. At both Reynolds number, frequency of oscillation of drag coefficient is twice the corresponding oscillation frequency of lift coefficient. Frequency of oscillation can be represented in terms of Strouhal number ($St = fD/U$, where f is vortex shedding frequency) which is equal to the vortex shedding frequency in case of non-dimensionalized length and time parameters. Therefore, Strouhal number can directly be acquired by frequency of oscillation of C_L versus time plot. The numerical solutions have been verified by comparing the resultant values of lift and drag coefficients and Strouhal number with results of previous researchers, as shown in Table 6.6 and are found to be in good agreement.

6.6.2 Computational performance test

It is understood that meshfree methods are computationally more expensive due to several reasons which include calculation of weights or kernels (often necessitating square root and matrix inversion operations) and requirement of larger number of neighbouring particles to ensure required order of accuracy as discussed by Wright and Fornberg (2006). Larger number of neighbouring particles results denser coefficient matrices which require more number of calculation operations to be solved (Fornberg (1980)).

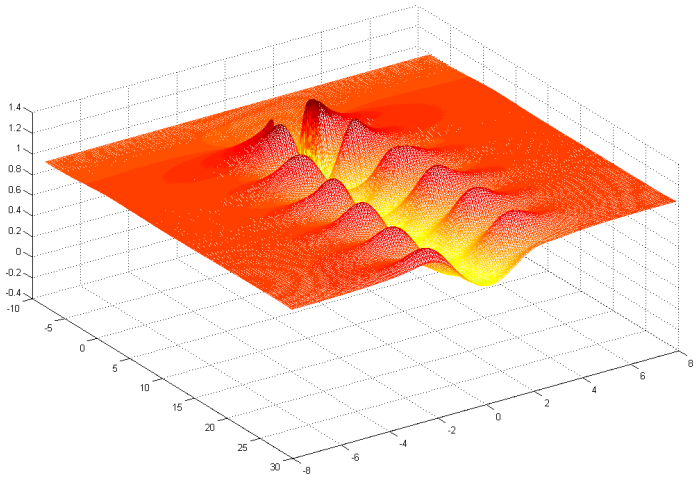

(a) $Re = 100$

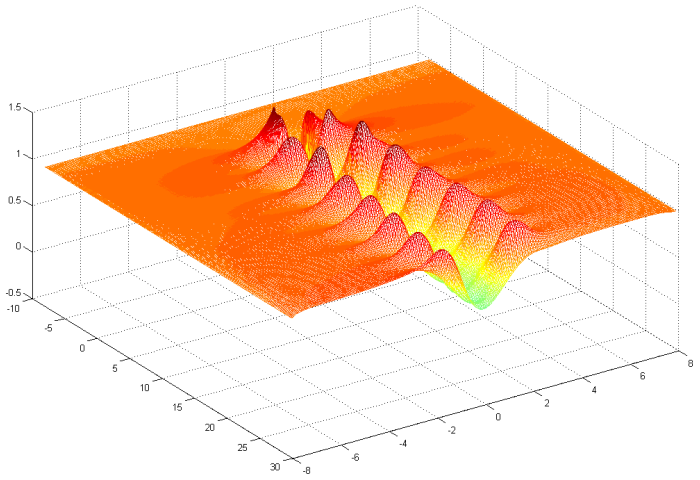

(b) $Re = 200$

Figure 6.21: 3-D profiles of u-velocity for unsteady flow cases (Re = 100 and 200).

Table 6.6: Solution parameters (lift coefficient C_L, drag coefficient C_D and Strouhal number S_t) for unsteady flow around static cylinder at Re =100 and 200

Re	100			200		
Source	C_L	C_D	S_t	C_L	C_D	S_t
Braza et al. (1986)	±0.25	1.364±0.015	0.16	±0.75	1.40±0.05	0.2
Ding et al. (2004)	±0.28	1.32±0.008	0.164	±0.60	1.327±0.045	0.196
Liu et al. (1998)	±0.34	1.35±0.012	0.164	±0.69	1.31±0.049	0.192
Present case (Hybrid)	±0.32	1.314±0.009	0.164	±0.62	1.302±0.039	0.194
Present case (Full meshfree)	±0.32	1.344±0.011	0.165	±0.77	1.395±0.07	0.20

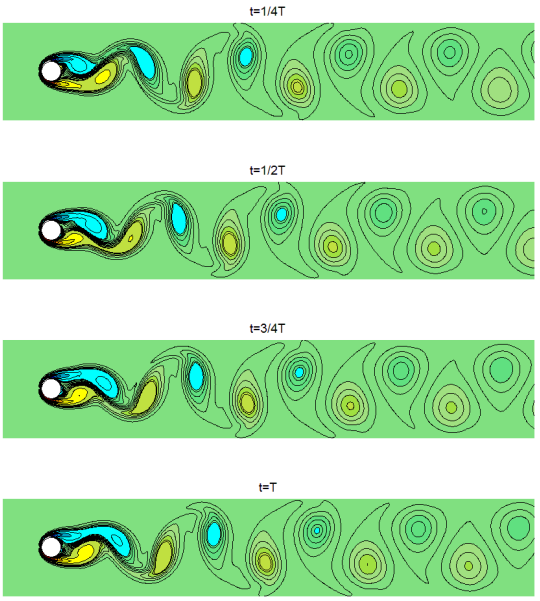

Figure 6.22: Screen-shots of oscillating vortex profiles behind static cylinder captured at various time instances during a single cycle at $Re = 100$

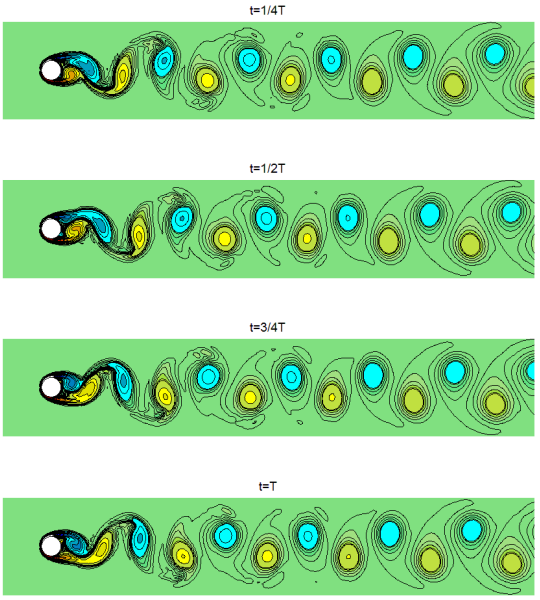

Figure 6.23: Screen-shots of oscillating vortex profiles behind static cylinder captured at various time instances during a single cycle at $Re = 200$

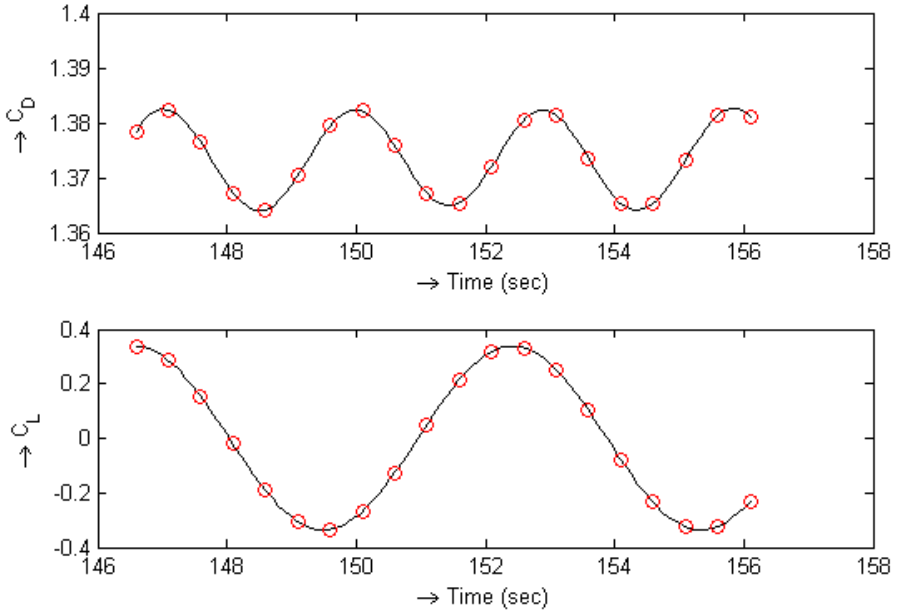

Figure 6.24: Variation of lift and drag profiles with time at $Re = 100$

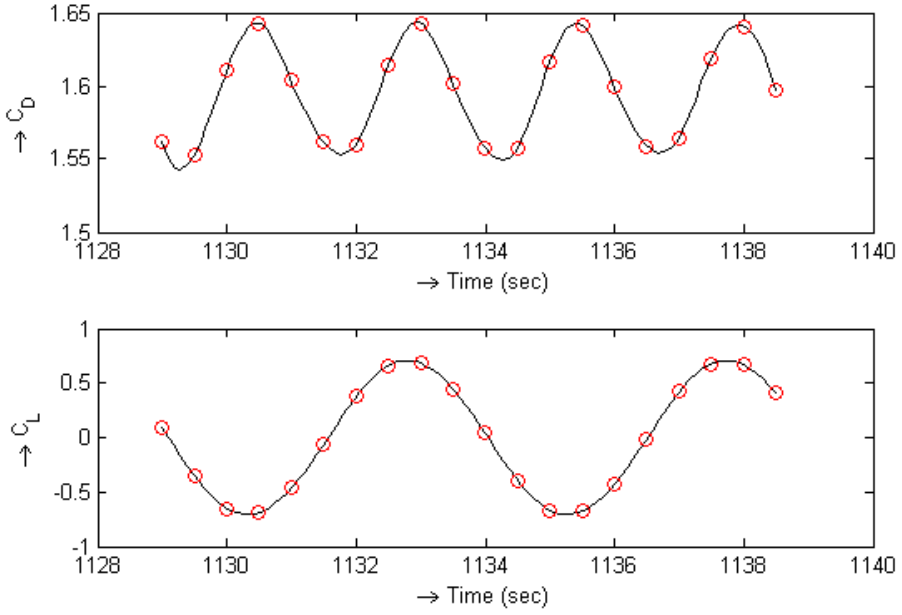

Figure 6.25: Variation of lift and drag profiles with time at $Re = 200$

The tests have been conducted here to study the variation of computational time with changing size of meshfree zone in hybrid grid. For this purpose, flow around static cylinder has been solved at $Re = 100$ over hybrid grid. Various test cases are run with different sizes of meshfree zone in fluid domain. The size of meshfree zone is gradually increased for every subsequent test case to study the effect on computational performance (calculation time) of the solver.

Computation time of first 500 iterations has been noted for different sizes of meshfree domain. The size of active meshfree zone is varied from $2D \times 2D$ (containing 2116 nodes) to $6D \times 6D$ (containing 11011 nodes) for different test cases. Changing the size of meshfree zone therefore varied the percentage number of meshfree nodes in the entire computational domain. Variation of computation time with changing percentage of meshfree nodes is plotted in Figure 6.26(a). Increasing the proportion of meshfree nodes from 10.5% to 36.5% actually increased the computational cost by 2.3 times. However, during this change, computation time of meshfree solver only, increased by as much as 9.5 times approximately. This increase in computation time is caused by increasing orders of coefficient matrices which happen to be more resource intensive during solution process. In order to find average increase in computational time for each node, a plot of average calculation time by each computational node, in a single iteration, is shown in Figure 6.26(b). It can be observed that average computational time by each meshfree node increases by enlarging the meshfree zone. On the contrary, average computation time of Cartesian nodes stays constant and significantly lower than their meshfree counterparts. Therefore, computationally efficient configuration would entail smaller sized meshfree zone in the entire domain.

6.6.3 Flow around vertically oscillating cylinder

These test cases are run to solve flow around cylinder which is forced to vibrate vertically with sinusoidal displacement profile over time. Vertical displacement $y(t)$ of the solid about its mean position is expressed as:

$$y(t) = Y \sin 2\pi f t \tag{6.4}$$

where Y is the amplitude of vibration and f is the frequency of vibration. As the cylinder vibrates, the body conformal meshfree nodal clouds also convects with it along vertical axis. In order to allow cylindrical oscillation, length of meshfree zone along vertical axis is extended. Therefore, the size of meshfree zone around the cylinder is kept as $3D \times 5D$ for this case. Flow Reynolds number is set as 100. As mentioned before, periodic Kamran vortices are generated behind the cylinder at this Reynolds number. Therefore, problem is often characterized by frequency ratio $F = f/f_s$, where f_s is the vortex shedding frequency.

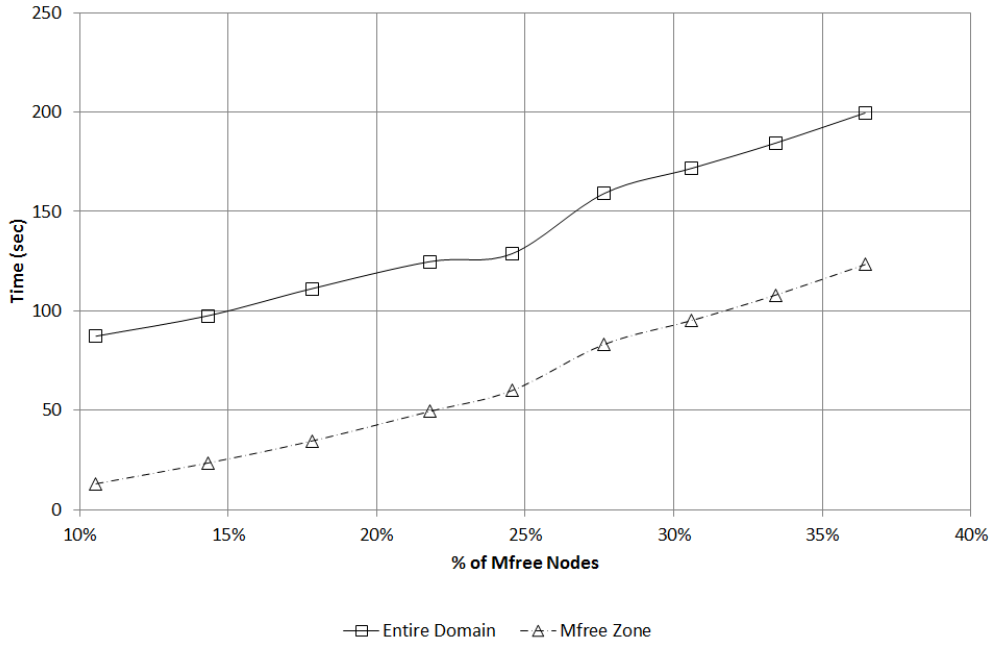

(a) Total computation time

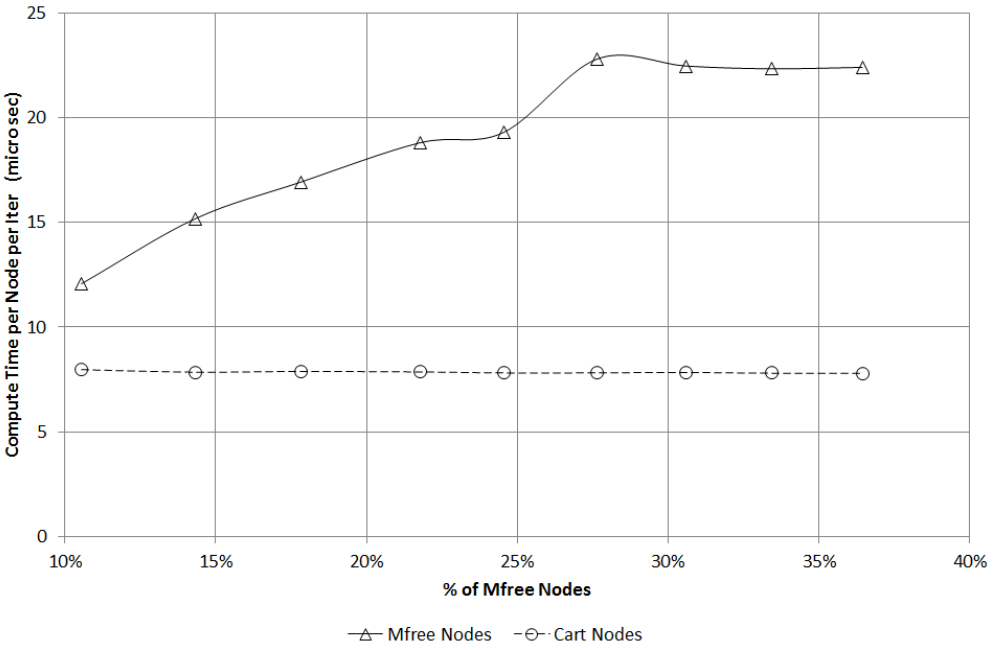

(b) Average computation time per node

Figure 6.26: Computational performance with changing size of meshfree zone. Calculation time of first 500 iteration for flow around static cylinder at $Re = 100$

An important characteristic of these test cases is the presence of lock-in zone which is defined as the domain of frequency ratios (F) and displacement amplitudes (Y), where vortex shedding frequency deviates from its original value and becomes equal to forced frequency (Nobari and Naderan (2006)). Koopmann (1967) performed extensive experiments for flow around vibrating cylinder at low Reynolds numbers and determined the bounds of this lock-in region on a (Y,F) plane. In current work, the computations are performed for vibration amplitude of $Y = 0.25D$ and range of forced frequencies (f) which correspond to different values of frequency ratios (F). Presence of lock-in zone can be identified by spectral analysis of time profile of lift coefficient. Time profiles of lift coefficients and corresponding power spectral density (PSD) plots, for $F = 0.90$ and $Y/D = 0.25$ are shown in Figure 6.27(a). Similar plots for $F = 1.10$ and $Y/D = 0.25$ are shown in Figure 6.27(b). In both the cases, vortex frequency equalizes with frequency of forced oscillation. As a result, Lift-time curves are purely sinusoidal and PSD plots show single peaks. These cases are therefore classified as 'locked-in' cases.

On the contrary, in unlocked configuration, vortex shedding frequency retains its identity. As a results, lift fluctuation profiles over time deviate from their pure sinusoidal behaviour (Placzek et al. (2009)) due to presence of multiple frequencies. For such cases, PSD plots of lift versus time curves also show two distinct peaks at frequencies f and f_s separately. The results for unlocked configurations are shown in Figure 6.28. Results for $F = 0.5$ are shown in Figure 6.28(a) and those for $F = 1.50$ are shown in Figure 6.28(b). Non-sinusoidal response of lift-time curves and separate peaks of forced as well as vortex shedding frequency on PSD plots are clearly visible in both the cases. Similar PSD plots were obtained by Placzek et al. (2009) during their study of flow around cylinders with forced oscillation at same parameters. Resultant plots obtained by Placzek et al. (2009) are shown in Figure 6.29. Presence of single and double peaks for locked and unlocked configurations is visible in the plots.

The phase portraits for 'locked-in' configuration are shown in Figures 6.30(a) and 6.30(b) for $F = 0.90$ and $F = 1.10$ respectively. The pure sinusoids of lift versus time results in regular elliptically shaped $y(t)$ vs C_L curve. Maximum lift coefficient is 0.4 in case of $F = 0.90$. However, maximum value of lift increases significantly and reaches to 0.74 for $F = 1.10$. Similar behaviour was observed by Placzek et al. (2009). For 'unlocked' configuration, lift-time profile no longer remains a sinusoid and a beating phenomenon is observed due to two different frequencies. As a result, phase portraits for un-locked configurations do not show a pattern with two absolute extremes. $y(t)$ vs C_L curves for $F = 0.50$ and $F = 1.50$ are shown in Figures 6.30(c) and 6.30(d) respectively.

Results from present simulations are also shown on (Y,D) plane and compared with the bounds of 'lock-in' zone identified by Koopmann (1967) in Figure 6.31. Present results agree well with experimental data of Koopmann (1967). Screen shots of vorticity profile of the flow ($Y = 0.25D,\ F = 0.50$) at various time intervals are shown in Figure 6.32. Similar vorticity profiles were obtained by Placzek et al. (2009) as shown in Figure 6.33.

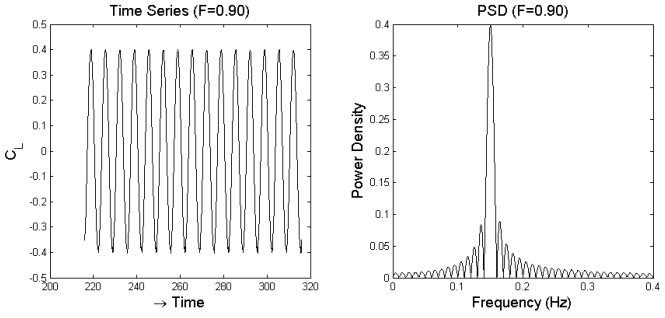

(a) Solution for F=0.90

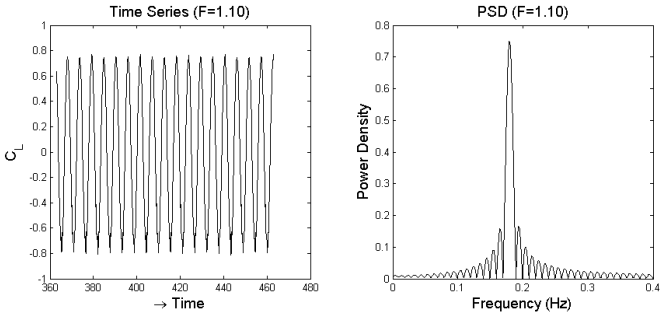

(b) Solution for F=1.10

Figure 6.27: Time series of lift coefficient (C_L) and Power spectral density (PSD) plots of fluctuating lift (locked configurations) for flow around vibrating cylinder with $Y/D = 0.25$ and $Re = 100$

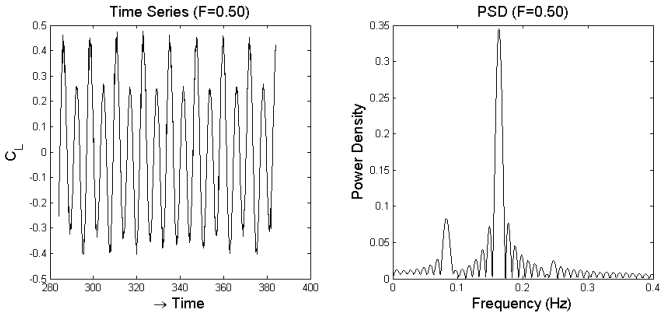

(a) Solution for F=0.50

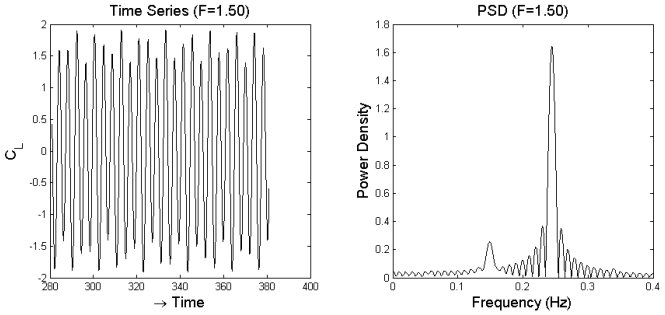

(b) Solution for F=1.50

Figure 6.28: Time series of lift coefficient (C_L) and Power spectral density (PSD) plots of fluctuating lift (unlocked configurations) for flow around vibrating cylinder with $Y/D = 0.25$ and $Re = 100$

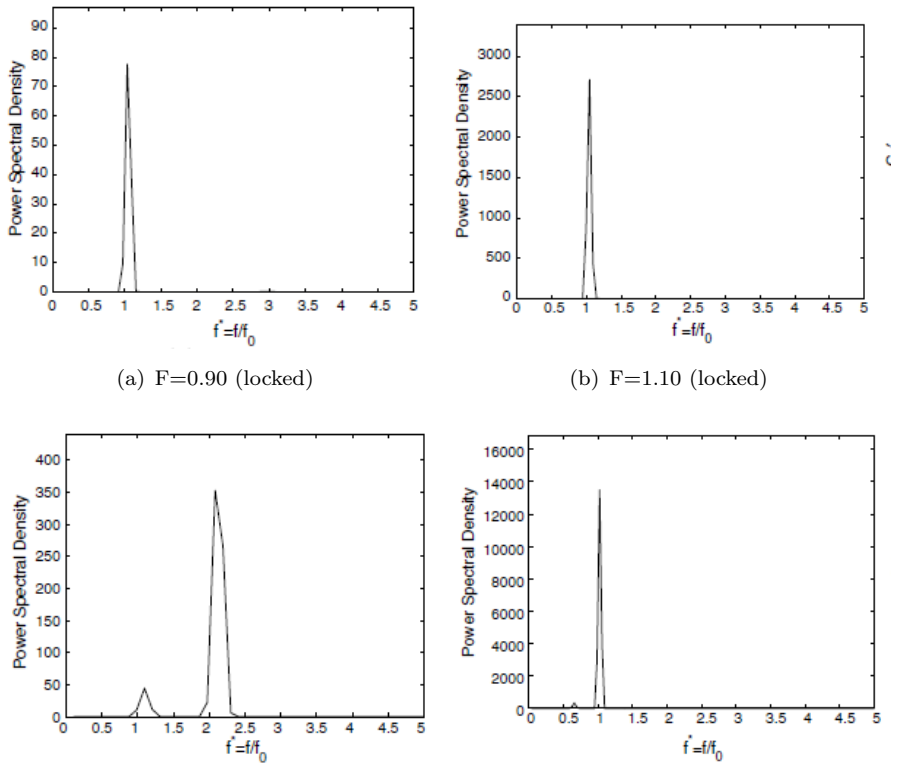

(a) F=0.90 (locked)

(b) F=1.10 (locked)

(c) F=0.50 (unlocked)

(d) F=1.50 (unlocked)

Figure 6.29: Power spectral density (PSD) plots of fluctuating lift (locked and unlocked configurations) for flow around vibrating cylinder obtained by Placzek et al. (2009) (at $Y/D = 0.25$ and $Re = 100$)

6.7 Flow around airfoil

The coupled solution scheme over hybrid grid is now used for solving flow around airfoil. Flow Reynolds number, for these problems is defined as $Re = \rho U c/\mu$ where ρ is the flow density, U is free stream velocity, c is the chord length and μ is the dynamic viscosity. Before moving for the solution of flow problems around airfoil, various aspects relating to grid generation and RBF influence domain are needed to be discussed. The description about these is given in Subsections 6.7.1, 6.7.2 and 6.7.3.

6.7.1 Generating hybrid grid around airfoil

For flow around airfoil, the movement of solid boundary is also accommodated using hybrid fluid grid approach as before. However, the meshfree nodes are arranged in C-mesh configuration around the airfoil. A typical hybrid grid around an airfoil is shown in Figure 6.34(a). Grid resolution is kept high close to the airfoil surface to accurately capture the boundary layer. For laminar flow, vortex characteristics near leading edge is also of great importance. Therefore, the nodal spacing is kept small near leading edge too. Nodal spacing is gradually increased as the distance from airfoil surface and

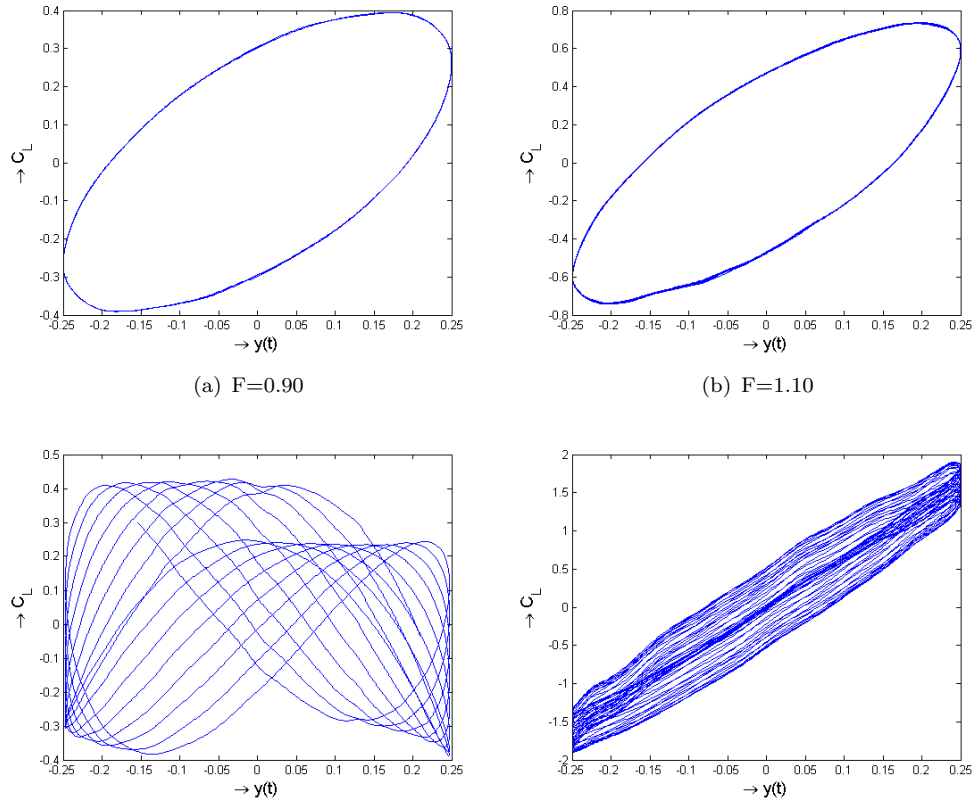

(a) F=0.90 (b) F=1.10

(c) F=0.50 (d) F=1.50

Figure 6.30: Phase portraits ($y(t)$ vs C_L plots) for flow around vibrating cylinder with $Y/D = 0.25$ and $Re = 100$.

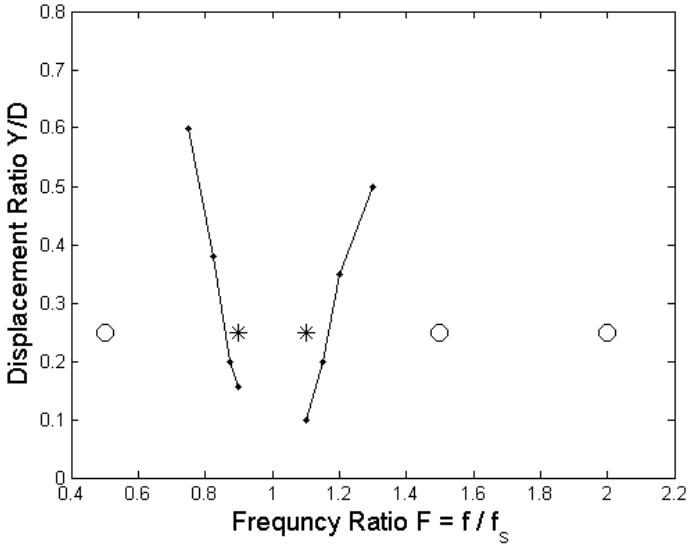

Figure 6.31: Bounds of Lock-in zone at $Re = 100$ (.- Experimental data of Koopmann (1967), o 'Unlocked' results in present work, * 'Lock-in' results in present work)

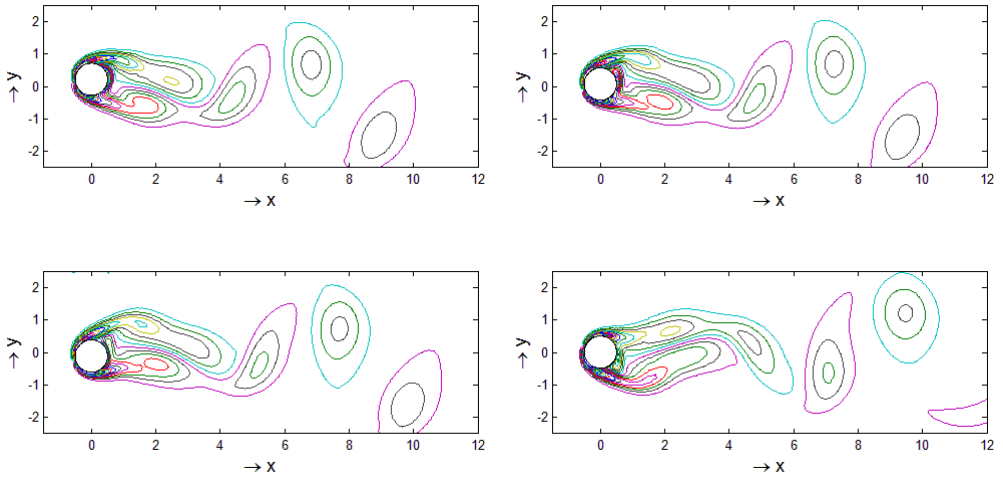

Figure 6.32: Vorticity profile at different time instances around vibrating cylinder at $Re = 100$ (Y=0.25D, F=1.50)

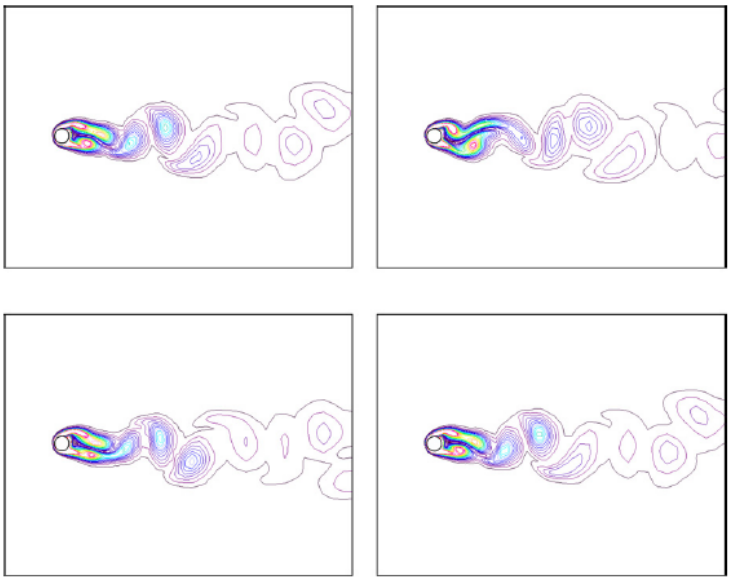

Figure 6.33: Vorticity profiles around cylinder oscillating at $Re = 100$, $Y = 0.25D$, $F = 1.5$ obtained by Placzek et al. (2009)

leading edge is increased. Moreover, in order to apply Neumann boundary conditions for pressure, nodal layers next to the solid surface are kept orthogonal. Closed in views of grid at leading and trailing edges are shown in Figures 6.34(b) and 6.34(c) respectively. It can be observed in Figure 6.34(c) that the two layers of nodes originating from the tip of the trailing edge are very close to each other compared to the other layers. This sudden non-uniformity in nodal spacing may cause instabilities in the solution. Therefore, one of the layers (shown with green colour) is de-activated. This means that the nodes in that layer will be treated as the nodes of 'inactive zone'. This will ensure uniformity in nodal distribution.

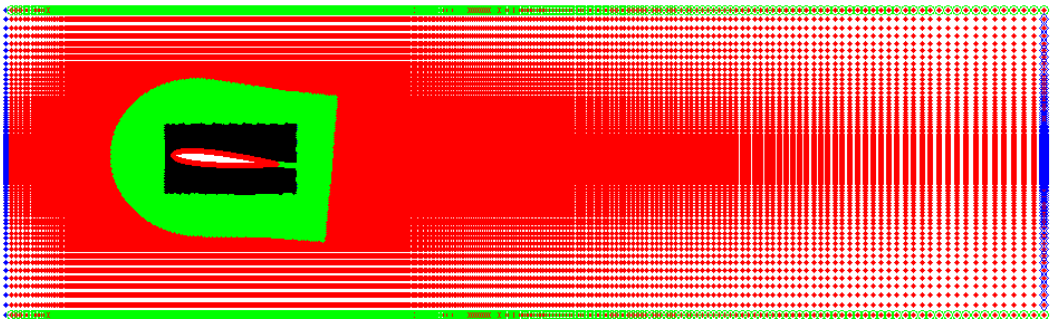

(a) Full domain

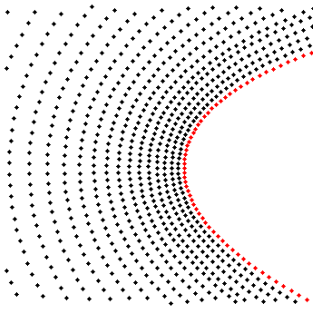

(b) Leading edge

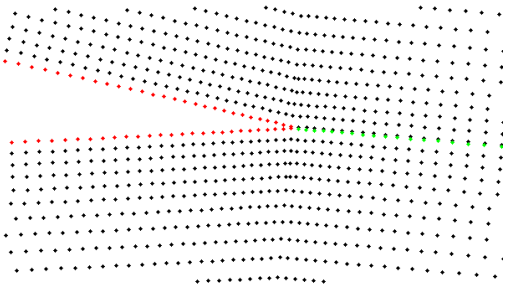

(c) Trailing edge

Figure 6.34: Hybrid grid around airfoil

6.7.2 Adaptive sizing of RBF influence domain

Accuracy of RBF based schemes largely depends on the well conditioning of interpolation matrix (Kansa (1990)). In fact, condition number of interpolation matrix for RBFs grows with increasing the number of computational nodes participating in derivative approximation at a certain point (Schaback (1995)). Larger number of particles, participating in RBF interpolation, will also require more number of arithmetic operations for single derivative approximation. Therefore in local RBF, the solution process tends to be computationally intensive with more number of neighbouring particles taking part in derivative approximation at point of interest. At the same time, requirement of sufficient number of collocation data points in the influence domain cannot be subdued to ensure accurate derivative approximation using local RBFs (De Rosis et al. (2013)). It is therefore important to keep suitable number of particles in the influence domain of every computational node. In practice, this is achieved by specifying size of the influence domain. However, for problems relating to flow around airfoil, the grid resolution changes significantly to accurately capture flow parameters near the surface. Therefore, a constant domain size will either place too many neighbouring particles in the influence domains closer to the airfoil or there will be too less neighbouring particles around nodes in low nodal density region. In order to overcome this, adaptive sizing of influence domain has been introduced. For this purpose, the size of influence (or neighbourhood)

domain for each node is selected based on the nodal density around it. An iterative algorithm is used to calculate the radius of influence domain around every node which encompass 25 to 35 neighbouring particles. The aim is to make sure that every node has enough number of neighbouring particles for accurate derivative approximation (using local RBF) and, at the same time, number of neighbouring nodes is not too high to render the interpolation matrix ill-conditioned or the process inefficient. This results in smaller sized neighbourhood domains around the nodes lying in high nodal density regions and vice versa. Adaptive domain sizing applied to a typical grid around airfoil is shown in Figure 6.35. The domain size progressively becomes larger as we go away from the airfoil to accommodate required number of neighbouring particles in coarser grid zones.

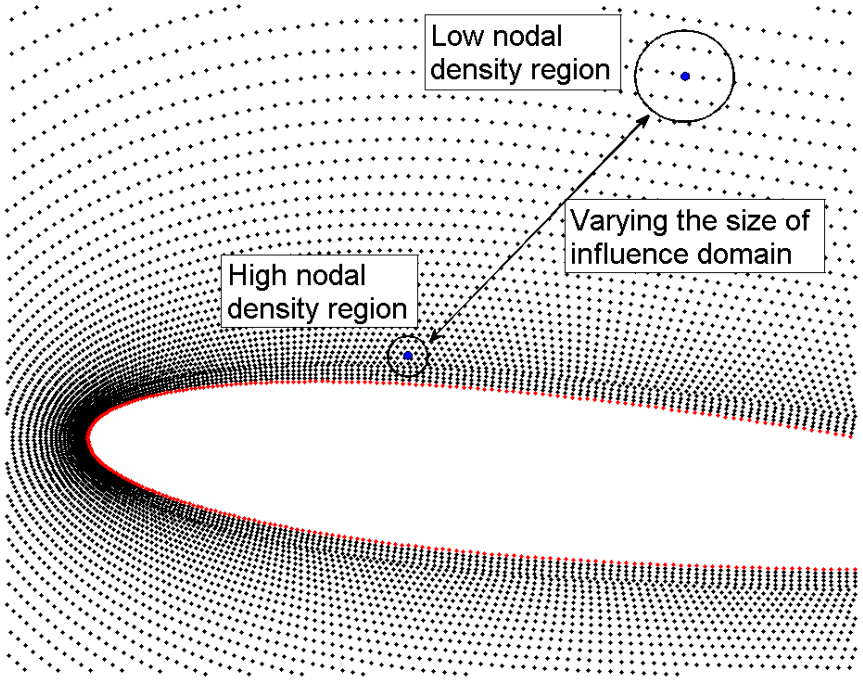

Figure 6.35: Adaptive sizing of influence domain applied to grid around airfoil

Effect of changing the number of neighbouring particles on conditions number of RBF matrix is investigated using one dimensional nodal arrangement. For this purpose, an array of nodes located between $0 \leq x \leq 10$ are considered. Nodal spacing is progressively reduced from edges to centre ($x = 5$). Therefore, if RBF domain size is kept fixed, number of neighbouring particles can vary significantly across the length. However, if the domain size is varied corresponding to the nodal spacing, large variation in the population of neighbouring particles can be avoided. Figure 6.36(a) shows variation in number of neighbouring particles for fixed and adaptive domain sizes. At each point, RBF matrix is formulated and its condition number is evaluated. Figure 6.36(b) shows variation of condition number of RBF matrix at different spatial locations for both fixed and adaptive domain sizing. Improvement in condition number of coefficient matrices is

obvious with the use of adaptive sizing. With increasing nodal density, total number of neighbouring particles increases for fixed domain sizing. This results in enormously high condition number in refined grid region. On the contrary, adaptive domain sizing ensures only the required number of neighbouring particles thus maintaining well conditioned matrices all over the domain.

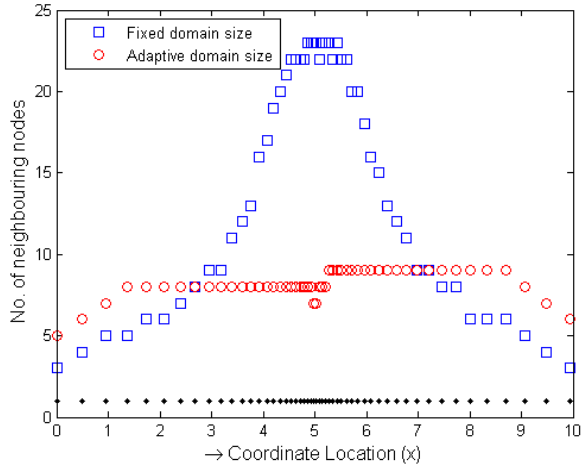

(a) Variation in number of neighbouring particles

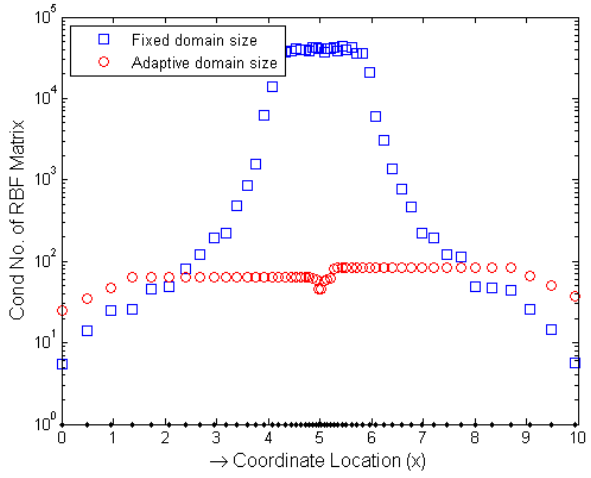

(b) Variation of Condition Number

Figure 6.36: Fixed and Adaptive sizing applied to 1-dimensional non-uniform particle distribution

6.7.3 Treatment of RBF influence domain near trailing edge

An important aspect to be considered here is the treatment of influence domain for meshfree nodes near trailing edge of the airfoil. At trailing edge, the airfoil surface becomes more like a non-convex boundary. The surface acts as a discontinuity in the flow domain in such cases and nodes on either sides of the boundary (upper and lower

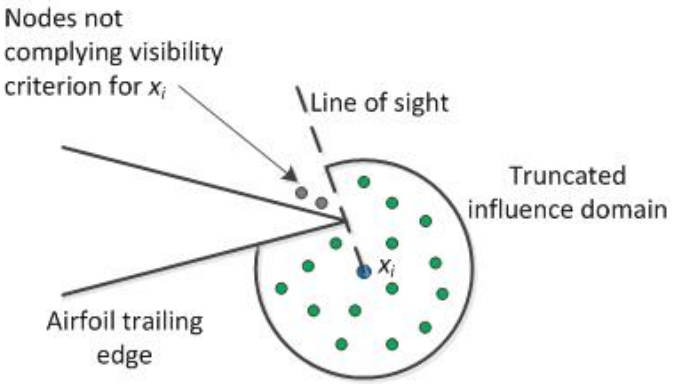

Figure 6.37: Influence domain truncated as per visibility criterion near trailing edge of airfoil

airfoil surfaces) actually cast minimal influence on flow field parameters on the nodes on opposite side. However, the spatial distance between the nodes on opposite sides is not large enough to diminish their effect through usual numerical treatment which relies on distance based function (like RBF). Therefore, special treatment is needed to have reduced effect due to presence of non-convex boundary. For current work, the influence domains for such nodes are modified as per visibility method by Belytschko et al. (1994). According to this, the influence domain of any meshfree node x_i is truncated in such a manner that only those neighbouring nodes fall in the influence domain which can be linked with x_i through a straight line without intersecting the boundary. Influence domain truncated in this manner is shown in Figure 6.37.

6.7.4 Flow around airfoil in prescribed pitch and heave motion

Application of coupled meshfree and mesh-based solver is investigated here for an airfoil in simultaneous pitch and heave motion. In present study, numerical tests are conducted for flow around NACA0015 airfoil which has been subjected to prescribed pitching and heaving motion defined as:

$$\theta(t) = \theta_0 \sin(\omega t) \tag{6.5}$$

$$h(t) = H_0 \sin(\omega t + \phi) \tag{6.6}$$

where θ_0 and H_0 are maximum pitch and heave amplitudes and ϕ is the phase difference between pitch and heave motion. The tests are conducted at $Re = 1100$. The flow is predominantly laminar at this Reynolds number. Heave amplitude is fixed at $H_0/c = 1.0$ and phase difference $\phi = -\pi/2$ is used. The problem is set up in a way that heave reference frame is attached with the airfoil. In this manner, the airfoil performs pitching motion in a heaving reference frame. The heaving displacement is therefore, not imparted

to the moving mesh. Similar tests were conducted by Kinsey and Dumas Kinsey and Dumas (2008).

Grid configuration is the same as in Figure 6.34(a), while closer views of meshfree nodal arrangement near the airfoil surface are shown in Figures 6.34(b) and 6.34(c) respectively. The Airfoil is placed at a distance of $4c$ from inlet and $12c$ from outlet. Width of fluid domain is set as $10c$. Dimensions of active meshfree zone around airfoil are set as $1.35c \times 1.6c$. A total of 300 nodes are placed at airfoil surface. Computational domain comprises of a total of 25880 meshfree and 65354 Cartesian nodes. The movement of mesh is accomplished by displacing the meshfree zone according to prescribed pitching motion. The problem is set up in heave reference frame. Therefore, heave displacement is imparted to the moving mesh. However, heave velocity does contribute in the vertical velocity of moving nodes when formulating momentum equation in ALE formulation. Similar strategy was used by Kinsey and Dumas (2008) in their work. Numerical simulations are carried out using two different parameters. First case is solved for $\theta_0 = 76.33^o$ and $\omega = 0.28\pi$. Second case is run for $\theta_0 = 60.0^o$ and $\omega = 0.36\pi$. Time step is set as $\Delta t = 5 \times 10^{-4}$ for both the cases.

Variation of heave and pitch displacements in a single oscillation period of airfoil, for $\theta_0 = 76.33^o$, $\omega = 0.28\pi$ case, is shown in Figure 6.38(a). Variation of aerodynamic forces during the same period is plotted in Figure 6.38(b). Vorticity profiles around the airfoil at different stages of periodic motion are shown in Figure 6.39. As the pitch angle is increased in the initial phase of oscillation, the lift achieves its maximum value. The flow remains largely attached with airfoil top surface for $t < T/8$ as shown in Figure 6.39(a). The first peak in lift profile appears at around $t = T/8$. Increasing lift also causes increase in pressure drag and therefore, drag coefficient also increases. This initial rise in lift is followed by flow separation close to leading edge as shown in Figure 6.39(b) and causes reduction in lift. During $T/4 \leq t \leq 3T/8$, airfoil is subjected to positive heave acceleration and rate of decrease in pitch angle is relatively low. In this situation, the separated flow from leading edge reattaches at trailing edge, as shown in Figure 6.39(c). As a results, airfoil quickly overcomes the stall like situation when the separated leading edge vortex re-attaches with top surface near trailing edge. The lift increases again and a second peak is observed at $t = 3T/8$. Subsequently, the leading edge vortex leaves the airfoil from trailing edge at around $t = T/2$ and moves further downstream. By this time airfoil is put in downward heave and pitch angle is also negative. Therefore, a sharp decline in lift is observed between $3T/8T/8$. The lift reduce to zero and then shows similar profile in negative direction. Similar results were obtained by Kinsey and Dumas (2008) during numerical simulation of flow around NACA0015 in simultaneous pitch and heave motion. Figure 6.40 shows instantaneous vortex profiles along with variation of aerodynamic forces during single oscillation period obtained by Kinsey and Dumas (2008). Mean value of drag coefficient $\bar{C}_D$ and maximum value of lift coefficient

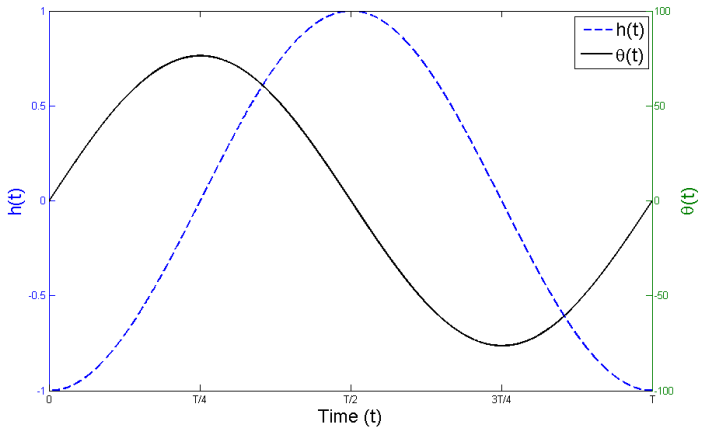

(a) Pitch and heave displacement

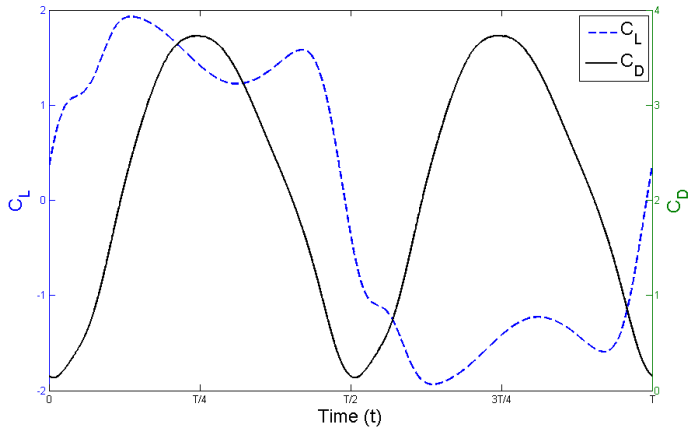

(b) Aerodynamic forces

Figure 6.38: Variation of pitch and heave displacements and aerodynamic force coefficients around NACA0015 for a single period of oscillation at $Re = 1100,\ \theta_0 = 76.33^o,\ \omega = 0.28\pi$

$\hat{C}_L$ calculated in current study are also compared with previous results in Table 6.7. Results found here are in good agreement with those found in previous studies.

6.8 Conclusion

RBF-FD is a highly flexible meshfree method which is known for accurate and efficient approximation of the derivatives of field variables over a scattered data points. However, like other meshfree methods, it lacks computational efficiency compared with the conventional mesh based methods. Hybrid grid approach attempts to circumvent the performance related limitations of meshfree methods by restricting their use to the locations where these methods can supersede their mesh-based counterparts due to their inherent features. The presented scheme works well for both stationary and moving

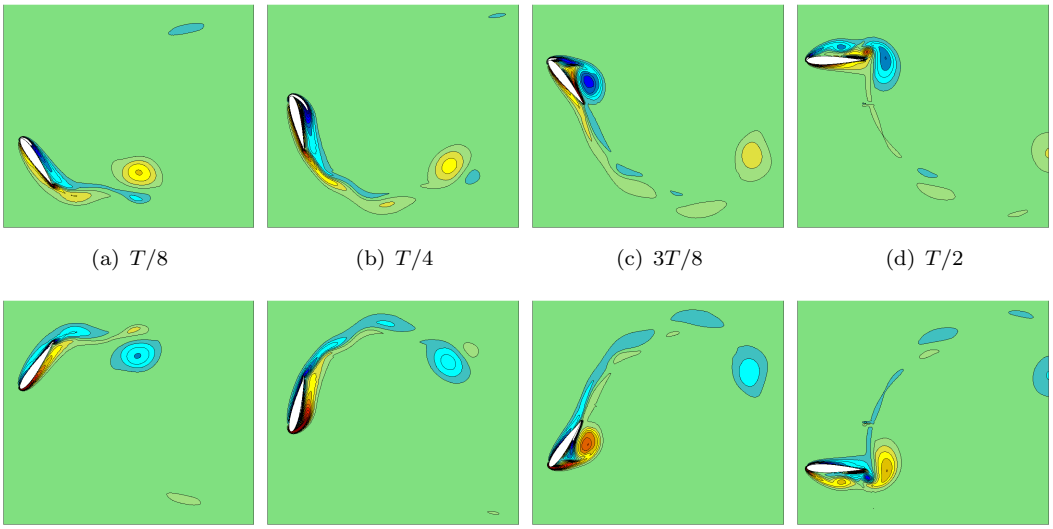

(a) $T/8$ (b) $T/4$ (c) $3T/8$ (d) $T/2$

(e) $5T/8$ (f) $3T/4$ (g) $7T/8$ (h) T

Figure 6.39: Instantaneous vorticity profiles around NACA0015 at $Re = 1100,\ \theta_0 = 76.33^o,\ \omega = 0.28\pi$

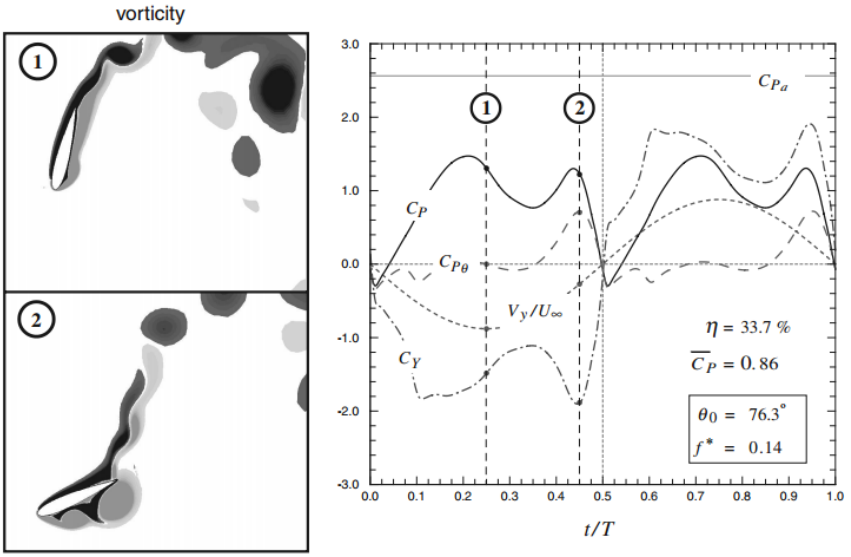

Figure 6.40: Results obtained by Kinsey and Dumas (2008). Instantaneous vorticity profiles and variation of aerodynamic forces during a single oscillation period around NACA0015 at $Re = 1100,\ \theta_0 = 76.33^o,\ \omega = 0.28\pi$

Table 6.7: Comparison of aerodynamic force coefficients for sinusoidally pitching and heaving motion of NACA0015 airfoil at $Re = 1100$ and $H_0 = c$

Source	$\bar{C_D}$	$\hat{C_L}$
Case-I: $\theta_0 = 76.33,\ \omega = 0.28\pi$		
Present	1.93	2.15
Kinsey and Dumas (2008)	2.014	1.91
Wu et al. (2014)	2.107	1.97
Case-II: $\theta_0 = 60.0,\ \omega = 0.36\pi$		
Present	0.72	1.238
Kinsey and Dumas (2008)	0.727	1.256
Wu et al. (2014)	0.711	1.248

boundary cases. Phenomenon of locking-in was accurately predicted during forced vibration cases. Resultant amplitudes and frequencies of solid vibration were found in good agreement with previous solutions. Significant reduction in computational time was achieved by limiting the size of meshfree zone in the domain. However, the size of active and inactive meshfree zone should still be large enough to allow the movement of the solid boundary. In case of multiple moving bodies, separate nodal clouds can also be formed around each moving body. For multiple degrees of freedom systems, dimensions of meshfree zone may accordingly be adjusted to accommodate movement of boundary in more than one direction. The hybrid grid scheme for static and moving solid objects has been presented in Javed et al. (2013b) and Javed et al. (2014a) respectively.

Chapter 7

A coupled FSI scheme on hybrid fluid grid

7.1 Background

As discussed in Chapter 1, partitioned methods are commonly used to deal with fluid-solid coupling. In this regard, closely coupled algorithms offer better stability and accuracy at interface boundaries. These algorithms perform several sub-iterations of fluid and solid solvers, to reach convergence at interface boundary, before moving on to the next time step. Closely coupled models are however often criticized for their complexity and inefficiency caused by increased number of computations during sub-iterations (Farhat et al. (2006)). It is however understood that convergence between fluid forces and solid deflection is required only at the fluid-solid interface for closely coupled system, for which the solution over near field flow is more significant. Therefore, considerable computational cost can be saved if far field flow region is excluded during sub-iteration process, and solution is sought only over near field flow region around the solid during sub-iterations. The flow solution over the entire fluid domain can be obtained only during the outer iteration while marching on to next time step. Using this approach, yhe gain in computational performance can be far more pronounced than loss of accuracy in the bargain by excluding the far field grid during sub-iterative solutions.

In view of the foregone, a closely coupled FSI algorithm is presented, for flow induced vibration problems, which attempts to reach convergence at fluid-solid interface using only near field flow during inner (or sub) iterations. Closed coupling between fluid and structural solvers has been achieved by performing a sub-iterative predictor-corrector algorithm, within each time step, until mutual convergence is reached between fluid forces and solid deflections, at fluid-structure interface. The fluid grid is represented by a hybrid grid as explained in Section 6.2. Use of hybrid grid makes it simpler to exclude far field flow during sub-iterations as the flow equations are already being solved using

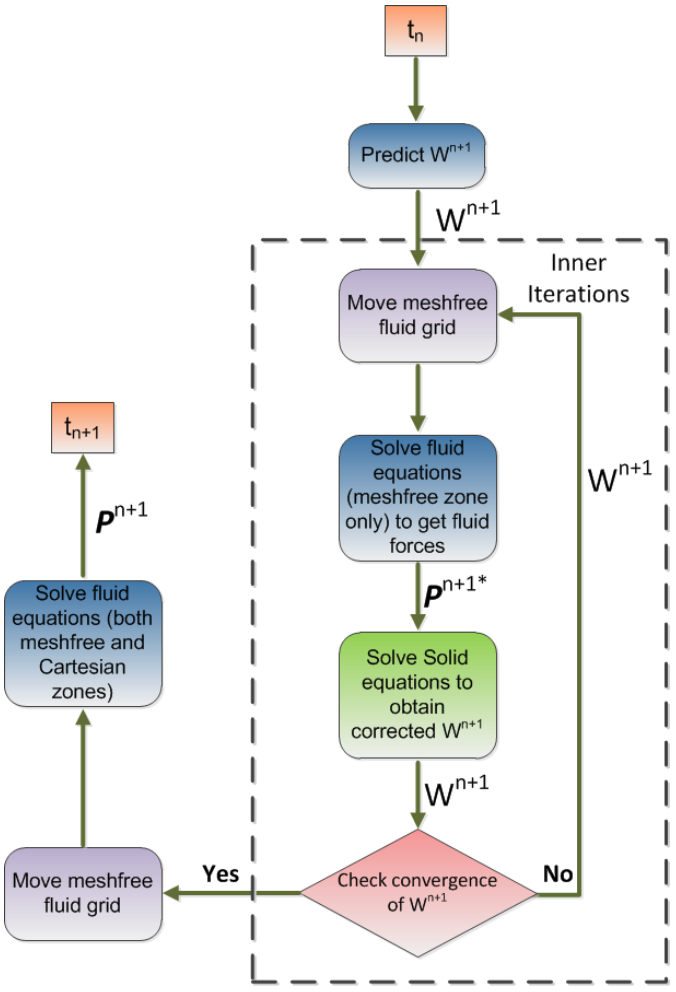

Figure 7.1: Flow chart of the FSI solution scheme, over hybrid grid, at a single time step

a coupled solver. Therefore, during sub-iteration process, flow equations are solved only over meshfree zone. Full flow field (meshfree and Cartesian zones) is solved during outer (time marching) iterations only.

7.2 FSI coupling algorithm

As mentioned earlier, a closely coupled model has been used to transfer data between fluid and structural solvers. Close coupling has achieved by iteratively running fluid and structural solvers at a single time step. During this process, exchange of fluid and structural data (fluid forces and structural deformations) takes place at solid boundary, after every sub-iteration, until the convergence between results of fluid and structural solver is reached. Use of closely coupled systems brings in high computational cost which is primarily caused by repeated flow solutions at a single time step value. It is however understood that the very purpose of running fluid solver during sub-iterations is to obtain fluid forces at fluid-structure interface, which are required to be transferred to

structural solver for onward calculation of structural deformation. Flow parameters at far field show minimal variation when the results are being *fine tuned* at solid boundary during sub-iterations. It is therefore logical to include only near field fluid grid for iterative refinement of fluid forces at solid boundary. In view of this, only meshfree zone is included in sub-iteration calculations of fluid solver. In fact, Cartesian grid zone is included in computation only during outer (time step marching) iteration of solver. During sub iterations, the results are updated only over the meshfree zone to get fluid forces as shown in the flow chart of solution scheme at a single time step in Figure 7.1. The scheme is named *Closely Coupled FSI with Reduced Fluid Domain* (CFSI-RFD) here. Conventional closely coupled FSI with full fluid domain will be written as CFSI-FFD in short form in thesis. Whereas loosely coupled FSI will be written as LFSI.

The coupling algorithm of the two field solution during FSI marching of CFSI-RFD is shown in Figure 7.2 and is carried out in following manner:

1. Structural displacement W^{n+1} is predicted at time t^{n+1} using velocity and acceleration of previous time step t^n.
2. Predicted structural displacement is mapped over the fluid grid.
3. Mesfhree fluid grid is displaced according to predicted structure displacement and fluid equations are solved only in meshfree zone. The fluid forces P^{n+1*} are thus calculated, at solid surface, using flow parameters.
4. An average of fluid forces P^{n+1*} and P^n is mapped over structural grid to get applied loads.
5. Solid equations are solved using averaged fluid forces to get the corrected structural deflection W^{n+1}. At this stage, corrected structural deflections are compared with previously obtained values.
6. Process from step 2 to 5 is repeated until the resultant structural deflection values achieve desired convergence level. Outer iteration is then run in which both Cartesian and meshfree fluid zones participate to march to next time step t^{n+1} and get P^{n+1}.

It is understood that exclusion of Cartesian grid, for inner iterations of CFSI-RFD, may cause some inaccuracies. However, the effect of using reduced fluid domain for inner iterations was found to be minimal during numerical tests. It is also pertinent to highlight that suggested closed coupling scheme is anyway more accurate than corresponding loosely coupled FSI (LFSI) which does not attempt to converge the two field solutions before marching to next time step.

The problem is solved using Hybrid fluid grid. Meshfree zone comprises of body conformal nodal cloud which moves with the solid object during motion. Static Cartesian grid

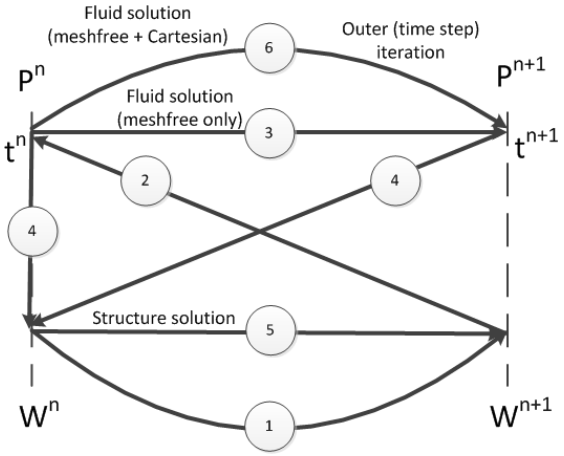

Figure 7.2: Coupling algorithm of two field solution for CFSI-RFD (Closely coupled FSI with reduced fluid domain). P^n and W^n represent fluid forces and solid deformation respectively, at n^{th} iteration

surrounds the meshfree zone as discussed earlier. Incompressible viscous flow equations are expressed in non-dimensionalized pressure-velocity $(\vec{P}, \vec{\mathbf{u}})$ form. The movement of meshfree nodes is accounted for with Aribitrary-Langrangian-Eulerian (ALE) formulation of N-S equations (Hirt et al. (1974)). Over moving meshfree grid, flow momentum equations are expressed in ALE formulation as shown in Eq. (2.11) (Takashi and Hughes (1992)). At each node, ALE velocity is set equal to the velocity of node. For static grid, the nodal velocity $\vec{\mathbf{v}}$ becomes zero and the momentum Eq. (2.11) transforms to its corresponding Eulerain form. Spatial and implicit time discretization is carried out in the same manner as mentioned in Chapter 5. This formulation provides an elegant way of solving the flow equations over moving data points. Flow equations are solved in their Eulerian form over static Cartesian grid. Elastically supported solid objects are assumed to be rigid with one or two degrees of freedom. Equations of solid mentioned in Section 2.4.1 are used. Time integration of equations of solid is carried out using Runge Kutta-4 method.

7.3 Stabilization at high Reynolds number flow

It is well known that convection becomes an increasingly dominant factor in the flow at high Reynold numbers. Therefore, implementation of some stabilization technique becomes essential for such problems. Use of Upwind finite differencing (Hirsch (2002)), anisotropic balancing diffusion and streamline upwind Petrove Galerkin (SUPG) method (Brooks and Hughes (1982)) are generally employed for stabilizing such equations.

In this section, a stabilization technique has been worked out to deal with such non-physical fluctuations in the flow. The lead has been taken from pioneering work of Oñate (1998) who came up with stabilized equations for advective-diffusive transport and flow

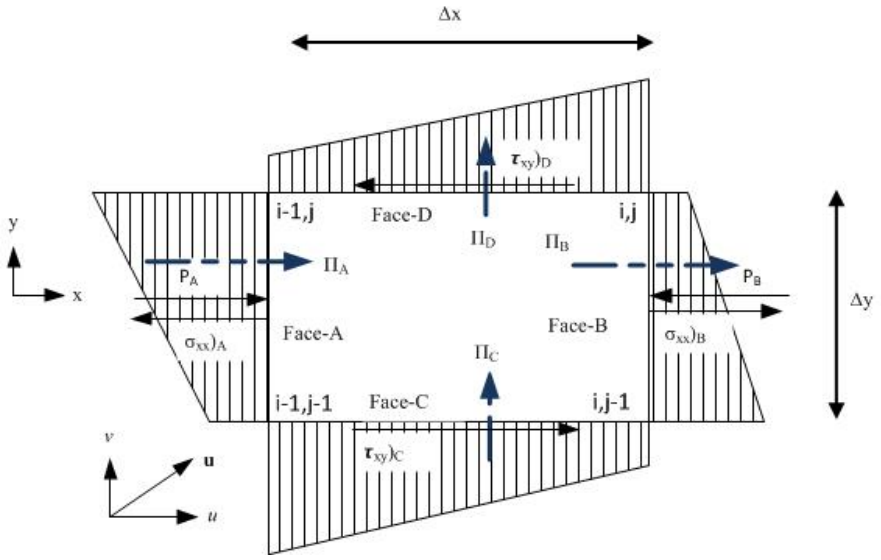

Figure 7.3: Control volume for balancing of forces and moments (σ_{xx} is normal stress along x-axis, τ_{xy} is in-plane shear stress, P is fluid pressure and Π is the flow momentum)

problems by applying balancing of fluxes. They showed that the stabilizing diffusion terms emerge naturally from within the governing equations of the problem when higher order approximations of differential equations are introduced in the formulation. Here, a similar concept has been employed over a finite control volume. However, stabilization terms are derived by applying the conditions of force and momentum equilibrium using Newton's second law of motion. It is opined that such approach would provide a direct correlation of derivation with physical flow problem. Nevertheless, finally obtained stabilization terms for one and two dimensional flow equations are the same as obtained previously by Oñate (1998). The stabilization is then applied with coupled RBF-FD and Cartesian FD solver to solve problems involving high Reynolds number flow. Derivation of stabilization term is shown in subsequent subsection.

7.3.1 Derivation of stabilized equation for incompressible flow

Let us consider the two dimensional control volume defined by vortices $[(i-1,j-1),(i,j-1),(i,j),(i-1,j)]$ as shown in Figure 7.3. The horizontal and vertical dimensions of the domain are Δx and Δy respectively. It is assumed that the distribution of momentum fluxes and stresses on all the four faces of control volume is varying linearly. Using

Newton's second law of motion in x-direction, we can state that:

$$\begin{aligned} Rate\ of\ change\ of\ u-momentum\ within\ CV = \\ (Net\ u-momentum\ entering\ the\ CV)- \\ (Net\ u-momentum\ leaving\ the\ CV)+ \\ (Sum\ of\ x-forces\ acting\ on\ CV\ surface)+ \\ (Sum\ of\ x-body\ forces\ acting\ on\ CV) \end{aligned} \tag{7.1}$$

‘

If ρ is the density of fluid and $\mathbf{u} = [u, v]^T$ is the velocity vector, then

$$\begin{aligned} Rate\ of\ change\ of\ u-momentum\ within\ CV &= \partial\rho u/\partial t\Delta x\Delta y \\ Net\ u-momentum\ entering\ the\ CV &= \Pi_A + \Pi_C \\ &= (\rho u^2)_A\Delta y + (\rho uv)_C\Delta x \\ Net\ u-momentum\ leaving\ the\ CV &= \Pi_B + \Pi_D \\ &= (\rho u^2)_B\Delta y + (\rho uv)_D\Delta x \\ Sum\ of\ x-forces\ acting\ on\ CV\ surface &= [P_A - P_B]\,\Delta y \\ &\quad - [(\sigma_{xx})_A - (\sigma_{xx})_B]\,\Delta y \\ &\quad - [(\tau_{xy})_C - (\tau_{xy})_D]\,\Delta x \\ Sum\ of\ x-body\ forces\ acting\ on\ CV &= F_x\Delta x\Delta y \end{aligned}$$

Therefore, Eq. (7.1) can be written as:

$$\begin{aligned} \frac{\partial\rho u}{\partial t}\Delta x\Delta y = &\left[(\rho u^2)_A - (\rho u^2)_B\right]\Delta y + [(\rho uv)_C - (\rho uv)_D]\,\Delta x \\ &+ [P_A - P_B]\,\Delta y - [(\sigma_{xx})_A - (\sigma_{xx})_B]\,\Delta y \\ &- [(\tau_{xy})_C - (\tau_{xy})_D]\,\Delta x + F_x\Delta x\Delta y \end{aligned} \tag{7.2}$$

As momentum flux is linearly varying on the faces of CV. Therefore, total momentum flux in the CV through face-A can be expressed in terms of the values of momentum flux at nodes $(i-1, j-1)$ and $(i-1, j)$:

$$(\rho u^2)_A = \frac{(\rho u^2)_{i-1,j} + (\rho u^2)_{i-1,j-1}}{2} \tag{7.3}$$

Using Taylor expansion of the order $O(h^2)$ we get:

$$(\rho u^2)_A = \frac{1}{2}\left[\left((\rho u^2)_{i,j} - \Delta x\frac{\partial \rho u^2}{\partial x} + \frac{\Delta x^2}{2}\frac{\partial^2 \rho u^2}{\partial x^2}\right) + \left((\rho u^2)_{i,j} - \Delta x\frac{\partial \rho u^2}{\partial x} - \Delta y\frac{\partial \rho u^2}{\partial y} + \Delta x\Delta y\frac{\partial \rho u^2}{\partial x \partial y} + \frac{\Delta x^2}{2}\frac{\partial^2 \rho u^2}{\partial x^2} + \frac{\Delta y^2}{2}\frac{\partial^2 \rho u^2}{\partial y^2}\right)\right] \tag{7.4}$$

Similarly, momentum flux across face-B can be written as:

$$\begin{aligned}(\rho u^2)_B =& \frac{(\rho u^2)_{i,j} + (\rho u^2)_{i,j-1}}{2} \\ =& \frac{1}{2}\left[\left((\rho u^2)_{i,j}\right) + \left((\rho u^2)_{i,j} - \Delta y\frac{\partial \rho u^2}{\partial y} + \frac{\Delta y^2}{2}\frac{\partial^2 \rho u^2}{\partial y^2}\right)\right]\end{aligned} \tag{7.5}$$

therefore,

$$(\rho u^2)_A - (\rho u^2)_B = -\Delta x\frac{\partial \rho u^2}{\partial x} + \frac{\Delta x\Delta y}{2}\frac{\partial^2 \rho u^2}{\partial x \partial y} + \frac{\Delta x^2}{2}\frac{\partial^2 \rho u^2}{\partial x^2} \tag{7.6}$$

Now finding Taylor expansion of terms $(\rho uv)_C$ and $(\rho uv)_D$:

$$\begin{aligned}(\rho uv)_C =& \frac{(\rho uv)_{i-1,j-1} + (\rho uv)_{i,j-1}}{2} \\ =& \frac{1}{2}\left[\left((\rho uv)_{i,j} - \Delta x\frac{\partial \rho uv}{\partial x} - \Delta y\frac{\partial \rho uv}{\partial y} + \Delta x\Delta y\frac{\partial^2 \rho uv}{\partial x \partial y} + \frac{\Delta x^2}{2}\frac{\partial^2 \rho uv}{\partial x^2} + \frac{\Delta y^2}{2}\frac{\partial^2 \rho uv}{\partial y^2}\right) + \left((\rho uv)_{i,j} - \Delta y\frac{\partial \rho uv}{\partial y} + \frac{\Delta y^2}{2}\frac{\partial^2 \rho uv}{\partial y^2}\right)\right]\end{aligned} \tag{7.7}$$

$$\begin{aligned}(\rho uv)_D =& \frac{(\rho uv)_{i-1,j} + (\rho uv)_{i,j}}{2} \\ =& \frac{1}{2}\left[\left((\rho uv)_{i,j} - \Delta x\frac{\partial \rho uv}{\partial x} + \frac{\Delta x^2}{2}\frac{\partial^2 \rho uv}{\partial x^2}\right) + \left((\rho uv)_{i,j}\right)\right]\end{aligned} \tag{7.8}$$

therefore,

$$(\rho uv)_C - (\rho uv)_D = -\Delta y\frac{\partial \rho uv}{\partial y} + \frac{\Delta x\Delta y}{2}\frac{\partial^2 \rho uv}{\partial x \partial y} + \frac{\Delta y^2}{2}\frac{\partial^2 \rho uv}{\partial y^2} \tag{7.9}$$

Taylor expansion of force terms, due to normal and shear stresses (σ_{xx} and τ_{xy}) and pressure, appearing in Eq. (7.2), can similarly be found resulting in following expressions:

$$(\sigma_{xx})_A - (\sigma xx)_B = -\Delta x\frac{\partial \sigma_{xx}}{\partial x} + \frac{\Delta x\Delta y}{2}\frac{\partial^2 \sigma_{xx}}{\partial x\partial y} + \frac{\Delta x^2}{2}\frac{\partial^2 \sigma_{xx}}{\partial x^2} \tag{7.10}$$

$$(\tau_{xy})_C - (\tau_{xy})_D = -\Delta y\frac{\partial \tau_{xy}}{\partial y} + \frac{\Delta x\Delta y}{2}\frac{\partial^2 \tau_{xy}}{\partial x\partial y} + \frac{\Delta y^2}{2}\frac{\partial^2 \tau_{xy}}{\partial y^2} \tag{7.11}$$

$$P_A - P_B = -\Delta x\frac{\partial P}{\partial x} + \frac{\Delta x\Delta y}{2}\frac{\partial^2 P}{\partial x\partial y} + \frac{\Delta x^2}{2}\frac{\partial^2 P}{\partial x^2} \tag{7.12}$$

Ignoring body forces and substituting expressions from Eqs. (7.6), (7.9)-(7.12) in Eq. (7.2), we get:

$$\begin{aligned}\frac{\partial \rho u}{\partial t}\Delta x\Delta y = &\left[-\Delta x\frac{\partial \rho u^2}{\partial x} + \frac{\Delta x\Delta y}{2}\frac{\partial^2 \rho u^2}{\partial x\partial y} + \frac{\Delta x^2}{2}\frac{\partial^2 \rho u^2}{\partial x^2}\right]\Delta y\\ &+\left[-\Delta y\frac{\partial \rho uv}{\partial y} + \frac{\Delta x\Delta y}{2}\frac{\partial^2 \rho uv}{\partial x\partial y} + \frac{\Delta y^2}{2}\frac{\partial^2 \rho uv}{\partial y^2}\right]\Delta x\\ &+\left[-\Delta x\frac{\partial P}{\partial x} + \frac{\Delta x\Delta y}{2}\frac{\partial^2 P}{\partial x\partial y} + \frac{\Delta x^2}{2}\frac{\partial^2 P}{\partial x^2}\right]\Delta y\\ &-\left[-\Delta x\frac{\partial \sigma_{xx}}{\partial x} + \frac{\Delta x\Delta y}{2}\frac{\partial^2 \sigma_{xx}}{\partial x\partial y} + \frac{\Delta x^2}{2}\frac{\partial^2 \sigma_{xx}}{\partial x^2}\right]\Delta y\\ &-\left[-\Delta y\frac{\partial \tau_{xy}}{\partial y} + \frac{\Delta x\Delta y}{2}\frac{\partial^2 \tau_{xy}}{\partial x\partial y} + \frac{\Delta y^2}{2}\frac{\partial^2 \tau_{xy}}{\partial y^2}\right]\Delta x\end{aligned} \tag{7.13}$$

after rearranging and simplifying Eq. (7.13), we get:

$$\begin{aligned}\frac{\partial \rho u}{\partial t} = &\left[-\frac{\partial \rho u^2}{\partial x} - \frac{\partial \rho uv}{\partial y} - \frac{\partial P}{\partial x} + \frac{\partial \sigma_{xx}}{\partial x} + \frac{\partial \tau_{xy}}{\partial y}\right]\\ &-\frac{\Delta x}{2}\frac{\partial}{\partial x}\left[-\frac{\partial \rho u^2}{\partial x} - \frac{\partial \rho uv}{\partial y} - \frac{\partial P}{\partial x} + \frac{\partial \sigma_{xx}}{\partial x} + \frac{\partial \tau_{xy}}{\partial y}\right]\\ &-\frac{\Delta y}{2}\frac{\partial}{\partial y}\left[-\frac{\partial \rho u^2}{\partial x} - \frac{\partial \rho uv}{\partial y} - \frac{\partial P}{\partial x} + \frac{\partial \sigma_{xx}}{\partial x} + \frac{\partial \tau_{xy}}{\partial y}\right]\end{aligned} \tag{7.14}$$

For viscous flow, general stress-strain relations can be written as viscous stresses. These stresses are linearly related with strain rates for Newtonian fluids as:

$$\sigma_{xx} = 2\mu\frac{\partial u}{\partial x}, \qquad \tau_{xy} = \mu\frac{\partial u}{\partial x}$$

where μ is the dynamic viscosity of flow. Ignoring third derivatives, Eq. (7.14) can be expressed for incompressible flow as:

$$\begin{aligned}\frac{\partial u}{\partial t} = &\left[-u\frac{\partial u}{\partial x} - v\frac{\partial u}{\partial y} - \frac{1}{\rho}\frac{\partial P}{\partial x} + \frac{\mu}{\rho}\left(\frac{\partial^2 u}{\partial x^2} + \frac{\partial^2 u}{\partial x^2}\right)\right] \\ &- \frac{\Delta x}{2}\frac{\partial}{\partial x}\left[-u\frac{\partial u}{\partial x} - v\frac{\partial u}{\partial y} - \frac{1}{\rho}\frac{\partial P}{\partial x}\right] \\ &- \frac{\Delta y}{2}\frac{\partial}{\partial y}\left[-u\frac{\partial u}{\partial x} - v\frac{\partial u}{\partial y} - \frac{1}{\rho}\frac{\partial P}{\partial x}\right]\end{aligned} \tag{7.15}$$

Eq. (7.15) can be non-dimensionalized using characteristic velocity U, length c, time c/U and pressure ρU^2 respectively and defining Reynolds number as $Re = \rho U c/\mu$. For simplicity, non-dimensionalized parameter will be expressed using the same symbols as their dimensionalized counterparts. Non-dimensional form of Eq. (7.15) is therefore expressed as:

$$\begin{aligned}\frac{\partial u}{\partial t} = &\left[-u\frac{\partial u}{\partial x} - v\frac{\partial u}{\partial y} - \frac{\partial P}{\partial x} + \frac{1}{Re}\left(\frac{\partial^2 u}{\partial x^2} + \frac{\partial^2 u}{\partial x^2}\right)\right] \\ &- \frac{\Delta x}{2}\frac{\partial}{\partial x}\left[-u\frac{\partial u}{\partial x} - v\frac{\partial u}{\partial y} - \frac{\partial P}{\partial x}\right] \\ &- \frac{\Delta y}{2}\frac{\partial}{\partial y}\left[-u\frac{\partial u}{\partial x} - v\frac{\partial u}{\partial y} - \frac{\partial P}{\partial x}\right]\end{aligned} \tag{7.16}$$

Horizontal and vertical dimensions of control volume (at which stabilization is being enforced) can be linked by a characteristic length Δs such that $\Delta x = \Delta s \cos\alpha$ and $\Delta y = \Delta s \sin\alpha$, where α is the angle between velocity vector $\mathbf{u}$ with x-axis. Then,

$$\Delta x = \Delta s \frac{u}{|\mathbf{u}|}, \qquad \Delta y = \Delta s \frac{v}{|\mathbf{u}|}$$

Eq. (7.16) can therefore, be written as:

$$\begin{aligned}\frac{\partial u}{\partial t} = &\left[-u\frac{\partial u}{\partial x} - v\frac{\partial u}{\partial y} - \frac{\partial P}{\partial x} + \frac{1}{Re}\left(\frac{\partial^2 u}{\partial x^2} + \frac{\partial^2 u}{\partial x^2}\right)\right] \\ &- \frac{\Delta s}{2|\mathbf{u}|}\left(u\frac{\partial}{\partial x}\left[-u\frac{\partial u}{\partial x} - v\frac{\partial u}{\partial y} - \frac{\partial P}{\partial x}\right] - v\frac{\partial}{\partial y}\left[-u\frac{\partial u}{\partial x} - v\frac{\partial u}{\partial y} - \frac{\partial P}{\partial x}\right]\right)\end{aligned} \tag{7.17}$$

Eq. (7.17) can be represented in vector form as:

$$\frac{\partial \vec{\mathbf{u}}}{\partial t} = -\vec{\mathbf{u}}.\nabla\vec{\mathbf{u}} - \nabla P + \frac{1}{Re}\nabla^2\vec{\mathbf{u}} - \frac{\Delta s}{2|\mathbf{u}|}\vec{\mathbf{u}}^T.\nabla\mathbf{g}(\vec{\mathbf{u}}) \tag{7.18}$$
$$(where, \quad \mathbf{g}(\phi) = -\vec{\mathbf{u}}.\nabla\phi - \nabla P)$$

For 1-D, the equation reduces to:

$$\frac{\partial u}{\partial t} = -u\frac{\partial u}{\partial x} - \frac{\partial P}{\partial x} + \frac{1}{Re}\frac{\partial^2 u}{\partial x^2} - \frac{\Delta x}{2}u\frac{\partial \mathbf{g}(u)}{\partial x} \tag{7.19}$$
$$(where, \quad \mathbf{g}(\phi) = -u\partial\phi/\partial x - \partial P/\partial x)$$

7.3.2 Stabilized momentum equation

Modified momentum equation with stabilized term is given as:

$$\frac{\partial \vec{\mathbf{u}}}{\partial t} = -\vec{\mathbf{u}}.\nabla\vec{\mathbf{u}} - \nabla P + \frac{1}{Re}\nabla^2\vec{\mathbf{u}} - \frac{\Delta s}{2|\mathbf{u}|}\vec{\mathbf{u}}^T.\nabla\mathbf{g}(\vec{\mathbf{u}}) \tag{7.20}$$
$$(for \quad \mathbf{g}(\phi) = -\vec{\mathbf{u}}.\nabla\phi - \nabla P)$$

The equation can be perceived as conventional momentum equation for incompressible, viscous flow with stabilization term $-\Delta s/(2|\mathbf{u}|)\vec{\mathbf{u}}^T.\nabla\mathbf{g}(\vec{\mathbf{u}})$ (where Δs is the characteristic length defining the size of finite domain at which stabilization is applied) appearing at the end. Similar expression for stabilization term has been obtained in previous studies, by Oñate (1998) and Oñate et al. (1996), relating to convective-diffusive equation. However, here we have adopted a different derivation approach which relates conditions of force equilibrium with momentum balance within a control volume to reach the final equation. Derivation of Eq.(7.20) has been carried out using Taylor expansion of the order of $O(h^2)$ for terms appearing in momentum balance equation. In fact, by reducing the order of Taylor expansion, during derivation, to $O(h)$, the balancing term disappears and momentum equation, shown in Eq. (5.2), is obtained. Hence, stabilization term is actually an additional term resulting from higher order approximation of derivatives during balancing of forces and moments in finite control volume. The stabilized momentum equations can be used for both meshfree and Cartesian methods and are therefore, suited for Hybrid grid scheme.

The stabilized momentum equation (7.20) is solved using non-incremental pressure projection method with implicit time discretization as discussed in Section 5.1.2.2. Intermediate momentum equation, including stabilization term, can therefore, be expressed as:

$$\frac{\vec{\mathbf{u}}^* - \vec{\mathbf{u}}^n}{\Delta t} = -\left(\vec{\mathbf{u}}.\nabla\right)\vec{\mathbf{u}} + \left(1/Re\right)\nabla^2\vec{\mathbf{u}} - \frac{\Delta s}{2|\mathbf{u}|}\vec{\mathbf{u}}^T.\nabla\mathbf{g}(\vec{\mathbf{u}}) \tag{7.21}$$

As before, the convective and diffusive terms are dicretized using explicit Adams-Bashforth and implicit Crank-Nicolson schemes respectively. Stabilized term is discretized using Euler explicit scheme. The resultant discretized form of intermediate momentum equation is written as:

$$\begin{aligned}\frac{\vec{\mathbf{u}}^* - \vec{\mathbf{u}}^n}{\Delta t} = &-\frac{1}{2}\left[3\left(\vec{\mathbf{u}}^n.\nabla\right)\vec{\mathbf{u}}^n - \left(\vec{\mathbf{u}}^{n-1}.\nabla\right)\vec{\mathbf{u}}^{n-1}\right] \\ &+\frac{1}{2Re}\left[\nabla^2\left(\vec{\mathbf{u}}^n + \vec{\mathbf{u}}^*\right)\right] - \frac{\Delta s}{2|\mathbf{u}^n|}\vec{\mathbf{u}}^{nT}.\nabla\mathbf{g}(\vec{\mathbf{u}}^n)\end{aligned} \tag{7.22}$$

Subsequent solution process is the same as mentioned in Section 5.1.

7.3.3 Characteristic length for stabilization

One of the important aspect for implementing stabilization term is the selection of appropriate characteristic length at which equilibrium of forces and moments is to be applied. Oñate et al. (1996) suggested that characteristic length be the function of local flow velocity and Reynolds number. For non-dimensionalized parameters, characteristic length Δs is defined as:

$$\Delta s = \beta \Delta \bar{s} \tag{7.23}$$

$$where, \qquad \beta = \coth|\gamma| - \frac{1}{|\gamma|} \tag{7.24}$$

$$and \qquad \gamma = \frac{|\mathbf{u}|\ \Delta\bar{s}Re}{2} \tag{7.25}$$

In Cartesian zone, $\Delta\bar{s}$ is defined as the average distance between two neighbouring nodes at point of interest. For meshfree nodal distribution, $\Delta\bar{s}$ is defined as the average distance represented by each node in any local influence domain. Therefore, $\Delta\bar{s} = 2r/N$ for a domain of radius r and N neighbouring points. α is the control parameter which allows variation of characteristic length (and hence the amount of stabilization) in different regions based on flow conditions. Figure 7.4 shows variation of β with magnitude of flow velocity $|u|$ for different value of Reynolds numbers. It can be observed that the value of control parameter α varies from $0-1$ as flow velocity increases from $0-\infty$. In this manner, the value of characteristic length is controlled to have greater stabilization in the regions which are more susceptible to numerical instabilities caused by highly convective flow and vice versa. At high Reynolds numbers, the value of β increases more rapidly in the beginning. Therefore, stabilization term increases more rapidly at higher Reynolds

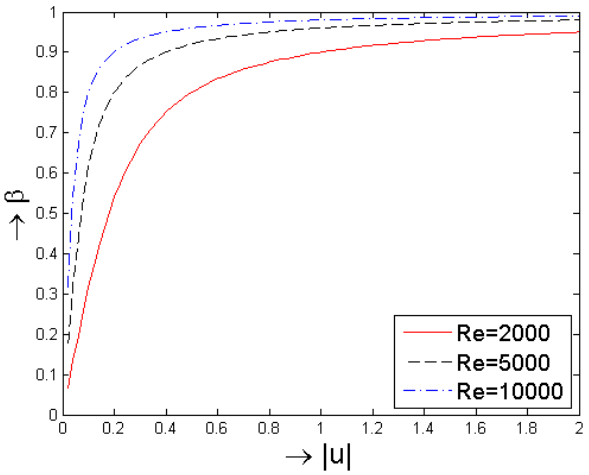

Figure 7.4: Variation of β with flow velocity $|\mathbf{u}|$ at $\Delta\bar{s} = 0.01$

number and achieves its maximum value at lower flow velocities compared with lower values of Re.

7.4 Stabilization for of 1-D Convection-Diffusion equations

The effect of stabilization can best be observed by solving convective diffusive equation with a step field functions. For this purpose, the one dimensional convective-diffusive Eq.(7.19) is considered. The equation is in non-dimensionalized form. $u(x,t)$ is the normalized velocity and Re is the Reynolds number. The solutions are obtained for following cases:

1. With step field function as initial condition
2. With known field functions
3. with known field functions over hybrid grid

7.4.1 Solution with step field function as initial condition

For this test case, Eq. (7.19) is considered with pressure field and is solved over domain $0 \leq x \leq 10$. Initial velocity field $u(0,x)$ is defined by two step functions with opposite signs. So, the initial conditions are:

$$\begin{aligned} u(x,0) &= 1 && for\ 2 \leq x \leq 3 \\ u(x,0) &= -1 && for\ 7 \leq x \leq 8 \\ u(x,0) &= 0 && elsewhere \end{aligned}$$

At both ends of domain, Neumann boundary conditions are applied with $\partial u/\partial x = 0$. The solutions are obtained, with and without the stabilization term, at different Reynolds numbers. Test cases are run for spatial derivatives calculated using central differencing as well as with RBF-FD method. Velocity time marching is carried out using Euler explicit method. Figure 7.5(a) shows velocity profiles at $t = 0$ and $t = 2$ when spatial derivatives calculated using central difference scheme. Similar solutions with RBF-FD are shown in Figure 7.5(b). It can be observed that spurious fluctuations are experienced when stabilization term is not included in the solution. Although these fluctuations are observed for both central differencing as well as RBF-FD based solutions, severity of these oscillations is higher for central differencing. The reason for this is that RBF-FD needs more particles for calculation of RBF weights than conventional finite difference. In doing so, number of upstream particles are naturally increased in RBF-FD case compared with central differencing. As a result spurious oscillations are relatively suppressed. Nevertheless, fluctuations are still present in both the solution.

These fluctuations tend to increase at higher Reynolds number due to reduced diffusion. However, inclusion of stabilization term in momentum equation helps avoid these non-physical fluctuations in the solution. As a result, smooth profiles of flow variables are obtained especially at high Reynolds numbers.

7.4.2 Solution with known field functions

In the previous sub-section, capability of stabilization term to suppress flow field fluctuations was demonstrated. Now, another numerical test has been carried out to compare the accuracy of the solution with and without the aid of stabilization term. For this purpose, Eq.(7.19) has been used with pressure term included. The initial and boundary values for pressure and velocity have been defined using following expressions:

$$\begin{aligned} u(x,t) &= \sin(\pi x)\exp\left[-(\pi^2 t)/Re\right] \\ p(x,t) &= -\frac{1}{4}\cos(\pi x)\exp\left[-2(\pi^2 t)/Re\right] \end{aligned} \tag{7.26}$$

The initial conditions are defined by evaluating velocity and pressure values at $t = 0$ using Eq.(7.26). Similarly, boundary conditions are obtained by substituting coordinate values of the boundary node at given time t. Expressions for velocity and pressure, defined in Eq.(7.26), are in fact the solutions of Eq.(7.19). This provides an opportunity to examine the accuracy of numerical solution by comparing it with true solution (obtained by Eq.(7.26)) at any given values of x and t. The solutions of Eq.(7.19) have been obtained, at different Reynolds numbers, with and without stabilization term. At every time instance, spatial derivatives are obtained using finite differencing as well as

RBF-FD method. Euler explicit time marching has been used for velocity. Pressure profile is directly evaluated using Eq. (7.26). Domain size is kept as $0 \leq x \leq 2$ with space step of 0.1. Time step of 0.05 is used. The profiles of velocity field, obtained at $t = 2$, are compared with analytical solutions as shown in Figure 7.6. Fluctuations are observed in the numerical solution, without stabilization, which tend to become more pronounced at high Reynolds number and at regions of higher velocities. These fluctuations are non-physical and truly numerical in nature as these tend to take the solution away from true solution. This behaviour is observed for both FD and RBF-FD based solutions. However, these spurious fluctuations remain effectively suppressed with the use of stabilization. Although, stabilization term is not needed at low Reynolds number; use of stabilized momentum equation does not affect the quality or accuracy of solutions for these cases.

With increasing Reynolds number, the effect of diffusion gradually decreases and flow becomes convection dominated. This calls for the use of special treatment like upwind differencing or artificial viscosity. The stabilization term, used here, can be seen as an additional diffusion term as appear in FE literature (Oñate et al. (1996)) which is found to effectively controls non-physical oscillations in such cases.

7.4.3 Known field functions over hybrid grid

Finally, the solution of Eq.(7.19) is obtained on 1-D hybrid grid using initial and boundary conditions defined by Eq.(7.26) at Re 1000. Computational domain spans for $0 \leq x \leq 2$. Nodes are uniformly distributed with step size of 0.1. The nodes falling within $0.8 \leq x \leq 1.2$ are treated with RBF-FD whereas conventional central differencing scheme is used elsewhere. Figure 7.7 shows the velocity plots for solutions with and without stabilization at $t = 2$. Methodology of data transfer between *meshfree* and *mesh based* zones is the same as mentioned in Section 6.2. Smooth transition of velocity profiles is observed between *meshfree* and *mesh based* zones. Use of stabilization is also found useful in dealing with spurious oscillations in this case.

7.5 Flow induced vibration of cylinder with 1-DoF

CFSI-RFD scheme, discussed above, is used to solve flow induced vibration of an elastically mounted cylinder. This basic test case of fluid-structure interface is amongst the most revealing problem pertaining to bluff bodies. Simple geometry and well established results available in literature make it an attractive choice to test current FSI solution scheme. Schematic of the problem is the same as Figure 2.4(a) except that horizontal degree of freedom is removed and the cylinder has only single degree of freedom in cross flow direction. Flow Reynolds number is set as 100. At this Reynolds number,

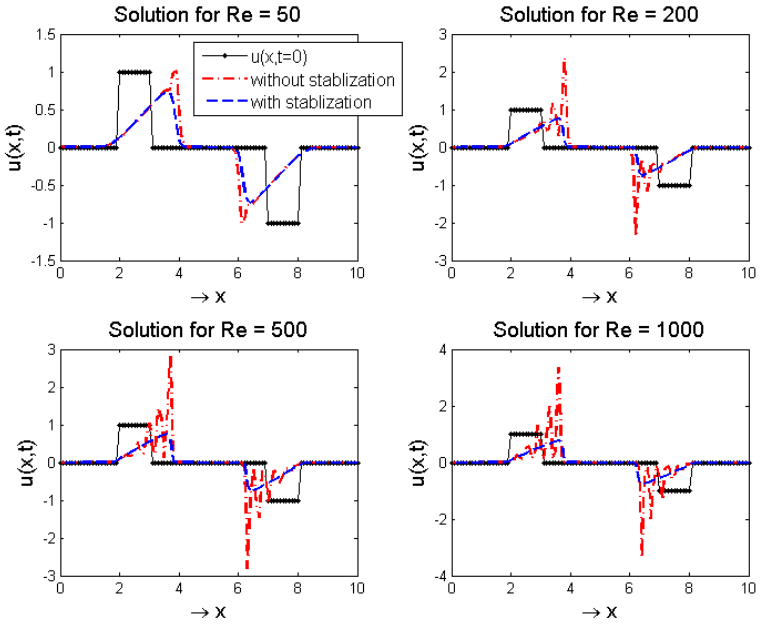

(a) Solution with central differencing

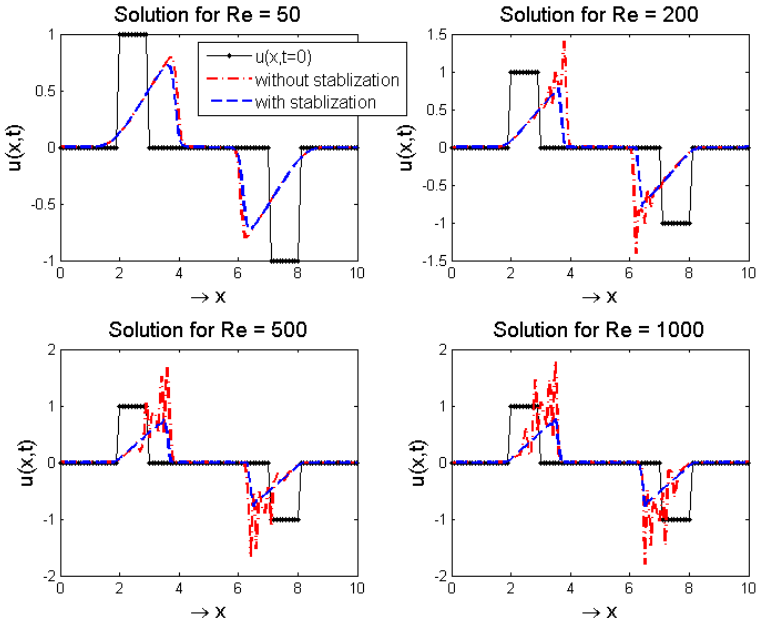

(b) Solution with RBF-FD

Figure 7.5: Solution of 1-D convective-diffusive equation for domain $0 \leq x \leq 10$ at t=2. $u(x, 0)$ is defined by two unit step functions in opposite directions. Solutions are obtained with and without stabilization term

oscillating flow vortices behind the cylinder will produce time varying lift profile. The cylinder is thus able to vibrate vertically under the influence of these forces. Cylindrical vibrations were stated as *self-limiting* by Mittal and Kumar (2001) in their analysis.

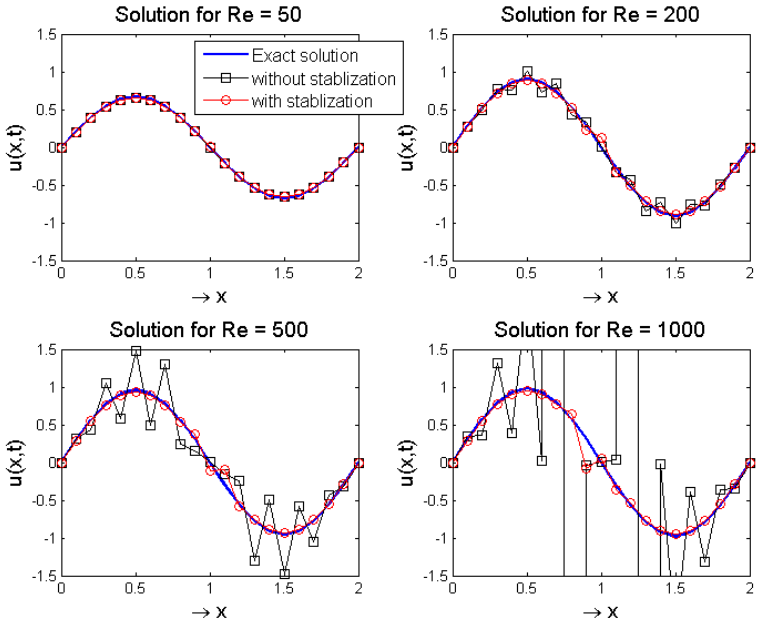

(a) Solution with central differencing

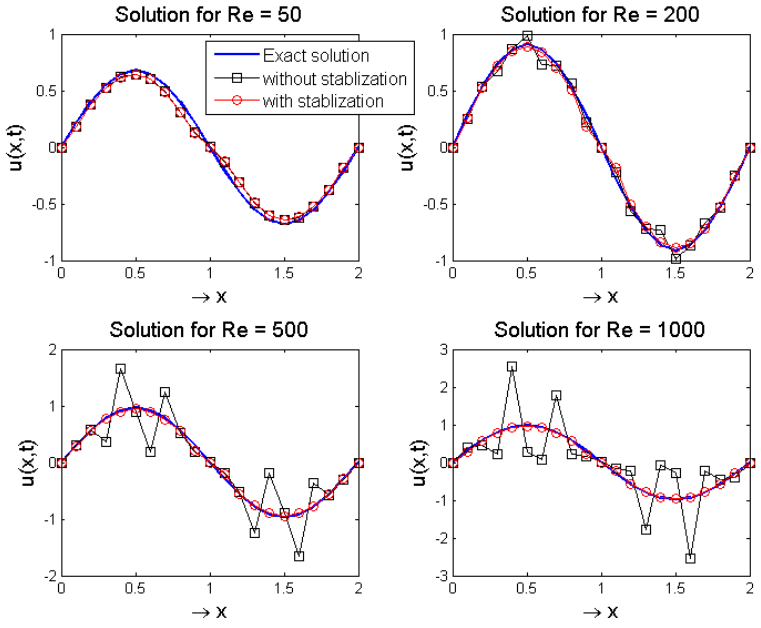

(b) Solution with RBF-FD

Figure 7.6: Solution of 1-D convective-diffusive equation for domain $0 \leq x \leq 2$ at t=2. Initial and boundary conditions are obtained from the expressions of true solution in Eq.(7.26). Solutions are obtained with and without stabilization term

This means that the vibration amplitudes retain their constant value after initial settling down period. Vibration of solid causes reduction in lift force and renders some additional frequency components in fluid force profiles which tend to limit the vibrating

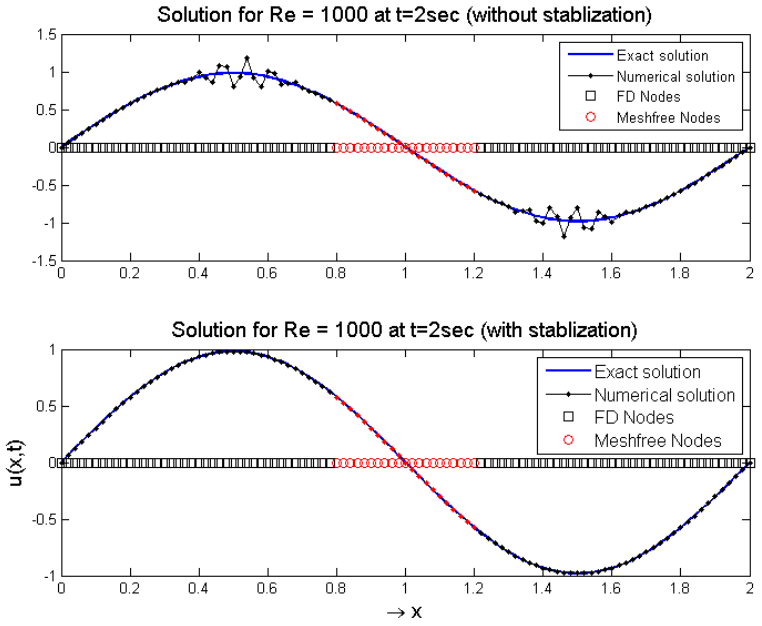

Figure 7.7: Solution of convective diffusive equation, at $Re = 1000$, over 1-D hybrid grid for domain $0 \leq x \leq 2$ at t=2. Meshfree zone spans for $0.6 \leq x \leq 1.2$. Initial and boundary conditions are obtained from the expressions of true solution in Eq. (7.26)

amplitudes to specific level (Placzek et al. (2009)). A parameter called *effective elasticity* k^*_{eff} is often used to characterize the system response for such problems. *Effective elasticity* combines the effect of system mass m, stiffness k and reduced vortex shedding frequency $f^* = fU/D$ through following expression (Shiels et al. (2001)):

$$k^*_{eff} = k - 4\pi^2 m f^{*2} \tag{7.27}$$

Effective elasticity therefore offers an inclusive representation of system parameters. For this work, dimensions of fluid domain are the same as for static case. The dimensions of meshfree zone are however changed to $3D \times 9D$ out of which $3D \times 6D$ constitutes active meshfree zone. Vertical dimension of meshfree zone is elongated to allow cross-flow vibration. Figure 7.8 shows nodal distribution around cylinder for this case. The solutions are sought on *ordered* as well as *randomized* meshfree nodal arrangement. Randomization is obtained by randomly disturbing the position of meshfree nodes from their corresponding location on the *ordered* grid. For this purpose, a random function of the order of $0.4\Delta r$ (Δr is the radial spacing of nodes) is used. Figures 7.9(a) and 7.9(b) show *ordered* and *randomized* nodal arrangements around the cylinder respectively.

Time step is kept as 5×10^{-3}. Mass of the cylinder is set as 3.3. The solutions are obtained by changing the values of spring stiffness k. For every test case, k^*_{eff} is calculated using spring stiffness k and resulting reduced frequency of vortex shedding f^*.

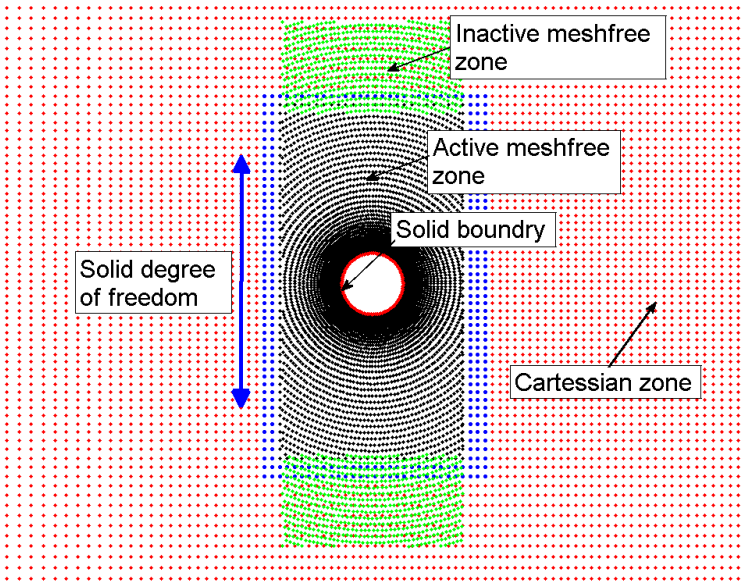

Figure 7.8: Computational grid around cylinder for 1-DoF vibration

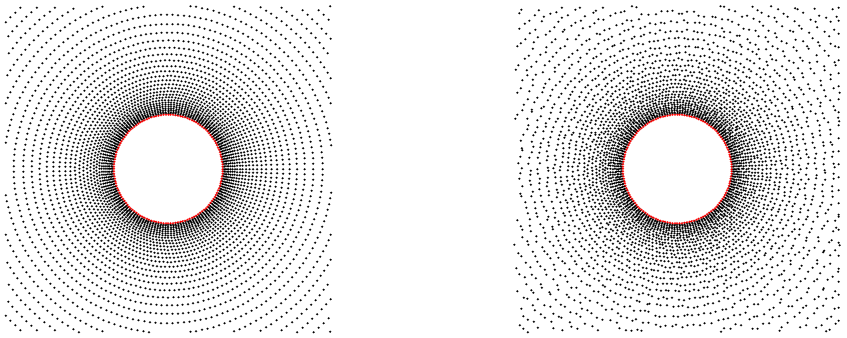

(a) *Ordered* arrangement (b) *Random* arrangement

Figure 7.9: Arrangement of meshfree nodes around circular solid

Corresponding values of non-dimensionalized vibration amplitudes (Y_{max}/D), reduced frequency (f^*), maximum lift coefficient ($C_{L_{max}}$) and RMS values of drag coefficient ($C_{D_{rms}}$) are plotted in Figure 7.10. The results are comparable to those obtained by Shiels et al. (2001). Moreover, the results from *ordered* as well as *randomized* meshfree nodal distribution match very closely with each other. This indicates that the solutions are not affected by randomization of meshfree nodes. Plots in Figure 7.10(a) indicate a high amplitude region between $0 \leq k^*_{eff} \leq 4$. The lift and drag values are also higher in this range as shown in Figures 7.10(c) and 7.10(d). This high amplitude zone is called 'locked-in' zone. In that, the vortex shedding frequency deviates from its original value and equalizes with natural frequency of vibrating system creating resonance. This

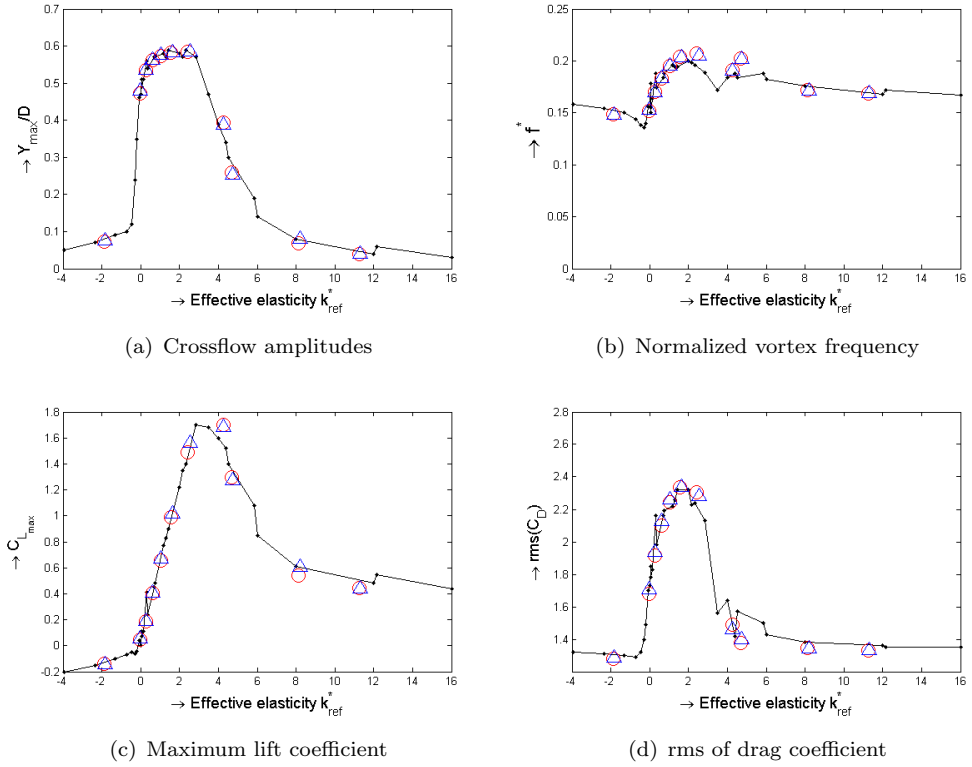

(a) Crossflow amplitudes

(b) Normalized vortex frequency

(c) Maximum lift coefficient

(d) rms of drag coefficient

Figure 7.10: 1-DoF cylindrical vibration at Re=100: Variation of parameters with effective elasticity (k^*_{eff}) (—●—Shiels et al Shiels et al. (2001), O Present work (*Ordered* grid), △ Present work (*Randomized* grid)

synchronization of fluid forces with vibrating system results in higher amplitudes. Figure 7.10(b) clearly indicates deviation of vortex frequency in 'locked-in' zone. Beyond 'locked-in' zone, a sharp decline in vibration amplitudes is observed. Figure 7.11 shows the difference in flow patterns around the cylinder for 'locked-in' and 'un-locked' configurations. Due to high vibration amplitudes in 'locked-in' zone, vortices are stretched and two distinct rows of vortices are formed behind the cylinder. In 'un-locked' zone, the vortex street resumes its conventional form. However, the vortices are being shed in 2S mode in both configurations and 2P mode of vortex shedding is not observed with change in k^*_{eff}. This observation is in line with what was obtained by Placzek et al. (2009) who argue that mode switch from 2S to 2P is only experienced at high Reynolds number which is not the case here. The vorticity plots, obtained by Shiels et al. (2001), for similar problem at locked-in and unlocked configurations are shown in Figures 7.12(a) and 7.12(b) respectively.

7.5.1 Effect of stabilization at low Reynolds number

During study of flow induced cylindrical vibrations with 1-DoF, the solutions are obtained at $Re = 100$. At this Reynolds number, the viscous forces are sufficiently high

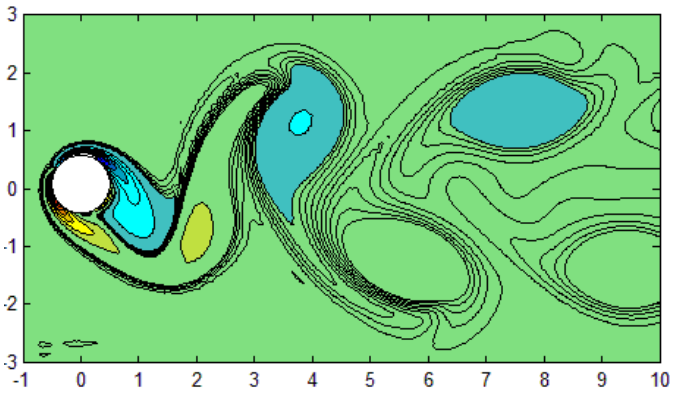

(a) Vorticity pattern in locked-in configuration ($k^*_{eff} = 1.57$)

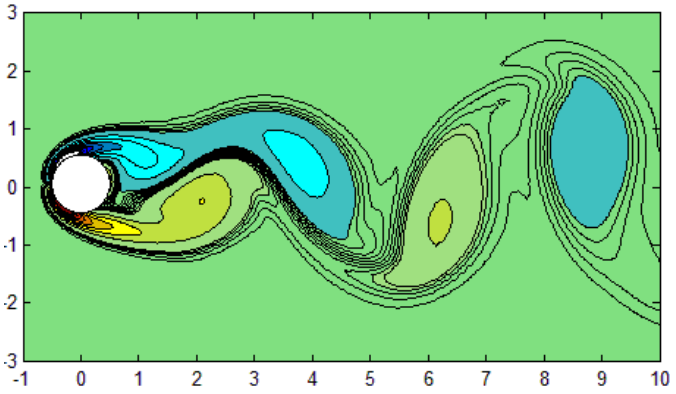

(b) Vorticity pattern in unlocked configuration ($k^*_{eff} = -1.89$)

Figure 7.11: Comparison of vorticity plots for 'locked-in' and 'un-locked' configurations

and use of stabilization, mentioned in Section 7.3, is not necessary. However, the solution should not be affected even if the stabilized momentum Eq. (7.20) is used, at these Reynolds numbers, and the results should be the same as those from the equation without stabilization term. In order to verify that stabilization has no effect on results at low Re, three different test cases are run with and without inclusion of stabilization term in momentum equation. The results are compared in Table 7.1. It can be observed that the solutions with stabilization are the same as those for without stabilization up to 3rd decimal place in most cases.

7.5.2 Comparison of FSI algorithms

The solutions of flow induced cylindrical vibration with 1 DoF discussed in Section 7.5, are carried out using closely coupled FSI with reduced fluid domain (CFSI-RFD) as mentioned in Section 7.2. The accuracy and computational efficiency of CFSI-RFD scheme is studied by comparing its solution and computation time with corresponding values from loosely coupled FSI (LFSI) as well as with closely coupled FSI with full fluid

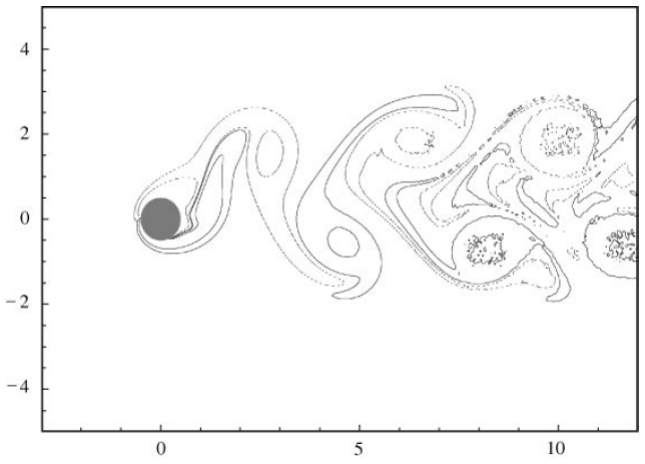

(a) Vorticity pattern in locked-in configuration ($k^*_{eff} = 1.414$)

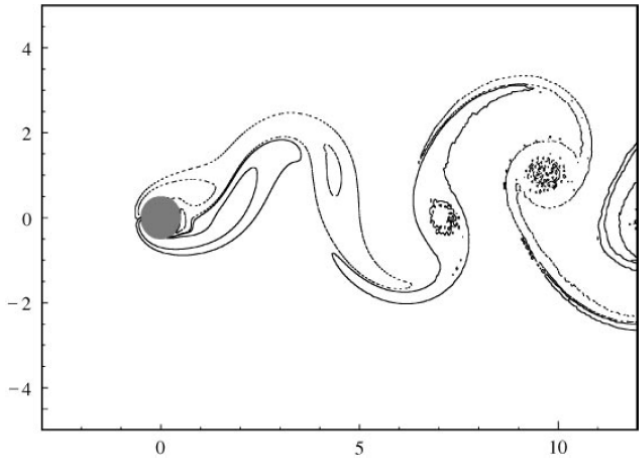

(b) Vorticity pattern in unlocked configuration ($k^*_{eff} = 0$)

Figure 7.12: Vorticity plots for 'locked-in' and 'un-locked' configurations obtained by Shiels et al. (2001)

domain (CFSI-FFD). For this purpose, the above mentioned problems, with $k^*_{eff} = 0.623$, is solved using all the three FSI algorithms. The curves in Figure 7.13 show computation time for calculation of 150 *sec* of simulation on Intel®2.6 GHz processor using different FSI schemes. As expected, the calculation time for loosely coupled FSI is the least and that for CFSI-FFD is the highest. Calculation time for CFSI-RFD is significantly lower than that for CFSI-FFD. This reduction has been achieved through reduced fluid domain. Computation time values for unit simulation time for each case have been shown in last column of Table 7.2. These results indicate that CFSI-FFD takes almost double computational time compared with LFSI. However, in case of CFSI-RFD, the computation time is increased only by 40% than that for LFSI. So, computational performance is significantly improved by reducing the fluid domain during sub-iterations.

For calculation of errors, the results of CFSI-FFD are taken as standard. Error values

Table 7.1: Comparison of parameters for test case with and without stabilization (1-DoF cylindrical vibration at Re=100)

Parameters	Stabilization	Y_{max}/D	f^*	$C_{L_{max}}$	$C_{D_{rms}}$
$m = 3.3$	No	0.0726	0.149	-0.1418	1.2806
$k = 1.0$	Yes	0.0727	0.1494	-0.1417	1.2807
$m = 3.3$	No	0.5606	0.1833	0.4067	2.102
$k = 1.0$	Yes	0.5604	0.1833	0.4092	2.114
$m = 3.3$	No	0.2593	0.2018	1.2954	1.3788
$k = 10.0$	Yes	0.2591	0.2006	1.2960	1.3789

are calculated by taking root mean square (RMS) of the difference of corresponding field value ,between LFSI or CFSI-RFD and standard values from CFSI-FFD, in the domain. For example

$$RMS\ error\ of\ v_x\ for\ CFSI-RFD\ =\ \sqrt{\frac{1}{N}\sum_{i=1}^{N}(v_{x_i}-v_{x_i}^{ref})} \tag{7.28}$$

where N is the total number of nodes, v_{x_i} is the x-component of flow velocity $\vec{\mathbf{u}} = (v_x, v_y)$ at node i using CFSI-RFD and $v_{x_i}^{ref}$ is the similar value calculated using CFSI-FFD at same spatial location and time.

The results are recorded after every 5 sec of simulation time and RMS error has been calculated for velocity components $\vec{u} = (v_x, v_y)$ and pressure P. Time profiles of these RMS errors in meshfree and Cartesian zone as well as in the entire computational domain are shown in Figures 7.14(a) - 7.14(c) respectively. As the cylinder starts its motion, the results from LFSI starts to deviate from corresponding values of CFSI-FFD. Therefore, RMS error keeps rising. On the contrary, RMS error for CFSI-RFD scheme stabilize at much lower level compared with LFSI error. The error is more pronounced in meshfree zone which is due to the presence of near field flow around moving boundary. The flow variables experience large variation due to moving boundaries and effect of better coupling are more pronounced. However, CFSI-RFD depicts far more accuracy even in this zone. Far field flow in Cartesian zone shows significantly lower error values. Similar trend is observed in the time profiles of resultant vertical displacement of cylinder, lift and drag coefficients for the three FSI schemes which are co-plotted in Figures 7.15(a) to 7.15(c) respectively. It can be observed that profile curves of CFSI-RFD closely follow the curves of CFSI-FFD. However, the curves from LFSI are relatively off.

In order to compare the overall error during the entire course of simulation, the RMS has been calculated of all the error values recorded during the simulation for each variable separately. For example $RMS(E_{vx})$ is calculated using all the values shown in Figure 7.14(a). These values are tabulated in Table 7.3. Error values from CFSI-RFD are significantly lower than their counterpart values from LFSI.

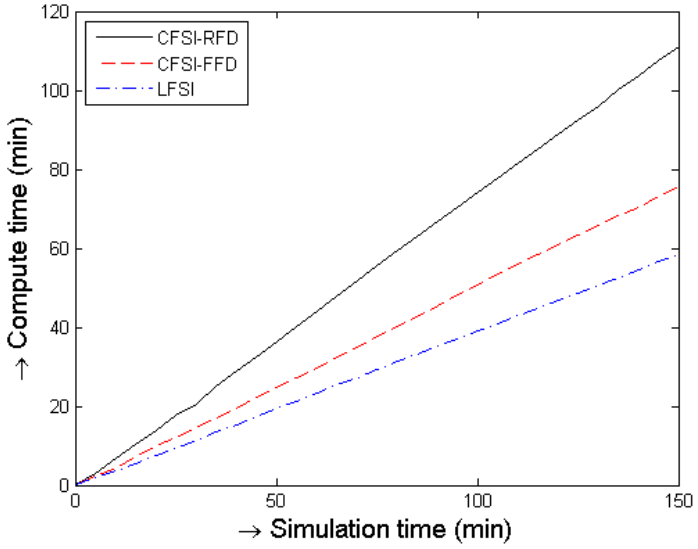

Figure 7.13: Computation time versus simulation time for 1-DoF cylindrical vibration at Re=100 and $k^*_{eff} = 0.623$. Comparison of i) closely coupled with full fluid domain (CFSI-FFD). ii) closely coupled with reduced fluid domain (CFSI-RFD) and iii) loosely coupled (LFSI) cases.

Table 7.2: Comparison of computation time per second of simulation time for different FSI schemes used for the solution of 1-DoF vibration of cylinder at $Re = 100$ and $k^*_{eff} = 0.623$

	LFSI	CFSI-RFD	CFSI-FFD
Computation time per Simulation time	0.3898	0.5043	0.7405

Table 7.3: RMS (root mean square) error for three different FSI schemes used for the solution of 1-DoF vibration of cylinder at $Re = 100$ and $k^*_{eff} = 0.623$

Error	LFSI	CFSI-RFD
$RMS(E_{vx})$	0.0665	0.0124
$RMS(E_{vy})$	0.063	0.006
$RMS(E_P)$	0.0464	0.0126
$RMS(E_Y)$	0.2169	0.0078
$RMS(E_{CL})$	0.144	0.0084
$RMS(E_{CD})$	0.4626	0.0183

Comparing error values and computation time, it can be inferred that closely coupled FSI case with reduced fluid domain calculations offer an efficient computation of FSI problems without much loss in accuracy.

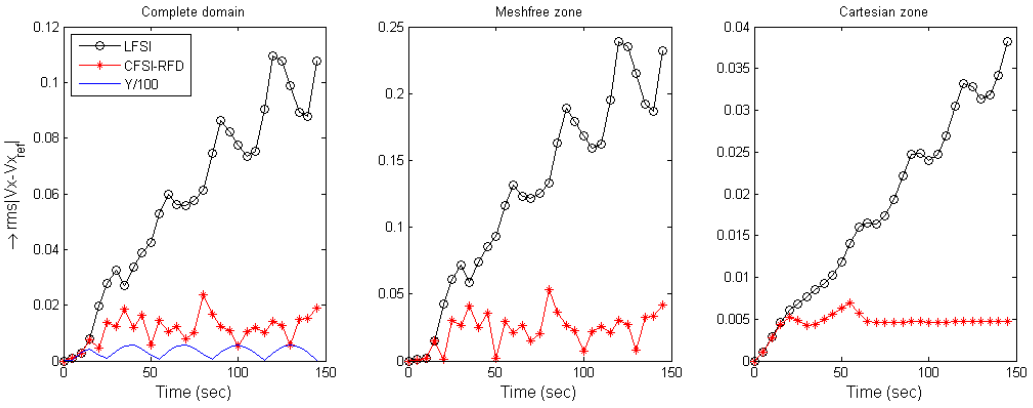

(a) v_x error ($rms(v_x - v_x^{ref})$)

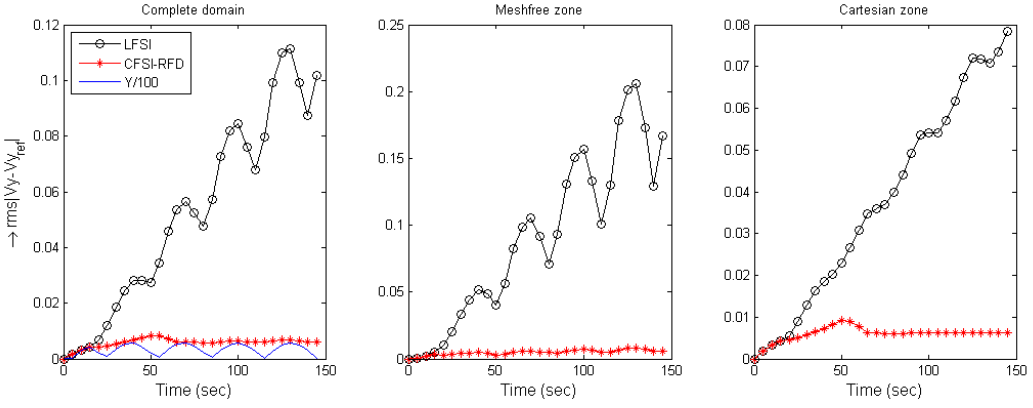

(b) v_y error ($rms(v_y - v_y^{ref})$)

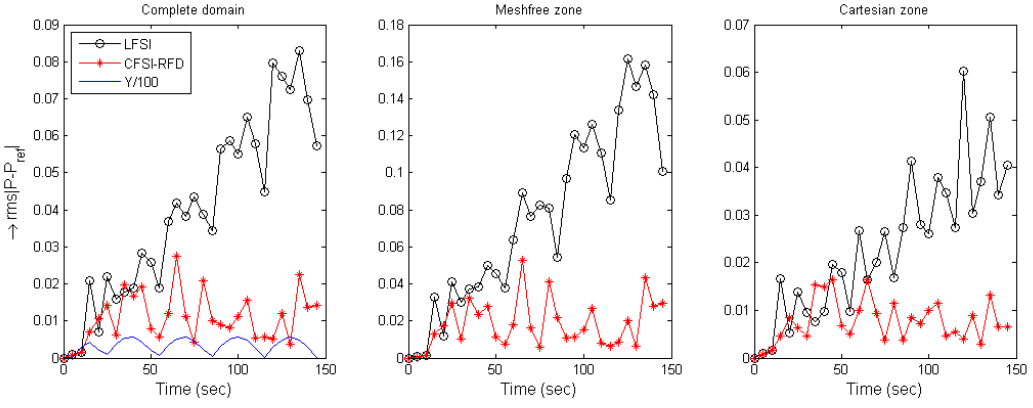

(c) P error ($rms(P - P^{ref})$)

Figure 7.14: Time profiles of error for LFSI and CFSI-RFD. Error calculated using results of CFSI-FFD as reference. 1-DoF cylindrical vibration at Re=100 and $k^*_{eff} = 0.623$.

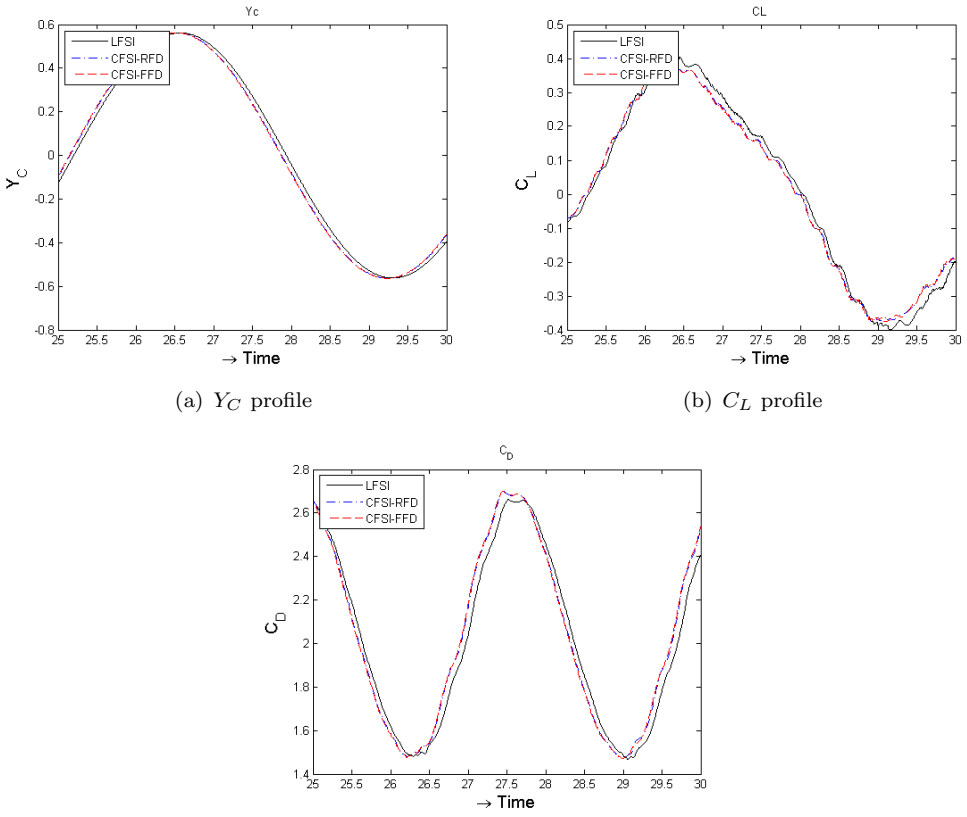

(a) Y_C profile

(b) C_L profile

(c) C_D profile

Figure 7.15: 1-DoF cylindrical vibration at Re=100 and $k^*_{eff} = 0.623$. Comparison of time profiles of displacement, lift and drag for i) LFSI (-), ii) CFSI-RFD (-.-) and iii) CFSI-FFD (- -) cases.

7.6 Flow induced vibration of cylinder with 2-DoF

Applicability of CFSI-RFD is tested for two degree of freedom problem here. For this purpose, vortex induced vibration (VIV) of cylinder with two degrees of freedom (in-flow direction X and cross-flow direction Y) has been chosen. The problem is of practical importance in many engineering applications including offshore cylindrical structures, underwater flexibly mounted pipelines and large electrical cables. For flexibly mounted cylindrical objects, incoming flow can initiate modes of vibration both along the flow as well as in cross-flow directions. The problem is therefore studied as 2-DoF vortex induced vibration (Dai Zhou (2012); Dahl et al. (2010)). The system vibrational response is often studied with changing reduced velocity ($v_r = U/(f_N D)$, where U is free stream velocity, D is cylindrical diameter and f_N is natural frequency of vibration). Dahl et al. (2010) found that the in-flow vibrations of cylinder show significantly higher amplitudes, due to dual resonant response, when ratio of in-line to transverse natural frequencies (f_{Nx}/f_{Ny}) is set around 2.0 . For other frequency ratios, cylindrical vibration is predominantly cross-flow and very low amplitudes of in-flow vibrations are observed.

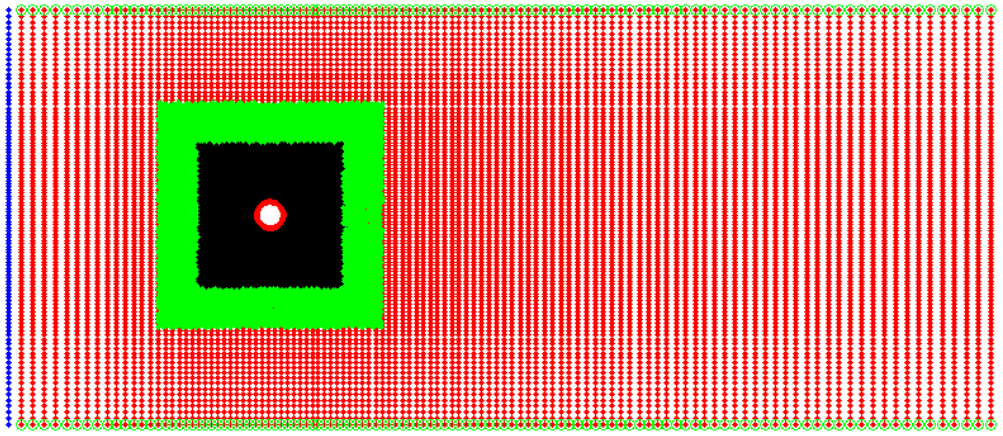

(a) Full Domain

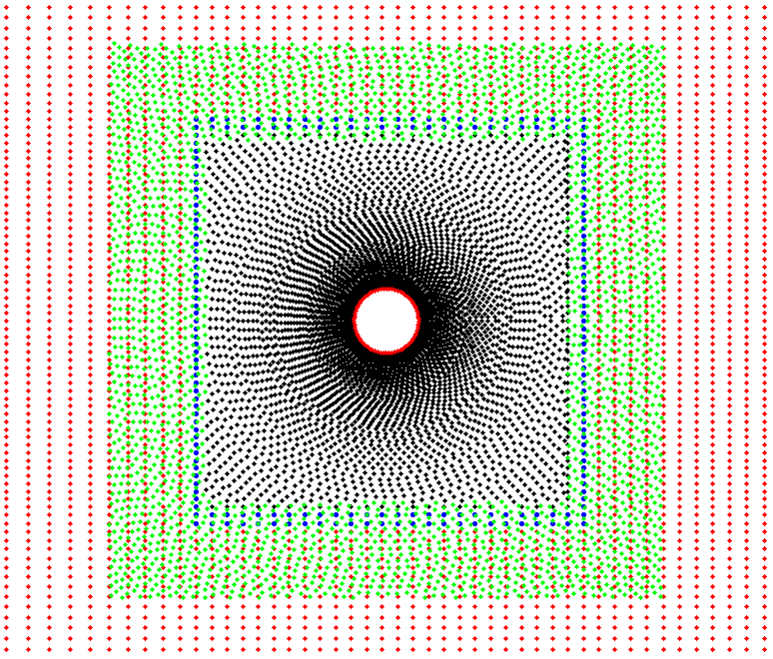

(b) Domain near solid object

Figure 7.16: Hybrid grid around cylinder for 2-DoF cylindrical vibration

In the present study, numerical tests are carried out to investigate the effect of changing reduced velocity ($v_r = U/(f_N D)$), frequency ratio (f_{Nx}/f_{Ny}), mass ratio (m^*=(Mass of cylinder)/(Displaced fluid mass)) and Reynolds number on in-flow (X) and cross-flow (Y) vibrational amplitudes of vibrating cylinder. Damping is set as zero to achieve high amplitudes. Meshfree zone spans $5D \times 5D$ around the cylinder. Out of this, size of active meshfree zone is $5D \times 5D$. An inactive zone (overshadowed region of meshfree grid) $1.5D$ wide is left on all the four sides of the cylinder to cater for solid movement. Nodal distribution in fluid domain is shown in Figure 7.16.

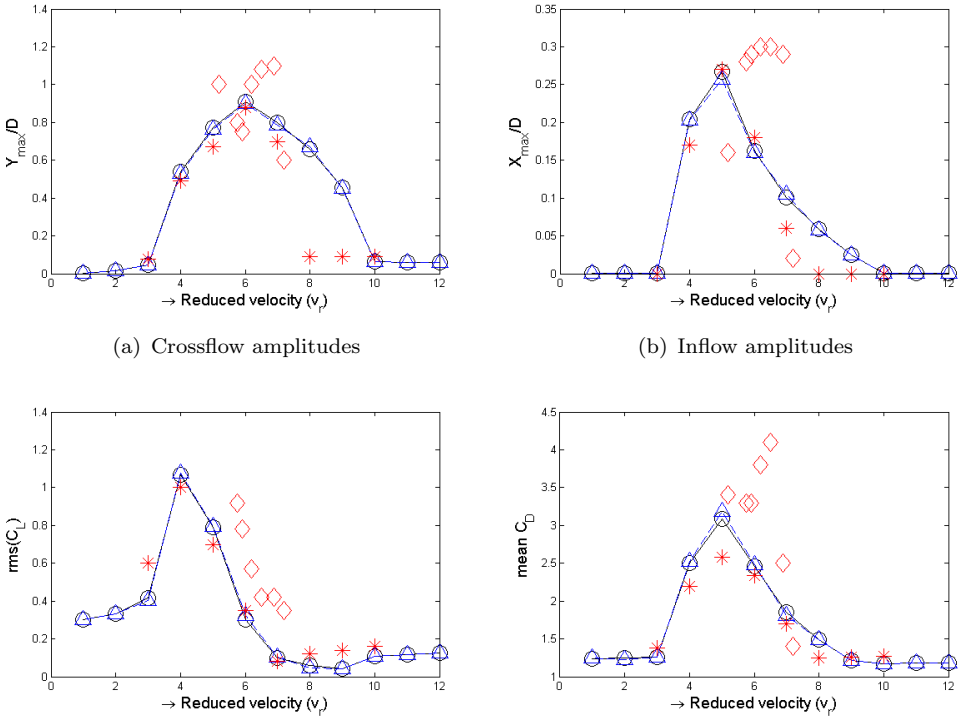

(a) Crossflow amplitudes

(b) Inflow amplitudes

(c) RMS of Lift coefficient

(d) Mean Drag coefficient

Figure 7.17: Variation of parameters with reduced velocity (v_r) for cylindrical vibration with 2-DoF (Mass ratio= $m^* = 2.0$, frequency ratio= $f_{Nx}/f_{Ny} = 2.0$, $Re = 150$), —o —present results (*ordered* meshfree nodes), —△ —present results (*randomized* meshfree nodes), $*$ results from Dai Zhou (2012) (at $= m^* = 2.0$, $= f_{Nx}/f_{Ny} = 2.0$, $Re = 150$), $\diamond$ Experimental results from Dahl et al. (2010) (at $= m^* = 5.7$, $= f_{Nx}/f_{Ny} = 1.9$, $Re = 15000 - 60000$)

Validation test case is run at $Re = 150$. Mass ratio is set as 2.0 and In-line to transverse natural frequencies (f_{Nx}/f_{Ny}) is set around 2.0. Reduced velocity (v_r) is calculated according to transverse natural frequency (f_{Ny}) and tests are conducted for $v_r = 1 - 12$. Solutions are obtained for both *ordered* and *randomized* meshfree nodal arrangements. Resultant amplitudes of cross-flow (Y_{max}) and in-flow (X_{max}) vibrations, mean values of drag coefficient ($\bar{C_D}$) and root mean square (RMS) values of lift coefficient (C'_L) are shown in Figure 7.17 along with numerical solutions obtained by Dai Zhou (2012) and experimental results from Dahl et al. (2010). It can be observed that the results do not change significantly with randomization of meshfree nodes. Maximum in-flow amplitude reaches to 0.256 at $v_r = 5.0$. Cross-flow amplitude achieves its maximum value ($Y_{max}/D = 0.905$) at $v_r = 6.0$. Similar values of maximum amplitudes are obtained by Dahl et al. (2010) and Dai Zhou (2012). Vibration amplitudes and lift and drag coefficients tend to increase dramatically as the resonance conditions are approached near $v_r = 6$. Beyond this regime, in-flow vibration amplitudes are almost zero and even cross-flow amplitudes are also very low. These observations are in agreement with previous studies.

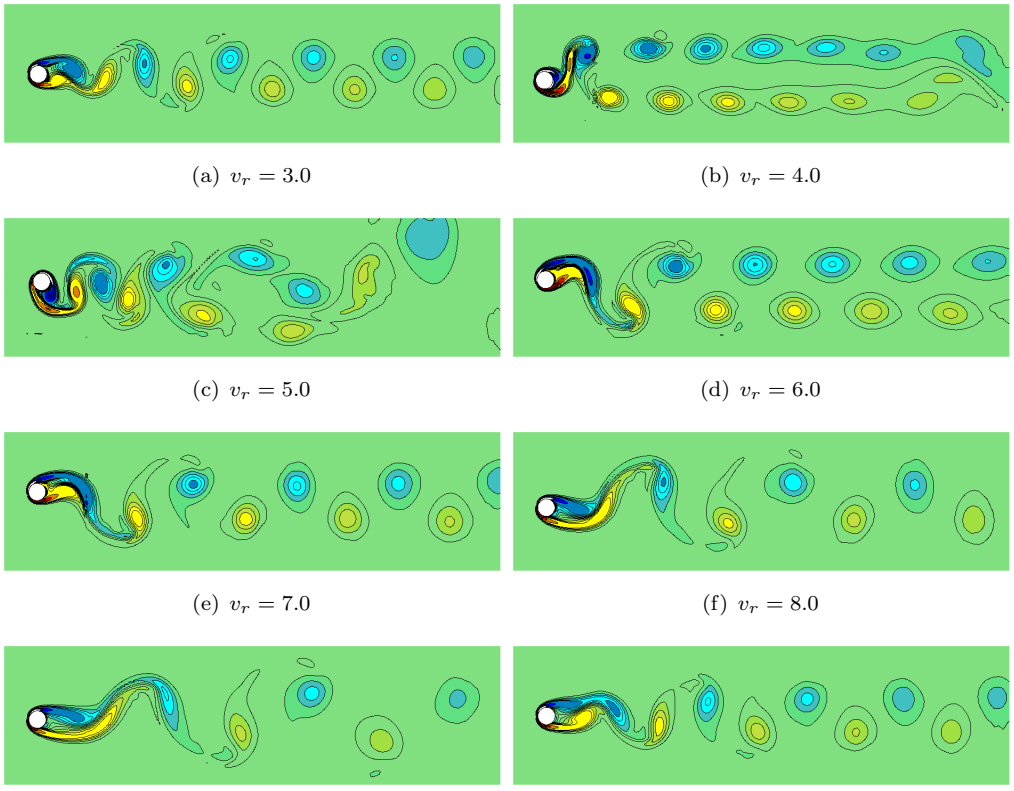

(a) $v_r = 3.0$ (b) $v_r = 4.0$

(c) $v_r = 5.0$ (d) $v_r = 6.0$

(e) $v_r = 7.0$ (f) $v_r = 8.0$

(g) $v_r = 9.0$ (h) $v_r = 10.0$

Figure 7.18: Vortex structure behind cylinder vibrating with 2-DoF at $f_{Nx}/f_{Ny} = 2.0$

7.6.1 Vortex structure of flow

Figure 7.18 shows vorticity profile behind the cylinder at various reduced velocities. For small values of reduced velocities (e.g. $v_r = 3$), where amplitudes of vibrations are also small, the vortex structure is similar to those for stationary cylinder cases (shown in Chapter 6). However, as reduced velocity increases the vibration amplitudes becomes higher resulting in two distinct rows of vortices appearing behind the cylinder. The distance between these rows increases at higher cross-flow amplitudes. With further increase in reduced velocities, the vibration amplitudes start to decrease. Therefore, rows of vortices gradually come close and ultimately merge with each other to form a single row of vortices. The vortex pattern is 2S for all the cases except that for $v_r = 5$. This means that two single opposite signed vortices (one positive and other negative vortex) are alternatively shed behind the cylinder. At $v_r = 5$, the vortex pattern is more like S+P. This means that shedding of a single vortex is followed by a pair of vortices with opposite sign. Difference in vortex pattern is caused by higher in-flow vibration amplitudes. However, this difference is caused by in-flow vibration as high as at $v_r = 5$ and frequency ratio of 2.0. For other cases, when in-flow vibration amplitudes are relatively small, vortex structure resumes its usual 2S pattern.

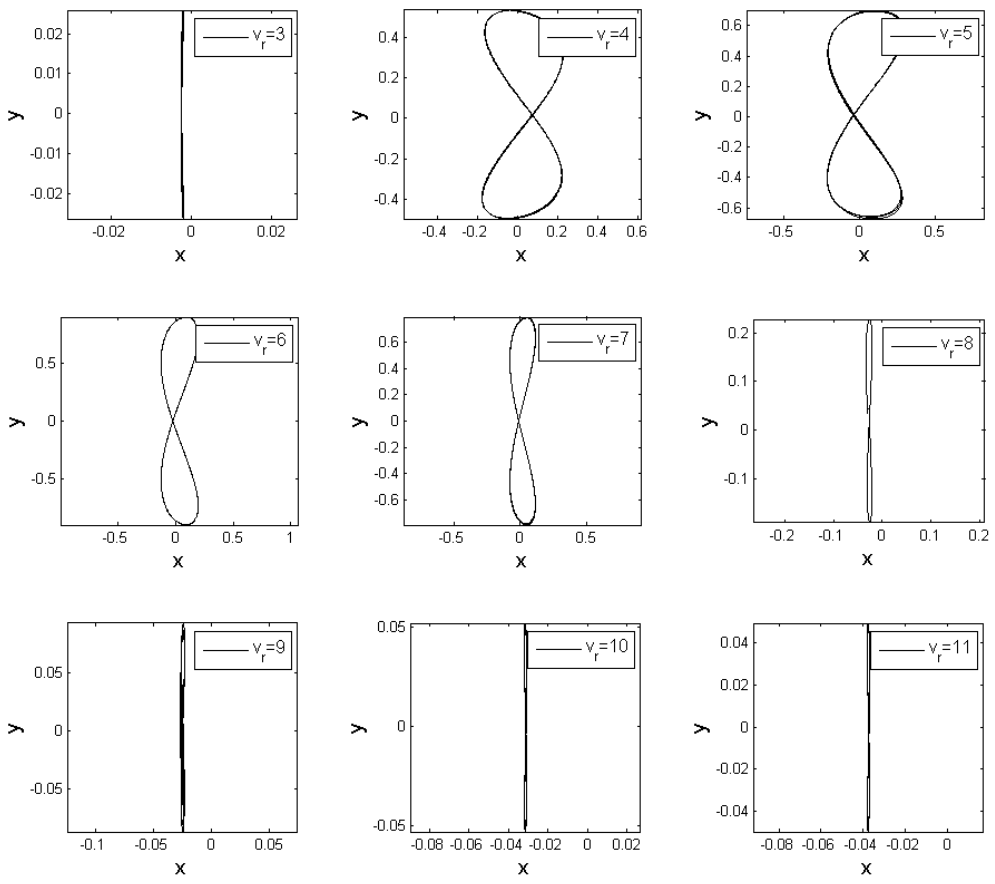

Figure 7.19: Cylindrical trajectories for 2-DoF problems. (Mass ratio= $m^* = 2.0$, frequency ratio= $f_{Nx}/f_{Ny} = 2.0$, $Re = 150$)

XY trajectories of cylinder at different reduced velocities are plotted in Figure 7.19. For the case when frequency ratio is 2.0, the dominant frequency in drag oscillation is twice that for lift. This results in significantly higher in-flow vibration amplitudes and therefore, the combined in-flow and cross-flow vibration trajectory typically depicts *figure-of-eight* motion. However, shape of the trajectory also depends upon reduced velocity. For cases where in-flow vibration is minimal, this *figure-of-eight* progressively thins out to show predominantly vertical vibration only. Figures 7.20(a)-7.20(k) show screen-shots of cylindrical motion during one complete cycle for $v_r = 5$. Shedding of two negative signed vortices from top side of the cylinder are obvious after positive signed vortex is shed from the bottom side. This would result in P+S type of vortex structure. Corresponding position of every screen-shot on XY trajectory is also indicated in Figure 7.20(l). It can be observed that the path direction is counter clockwise. Path direction remains unchanged in all the cases and these paths are found to be highly repeatable. Dahl et al. (2007) observed similar behaviour. They argued that counter clockwise path directions are highly repetitive and the path direction and orbit shapes are indicators of high harmonic force.

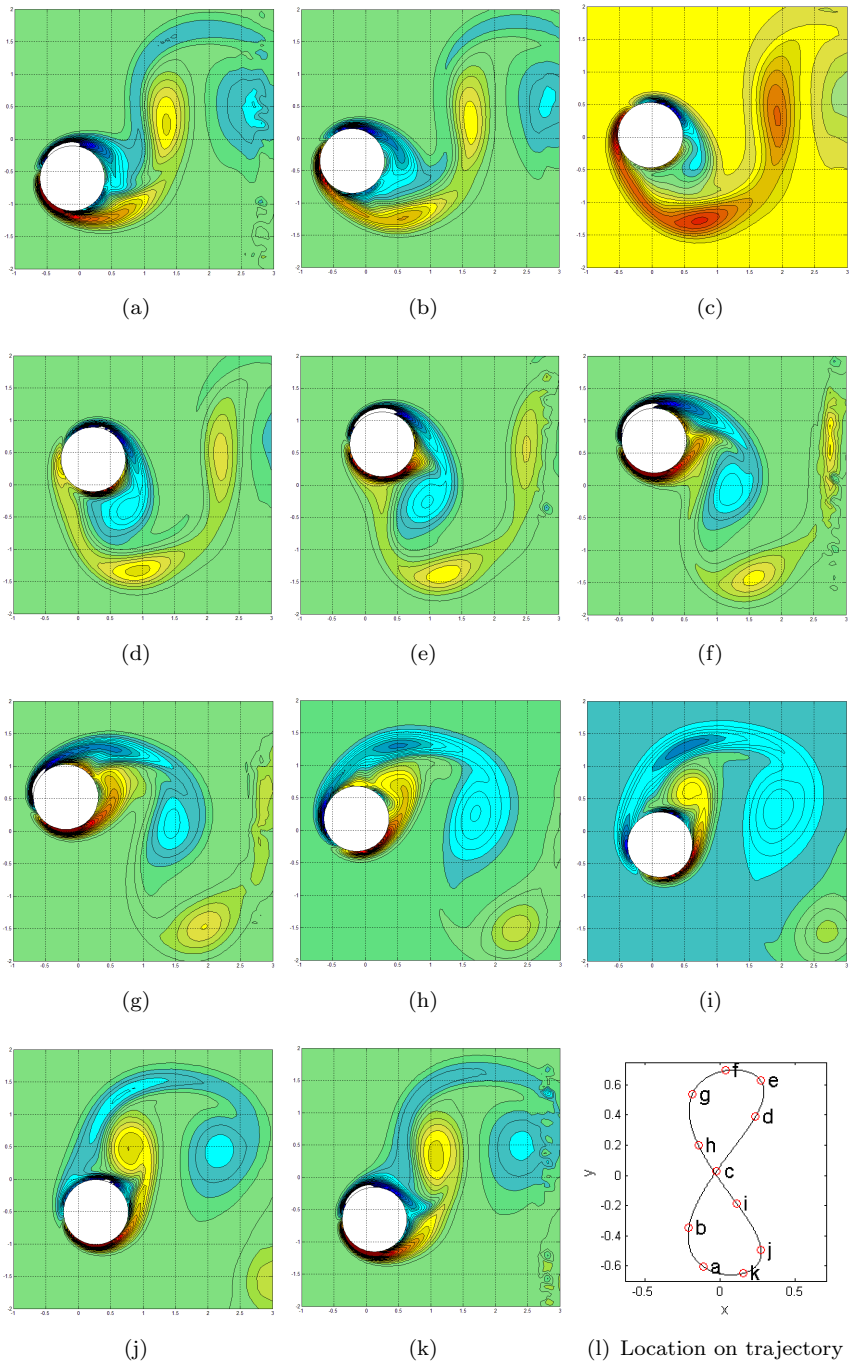

Figure 7.20: Screen-shots of vibrating cylinder at various time instances during one complete cycle. 2-DoF flow induced vibration of cylinder at $Re = 150$, $= m^* = 2.0$, $= f_{Nx}/f_{Ny} = 2.0$ and $v_r = 5.0$.

7.6.2 Effect of changing frequency ratio

The effect of changing frequency ratio $= f_{Nx}/f_{Ny}$ on system response (amplitudes of aerodynamic forces and solid motion) along in-flow and cross-flow directions is investigated here. For this purpose, the test cases are run at $Re = 150$ and $m^* = 1.25$. Figure 7.21 shows response curves at various reduced velocities v_r and frequency ratios. High

vibrational amplitudes (both cross-flow and in-flow directions) are observed for range of reduced velocities $4 \leq v_r \leq 9$ indicating the presence of resonance zone in both directions. Although this resonance zone is present at all tested values of frequency ratio, the vibration amplitudes dramatically increase typically at $= f_{Nx}/f_{Ny} = 2.0$. This increase is more pronounced for in-flow amplitudes where maximum vibrational amplitude soared by 3.4 times when frequency ratio was increased from 1.5 to 2.0. An increase of 1.25 times was observed in maximum cross-flow amplitude for same variation of frequency ratio. Moreover, reduced velocity corresponding to maximum vibrational amplitude tends to shift to higher value with increasing frequency ratio. However, bounds of resonant zone remain unaffected during this change.

Figure 7.21(c) indicate that lift coefficient largely remains unaffected by variation of frequency ratio except at $= f_{Nx}/f_{Ny} = 2.0$. At this value, significant reduction in the maximum value of C_L is observed. On the contrary, the drag coefficient depicts an increase in its maximum value at same frequency ratio.

In order to explain the presence of resonance zone between $4 \leq v_r \leq 9$, Strouhal numbers along cross-flow and in-flow directions are plotted in Figure 7.22. These strouhal numbers are obtained using first natural frequencies of lift and drag profiles over time. On the same plot corresponding natural frequencies of the structure are also plotted. In cross-flow directions, Strouhal numbers match closely with system natural frequency curves between $4 \leq v_r \leq 9$ yielding high cross-flow vibrational amplitudes. At $v_r = 9$, st_y for $f_{Nx}/f_{Ny} = 2.0$ is still close to f_{Ny} curve whereas st_y for $f_{Nx}/f_{Ny} = 1.0$ and 1.5 tend to deviate. As a result, cross-flow amplitude for $f_{Nx}/f_{Ny} = 2.0$ is higher at $v_r = 2.0$ than the other two cases.

Strouhal number curves for in-flow direction are quite interesting. Strouhal number values do not change much with changing frequency ratio. They largely remains close to $f_{Nx} = 2f_{Ny}$ curve between $4 \leq v_r \leq 9$. This means that Strouhal number along in-flow direction naturally remains twice its value along cross-flow direction. Therefore, for the case when $f_{Nx}/f_{Ny} = 2.0$, the value of St_x exactly matches with system natural frequency and high vibrational amplitudes are observed along in-flow direction. For the other cases, relatively higher amplitudes are caused by higher vortex shedding modes. However, these cannot produce very large vibration. For $f_{Nx}/f_{Ny} = 1.5$ case, st_x touches $f_{Nx} = 1.5f_{Ny}$ curve at $v_r = 4$. Therefore, highest in-flow amplitude is observed at this reduced velocity for $f_{Nx}/f_{Ny} = 1.5$ case.

7.6.3 Effect of changing mass ratio

The effect of changing mass ratio on system response has been investigated at $Re = 150$ and $f_{Nx}/f_{Ny} = 2.0$. At these settings, the solution parameters are obtained different values of mass ratio and for changing reduced velocities. The results are summarized

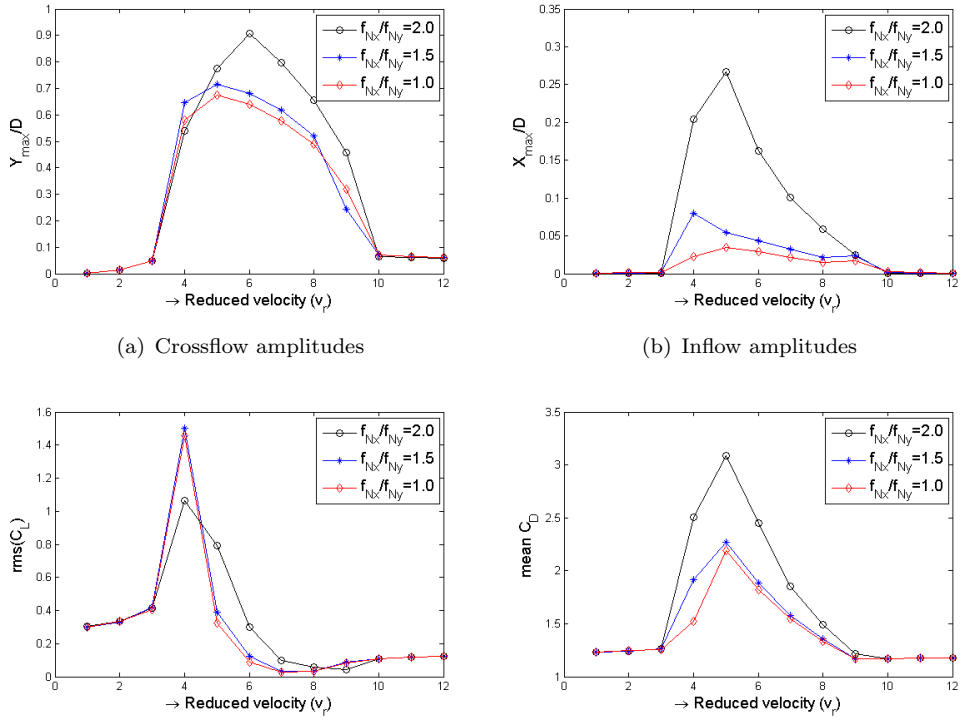

(a) Crossflow amplitudes

(b) Inflow amplitudes

(c) RMS of Lift coefficient

(d) Mean Drag coefficient

Figure 7.21: Variation in system response with changing frequency ratio (f_{Nx}/f_{Ny}) for cylindrical vibration with 2-DoF at $= m^* = 1.25$ and $Re = 150$. $-o-$ $f_{Nx}/f_{Ny} = 2.0$, $-*-$ $f_{Nx}/f_{Ny} = 1.5$, $-\diamond-$ $f_{Nx}/f_{Ny} = 1.0$

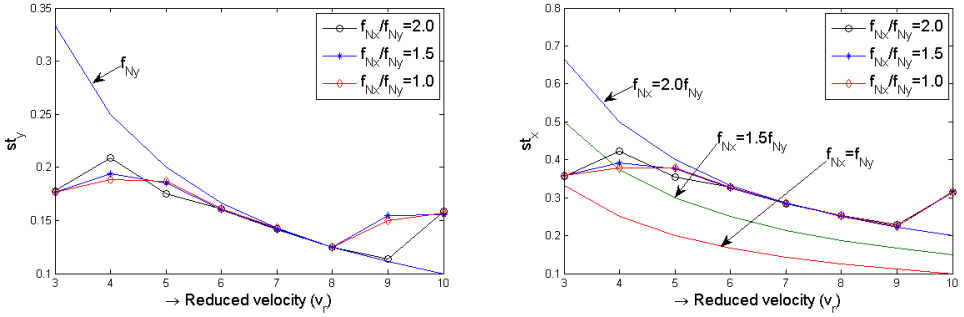

(a) Cross-flow direction

(b) In-flow direction

Figure 7.22: Variation of Strouhal number with reduced velocity (v_r) and frequency ratio (f_{Nx}/f_{Ny}) for cylindrical vibration with 2-DoF at $= m^* = 1.25$ and $Re = 150$. $-o-$ $f_{Nx}/f_{Ny} = 2.0$, $-*-$ $f_{Nx}/f_{Ny} = 2.0$, $-\diamond-$ $f_{Nx}/f_{Ny} = 1.0$

in the plots shown in Figure 7.23. The most prominent effect of changing mass ratio is that the resonance zone tends to shrink with increasing mass ratios. Though the peak values appear at same location (i.e same value of v_r), the lower and upper limits of high amplitude regime tend to squeeze inward with increasing mass ratio. The maximum vibration amplitudes remains largely unchanged until $m^* = 2.0$. However, they start to decline later and relatively lower amplitudes (both in-flow and cross-flow) are observed

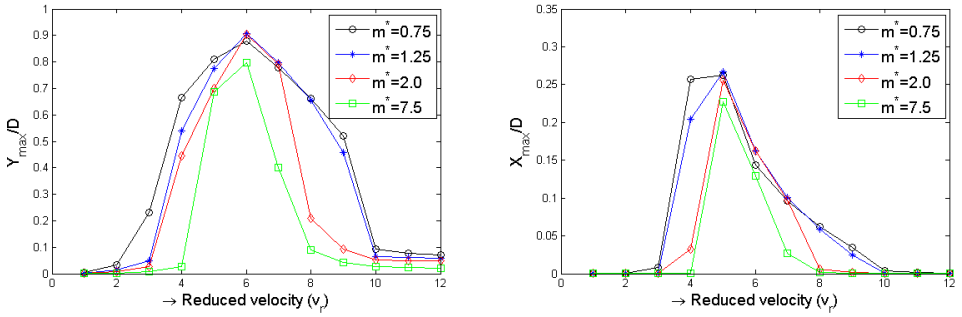

(a) Crossflow amplitudes

(b) Inflow amplitudes

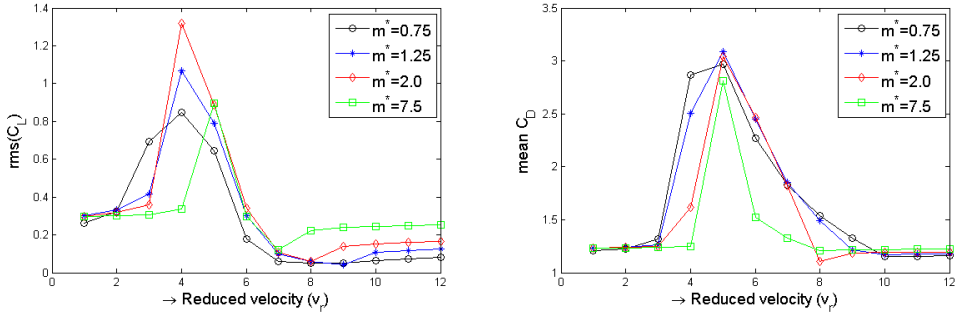

(c) RMS of Lift coefficient

(d) Mean Drag coefficient

Figure 7.23: Variation in system response with changing mass ratio for cylindrical vibration with 2-DoF at $f_{Nx}/f_{Ny} = 2.0$ and $Re = 150$. $-o-$ $m^* = 0.75$, $-*-$ $m^* = 1.25$, $-\diamond-$ $m^* = 2.0$, $-\square-$ $m^* = 7.5$

at $m^* = 7.5$. Mass ratio seems to have significant effect on lift coefficient. The maximum value of lift coefficient keeps increasing from $m^* = 0.75$ to $m^* = 2.0$. However, dramatic decline in lift coefficient is observed at $m^* = 7.5$. Moreover, the value of reduced velocity, corresponding to highest value of C_L, also shifts from 4.0 to 5.0. Beyond the resonance zone ($v_r \geq 10$), RMS value of C_L depicts a steadily increasing trend with increasing mass ratio whereas cross-flow amplitudes decrease during same range of v_r.

7.7 Flow around static airfoil

The Solution scheme is now used for solving incompressible flow, at various Reynolds numbers, around static and moving airfoil. The static tests are conducted for flow at $Re = 5000,\ 10000$ and 50000 around NACA0012 airfoil. In order to suppress instabilities caused by increased convection at high Reynolds number flow, stabilized momentum Eq. (7.20) is used here. The flow parameters are set according to properties of air. Followings are the flow parameters : Chord length $c = 1.0m$, density $\rho = 1.225kg/m^3$, dynamic viscosity $\mu = 1.8375N.s/m^2$. Free stream velocity U is calculated according to the required value of Reynolds number ($U = \mu Re/(\rho c)$). Hybrid grid around the airfoil is generated using the method discussed in Section 6.7.1. Computational grid is therefore,

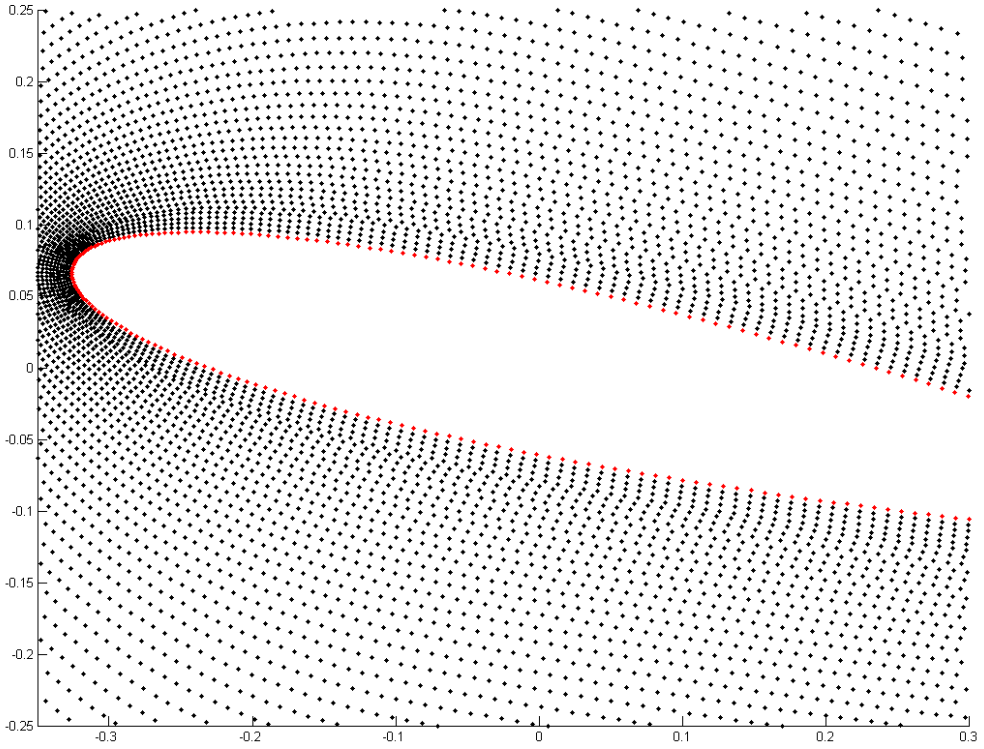

(a) Grid for $Re = 5000$ and 10000

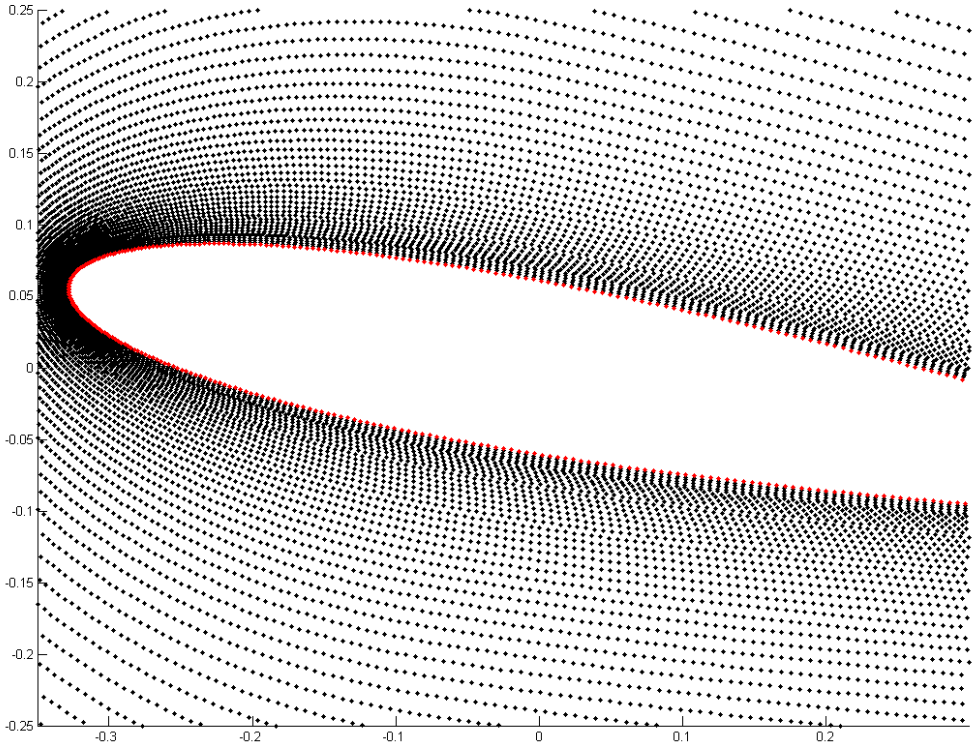

(b) Grid for $Re = 50,000$

Figure 7.24: Fluid grid around NACA0012 at different Reynolds numbers

similar to what is shown in Figure 6.34(a). At each value of Reynolds number, nodal resolution near airfoil surface is set to ensure sufficient number of nodal layers within the boundary layer region. Therefore, the grid for $Re = 50000$ is finer than that for $Re = 5000$ and 10000, near the airfoil, as shown in Figure 7.24. Boundary conditions are used as mentioned in Section 5.5. Time step is set as 5.0×10^{-4} for all cases.

In order to study the effect of stabilization term, the solutions are obtained for $Re = 10000$ and $\alpha = 10^o$ case at $t = 5$ *sec* with and without the use of stabilization term in the momentum equation. The resultant 3D velocity plots as well as velocity vector plots are shown in Figure 7.25. For the case without stabilization, significant fluctuation is observed in the velocity field at the upper side of airfoil as can be seen in Figures 7.25(a) and 7.25(c). A zoomed in view of area with fluctuations is shown in Figure 7.25(d). As the solution proceeded, these fluctuations were found to become more severe and ultimately caused breakdown of iteration process. Use of stabilized momentum equations however, managed to suppress these fluctuations. The velocity 3D plot shown in Figure 7.25(b) depicts smooth velocity profile when stabilized momentum equation is used. At high Reynolds numbers, use of stabilization is therefore, necessitated to avoid possible errors and breakdown of solution due to non-physical flow field fluctuations.

Static solutions are obtained at various angles of attack between $0 \leq \alpha \leq 20$. RMS values coefficient of lift C_L are plotted for $Re = 10000$ and $Re = 50000$ in Figures 7.26(a) and 7.26(b) respectively. At $Re = 10000$, the results are compared with numerical solution of Akbari and Price (2003) and experimental results of Alam et al. (2010). At $Re = 50000$, solutions are compared with experimental results from Alam et al. (2010) and Huang and Lee (1999). Effect of Reynolds number on lift, drag and moment coefficients over the airfoil is shown in Figure 7.27. A gradual increase can be observed in lift values with increasing Reynolds number in Figure 7.27(a). Moreover, coefficient of drag tends to be less at high Reynolds number before stall angle ($\approx 10^o$) due to lower viscous effects as can be seen in Figure 7.27(b). However at higher angles of attack, when effect of pressure drag becomes more dominant, overall drag coefficient becomes more for higher Reynolds numbers. Pressure drag increases at high Reynolds numbers due to increased lift. Variation of lift and drag with Reynolds number is in agreement with previous studies. For example, Massey (1979) presented coefficient of lift (C_L) and drag (C_D) for a particular airfoil at two different Reynolds numbers and at $\alpha = 10^o$. They observed an increase in the value of C_L from 0.49 to 1.4 when the Reynolds number was increased from 21000 to 430000. The value of C_D reduced from 0.19 to 0.07 during same variation of Reynolds number.

Instantaneous vortex profiles are also shown at various angles of attack for three Reynolds numbers in Figure 7.28. At $Re = 5000$, the flow separates from the airfoil upper surface after leading edge and is not able to reattach later. Also at $Re = 10000$, the flow separates early but this time the flow does show a tendency to reattach at $\alpha = 10^o$ resulting in relatively higher lift before the onset of stall. However, there is still a big separation

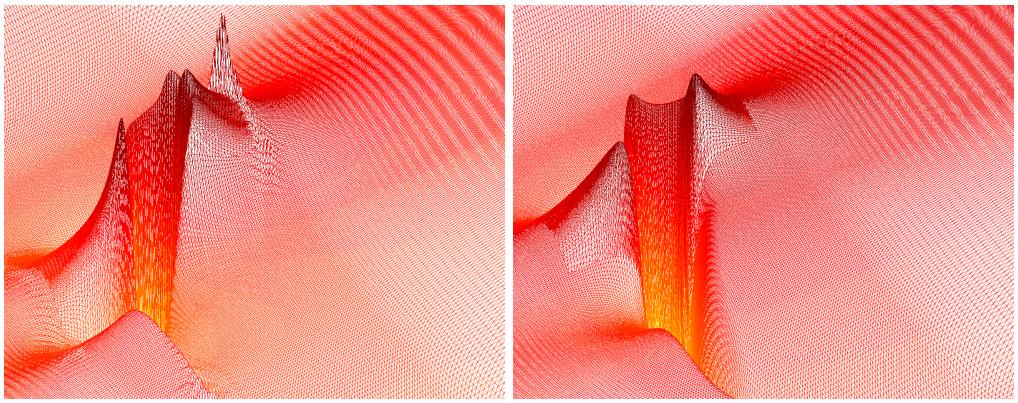

(a) 3D-Velocity plot (without stabilization)

(b) 3D-Velocity plot (with stabilization)

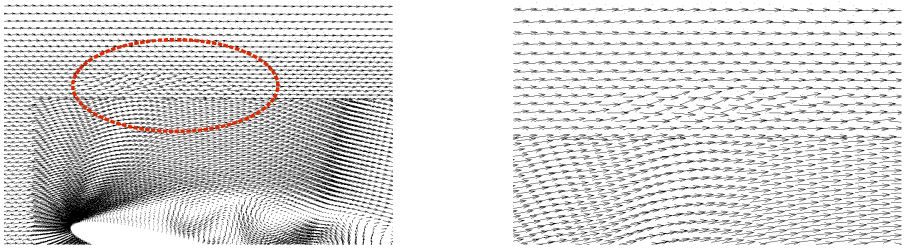

(c) Velocity vector plot (without stabilization)

(d) Zoomed in view

Figure 7.25: Comparison of flow around NACA0012 with and without stabilization at $Re = 10000$, $\alpha = 10^o$, $t = 5.0$ *sec*

region between flow detachment and reattachment points as shown in Figure 7.28(e). As the angle of attack is increased, the reattachment point moves upstream reducing the size of separated flow region and increasing the lift (see Figure 7.28(f)). At $Re = 50000$, an increased tenancy of the flow to re-attach the airfoil surface is observed. At $\alpha = 5^o$, the flow reattaches soon after separation. The separation region therefore remains sufficiently small even at $\alpha = 10^o$ and therefore large amount of lift is produced. However, as the angle of attack is further increased, separation region progressively becomes larger causing a decline in lift at $\alpha = 15^o$. Oscillating vortex profiles in all cases result in time varying profiles of aerodynamic forces. Therefore, RMS values of lift, drag and moment coefficients are shown in Figures 7.26 and 7.27.

7.8 Flow induced airfoil vibration

After demonstrating the applicability of stabilized coupled meshfree-mesh based solver for flow around static airfoil, the solution scheme is now used for flow induced airfoil vibration problem. For this purpose, flow cases are solved around NACA0012 airfoil with two degrees of freedom. Airfoil is able to vibrate vertically as well as rotate about

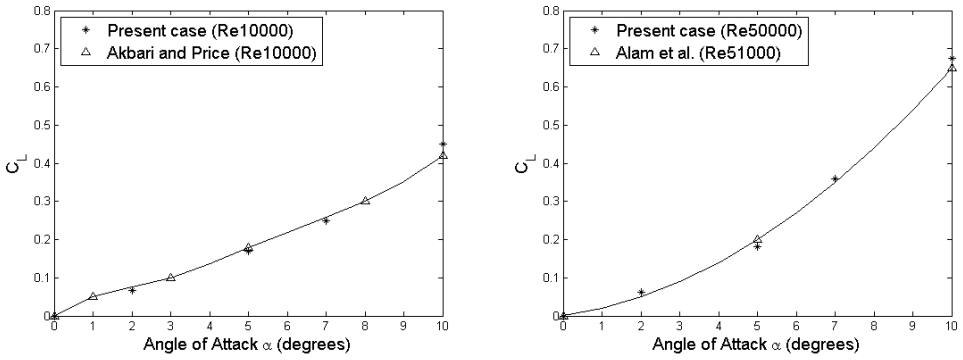

(a) $Re = 10000$ (b) $Re = 50,000$

Figure 7.26: C_L vs α curves for NACA0012 airfoil at various Reynolds number

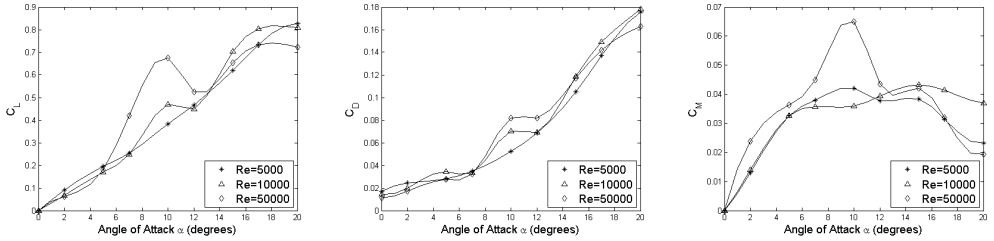

(a) C_L *vs* α (b) C_D *vs* α (c) C_M *vs* α

Figure 7.27: Variation of lift, drag and moment coefficients with Reynolds number at NACA 0012 airfoil

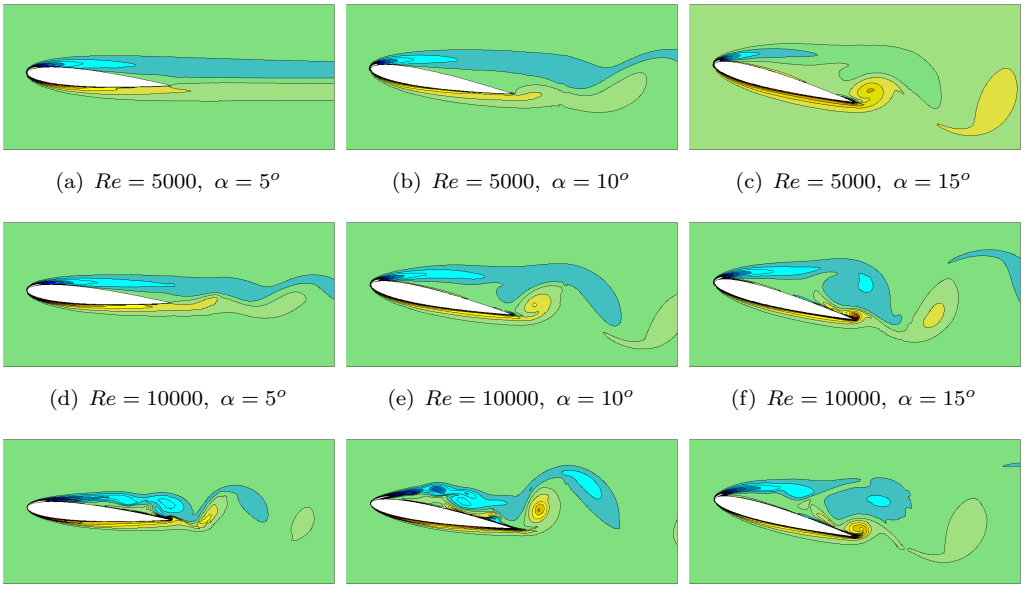

(a) $Re = 5000,\ \alpha = 5^o$ (b) $Re = 5000,\ \alpha = 10^o$ (c) $Re = 5000,\ \alpha = 15^o$

(d) $Re = 10000,\ \alpha = 5^o$ (e) $Re = 10000,\ \alpha = 10^o$ (f) $Re = 10000,\ \alpha = 15^o$

(g) $Re = 50000,\ \alpha = 5^o$ (h) $Re = 50000,\ \alpha = 10^o$ (i) $Re = 50000,\ \alpha = 15^o$

Figure 7.28: Instantaneous vortex profiles around NACA0012 airfoil at various Reynolds numbers and angles of attack

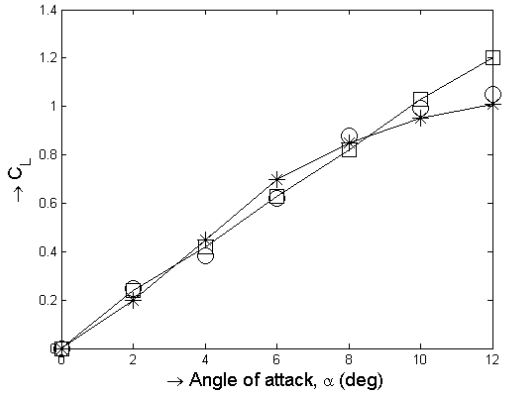

Figure 7.29: C_L vs α plots for NACA0012 airfoil, o present solution at $Re = 8 \times 10^5$, * solution from Critzos et al. (1955) at $Re = 5 \times 10^5$, □ solution from Critzos et al. (1955) at $Re = 1.8 \times 10^6$

its elastic axis as shown in Figure 2.4(b). Motion of airfoil, under fluid forces, will therefore be governed by set of differential Eqs. (2.31) and (2.32). Interaction of fluid forces and solid displacement is realized by a closely coupled FSI algorithm with reduced fluid domain (CFSI-RFD). Only meshfree zone participates in the inner FSI iterations to reach fluid-solid convergence as discussed in Section 7.2. Grid configuration is the same as in discussed in Section 6.7.1. Airfoil chord length is set as $c = 0.3\ m$, fluid density is $\rho = 1.225\ kg.m^{-3}$ and kinematic viscosity is $\nu = 1.5 \times 10^{-5}\ m.s^{-2}$. Dynamic test cases are run for free stream velocity in the range of $U = 20-45\ m/s$. This corresponds to flow Reynolds number range $Re = 4 \times 10^5 - 9 \times 10^5$. At such high Reynolds numbers, use of stabilization term is necessary to achieve stable solution. Therefore, stabilization term is included in the flow equations. Moreover, it is understood that the use of a suitable turbulence model might be necessary for high Reynolds number problems especially to get accurate drag values. However, drag does not play critical role in aero-elastic problems with vertical vibrations and therefore scope of this research is limited to the use of laminar solver only. Similar approach has also been followed in previous works by Sváček et al. (2007) and Feistauer et al. (2011) also.

Prior to running flow induced vibration cases, validation has been done by running static solutions at above mentioned flow parameters with $Re = Uc/\nu = 800000$ and at range of angles of attack $\alpha = 0 - 14$. Resultant lift coefficients have been compared with standard data from Critzos et al. (1955) in Figure 7.29. Lift coefficient values from this solution are in agreement with standard data before stall angle.

Dynamic problem has been solved using following structural dynamics parameters: $m = 0.08622\ kg$, $S_\alpha = -0.000779673\ kg.m$, $I_\alpha = 0.00048791\ kg.m^2$, $k_h = 105.109\ N.m^{-1}$, $k_\alpha = 3.695582\ N.m/rad$, $span = l = 0.05\ m$, $d_h = 0.001k_h$ and $d_\alpha = 0.01k_\alpha$. Elastic axis is at $0.4c$ aft of leading edge. Airfoil is initially kept at an angle of attack of 5^o. To avoid possible instability caused by initial numerical fluctuations, the airfoil vibration is allowed when the flow is already stabilized around the arfoil. Time profile of

pitch angle (α) and vertical displacement (y) are shown in Figure 7.30 for different free stream velocities. The divergence is observed for flow velocities greater than 35.0 m/s. The solution at $U = 45$ m/s is unstable due to very high vibrational amplitudes. The solutions are compared with NASTRAN flutter analysis from Cecrdle and J (2002) which was carried using similar flow and structural parameters. According to Cecrdle and J (2002), critical velocity for divergence is 37.7 m/s and that for flutter is 42.4 m/s. These values are in agreement with what are found in present study study. The results are also in agreement with computational solutions from Sváček et al. (2007) and Furmnek and Kozel (2013). Pressure and vorticity profiles around the airfoil at various pitch angles are shown in Figure 7.31.

Above calculations are carried out using closely coupled FSI with partial fluid domain. Calculation for simulation time of 0.1 sec were performed in 295 sec on Intel®2.4 GHz processor. On the contrary, similar calculations for full fluid domain were carried out in 840 sec on same machine. Therefore, the computation time was reduced by 65 percent by reducing the fluid domain for inner FSI iterations.

7.9 Energy harvesting using flow around oscillating airfoil

In the past decade, there has been a growing interest of researchers in extracting energy from tidal stream and wind. The energy available in moving fluid (wind or tidal power) can be converted to useful mechanical work in a variety of ways. Traditionally this has been achieved using rotary turbines. Lately, oscillating foils are increasingly becoming the focus of research for energy harvesting devices (Xiao and Zhu (2014); Young et al. (2014)). Compared with conventional rotary turbines, these bio inspired energy converters are less noisy, possess greater structural resilience and are operable even in shallow water (Xiao and Zhu (2014)). Flapping foil based power extracting systems developed so far can be classified in three categories:

1. Systems with forced (or prescribed) pitching and heaving motion. These are also called fully activated systems.
2. Systems with imposed pitching and induced heaving motion. These are also called semi-activated systems.
3. Systems with flow induced flow-induced pitching and heaving motion. These are called fully-passive systems.

The performance of these energy harvesters largely depends upon vortex structure and flow behaviour around oscillating airfoil. It is therefore, important to understand flow behaviour and performance and efficiency of these mechanism at various system parameters.

7.9.1 Extracted power by oscillating and heaving airfoil

Let us consider an airfoil in simultaneous pitch and heave as shown in Figure 7.32. For a wing with unit depth, the power extracted during heaving and pitching motion can be expressed mathematically as (Kinsey and Dumas (2008)):

$$Power\ extracted\ due\ to\ heaving\ = P_y(t) = h(t)V_y(t) \tag{7.29}$$

$$Power\ extracted\ due\ to\ pitching\ = P_\theta(t) = M(t)\omega(t) \tag{7.30}$$

where $h(t)$, $V_y(t)$, $M(t)$ and $\omega(t)$ are instantaneous heave, vertical velocity, pitching moment and angular velocity in pitch respectively. The total power extracted over one cycle can be calculated by integrating the extracted power over time:

$$Total\ power\ extracted\ in\ one\ cycle\ = P = 1/T \int (P_y(t) + P_\theta(t))\, dt \tag{7.31}$$

In non-dimensionalized form, the extracted power is written as:

$$C_{op} = \frac{P}{1/2\rho U_\infty^3 c} \tag{7.32}$$

Therefore, coefficient of extracted power is written as:

$$C_{op} = C_{p_y} + C_{p_\theta} = \frac{1}{T} \int \left(C_y(t) \frac{V_y(t)}{U_\infty} + C_M(t) \frac{\omega(t)c}{U_\infty} \right) dt \tag{7.33}$$

Power extraction efficiency η is defined as the ratio of extracted power to power available:

$$\eta = \frac{P}{P_a} = \frac{P_y + P_\theta}{1/2\rho U_\infty^3 d} = C_{op} \frac{c}{d} \tag{7.34}$$

where d is the overall extent of airfoil vertical displacement as shown in Figure 7.32.

7.9.2 Energy extraction through fully activated system

An airfoil in simultaneous pitch and heave may impart as well as extract energy from oncoming flow in various modes of its motion. Carefully tuned pitch and heave motion of airfoil can therefore, result in net energy extracted from oncoming flow. Such oscillating airfoil acts as turbine. Kinsey and Dumas (2008) performed a parametric study for such an airfoil in the power extraction regime and related overall energy extraction condition

Table 7.4: Comparison of aerodynamic parameters and power extraction efficiency over NACA0015 airfoil at $Re = 1100$ and $H_0 = c$

Source	$\bar{C_D}$	$\hat{C_L}$	$\eta(\%)$
	Case-I: $\theta_0 = 76.33,\ \omega = 0.28\pi$		
Present	1.93	2.15	34.66
Kinsey and Dumas (2008)	2.014	1.91	33.7
Wu et al. (2014)	2.107	1.97	34.7
	Case-II: $\theta_0 = 60.0,\ \omega = 0.36\pi$		
Present	0.72	1.238	12.04
Kinsey and Dumas (2008)	0.727	1.256	11.4
Wu et al. (2014)	0.711	1.248	12.2

with a feathering parameter $\mathcal{X}$. In current work, flow around NACA0015 airfoil, subject to prescribed pitching and heaving motion, was solved in Section 6.7.4 at two different sets of parameters. The results of these simulations are used here for calculating the coefficient of performance and power extraction efficiency values for corresponding system parameters using equations described in Section 7.9.1. As mentioned earlier (in Section 6.7.4), the pitching and heaving motion of the airfoil is governed by following equation (Kinsey and Dumas (2008)):

$$\theta(t) = \theta_0 \sin(\omega t) \tag{7.35}$$

$$h(t) = H_0 \sin(\omega t + \phi) \tag{7.36}$$

Therefore, pitch and heave displacement rates over time can be expressed as:

$$\frac{d\theta}{dt} = \omega\theta_0 \cos(\omega t) \tag{7.37}$$

$$\frac{dh}{dt} = \omega H_0 \cos(\omega t + \phi) \tag{7.38}$$

For test case with $\theta_0 = 76.33^o$, $\omega = 0.28\pi$, time variation of heave and pitch displacement rates (dh/dt and $d\theta/dt$) of airfoil are shown in Figure 7.33(a), during a single oscillation period. Coefficients of lift and drag forces as well as coefficient of performance are plotted in Figure 7.33(b) during the same period. These parameters are used to calculate the power extraction efficiency of the system using Eq. (7.34). Results are also obtained for test case with $\theta_0 = 60.0^o$ and $\omega = 0.36\pi$. Mean drag coefficient $\bar{C_D}$, maximum lift coefficient $\hat{C_L}$ and energy extraction efficiency η are shown in Table 7.4. Results found here are in good agreement with previous solutions from Kinsey and Dumas (2008) and Wu et al. (2014).

Table 7.5: Comparison of maximum values of coefficients of lift ($C_{L_{max}}$), mean values of coefficients of drag ($\bar{C}_D$) and maximum values of coefficients of moment ($C_{M_{max}}$) for pitching-motion-activated-flapping NACA0015 airfoil

Mechanical Parameters	Source	$C_{L_{max}}$	$\bar{C}_D$	$C_{M_{max}}$
$Re = 1100$, $\theta_0 = 15^o$, $f^* = 0.2$, $d^* = 2\pi$, $k^* = 10$, $m^* = 1$	Wu et al. (2014)	0.704	0.179	-
	Present work	0.69	0.17	-
$Re = 1100$, $\theta_0 = 30^o$, $f^* = 0.1$, $d^* = \pi$, $k^* = 0$, $m^* = 1$	Wu et al. (2014)	0.905	0.345	-
	Present work	0.885	0.334	-
$Re = 1000$, $\theta_0 = 75^o$, $f^* = 0.12$, $d^* = \pi$, $k^* = 0$, $m^* = 0.1022$	Deng et al. (2015)	2.0	-	0.33
	Present work	2.017	-	0.31
$Re = 1000$, $\theta_0 = 75^o$, $f^* = 0.22$, $d^* = \pi$, $k^* = 0$, $m^* = 0.1022$	Deng et al. (2015)	2.8	-	0.6
	Present work	2.55	-	0.56

7.10 Pitching-motion-activated-flapping foil for power extraction

Semi-activated flapping airfoil system is studied here. In this case, the airfoil is subjected to a prescribed pitching motion about its elastic axis and is allowed to move freely along heave axis due to fluid forces. Airfoil is mounted on a translational spring-damper system. When, airfoil is subjected to periodic pitch oscillation, it causes corresponding variation of fluid forces over time. These time varying fluid forces induce heaving motion. Such mechanisms have recently gained focus for their potential application in tidal and wind energy extraction systems (Wu et al. (2014); Deng et al. (2015)). Pitch displacement ($\theta(t)$) for the airfoil is defined by Eq. (6.5). Resulting heave displacement is calculated using Eq. (2.33). Solid equations are solved in non-dimensionalized form. The non-dimensionalized mass (m^*), damping (d^*), spring stiffness (k^*) and frequency (f^*) are defined as:

$$m^* = \frac{m}{\frac{1}{2}\rho c^2},\ d^* = \frac{d}{\frac{1}{2}\rho U c},\ k^* = \frac{k}{\frac{1}{2}\rho U^2},\ f^* = \frac{fc}{U}$$

where ρ, U and c are flow density, free stream velocity and airfoil chord length respectively. The test cases are run for flow around NACA0015 airfoil. with its elastic axis located at a distance $c/3$ from leading edge. Results are obtained at $Re = 1100$ and $Re = 1000$. Laminar flow equations can safely be used at these Reynolds numbers. Simulations are run at four different sets of mechanical parameters (θ_0, f^*, d^* k^*, m^*) and resultant values are summarized in Table 7.5. The results are compared with the solutions from Wu et al. (2014) and Deng et al. (2015) respectively and are found to be in good agreement with the previous studies. For both test cases conducted at $Re = 1000$, variation of C_L during a single pitch oscillation period is compared, in Figure 7.34. It can be observed that the peak value of lift coefficient increases at higher frequency (f^*). Similar behaviour was observed by Wu et al. (2014) in their work.

After performing validation, test cases are run to study the effect of Reynolds number (Re) and translational stiffness k on system response and power extraction efficiency of semi-activated flapping foil. For this purpose, tests are conducted for varying values of pitch frequencies ($f = \omega/(2\pi)$) at three different Reynolds numbers ($Re = 5000,\ 10000$ and 50000) for NACA0015 airfoil. Effect of changing elastic stiffness (k) is also studied by performing calculations at two different values ($k = 10$ and $k = 100$). Values of non-dimensionalized mass and damping constant are set as $m^* = 1$ and $d^* = 2\pi$ for all test cases and elastic axis is placed at $c/3$ aft of leading edge.

7.10.1 Effect of changing stiffness

In order to investigate the effect of changing stiffness on system response, the curves of rms values lift coefficients ($C_{L_{rms}}$), power extraction efficiency (η), rms of moment coefficient ($C_{M_{rms}}$) and rms of heave displacement ($Y_{C_{rms}}$) are plotted against changing values of pitching frequency (f^*) at $Re = 5000$ in Figure 7.35. Power extraction efficiency (η) is calculated using Eqs. (7.32) - (7.34). It can be observed that lift coefficient initially reduces with increasing frequency (f^*) but later tends to increase. This behaviour is similar for both values of k^*. However for $k^* = 100$, values of $C_{L_{rms}}$ are higher and subsequent rise (after reaching local minimum) is also more prominent compared with that for $k^* = 10$. The power extraction efficiency (η) always reduces with increasing pitching frequency. At $k^* = 10$, positive values of η are obtained for the range of frequencies tested. This indicates that net energy is extracted from the flow. Moreover, the drop in the values of η is rather linear. On the contrary, power extraction efficiency values are negative for $k^* = 100$. Moreover, the slope of η with f^* keeps decreasing with increasing values f^*. These trends are similar to what were observed by Wu et al. (2014) in their work.

7.10.2 Effect of changing Reynolds number

The response of semi activated flapping foil is studied with changing Reynolds number. For this purpose, three different Reynolds numbers ($Re = 5000,\ 10000$ and 50000) are considered. System response curves at different Reynolds numbers and at $k^* = 10$ are shown in Figure 7.36. Similar plots $k^* = 100$ are shown in Figure 7.37. At low pitching frequencies, $C_{L_{rms}}$ is higher for higher Reynolds numbers. This aspect is particularly prominent at $k^* = 100$. However, this difference in the values of $C_{L_{rms}}$ diminishes at higher values of f^*. Similarly, at $f^* = 0.1$, the power extraction efficiencies are also higher for high values of Re. But the efficiency values become almost similar for higher values of f^*. Therefore, it can be stated that effect of flow Reynolds number on efficiency of pitching-motion-activated-flapping-foil is more prominent at lower values of pitching frequencies. At higher values of f^*, the Reynolds number does not significantly affect the efficiency of the system.

Instantaneous flow vortex structures at different stages of periodic pitch oscillations are shown for the three Reynolds number in Figure 7.38. The flow seperation occurs close to leading edge during pitch-up and pitch-down motion. For $Re = 5000$, the detach flow does not re-attaches the airfoil surface. However as the Reynolds number increases, the inertial forces in the flow enable it to re-attach the airfoil surface after it has been separated due to pitching motion. As a result, the lift can achieve higher values both in positive and negative directions. Variation of C_L during a complete pitch oscillation period has been plotted for all the three Reynolds numbers in Figure 7.39. It can be observed that C_L profiles for $Re = 10000$ and 50000 tend to rise further after a temporary *ridge* at around $t = T/4$. As a result, higher peak lift values are achieved. The *ridge* is caused due to leading edge vortex separation. However, as the flow re-attaches the airfoil, lift starts to increase further high. The *ridge* in the lift profile is more prominent at $Re = 50000$ due to more effective flow re-attachment which can also be seen in corresponding vortex plots shown in Figure 7.34.

7.11 Conclusion

Closely coupled FSI algorithm with reduced fluid domain is found to be highly efficient for flow induced vibration problems. Accuracy of the solution scheme is greatly improved with relatively smaller computational overheads compared with conventional closely coupled FSI systems. The computational cost (in terms of calculation time) is found to be around 30 % less than that for closely coupled system with full fluid domain. It is envisaged that this computational advantage will be even more pronounced for problems which require a larger number of inner iterations to converge (like problems involving flexible solids). Use of reduced fluid domain is greatly facilitated by inherent capability of meshfree-mesh based solver over hybrid grid as it already solves the flow in two different grid zones separately. Accuracy of the solution is verified for flow around solids with one and two degrees of freedom. The solution scheme is found to be capable of providing an insightful information about complex flow structure around vibrating bodies. A Journal paper, outlining the details of this scheme and its findings, has been submitted for review Javed et al. (2015). The scope of present study has been restricted to low Reynolds number flow around rigid solid objects. However, meshfree methods possess great capabilities to deal with flexible solids with multiple degrees of freedom. Therefore, future studies may be focused on investigating the applicability of presented scheme for such problems.

The problems relating to high Reynolds number need special treatments to deal with stability related issues. In this regard, use of stabilized momentum equation enables the application of coupled solution scheme for high Reynolds number problems and enhances the applicability of this solver for a wide range of application including wing flutter analysis, energy harvesting problems etc. At high Reynolds numbers, turbulent

flow equations are better representative of flow behaviour. However, the scope of this study has been limited to laminar flows only. Future studies may therefore, focus the use of turbulent flow equations with similar solution method.

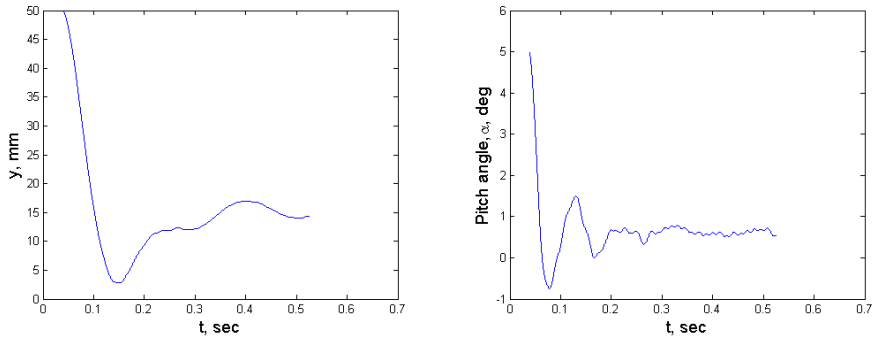

(a) $U_\infty = 20\ m/s$

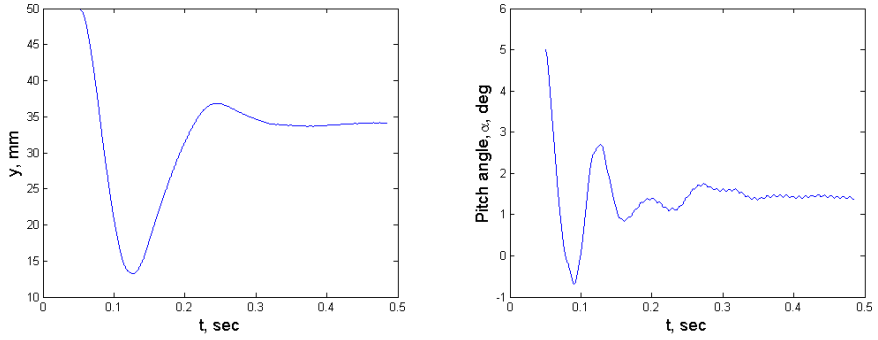

(b) $U_\infty = 30\ m/s$

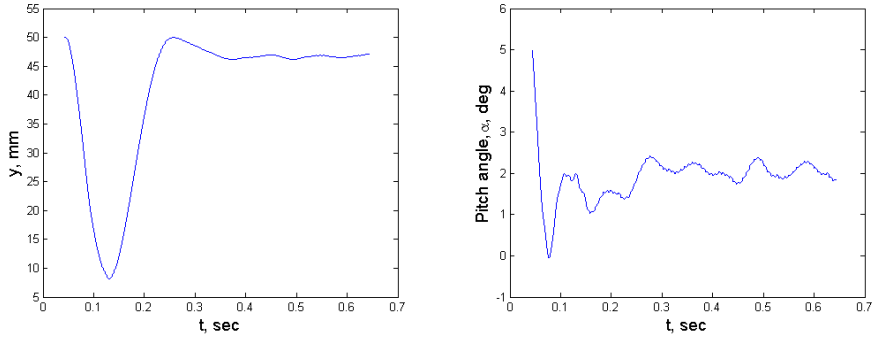

(c) $U_\infty = 35\ m/s$

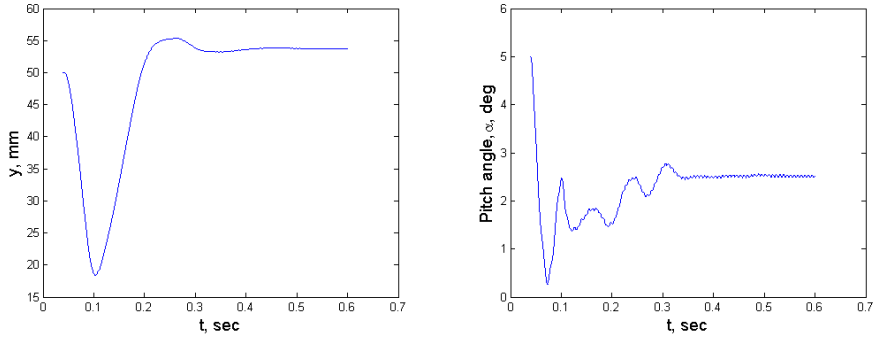

(d) $U_\infty = 37.5\ m/s$

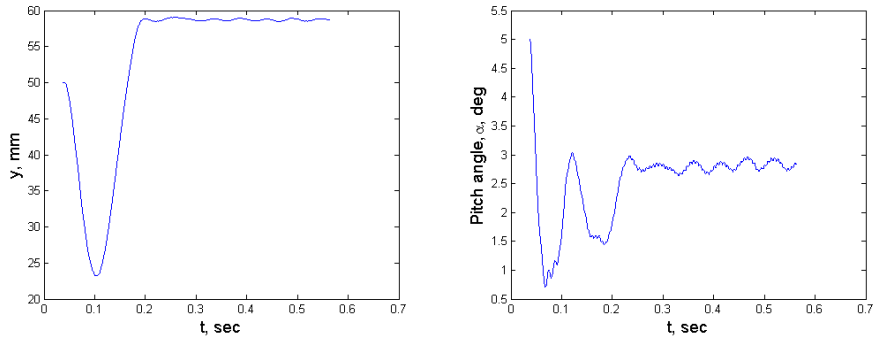

(e) $U_\infty = 40\ m/s$

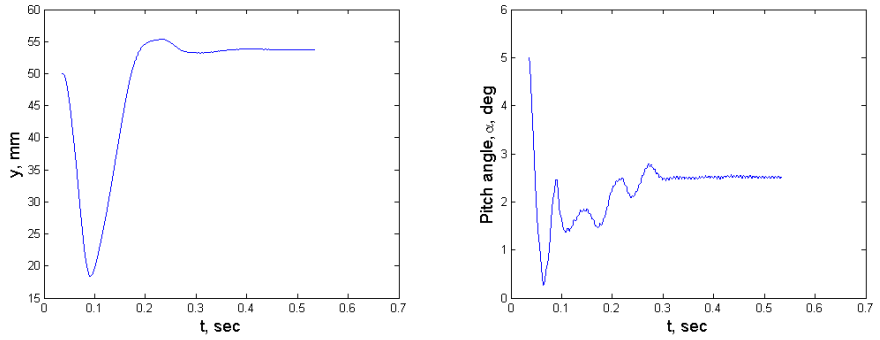

(f) $U_\infty = 42.5\ m/s$

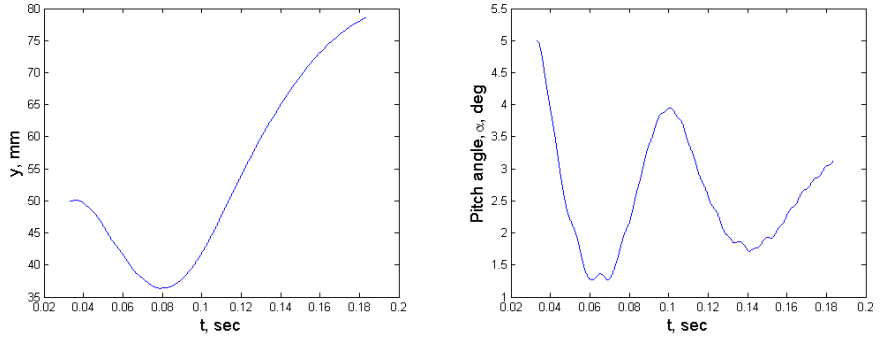

(g) $U_\infty = 45\ m/s$

Figure 7.30: Time profiles of pitch angle α and vertical position for flow induced vibration of NACA 0012 airfoil

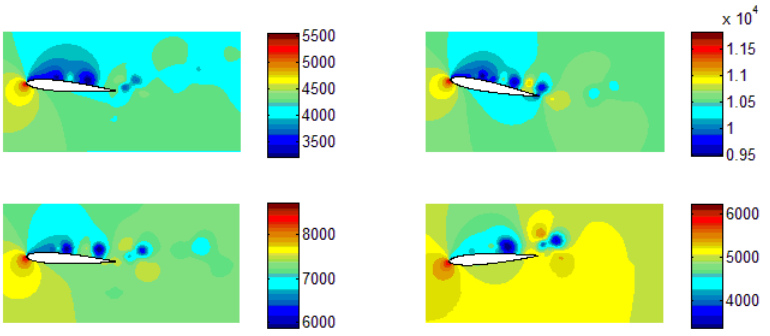

(a) Pressure profiles at different time instances

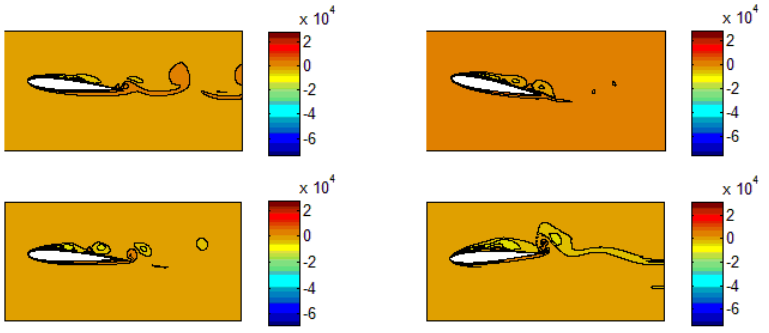

(b) Vorticity profiles at different time instances

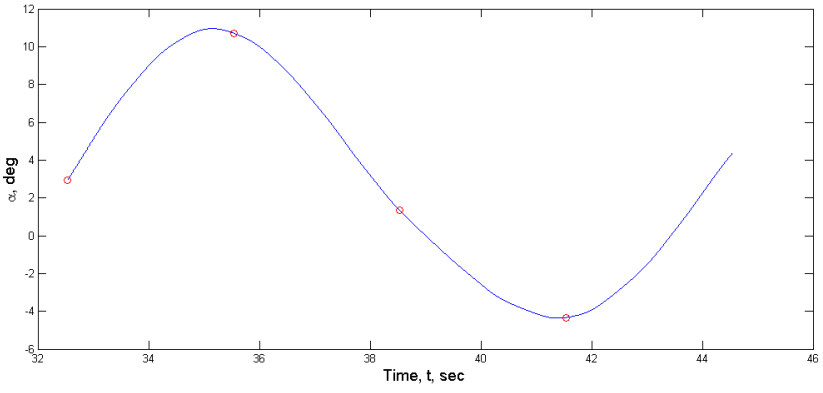

(c) Pitch angle variation, marked points correspond instances where pressure and vorticity profiles, in (a) and (b), are captured

Figure 7.31: Flow profiles around NACA0012 during aeroelastic vibration at $Re = 9 \times 10^5$.

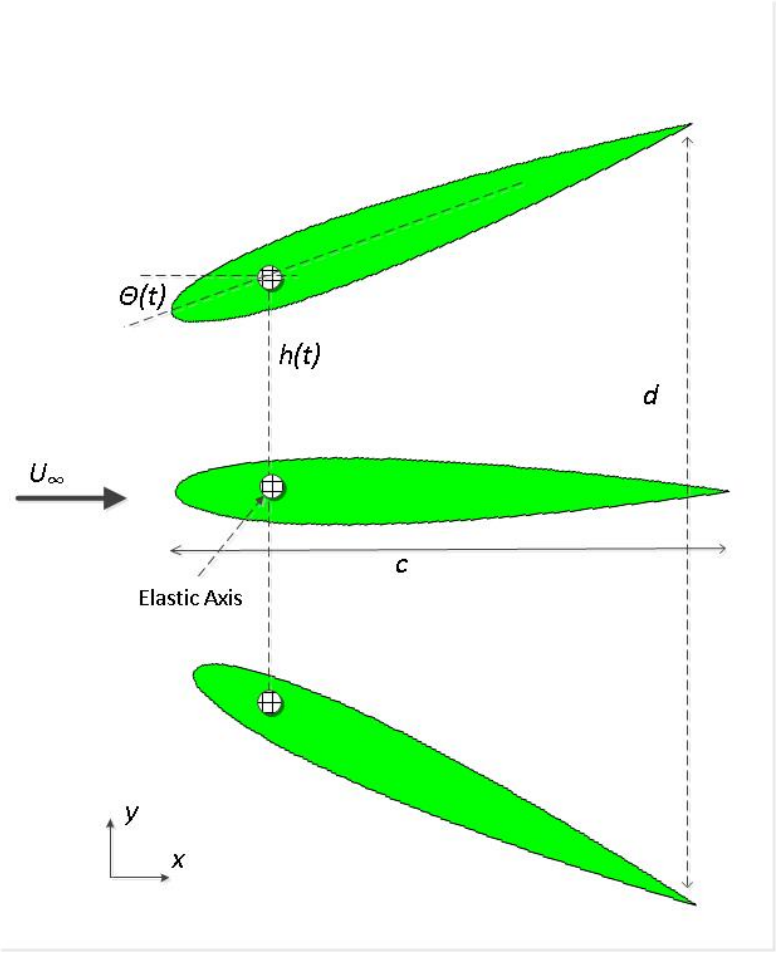

Figure 7.32: Airfoil pitch and heave with respect to oncoming flow

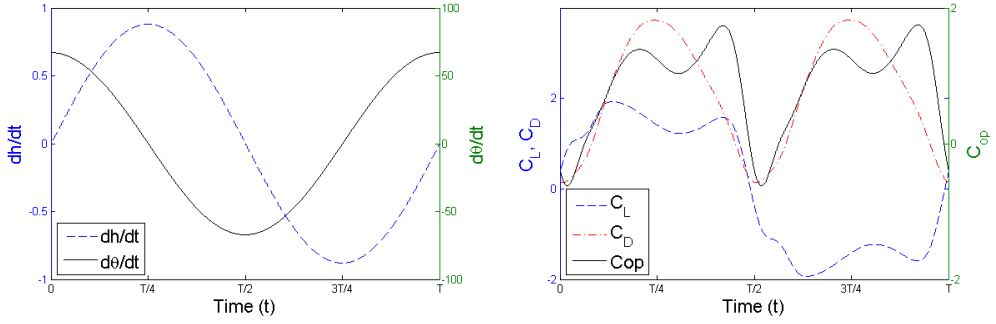

(a) Pitch and heave displacement

(b) Aerodynamic forces

Figure 7.33: Variation of heave and pitch displacement rates, aerodynamic force coefficients and coefficient of performance around NACA0015 at $Re = 1100$, $\theta_0 = 76.33^o$, $\omega = 0.28\pi$

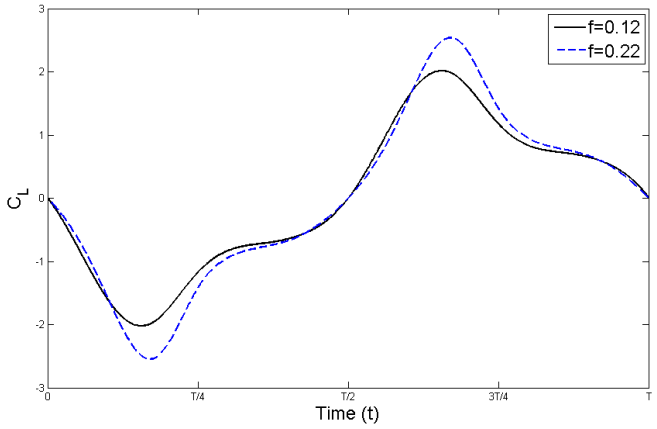

Figure 7.34: Variation of coefficient of lift C_L around pitching-motion-activated flapping NACA0015 airfoil during a single oscillation period ($Re = 1000,\ \theta_0 = 75^o,\ k^* = 0,\ d^* = \pi, m^* = 0.1022$)

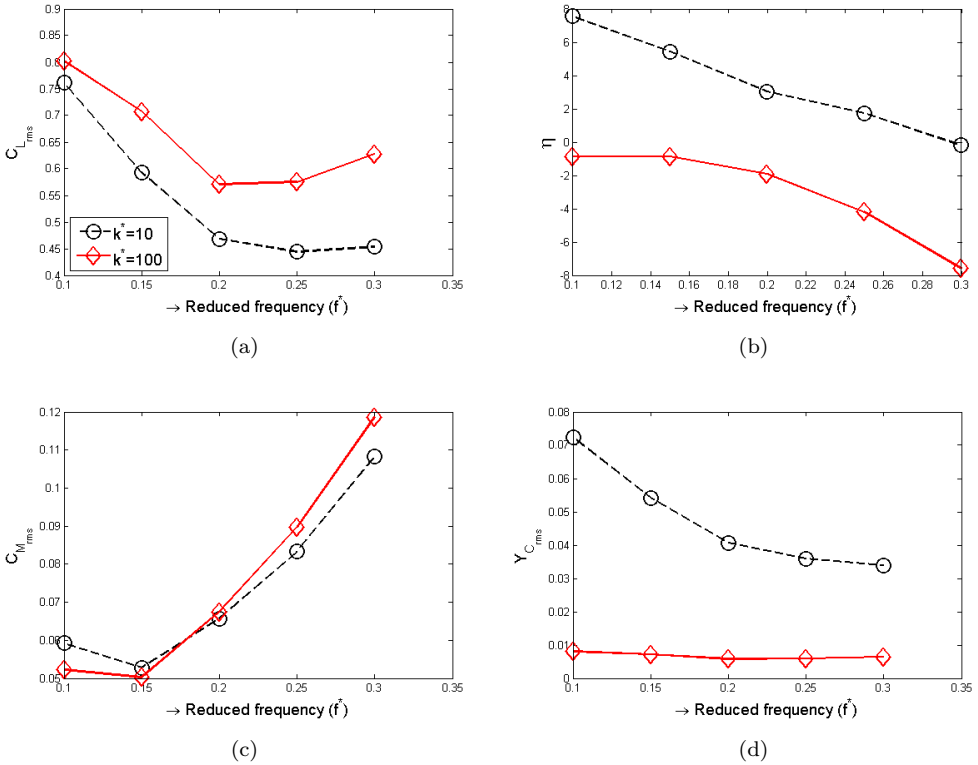

Figure 7.35: Variation of rms values lift coefficients ($C_{L_{rms}}$), power extraction efficiency (η), rms of moment coefficient ($C_{M_{rms}}$) and rms of heave displacement ($Y_{C_{rms}}$) with changing Reynolds number and pitch frequencies (f) for pitching-motion-activated-flapping NACA0015 airfoil at $Re = 5000,\ b = 2\pi,\ \theta_0 = 15^o$

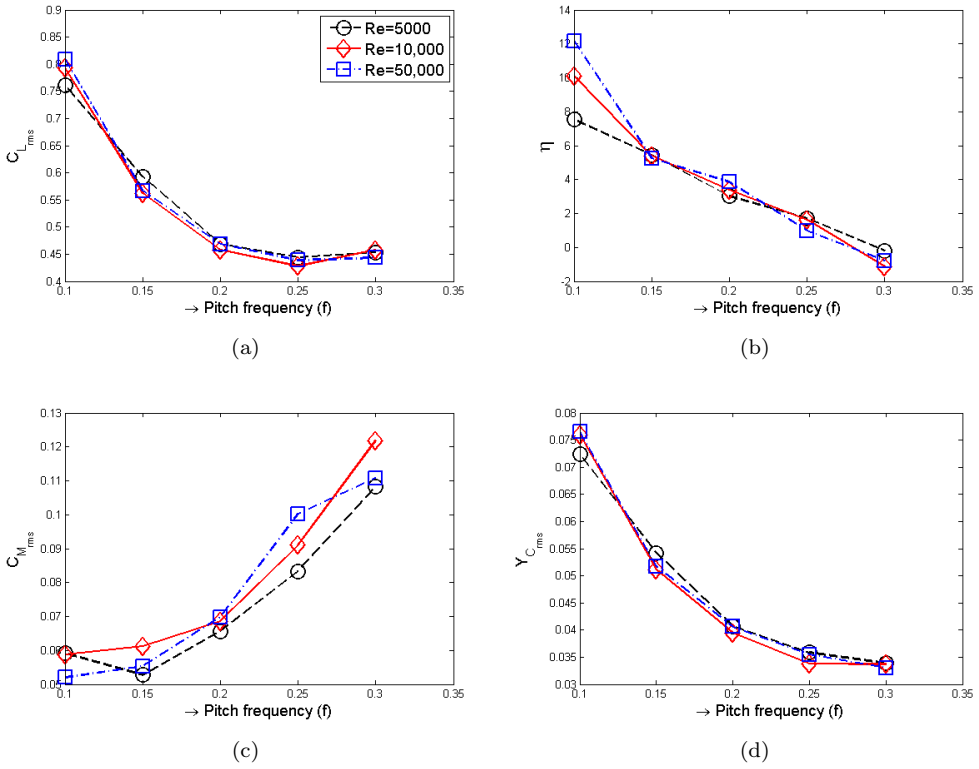

Figure 7.36: Variation of rms values lift coefficients ($C_{L_{rms}}$), power extraction efficiency (η), rms of moment coefficient ($C_{M_{rms}}$) and rms of heave displacement ($Y_{C_{rms}}$) with changing Reynolds number and pitch frequencies (f) for pitching-motion-activated-flapping NACA0015 airfoil at $k = 10,\ b = 2\pi,\ \theta_0 = 15^o$

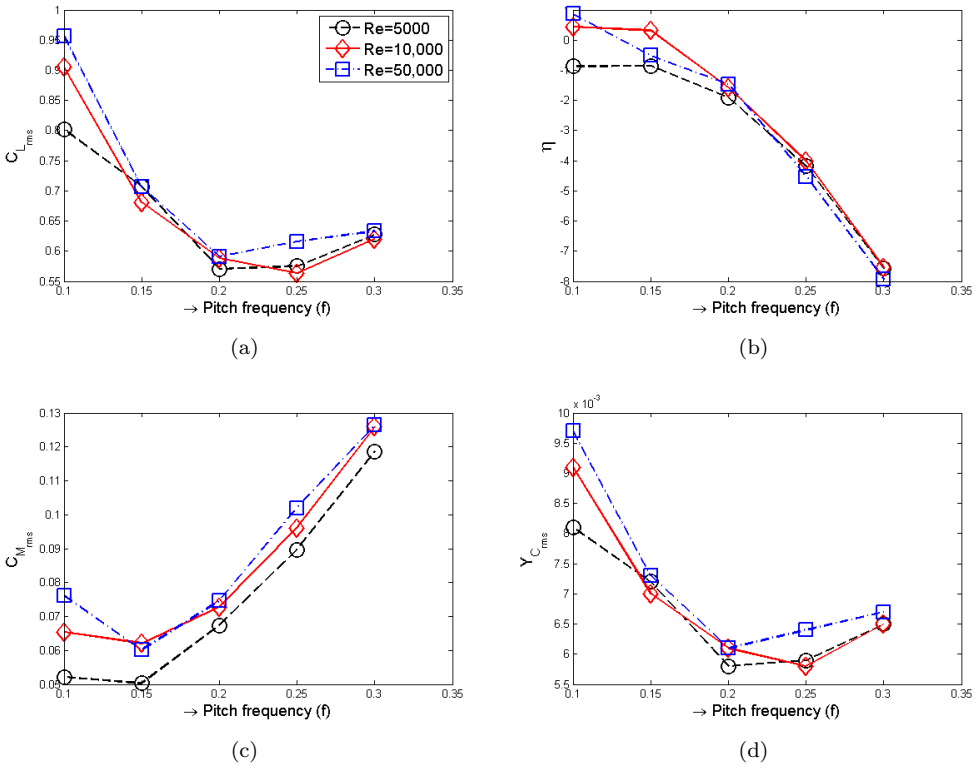

Figure 7.37: Variation of rms values lift coefficients ($C_{L_{rms}}$), power extraction efficiency (η), rms of moment coefficient ($C_{M_{rms}}$) and rms of heave displacement ($Y_{C_{rms}}$) with changing Reynolds number and pitch frequencies (f) for pitching-motion-activated-flapping NACA0015 airfoil at $k = 100,\ b = 2\pi,\ \theta_0 = 15^o$

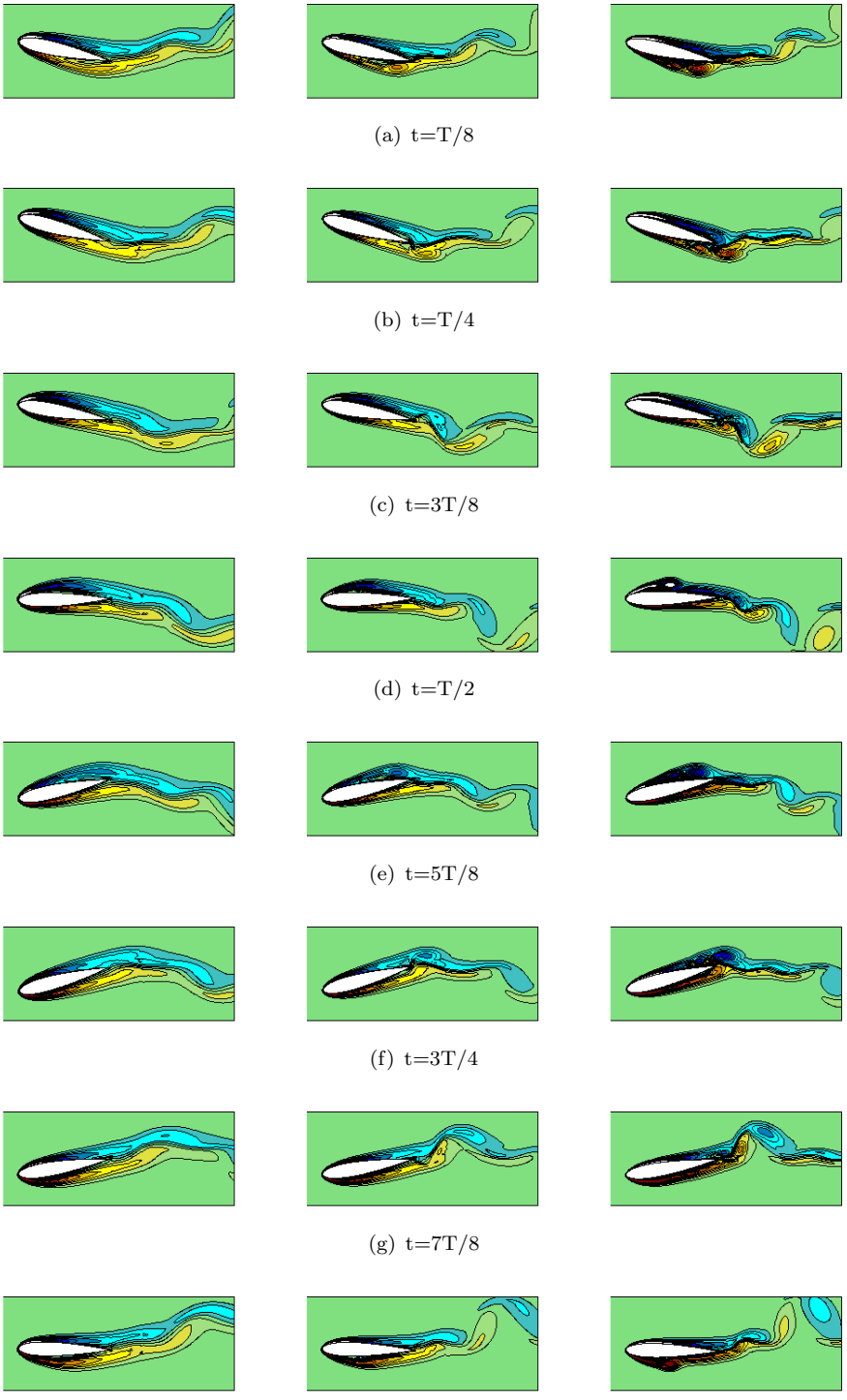

(a) t=T/8

(b) t=T/4

(c) t=3T/8

(d) t=T/2

(e) t=5T/8

(f) t=3T/4

(g) t=7T/8

(h) t=T

Figure 7.38: Comparison of instantaneous vortex structure for pitching-motion-activated-flapping NACA0015 airfoil at $k^* = 10$, $b^* = 2\pi$, $\theta_0 = 15^o$, $f^8 = 0.2$. Left column: $Re = 5000$, middle column: $Re = 10000$, right column: $Re = 50000$

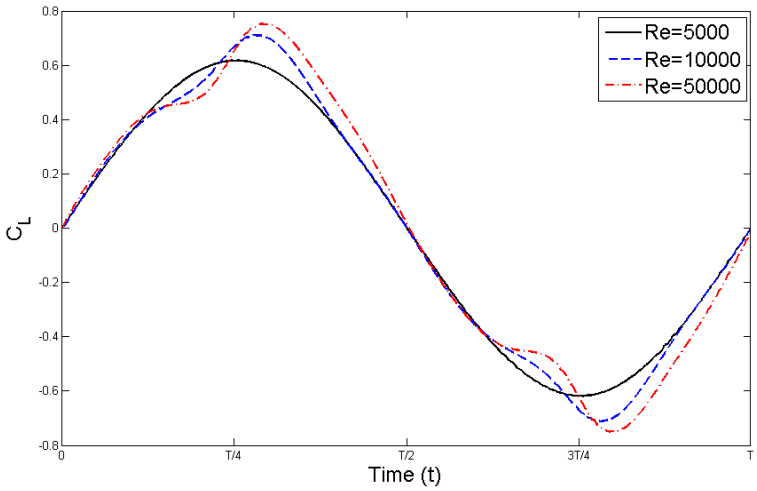

Figure 7.39: Variation of coefficient of lift C_L during a single pitch oscillation period for pitching-motion-activated-flapping NACA0015 airfoil at $k^* = 10,\ b^* = 2\pi,\ \theta_0 = 15^o,\ f^* = 0.2$.

Chapter 8

Conclusions

The solution scheme presented in this research is found to possess both flexibility and computational efficiency to deal with problems pertaining to moving boundaries in general and fluid structure interaction in particular. RBF-FD was found to provide accurate derivative approximations especially at random particle distribution. However, well conditioning of the problem was affected when nodal density was significantly varied across the domain. In order to overcome this issue, shape adaptive RBFs were introduced which were able to retain well-conditioning of coefficient matrix in changing nodal density. Shape adaptive RBFs allowed much larger variation of nodal density within the domain compared with conventionally used RBFs. This was found to be particularly useful for fluid flow problems where an optimum grid necessitates variation of nodal density in different parts of fluid domain.

The spatial derivatives obtained from shape adaptive RBF-FD were used to find the solution of flow equations in vorticity-stream function as well as pressure-velocity formulations. Transient Navier Stokes equations in pressure-velocity formulation were dealt with using explicit and implicit time marching techniques. Unsurprisingly, implicit time marching scheme provided better accuracy and stability compared with their explicit time marching counterparts. Excellent numerical results were obtained on non-uniform node distribution using the implicit RBF-FD method and therefore the same scheme was used for further analysis during the research.

RBF-FD was found to be a highly flexible meshfree scheme for accurate approximation of spatial derivatives at various nodal distributions. The applications of solution scheme were tested for problems relating to lid driven cavity flow and flow around circular cylinder. However, like other meshfree methods, RBF-FD was found to be lacking computational efficiency compared with the mesh based methods. In order to overcome this computational performance related issue, a coupled solution scheme was proposed. The scheme employed RBF-FD meshfree method and conventional finite differencing method over a hybrid fluid grid comprising of meshfree nodal cloud and structured Cartesian

grid. The aim of this proposed scheme is to circumvent the performance related limitations of RBF-FD methods by restricting its application to only those locations where the use of meshfree method is required to flexibly negotiate with moving boundary or complex geometrical shapes. The remaining part of fluid domain is treated with computationally efficient finite difference scheme over a Cartesian grid. Hybrid grid scheme was found to work well for both stationary and moving boundaries. Performance and applicability of the scheme was tested for problems relating to flow around stationary cylinder as well as cylinder vibrating with one and two degrees of freedom. For moving boundary cases, problems with forced and flow induced oscillations were studied. Computational time was found to decline rapidly with reducing the size of meshfree domain. However, minimum size requirements of meshfree zone were dictated by expected vibration amplitudes and degrees of freedom of solid.

The solution scheme was also applied for closely coupled FSI model with reduced fluid domain (CFSI-RFD). In order to reduce computational cost involved in closely coupled model, solution on partial fluid domain was sought during inner FSI iterations which are performed to converge fluid and solid solutions at interface boundary. For CFSI-RFD, an arrangement for solution on partial fluid grid was naturally provided by hybrid grid as it treats meshfree and Cartesian zones separately. Therefore, only the meshfree zone was used during inner (sub) iterations and full fluid domain was used during outer (time step) iterations. Significant reduction (approximately 30% reduction in calculation time for flow around static cylinder case) in computational overheads was achieved compared with conventional closely coupled FSI systems. The computational advantage associated with the use of partial fluid domain is envisaged to be more pronounced for flexible structures which need higher numbers of inner iterations to achieve convergence at fluid-solid boundary. It is pertinent to highlight that CFSI-RFD does not supersede the its counterpart using full fluid domain (conventionally used closed coupling). However, the method is more accurate than loosely coupled algorithm and is computationally more efficient compared with conventional closely coupled method. The solution scheme was applied to fluid around solid objects with one and two degrees of freedom. Bounds of stability, amplitudes of vibrations and vortex shedding frequencies were accurately predicted. The solutions provided insightful information about complex flow structure around vibrating objects.

Stabilized solution scheme was suggested to deal with instabilities arising in convection dominated flows. Stabilization technique discussed during the research is equally applicable to both RBF-FD and conventional finite difference based schemes. The stabilized flow momentum equations were derived using higher order Taylor series approximations of spatial derivatives evolved by equilibrium conditions over control volume. The stabilization term was found to effectively suppress spurious oscillations caused by dominating convection. The hybrid solution scheme with stabilization was then applied to FSI problems with relatively high flow Reynolds number. Flow induced airfoil vibration

problems were solved for applications in flutter analysis and energy extraction by flapping foil. The solution, which was otherwise not stable due to spurious oscillations, was found to be stable and accurate with the use of stabilization terms.

Usability of meshfree methods, for flow problems, has always been inhibited due to their high computational cost. On the other hand, mesh-based methods are, in general, inferior to meshfree methods in offering required flexibility to deal with moving boundaries. Therefore, use of coupled meshfree and mesh-based solvers provides an optimum modelling approach which can benefit from the strengths of both classes of numerical techniques. The coupled solution scheme over hybrid grid, suggested in this research, is found to be highly effective in dealing with flows around solid vibrating around their mean positions. However, there is still a lot of further research required to fully understand the strengths and limitations of presented work. Some of these areas are identified in the next section.

8.1 Future work

As mentioned earlier, there lies a good potential to further investigate the coupled solvers in various aspects. The following are some of the suggested directions towards which the future research can aim:

1. Usability of hybrid solution scheme may be investigated at high Re and turbulent flows. This may entail the use of other stabilization techniques, like flux limiting or upwinding etc., to deal with instabilities. However, the applicability of solution scheme can thus be extended to a wider range of flutter and vibrating wings related problems at higher speed flows.

2. Current solution scheme considers only laminar flows. However, it is understood that turbulent flow modelling represents an even wider range of flow problems. Therefore, the coupled solution schemes may also be extended for turbulent flows.

3. The computational costs associated with 3-D problems is far higher than for 2-D cases. Therefore, use of hybrid grid method would offer significant reduction in computational resources when applied to 3-D problems. It is therefore suggested that applicability of coupled solution scheme on hybrid grid may be studied for 3-D problems.

4. Application of coupled solution scheme can be investigated for FSI problems having flexible structures. Convergence of solutions at fluid-solid boundary needs more number of inner iterations, during closely coupled algorithms, when the structure is flexible. For such cases, CFSI-RFD will provide an efficient solution approach by reducing computational effort during convergence at fluid-solid interface.

5. Various authors have suggested different projection methods for N-S equations in pressure-velocity formulations. Those methods can also be tested in conjunction with current solution scheme.

6. Usability of coupled solution scheme is not restricted by non-linearity or large solid deflections. It can be applied to complicated FSI problems without any further special treatment. The solution scheme can therefore be used to further investigate complex flow structures, response behaviour and parametric studies for problems relating to flow induced cylindrical vibrations, passive and active energy harvesters using flapping foils, wing flutter, etc.

References

Akbari, M. and Price, S. (2003). Simulation of dynamic stall for a NACA 0012 airfoil using a vortex method. *Journal of Fluids and Structures*, 17(6):855–874.

Alam, M. M., Zhou, Y., Yang, H., Guo, H., and Mi, J. (2010). The ultra-low Reynolds number airfoil wake. *Experiments in fluids*, 48(1):81–103.

Atluri, S. N. and Zhu, T. (1998). A new meshless local Petrov-Galerkin (MLPG) approach in computational mechanics. *Computational Mechanics*, 22(2):117–127.

Badia, S. and Codina, R. (2007). On some fluidstructure iterative algorithms using pressure segregation methods. Application to aeroelasticity. *International Journal for Numerical Methods in Engineering*, 72(1):46–71.

Badia, S., Nobile, F., and Vergara, C. (2008). Fluidstructure partitioned procedures based on Robin transmission conditions. *Journal of Computational Physics*, 227(14):7027–7051.

Bayona, V., Moscoso, M., Carretero, M., and Kindelan, M. (2010). RBF-FD formulas and convergence properties. *Journal of Computational Physics*, 229(22):8281–8295.

Bell, J. B., Colella, P., and Glaz, H. M. (1989). A second-order projection method for the incompressible Navier-Stokes equations. *Journal of Computational Physics*, 85(2):257–283.

Bell, J. B., Colella, P., and Howell, L. H. (1991). An efficient second-order projection method for viscous incompressible flow. In *Proceedings of the Tenth AIAA Computational Fluid Dynamics Conference, AIAA*, volume 360.

Belov, A., Martinelli, L., and Jameson, A. (1995). A new implicit algorithm with multigrid for unsteady incompressible flow calculations. *AIAA paper*, 95:0049.

Belytschko, T.; Ventura, G. X. J. X. (2002). New methods for discontinuity and crack modeling in EFG. In Griebel M.; Scheweitzer, M. A., editor, *Lectures Notes in Computational Science and Engineering*, volume 26. Springer Verlag.

Belytschko, T., Lu, Y. Y., and Gu, L. (1994). Element-free Galerkin methods. *International Journal for Numerical Methods in Engineering*, 37(2):229–256.

Belytschko, T., Mos, N., Usui, S., and Parimi, C. (2001). Arbitrary discontinuities in finite elements. *International Journal for Numerical Methods in Engineering*, 50(4):993–1013.

Bollig, E. F., Flyer, N., and Erlebacher, G. (2012). Solution to PDEs using radial basis function finite-differences (rbf-fd) on multiple gpus. *Journal of Computational Physics*, 231(21):7133–7151.

Botella, O. (1997). On the solution of the Navier-Stokes equations using Chebyshev projection schemes with third-order accuracy in time. *Computers & Fluids*, 26(2):107–116.

Braza, M., Chassaing, P., and Minh, H. H. (1986). Numerical study and physical analysis of the pressure and velocity fields in the near wake of a circular cylinder. *Journal of fluid mechanics*, 165:79–130.

Brooks, A. N. and Hughes, T. J. (1982). Streamline upwind/Petrov-Galerkin formulations for convection dominated flows with particular emphasis on the incompressible Navier-Stokes equations. *Computer Methods in Applied Mechanics and Engineering*, 32(13):199 – 259.

Brown, D. L., Cortez, R., and Minion, M. L. (2001). Accurate projection methods for the incompressible NavierStokes equations. *Journal of Computational Physics*, 168(2):464–499.

Calhoun, D. (2002). A cartesian grid method for solving the two-dimensional streamfunction-vorticity equations in irregular regions. *Journal of Computational Physics*, 176(2):231–275.

Carlos, A., Park, K. C., and Farhat, C. (2001). Partitioned analysis of coupled mechanical systems. *Computer Methods in Applied Mechanics and Engineering*, 190(2425):3247–3270.

Cecrdle, J. and J, M. (2002). Verification fem model of an aircraft construction with two and three degrees of freedom. Technical report, Aeronautical research and test establishment, Prague (in Czech).

Chan, Y., Shen, L., Wu, C., and Young, D. (2014). A novel upwind-based local radial basis function differential quadrature method for convection-dominated flows. *Computers & Fluids*, 89:157–166.

Chen, C. S. and Brebbia, C. A. (1998). The dual reciprocity method for Helmholtz-type operators. *Boundary Elements*, 4:495–504.

Chen, L. and Cheng, Y. (2010). The complex variable reproducing kernel particle method for elasto-plasticity problems. *Science China Physics, Mechanics and Astronomy*, 53(5):954–965.

Chen, W. and Tanaka, M. (2002). A meshless, integration-free, and boundary-only RBF technique. *Computers and Mathematics with Applications*, 43(3-5):379–391.

Chesshire, G. and Henshaw, W. D. (1990). Composite overlapping meshes for the solution of partial differential equations. *Journal of Computational Physics*, 90(1):1–64.

Chew, C. S., Yeo, K. S., and Shu, C. (2006). A generalized finite-difference (GFD) ALE scheme for incompressible flows around moving solid bodies on hybrid meshfreecartesian grids. *Journal of Computational Physics*, 218(2):510–548.

Chinchapatnam, P., Djidjeli, K., and Nair, P. (2006). Unsymmetric and symmetric meshless schemes for the unsteady convection–diffusion equation. *Computer methods in applied mechanics and engineering*, 195(19):2432–2453.

Chinchapatnam, P. P., Djidjeli, K., Nair, P., and Tan, M. (2009). A compact RBF-FD based meshless method for the incompressible NavierStokes equations. volume 223, pages 275–290. SAGE Publications.

Chinchapatnam, P. P., Djidjeli, K., and Nair, P. B. (2007). Radial basis function meshless method for the steady incompressible Navier-Stokes equations. *International Journal of Computer Mathematics*, 84(10):1509–1521.

Chorin, A. J. (1973). Numerical study of slightly viscous flow. *Journal of Fluid Mechanics*, 57:785–796.

Chow, P. and Addison, C. (2002). Putting domain decomposition at the heart of a mesh-based simulation process. *International journal for numerical methods in fluids*, 40(12):1471–1484.

Clarke, D. K., Hassan, H., and Salas, M. (1986). Euler calculations for multielement airfoils using cartesian grids. *AIAA journal*, 24(3):353–358.

Cleary, P. W. and Monaghan, J. J. (1999). Conduction modelling using smoothed particle hydrodynamics. *Journal of Computational Physics*, 148(1):227–264.

Critzos, C. C., Heyson, H. H., and Robert W. Boswinkle, J. (1955). Aerodynamic characteristics of NACA 0012 airfoil section at angles of attack from 0 to 180 degrees. Technical Report NACA TN 3361, National Advisory Committee for Aeronautics.

Dahl, J., Hover, F., Triantafyllou, M., Dong, S., and Karniadakis, G. (2007). Resonant vibrations of bluff bodies cause multivortex shedding and high frequency forces. *Physical review letters*, 99(14):144503.

Dahl, J., Hover, F., Triantafyllou, M., and Oakley, O. (2010). Dual resonance in vortex-induced vibrations at subcritical and supercritical Reynolds numbers. *Journal of Fluid Mechanics*, 643:395–424.

Dai Zhou, Jiahuang Tu, Y. B. (2012). Two degrees of freedom flow-induced vibrations on a cylinder. In *7th International colloquium on bluff body aerodynamics and applications BBAA7*, International association for wind engineering. American Institute of Aeronautics and Astronautics.

De Rosis, A., Falcucci, G., Ubertini, S., and Ubertini, F. (2013). A coupled lattice boltzmann-finite element approach for two-dimensional fluidstructure interaction. *Computers and Fluids*, 86(0):558–568.

De Zeeuw, D. and Powell, K. (1991). An adaptively-refined cartesian mesh solver for the euler equations. *AIAA Paper*, (91-1542).

Dehnen, W. and Aly, H. (2012). Improving convergence in smoothed particle hydrodynamics simulations without pairing instability. *Monthly Notices of the Royal Astronomical Society*, 425(2):1068–1082.

Deng, J., Teng, L., Pan, D., and Shao, X. (2015). Inertial effects of the semi-passive flapping foil on its energy extraction efficiency. *Physics of Fluids (1994-present)*, 27(5):053103.

Dennis, S. and Chang, G.-Z. (1970). Numerical solutions for steady flow past a circular cylinder at Reynolds numbers up to 100. *J. Fluid Mech*, 42(3):471–489.

Deriaz, E. (2010). Stability of explicit numerical schemes for smooth convection dominated problems. *bli*, 1:0.

Ding, H., Shu, C., Yeo, K. S., and Xu, D. (2004). Simulation of incompressible viscous flows past a circular cylinder by hybrid fd scheme and meshless least square-based finite difference method. *Computer Methods in Applied Mechanics and Engineering*, 193(9-11):727–744.

Dowell, E. and Hall, K. (2001). Modeling of fluid-structure interaction. *Annual Review of Fluid Mechanics*, 33(1):445–490.

Driscoll, T. A. and Fornberg, B. (2002). Interpolation in the limit of increasingly flat radial basis functions. *Computers & Mathematics with Applications*, 43(3-5):413–422.

Duarte, F., Gormaz, R., and Natesan, S. (2004). Arbitrary LagrangianEulerian method for NavierStokes equations with moving boundaries. *Computer Methods in Applied Mechanics and Engineering*, 193(4547):4819–4836.

Dubcová, L., Feistauer, M., Horáček, J., and Sváček, P. (2009). Numerical simulation of interaction between turbulent flow and a vibrating airfoil. *Computing and visualization in science*, 12(5):207–225.

Falcovitz, J., Alfandary, G., and Hanoch, G. (1997). A two-dimensional conservation laws scheme for compressible flows with moving boundaries. *Journal of Computational Physics*, 138(1):83–102.

Farhat, C., Lesoinne, M., and Le Tallec, P. (1998). Load and motion transfer algorithms for fluid/structure interaction problems with non-matching discrete interfaces: Momentum and energy conservation, optimal discretization and application to aeroelasticity. *Computer Methods in Applied Mechanics and Engineering*, 157(12):95–114.

Farhat, C., Lesoinne, M., and Maman, N. (1995). Mixed explicit/implicit time integration of coupled aeroelastic problems: Threefield formulation, geometric conservation and distributed solution. *International Journal for Numerical Methods in Fluids*, 21(10):807–835.

Farhat, C., Van Der Zee, K. G., and Geuzaine, P. (2006). Provably second-order time-accurate loosely-coupled solution algorithms for transient nonlinear computational aeroelasticity. *Computer Methods in Applied Mechanics and Engineering*, 195(1718):1973–2001.

Feistauer, M., Horacek, J., Ruzicka, M., and Sváček, P. (2011). Numerical analysis of flow-induced nonlinear vibrations of an airfoil with three degrees of freedom. *Computers and Fluids*, 49(1):110–127.

Ferrari, A., Dumbser, M., Toro, E. F., and Armanini, A. (2009). A new 3d parallel SPH scheme for free surface flows. *Computers & Fluids*, 38(6):1203–1217.

Firoozjaee, A. R. and Afshar, M. H. (2011). Steady-state solution of incompressible Navier-Stokes equations using discrete least-squares meshless method. *International Journal for Numerical Methods in Fluids*, 67(3):369–382.

Fornberg, B. (1980). A numerical study of steady viscous flow past a circular cylinder. *Journal of Fluid Mechanics*, 98(04):819–855.

Fornberg, B. and Lehto, E. (2011). Stabilization of RBF-generated finite difference methods for convective PDEs. *Journal of Computational Physics*, 230(6):2270–2285.

Franke, C. and Schaback, R. (1998). Solving partial differential equations by collocation using radial basis functions. *Applied Mathematics and Computation*, 93(1):73–82.

Franke, R. (1982). Scattered data interpolation: Tests of some method. *Mathematics of Computation*, 38(157):181–200.

Frazer, R. A., J. W. P. and Skan, S. W. (1937). *Approximations to functions and to the solutions of differential equations*, volume 1799 of *Reports and Memoranda*. HSMO, London.

Fries, T.-P. and Matthies, H. G. (2006a). A stabilized and coupled meshfree/meshbased method for the incompressible Navier–Stokes equationsPart I: Stabilization. *Computer methods in applied mechanics and engineering*, 195(44):6205–6224.

Fries, T.-P. and Matthies, H. G. (2006b). A stabilized and coupled meshfree/meshbased method for the incompressible navier–stokes equationsPart II: Coupling. *Computer methods in applied mechanics and engineering*, 195(44):6191–6204.

Furmnek, P. and Kozel, K. (2013). Deterministic unsteady and aeroelastic flow simulations with high-order FVM schemes. *Computing*, 95(1):145–161.

G. R. Liu, M. B. L. (2003). *Smoothed Particle Hydrodynamics - A Meshfree Particle Method*. World Scientific Publishing, Singapure.

G. R. Liu, Y. G. (2005). *An introduction to meshfree methods and their programming*. Springer, Dordrecht, Netherlands.

Garcia, J. A. and Guruswamy, G. P. (1999). Aeroelastic analysis of transonic wings using Navier-Stokes equations and a nonlinear beam finite element model. *AIAA Paper*, 1215:1999.

Ge, L. and Sotiropoulos, F. (2007). A numerical method for solving the 3d unsteady incompressible navier–stokes equations in curvilinear domains with complex immersed boundaries. *Journal of computational physics*, 225(2):1782–1809.

Gherlone, M., Iurlaro, L., and Di Sciuva, M. (2012). A novel algorithm for shape parameter selection in radial basis functions collocation method. *Composite Structures*, 94(2):453–461.

Ghia, U. K. N. G. and Shin, C. (1982). High-re solutions for incompressible flow using the Navier-Stokes equations and a multigrid method. *Journal of Computational Physics*, 48(3):387 – 411.

Gilmanov, A. and Sotiropoulos, F. (2005). A hybrid cartesian/immersed boundary method for simulating flows with 3d, geometrically complex, moving bodies. *Journal of Computational Physics*, 207(2):457–492.

Gilmanov, A., Sotiropoulos, F., and Balaras, E. (2003). A general reconstruction algorithm for simulating flows with complex 3d immersed boundaries on cartesian grids. *Journal of Computational Physics*, 191(2):660–669.

Gingold, R. A. and Monaghan, J. J. (1977). Smoothed particle hydrodynamics - theory and application to non-shperical stars. *Monthly Notices of the Royal Astronomical Society*, 181(2):375–389.

Girault, V. (1974). Theory of a finite difference method on irregular networks. *SIAM Journal on Numerical Analysis*, 11(2):260–282.

Glowinski, R., Pan, T.-W., and Periaux, J. (1994). A fictitious domain method for external incompressible viscous flow modeled by Navier-Stokes equations. *Computer Methods in Applied Mechanics and Engineering*, 112(1):133–148.

Goda, K. (1979). A multistep technique with implicit difference schemes for calculating two-or three-dimensional cavity flows. *Journal of Computational Physics*, 30(1):76–95.

Gu, Y. T. and Liu, G. R. (2002). A boundary point interpolation method for stress analysis of solids. *Computational Mechanics*, 28(1):47–54.

Guermond, J. L., Minev, P., and Shen, J. (2006). An overview of projection methods for incompressible flows. *Computer Methods in Applied Mechanics and Engineering*, 195(4447):6011–6045.

Günther, C., Hartmann, D., Schneiders, L., Meinke, M., and Schröder, W. (2011). A cartesian cut-cell method for sharp moving boundaries. *AIAA Paper*, 3387:27–30.

Guruswamy, G. P. and Byun, C. (1995). Direct coupling of euler flow equations with plate finite element structures. *AIAA journal*, 33(2):375–377.

Hamed Meraji, S., Ghaheri, A., and Malekzadeh, P. (2012). An efficient algorithm based on the differential quadrature method for solving Navier-Stokes equations. *International Journal for Numerical Methods in Fluids*, pages n/a–n/a.

Hardy, R. L. (1971). Multiquadric equations of topography and other irregular surfaces. *Journal of Geophysical Research*, 76(8):1905.

Henshaw, W. D. and Chesshire, G. (1987). Multigrid on composite meshes. *SIAM Journal on Scientific and Statistical Computing*, 8(6):914–923.

Hinatsu, M. and Ferziger, J. (1991). Numerical computation of unsteady incompressible flow in complex geometry using a composite multigrid technique. *International Journal for Numerical Methods in Fluids*, 13(8):971–997.

Hirsch, C. (2002). *Numerical computation of internal and external flows*, volume 2 of *Computational methods for inviscid and viscous flows*. Wiley-Interscience Publications.

Hirt, C., Amsden, A., and Cook, J. (1974). An arbitrary Lagrangian-Eulerian computing method for all flow speeds. *Journal of Computational Physics*, 14(3):227–253.

Holmes, P. and Marsden, J. (1978). Bifurcation to divergence and flutter in flow-induced oscillations: an infinite dimensional analysis. *Automatica*, 14(4):367–384.

Hon, Y.-C., Šarler, B., and Yun, D.-f. (2015). Local radial basis function collocation method for solving thermo-driven fluid-flow problems with free surface. *Engineering Analysis with Boundary Elements*, 57:2–8.

Hopkins, P. F. (2013). A general class of Lagrangian smoothed particle hydrodynamics methods and implications for fluid mixing problems. *Monthly Notices of the Royal Astronomical Society*, 428(4):2840–2856.

Hu, H. H., Patankar, N. A., and Zhu, M. (2001). Direct numerical simulations of fluidsolid systems using the arbitrary lagrangianeulerian technique. *Journal of Computational Physics*, 169(2):427–462.

Huang, C.-S., Lee, C.-F., and Cheng, A.-D. (2007). Error estimate, optimal shape factor, and high precision computation of multiquadric collocation method. *Engineering Analysis with Boundary Elements*, 31(7):614–623.

Huang, R. F. and Lee, H. W. (1999). Effects of freestream turbulence on wing-surface flow and aerodynamic performance. *Journal of aircraft*, 36(6):965–972.

Ii, S., Sugiyama, K., Takeuchi, S., Takagi, S., and Matsumoto, Y. (2011). An implicit full eulerian method for the fluid-structure interaction problem. *International Journal for Numerical Methods in Fluids*, 65(1-3):150–165.

Javed, A., Djidjeli, K., and Xing, J. T. (2013a). Adaptive shape parameter (ASP) technique for local radial basis functions (RBFs) and their application for solution of Navier Stokes equations. In *International Conference on Fluids and Thermal Engineering*. International Scientific Council.

Javed, A., Djidjeli, K., Xing, J. T., and Cox, S. (2013b). A hybrid meshfree local RBF-Cartesian FD scheme for incompressible flow around solid bodies. In Ariston, A., editor, *International Conference on Fluid Mechanics and Applications*. International Scientific Council.

Javed, A., Djidjeli, K., Xing, J. T., and Sun, Z. (2014a). *An ALE Based Hybrid Meshfree Local RBF-Cartesian FD scheme for Incompressible flow around moving boundaries*. AIAA Aviation. American Institute of Aeronautics and Astronautics. doi:10.2514/6.2014-2312.

Javed, A., Djijdeli, K., and Xing, Jing, T. (2014b). Shape adaptive RBF-FD implicit scheme for incompressible viscous Navier-Strokes equations. *Computers & Fluids*, 89(0):38–52.

Javed, A., Djijdeli, K., and Xing, Jing, T. (2015). A coupled meshfree-mesh based solution scheme on hybrid grid for flow induced vibrations. *Computers & Fluids*, under review(-):–.

Kamakoti, R. and Shyy, W. (2004). Fluidstructure interaction for aeroelastic applications. *Progress in Aerospace Sciences*, 40(8):535–558.

Kansa, E. J. (1990). Multiquadrics - a scattered data approximation scheme with applications to computational fluid-dynamics .2. solutions to parabolic, hyperbolic and elliptic partial-differential equations. *Computers and Mathematics with Applications*, 19(8-9):147–161.

Khayyer, A. and Gotoh, H. (2009). Modified moving particle semi-implicit methods for the prediction of 2D wave impact pressure. *Coastal Engineering*, 56(4):419–440.

Kim, D. and Choi, H. (2000). A second-order time-accurate finite volume method for unsteady incompressible flow on hybrid unstructured grids. *Journal of Computational Physics*, 162(2):411–428.

Kim, J. and Moin, P. (1985). Application of a fractional-step method to incompressible Navier-Stokes equations. *Journal of Computational Physics*, 59(2):308–323.

Kinsey, T. and Dumas, G. (2008). Parametric study of an oscillating airfoil in a power-extraction regime. *AIAA journal*, 46(6):1318–1330.

Koh, C. G., Gao, M., and Luo, C. (2012). A new particle method for simulation of incompressible free surface flow problems. *International Journal for Numerical Methods in Engineering*, 89(12):1582–1604.

Koopmann, G. (1967). The vortex wakes of vibrating cylinders at low Reynolds numbers. *Journal of Fluid Mechanics*, 28(03):501–512.

Koshizuka, S. and Oka, Y. (1996). Moving-particle semi-implicit method for fragmentation of incompressible fluid. *Nuclear science and engineering*, 123(3):421–434.

Krongauz, Y. and Belytschko, T. (1998). EFG approximation with discontinuous derivatives. *International Journal for Numerical Methods in Engineering*, 41(7):1215–1233.

Lancaster, P. and Salkauskas, K. (1981). Surfaces generated by moving least-squares methods. *Mathematics of Computation*, 37(155):141–158.

Lanczos, C. (1938). *Trigonometric interpolation of empirical and analytical functions.*

Larsson, E. and Fornberg, B. (2005). Theoretical and computational aspects of multivariate interpolation with increasingly flat radial basis functions. *Computers & Mathematics with Applications*, 49(1):103–130.

Lee, B.-H., Park, J.-C., Kim, M.-H., and Hwang, S.-C. (2011). Step-by-step improvement of MPS method in simulating violent free-surface motions and impact-loads. *Computer methods in applied mechanics and engineering*, 200(9):1113–1125.

Li, C., He-Ping, M., and Yu-Min, C. (2013). Combining the complex variable reproducing kernel particle method and the finite element method for solving transient heat conduction problems. *Chinese Physics B*, 22(5):050202.

Li, K., Huang, Q., Wang, J., and Lin, L. (2011). An improved localized radial basis function meshless method for computational aeroacoustics. *Engineering Analysis with Boundary Elements*, 35(1):47–55.

Li, X. (2011). The meshless Galerkin boundary node method for stokes problems in three dimensions. *International Journal for Numerical Methods in Engineering*, 88(5):442–472.

Li, X. and Zhu, J. (2009). A Galerkin boundary node method and its convergence analysis. *Journal of computational and applied mathematics*, 230(1):314–328.

Li Shaofan, W. K. L. (2007). *Meshfree Particle Methods*. Springer.

Libersky, L. D., Randles, P. W., Carney, T. C., and Dickinson, D. L. (1997). Recent improvements in SPH modeling of hypervelocity impact. *International Journal of Impact Engineering*, 20(6-10):525–532.

Liszka, T. and Orkisz, J. (1980). The finite-difference method at arbitrary irregular grids and its application in applied mechanics. *Computers and Structures*, 11(1-2):83–95.

Liu, C., Zheng, X., and Sung, C. (1998). Preconditioned multigrid methods for unsteady incompressible flows. *Journal of Computational Physics*, 139(1):35–57.

Liu, G. and Gu, Y. (2001a). A local radial point interpolation method (LRPIM) for free vibration analyses of 2-D solids. *Journal of Sound and vibration*, 246(1):29–46.

Liu, G. R. and Gu, Y. T. (2001b). A point interpolation method for two-dimensional solids. *International Journal for Numerical Methods in Engineering*, 50(4):937–951.

Liu, G. R. and Gu, Y. T. (2003). A meshfree method: meshfree weak-strong (MWS) form method, for 2-D solids. *Computational Mechanics*, 33(1):2–14.

Liu, G. R., Yan, L., Wang, J. G., and Gu, Y. T. (2002). Point interpolation method based on local residual formulation using radial basis functions. *Structural Engineering and Mechanics*, 14(6):713–732.

Liu, M., Liu, G., Zong, Z., and Lam, K. (2003). Numerical simulation of incompressible flows by SPH. In *International Conference on Scientific & Engineering Computational*.

Liu, W.-K., Li, S., and Belytschko, T. (1997). Moving least-square reproducing kernel methods (i) methodology and convergence. *Computer Methods in Applied Mechanics and Engineering*, 143(12):113 – 154.

Mai-Duy, N. and Tran-Cong, T. (2001). Numerical solution of differential equations using multiquadric radial basis function networks. *Neural Networks*, 14(2):185–199.

Massey, B. (1979). *Mechanics of Fluids*. Van Nostrand Reinhold Inc. US, 4 edition.

Mittal, S. and Kumar, V. (2001). Flow-induced vibrations of a light circular cylinder at Reynolds numbers 10^3 to 10^4. *Journal of Sound and Vibration*, 245(5):923–946.

Monaghan, J. J. (1994). Simulating free-surface flows with SPH. *Journal of Computational Physics*, 110(2):399–406.

Monaghan, J. J. and Lattanzio, J. C. (1985). A refined particle method for astrophysical problems. *Astronomy and Astrophysics*, 149(1):135–143.

Mukherjee, Y. X. and Mukherjee, S. (1997). The boundary node method for potential problems. *International Journal for Numerical Methods in Engineering*, 40(5):797–815.

Najafi, M., Arefmanesh, A., and Enjilela, V. (2012). Meshless local Petrov–Galerkin method-higher Reynolds numbers fluid flow applications. *Engineering Analysis with Boundary Elements*, 36(11):1671–1685.

Nayroles, B., Touzot, G., and Villon, P. (1992). Generalizing the finite element method: Diffuse approximation and diffuse elements. *Computational Mechanics*, 10(5):307–318.

Nobari, M. and Naderan, H. (2006). A numerical study of flow past a cylinder with cross flow and inline oscillation. *Computers & fluids*, 35(4):393–415.

Oñate, E. (1998). Derivation of stabilized equations for numerical solution of advective-diffusive transport and fluid flow problems. *Computer Methods in Applied Mechanics and Engineering*, 151(1):233–265.

Oñate, E., Idelsohn, S., Zienkiewicz, O. C., Taylor, R. L., and Sacco, C. (1996). A stabilized finite point method for analysis of fluid mechanics problems. *Computer Methods in Applied Mechanics and Engineering*, 139(1-4):315–346.

Organ, D., Fleming, M., Terry, T., and Belytschko, T. (1996). Continuous meshless approximations for nonconvex bodies by diffraction and transparency. *Computational Mechanics*, 18(3):225–235.

Örley, F., Pasquariello, V., Hickel, S., and Adams, N. A. (2015). Cut-element based immersed boundary method for moving geometries in compressible liquid flows with cavitation. *Journal of Computational Physics*, 283:1–22.

Park, K. (1980). Partitioned transient analysis procedures for coupled-field problems: stability analysis. *Journal of Applied Mechanics*, 47(2):370–376.

Pavlin, V. and Perrone, N. (1979). Finite-difference energy techniques for arbitrary meshes applied to linear plate problems. *International Journal for Numerical Methods in Engineering*, 14(5):647–664.

Pember, R. B., Bell, J. B., Colella, P., Curtchfield, W. Y., and Welcome, M. L. (1995). An adaptive cartesian grid method for unsteady compressible flow in irregular regions. *Journal of computational Physics*, 120(2):278–304.

Perng, C. and Street, R. (1991). A coupled multigrid-domain-splitting technique for simulating incompressible flows in geometrically complex domains. *International journal for numerical methods in fluids*, 13(3):269–286.

Perot, J. (1995). Comments on the fractional step method. *Journal of Computational Physics*, 121(1):190 – 191.

Peskin, C. S. (1977). Numerical analysis of blood flow in the heart. *Journal of Computational Physics*, 25(3):220–252.

Piperno, S., Farhat, C., and Larrouturou, B. (1995). Partitioned procedures for the transient solution of coupled aroelastic problems part i: Model problem, theory and two-dimensional application. *Computer Methods in Applied Mechanics and Engineering*, 124(12):79–112.

Placzek, A., Sigrist, J.-F., and Hamdouni, A. (2009). Numerical simulation of an oscillating cylinder in a cross-flow at low Reynolds number: Forced and free oscillations. *Computers & Fluids*, 38(1):80–100.

Price, D. J. (2008). Modelling discontinuities and Kelvin–Helmholtz instabilities in SPH. *Journal of Computational Physics*, 227(24):10040–10057.

Rabczuk, T., Gracie, R., Song, J.-H., and Belytschko, T. (2010). Immersed particle method for fluid–structure interaction. *International Journal for Numerical Methods in Engineering*, 81(1):48–71.

Read, J., Hayfield, T., and Agertz, O. (2010). Resolving mixing in smoothed particle hydrodynamics. *Monthly Notices of the Royal Astronomical Society*, 405(3):1513–1530.

Rippa, S. (1999). An algorithm for selecting a good value for the parameter c in radial basis function interpolation. *Advances in Computational Mathematics*, 11(2-3):193–210.

Ryoichi Amano, B. S. (2011). *Computational Fluid Dynamics and Heat Transfer-Emering Topics*. WIT Press.

Saad, Y. and Schultz, M. H. (1986). GMRES: A generalized minimal residual algorithm for solving nonsymmetric linear systems. *SIAM Journal on scientific and statistical computing*, 7(3):856–869.

Saitoh, T. R. and Makino, J. (2013). A density-independent formulation of smoothed particle hydrodynamics. *The Astrophysical Journal*, 768(1):44.

Salehi, R. and Dehghan, M. (2013). A moving least square reproducing polynomial meshless method. *Applied Numerical Mathematics*, 69:34–58.

Sanyasiraju, Y. and Chandhini, G. (2008). Local radial basis function based gridfree scheme for unsteady incompressible viscous flows. *Journal of Computational Physics*, 227(20):8922–8948.

Sarrate, J., Huerta, A., and Donea, J. (2001). Arbitrary lagrangianeulerian formulation for fluidrigid body interaction. *Computer Methods in Applied Mechanics and Engineering*, 190(24):3171–3188.

Schaback, R. (1995). Error estimates and condition numbers for radial basis function interpolation. *Advances in Computational Mathematics*, 3(3):251–264.

Schneiders, L., Meinke, M., and Schröder, W. (2013). *A robust cut-cell method for fluid-structure interaction on adaptive meshes*. AIAA Aviation. American Institute of Aeronautics and Astronautics.

Shadloo, M. S., Zainali, A., Sadek, S. H., and Yildiz, M. (2011). Improved incompressible smoothed particle hydrodynamics method for simulating flow around bluff bodies. *Computer methods in applied mechanics and engineering*, 200(9):1008–1020.

Shadloo, M. S., Zainali, A., Yildiz, M., and Suleman, A. (2012). A robust weakly compressible SPH method and its comparison with an incompressible SPH. *International Journal for Numerical Methods in Engineering*, 89(8):939–956.

Shan, Y., Shu, C., and Lu, Z. (2008). Application of local MQ-DQ method to solve 3d incompressible viscous flows with curved boundary. *Computer modeling in engineering and sciences*, 25(2):99.

Shen, Q. (2010). Local RBF-based differential quadrature collocation method for the boundary layer problems. *Engineering Analysis with Boundary Elements*, 34(3):213–228.

Shiels, D., Leonard, A., and Roshko, A. (2001). Flow-induced vibration of a circular cylinder at limiting structural parameters. *Journal of Fluids and Structures*, 15(1):3–21.

Shivanian, E. (2014). Analysis of meshless local and spectral meshless radial point interpolation (MLRPI and SMRPI) on 3-D nonlinear wave equations. *Ocean Engineering*, 89:173–188.

Shu, C., Ding, H., Chen, H., and Wang, T. (2005a). An upwind local RBF-DQ method for simulation of inviscid compressible flows. *Computer Methods in Applied Mechanics and Engineering*, 194(18):2001–2017.

Shu, C., Ding, H., and Yeo, K. (2003). Local radial basis function-based differential quadrature method and its application to solve two-dimensional incompressible navier–stokes equations. *Computer Methods in Applied Mechanics and Engineering*, 192(7):941–954.

Shu, C., Ding, H., and Yeo, K. (2005b). Computation of incompressible navier-stokes equations by local rbf-based differential quadrature method. *CMES: Computer Modeling in Engineering & Sciences*, 7(2):195–206.

Shu, C., Wang, L., and Chew, Y. (2004). Comparative studies of three approaches for GDQ computation of incompressible Navier–Stokes equations in primitive variable form. *International Journal of Computational Fluid Dynamics*, 18(5):401–412.

Siegel Jr, J. M., Parthasarathy, V., Kingsley, G. M., Dionne, P. J., Harrand, V. J., Luker, J. J., and Base, W.-P. A. F. (1998). Application of a multi-disciplinary computing environment (MDICE) for loosely coupled fluid-structural analysis. In *7th AIAA/USAF/NASA/ISSMO Symposium of MDO, AIAA*, pages 98–4866.

Slater, J. (1934). Electronic energy bands in metals. *Physical Review*, 45(11):794.

Smith, M. J., Schuster, D. M., Huttsell, L., and Buxton, B. (1996). Development of an euler/Navier-Stokes aeroelastic method for three-dimensional vehicles with multiple flexible surfaces. *AIAA paper*, (96-1400).

Snell, C., Vesey, D. G., and Mullord, P. (1981). The application of a general Finite-Difference method to some boundary-value-problems. *Computers and Structures*, 13(4):547–552.

Spotz, W. F. and Carey, G. F. (1995). High-order compact scheme for the steady stream-function vorticity equations. *International Journal for Numerical Methods in Engineering*, 38(20):3497–3512.

Steger, J. L. and Benek, J. A. (1987). On the use of composite grid schemes in computational aerodynamics. *Computer Methods in Applied Mechanics and Engineering*, 64(1):301–320.

Sun, Z., Djidjeli, K., Xing, J. T., and Javed, A. (2014). Some modifications of mps method for incompressible free surface flow.

Sváček, P. (2008). Application of finite element method in aeroelasticity. *Journal of Computational and Applied Mathematics*, 215(2):586–594.

Sváček, P., Feistauer, M., and Horacek, J. (2007). Numerical simulation of flow induced airfoil vibrations with large amplitudes. *Journal of Fluids and Structures*, 23(3):391–411.

Takami, H. and Keller, H. B. (1969). Steady two-dimensional viscous flow of an incompressible fluid past a circular cylinder. *Physics of Fluids*, 12(12):II–51–II–56.

Takashi, N. and Hughes, T. J. R. (1992). An arbitrary Lagrangian-Eulerian finite element method for interaction of fluid and a rigid body. *Computer Methods in Applied Mechanics and Engineering*, 95(1):115–138.

Tang, H. S., Casey Jones, S., and Sotiropoulos, F. (2003). An overset-grid method for 3d unsteady incompressible flows. *Journal of Computational Physics*, 191(2):567–600.

Tatari, M. and Ghasemi, F. (2014). The Galerkin boundary node method for magneto-hydrodynamic (MHD) equation. *Journal of Computational Physics*, 258:634–649.

Temam, R. (1991). Remark on the pressure boundary condition for the projection method. *Theoretical and Computational Fluid Dynamics*, 3(3):181–184.

Tolstykh, A. I. and Shirobokov, D. A. (2003). On using radial basis functions in a "finite difference mode" with applications to elasticity problems. *Computational Mechanics*, 33(1):68–79.

Tsuruta, N., Khayyer, A., and Gotoh, H. (2013). A short note on dynamic stabilization of moving particle semi-implicit method. *Computers & Fluids*, 82:158–164.

Tuann, S.-y. and Olson, M. D. (1978). Numerical studies of the flow around a circular cylinder by a finite element method. *Computers & Fluids*, 6(4):219–240.

Udaykumar, H., Shyy, W., and Rao, M. (1996). Elafint: a mixed EulerianLagrangian method for fluid flows with complex and moving boundaries. *International journal for numerical methods in fluids*, 22(8):691–712.

Van Kan, J. (1986). A second-order accurate pressure-correction scheme for viscous incompressible flow. *SIAM Journal on Scientific and Statistical Computing*, 7(3):870–891.

Wang, J. G. and Liu, G. R. (2002a). On the optimal shape parameters of radial basis functions used for 2-D meshless methods. *Computer Methods in Applied Mechanics and Engineering*, 191(23-24):2611–2630.

Wang, J. G. and Liu, G. R. (2002b). A point interpolation meshless method based on radial basis functions. *International Journal for Numerical Methods in Engineering*, 54(11):1623–1648.

Wang, X., Shu, C., Wu, J., and Yang, L. (2014). An efficient boundary condition-implemented immersed boundary-lattice Boltzmann method for simulation of 3d incompressible viscous flows. *Computers & Fluids*, 100:165 – 175.

Wang, Y., Shu, C., Teo, C., and Wu, J. (2015). An immersed boundary-lattice boltzmann flux solver and its applications to fluid–structure interaction problems. *Journal of Fluids and Structures*, 54:440–465.

Waters, J. and Pepper, D. (2015). Global versus localized RBF meshless methods for solving incompressible fluid flow with heat transfer. *Numerical Heat Transfer, Part B: Fundamentals*, 68(3):185–203.

Wing Kam, L., Sukky, J., and Yi Fei, Z. (1995). Reproducing kernel particle methods. *International Journal for Numerical Methods in Fluids*, 20(8-9):1081–1106.

Wright, G. B. and Fornberg, B. (2006). Scattered node compact finite difference-type formulas generated from radial basis functions. *Journal of Computational Physics*, 212(1):99–123.

Wu, J., Qiu, Y., Shu, C., and Zhao, N. (2014). Pitching-motion-activated flapping foil near solid walls for power extraction: A numerical investigation. *Physics of Fluids (1994-present)*, 26(8):083601.

Wu, X.-H., Tao, W.-Q., Shen, S.-P., and Zhu, X.-W. (2010). A stabilized MLPG method for steady state incompressible fluid flow simulation. *Journal of Computational Physics*, 229(22):8564–8577.

Xia, J. and Leung, D. (2003). *A Stable Numerical Method for the Time Dependent Navier-Stokes Equations and Its Application in Street Canyon Flows*. Springer Berlin Heidelberg.

Xiao, Q. and Zhu, Q. (2014). A review on flow energy harvesters based on flapping foils. *Journal of Fluids and Structures*, 46:174–191.

Ye, T., Mittal, R., Udaykumar, H., and Shyy, W. (1999). An accurate cartesian grid method for viscous incompressible flows with complex immersed boundaries. *Journal of Computational Physics*, 156(2):209–240.

Yeo, K., Ang, S., and Shu, C. (2010). Simulation of fish swimming and manoeuvring by an svd-gfd method on a hybrid meshfree-cartesian grid. *Computers & Fluids*, 39(3):403–430.

Young, J., Lai, J. C., and Platzer, M. F. (2014). A review of progress and challenges in flapping foil power generation. *Progress in Aerospace Sciences*, 67:2–28.

Zhuang, X., Cai, Y., and Augarde, C. (2014). A meshless sub-region radial point interpolation method for accurate calculation of crack tip fields. *Theoretical and Applied Fracture Mechanics*, 69:118–125.